THÈSE

En vue de l'obtention du

DOCTORAT DE L'UNIVERSITÉ DE TOULOUSE

Délivré par :

Institut National Polytechnique de Toulouse (INP Toulouse)

Discipline ou spécialité :

Energétique et Transferts

Présentée et soutenue par :

M. TRISTAN AGAESSE

le jeudi 10 novembre 2016

Titre :

Simulations of one and two-phase flows in porous microstructures, from tomographic images of gas diffusion layers of proton exchange membrane fuel cells

---

Ecole doctorale :

Mécanique, Energétique, Génie civil, Procédés (MEGeP)

Unité de recherche :

Institut de Mécanique des Fluides de Toulouse (I.M.F.T.)

Directeur(s) de Thèse :

M. MARC PRAT

Rapporteurs :

M. JEROME VICENTE, POLYTECH MARSEILLE
M. YANN BULTEL, INP DE GRENOBLE

Membre(s) du jury :

M. OLIVIER LOTTIN, UNIVERSITE DE LORRAINE, Président
M. JOEL PAUCHET, CEA GRENOBLE, Membre
M. MARC PRAT, INP TOULOUSE, Membre
Mme MARION CHANDESRIS, CEA GRENOBLE, Membre

Remerciements

Une thèse est une expérience riche. C’est une aventure intellectuelle, une exploration des frontières de la connaissance. C’est aussi une belle séquence de vie, faite de rencontres, de découvertes et de joies. Enfin, c’est un engagement personnel fort, dédié dans mon cas à la lutte contre le réchauffement climatique.

Je remercie les personnes avec qui j’ai eu la chance d’échanger pendant ces trois années et qui m’ont beaucoup appris, tant sur le plan professionnel que personnel. Je tiens à remercier tout particulièrement :

Mon directeur de thèse, Marc Prat, pour sa bienveillance, son soutien et ses conseils enrichissants tout au long de cette thèse.

Les membres du jury devant lesquels j'ai présenté cette thèse pour leur lecture attentive de mon manuscrit et leurs remarques et questions au cours de ma soutenance.

Mes collègues du Laboratoire des Composants pour Piles et du Laboratoire de Modélisation du CEA Liten, tout particulièrement Joël Pauchet et Marion Chandesris qui ont suivi avec attention mes travaux.

Mes amis grenoblois, mes camarades doctorants et les membres de l’association des jeunes chercheurs du CEA Grenoble, pour les excellents moments passés ensemble.

Mes professeurs tout au long de mes études.

Ma famille et mes parents qui m’ont soutenu avec amour pendant ces nombreuses années d’études.

Abstract

Hydrogen as an energy carrier is a promising solution for reducing emissions of greenhouse gases. Indeed, hydrogen can be used to store large amounts of energy in a completely carbon-free way. To promote the widespread use of hydrogen energy, it is essential to reduce the cost of fuel cells and increase their durability and performance.

The materials in the heart of fuel cells have a strong impact on their performance and durability. In this context, optimizing the materials is crucial. We develop in this thesis a modeling approach of porous materials in proton exchange membrane fuel cells. We focus on a specific material that takes part in the gas diffusion layers (GDL).

The gas diffusion layers are crossed by gas, electron, heat and water fluxes. To allow such multiple transports, GDL are composed of a fluid phase and a solid phase, itself consisting of several materials. The microstructure of the GDL plays an essential role on the tradeoffs between transports. To model these tradeoffs, we use X-ray tomography to image the microstructure at micrometer scales, and develop digital tools to simulate the transport on tomographic images. We validate the simulations with experimental characterizations and tomographic images of GDL. Great care has been taken in the computer performance of the numerical tools, because tomographic images in three dimensions are a challenge because of the size of the data.

The first chapter of this thesis is devoted to modeling of an ex-situ water injection experiment in a GDL. We develop a pore network model extracted from tomographic images, to simulate liquid water flows in GDL in the presence of capillary forces. We validate pore networks simulations using tomographic images showing the liquid water in a GDL during a water injection experiment. We show that the capillary pressure curves can be determined reliably by pore network simulations or full morphology simulations on tomographic images.

The second chapter is devoted to one-phase transport simulations in GDL. The first part of this chapter is devoted to the development of pore networks simulations for the diffusivity and the electrical conductivities of the GDL. We develop a two-scale simulation methodology, which consists of decomposing the image into elements having simple shapes, and to calibrate physical models on these elements. This method considers the effect of the microstructure on the physical transfers in an economical way, reducing the computing time. We compare the pore network simulations to direct simulation on microstructures and to analytical formulas. The second part is devoted to the comparison of transport simulations with experimental measurements. We show that the transports in the fluid phase can be determined reliably by direct simulations on the tomographic images, while transports in the solid phase require additional information not provided by X-ray tomography.

The third chapter is devoted to modeling of the condensation of water in the GDL. The steam produced by the reaction of the hydrogen with the oxygen passes through the GDL and condenses in the cold areas of the GDL. A pore network model coupling diffusion of steam, phase change and capillary forces is developed. We study this model on virtually generated pore networks.

The last chapter is devoted to the study of virtually designed microstructures. Virtually exploring new materials designs has advantages over the experimental approach, in terms of speed, cost and control over the microstructures. We show that it is possible to virtually produce microstructures close to those of real materials, to seek optimal microstructures, and control the microstructure to better study some physical effects using simulation.

Keywords

Fuel cell, Pore network, Tomography, Two-phase flow, Gas Diffusion Layers, Image analysis

Résumé

L’hydrogène comme vecteur énergétique est une solution prometteuse pour réduire les émissions de gaz à effet de serre. En effet, l’hydrogène permet de stocker de grandes quantités d’énergie de façon totalement décarbonée. Pour favoriser l’utilisation à grande échelle de l’énergie hydrogène, il est essentiel de réduire le coût des piles à combustible et d‘augmenter leur durabilité et leurs performances.

Les matériaux situés au cœur des piles à combustible ont un impact fort sur leurs performances et leur durabilité. Dans ce contexte, optimiser les matériaux est crucial. Nous développons dans cette thèse une démarche de modélisation des matériaux poreux des piles à combustible à membrane échangeuse de protons. Nous nous concentrons sur un matériau en particulier, celui intervenant dans les couches de diffusion des gaz (GDL).

Les GDL ont de multiples fonctions, notamment de permettre en leur sein des transports simultanés de gaz, d’électrons, de chaleur et d’eau sous forme vapeur et liquide. Pour permettre ces transports, les GDL sont composées d’une phase fluide et d’une phase solide, elle-même constituée de plusieurs matériaux. La microstructure des GDL joue un rôle crucial sur les compromis entre les fonctions des GDL et l’efficacité des transports. Nous utilisons la tomographie aux rayons X pour imager la structure interne des GDL à l’échelle micrométrique, et développons des outils numériques pour simuler les transports sur les microstructures. Nous montrons que des simulations sur des images de grandes tailles sont réalisables en temps raisonnables. Nous validons les simulations de transports dans les GDL numériquement et expérimentalement.

Le premier chapitre est consacré à la modélisation d’une expérience ex-situ d’injection d’eau dans les GDL. Nous développons un modèle réseau de pores extrait d’images tomographiques, pour simuler les écoulements d’eau dans les GDL en présence de forces capillaires. Nous validons les simulations réseaux de pores en utilisant des images tomographiques montrant l’eau liquide dans une GDL lors d’une expérience d’injection d’eau. Nous montrons que les courbes de pression capillaire peuvent être déterminées par simulations réseau de pores ou par simulations full morphology sur des images tomographiques.

Le deuxième chapitre est consacré à la simulation des transports de gaz et d’électrons dans les GDL. Nous développons une méthode de simulation réseau de pores, consistant à décomposer l’image en régions de formes simples et à calibrer des modèles physiques sur ces régions. Cette approche à deux échelles est économe en temps de calcul. Nous comparons ces simulations à des simulations directes et à des formules analytiques. Une seconde partie concerne la comparaison des simulations directes à des mesures expérimentales. Nous montrons que les transports dans la phase fluide peuvent être déterminés avec fiabilité par simulation directe sur les images tomographiques, tandis que la simulation des transports dans la phase solide nécessite des informations non fournies par la tomographie aux rayons X.

Le troisième chapitre est consacré à la modélisation de la condensation de l’eau dans les GDL. La vapeur d’eau produite par la réaction du dihydrogène avec le dioxygène traverse les GDL et condense dans les zones froides des GDL. Un modèle réseau de pores couplant diffusion de la vapeur d’eau, changement de phase et forces capillaires est développé. Nous étudions ce modèle sur des réseaux de pores générés virtuellement.

Le dernier chapitre est consacré à l’étude de microstructures conçues virtuellement. Explorer virtuellement de nouveaux designs de matériaux a des avantages par rapport à l’approche expérimentale, en termes de rapidité, de coût et de maitrise de la microstructure. Nous montrons qu’il est possible de produire virtuellement des microstructures proches de celles de matériaux réels, de chercher des microstructures optimales, et d’étudier des effets physiques par simulation sur matériaux virtuels.

Mots-clés

Pile à combustible, Réseaux de pores, Tomographie, Ecoulement diphasique, Couche de diffusion des gaz, Analyse d'image

Content

Abbreviations

GDL	Gas Diffusion Layer
EDP	Equation aux Dérivées Partielles
IBM	Immersed Boundary Method
JPS	Journal of Power Sources
LBM	Lattice Boltzmann Method
MIP	Mercury Intrusion Porosimetry
MPL	Microporous Layer
MRI	Magnetic Resonance Imaging
OCV	Open Circuit Voltage
PEM	Polymer Electrolyte Membrane
PEMFC	Polymer Electrolyte Membrane Fuel Cell
PTFE	Polytetrafluoroethylene

List of figures

List of tables

List of equations

Chapter 1 Introduction

Hydrogen used as an energy carrier is a promising solution for reducing greenhouse gas emissions. Indeed, the dihydrogen makes it possible to store large quantities of energy in a totally decarbonized way. The energy is stored in chemical form in dihydrogen molecules, H_2. When the dihydrogen, H_2, reacts with the oxygen from the air, O_2, to form water, H_2O, the chemical energy is released and can be used. The environmental emissions from this chemical reaction are water and heat.

The dihydrogen does not exist in the natural state; therefore, it must be produced. There are many methods to produce dihydrogen [Dincer2015]. These vary in terms of costs and emissions of greenhouse gases. When dihydrogen is produced from decarbonized energy, for example by electrolysis of water from electricity of renewable origin, or by reforming biogas, the carbon balance of the production of dihydrogen is quasi-neutral. This explains the interest of the dihydrogen from the environmental point of view.

Reducing greenhouse gas emissions is crucial to keeping global warming below 2°C. Beyond this threshold, risks to humanity are manifold: food insecurity due to deteriorating crop yields and declining animal populations, population migration due to rising sea levels, increased frequency of extreme climate events [IPCC2014]. Recall that global warming is due to greenhouse gas emissions during the industrial period, from 1870 to the present day, driven by the use of fossil fuels, which contributed to develop the economies of the industrialized countries [Paris2015]. CO_2 emissions are still increasing worldwide [IEA2013]. These increases are mainly due to economic growth in emerging countries [IPCC2014]. To reduce global greenhouse gas emissions while ensuring the economic development of emerging countries, economic, social and technological changes are required to drastically reduce emissions per gross domestic product (GDP). In Europe and France, the objective is to reduce greenhouse gas emissions of 1990 by a factor of 4 by 2050 [EuropeEnergy2011] [Tuot2007].

The storage of electric energy has an essential role to play in this context. A primary utility of storage is to ensure the stability of electrical networks in the presence of intermittent renewable energies [USStorage2013]. Having better means of energy storage would thus increase the share of renewables in electricity generation. Storing large quantities of energy is also important for the transport sector. This sector is responsible for more than 10% of greenhouse gas emissions [IEA2014]. Dihydrogen is relevant for transport because it has a high energy density, which allows to store large quantities of energies in a vehicle with a moderate mass [Durbin2013].

Fuel cells are the electrochemical devices used to control the chemical reaction between dihydrogen and dioxygen so that energy is released primarily in useful electrical form. Fuel cells therefore play an essential role in the use of dihydrogen as an energy carrier. Fuel cells account for a significant portion of the costs of using dihydrogen. They are the subject of much research aimed at reducing their cost, increasing their durability and improving their performance.

This thesis is part of a global approach to modeling fuel cells to improve the competitiveness of this technology. The objective of modeling is to improve our understanding and control of the physical phenomena taking place in fuel cells. In particular, transport in porous electrodes plays a crucial role in the operation of fuel cells.

In this thesis, we concentrate on a porous material involved in the electrodes of fuel cells, gas diffusion layers (GDL). GDLs have many functions, including allowing simultaneous transport of gases, electrons, heat and water in steam and liquid form. The microstructure of the GDL plays a crucial role on the compromises between the multiple functions of the GDL and the efficiency of transport in the electrodes. The objective of this thesis is to model the transport properties of GDLs, to better know them and to be able to optimize them. Modeling is an essential tool because the transport properties of GDLs are often difficult to measure experimentally because of their small thickness (300 µm). To better understand the effect of the microstructure of porous materials on transport, we take advantage of the advances in imaging techniques that allow us to know precisely the microstructure of porous electrode materials today. We concentrate on a component of the electrodes, the GDLs, because we have high-quality images of their microstructures obtained by X-ray tomography.

The remainder of this introduction consists of a presentation of the general operation of fuel cells and of the stakes represented by transport in the gas diffusion layers. We then present the objectives of this thesis and the approach implemented.

1.1 The proton exchange membrane fuel cell technology

In this section, we present the principle of proton exchange membrane (PEM) fuel cells, the different types of losses that occur in the cells, the materials that make up the core of the cells, and finally the problem of the water management in the cells.

1.1.1 General operation

The fuel cell is for the dihydrogen what the combustion engine is for oil: the device by which the chemical energy of hydrogen gas is converted into usable energy. We describe here the principle of operation of a PEM fuel cell.

The chemical energy contained in the H_2 dihydrogen molecules is released during the oxidation-reduction reaction with O_2 dioxygen. The equation of this reaction is :

$$2H_2 + O_2 \rightarrow 2H_20$$

Équation 1.1

If this reaction took place in the open air, by direct combustion of the dihydrogen in the dioxygen, the energy would be violently released in the form of heat. For the reaction to produce electricity, it is controlled in an electrochemical device, the fuel cell. Figure 1.1 illustrates the principle of proton exchange membrane fuel cells.

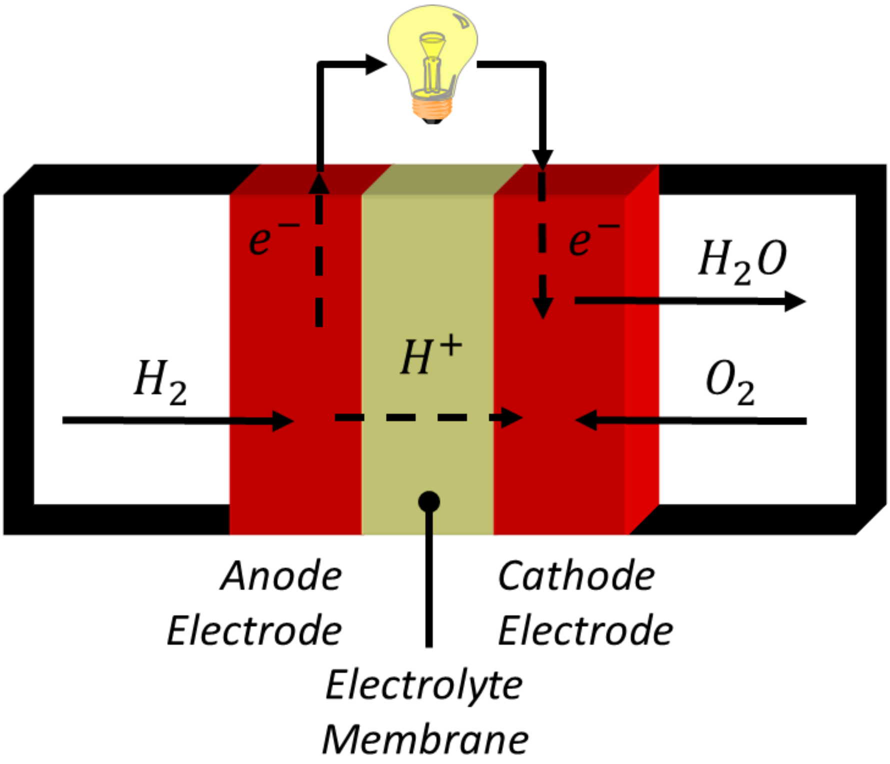

Figure 1.1 Schematic diagram of a proton-exchange membrane fuel cell.

The reaction is decomposed into two half-reactions occurring in two separate compartments, the anode and the cathode.

At the anode, the dihydrogen decomposes into protons and electrons, in contact with a catalyst. This reaction is endothermic at normal operating temperatures.

$$2H_2 \rightarrow 4H^+ + 4e^-$$

Équation 1.2

At the cathode, protons and electrons combine with the dioxygen to form water, with the aid of a catalyst. This reaction is exothermic at normal operating temperatures.

$$0_2 + 4H^+ + 4e^- \rightarrow 2H_20$$

Équation 1.3

The two reactive gases 0_2 and H_2 are in principle never in direct contact. They are kept separated by a solid electrolyte, the proton exchange membrane (PEM), almost impermeable to gases but letting the protons pass. The electrons are guided by electrical conductors to an external electrical circuit, so that their energy is used in electrical form. The fuel cell is fed continuously with H_2 and 0_2, which allows the production of electricity continuously.

Although the reactive gases are not in physical contact, the reaction nevertheless occurs because these gases are indirectly in electrical contact, via the electrons and the ions which can circulate between the anode and the cathode. The molecules see electrical potentials linked to the oxidation-reduction couple, allowing the release or capture of electrons.

1.1.2 Performance and losses

The chemical energy of gases is converted largely into electrical energy in the fuel cell. But, because of a certain number of physical phenomena which we describe in this section, this conversion is not perfect. Losses occur and reduce system performance.

Generation of electricity by the fuel cell is measured by the cell voltage, V_{cell}, and by the quantity of current produced, I. When the current is zero, the theoretical voltage of the cell corresponds to the Nernst electrochemical potential of the two half-reactions, $V_{Nernst} = 1.229\ V$ at 25°C and normal pressure conditions. The voltage at zero current is denoted V_{OCV} in the following. The voltage V_{OCV} measured is slightly lower than the theoretical value V_{Nernst}, because of the small amounts of 0_2 and H_2 which pass through the membrane [Vilekar2010]. Figure 1.2 shows the typical electrical behavior of a PEM fuel cell.

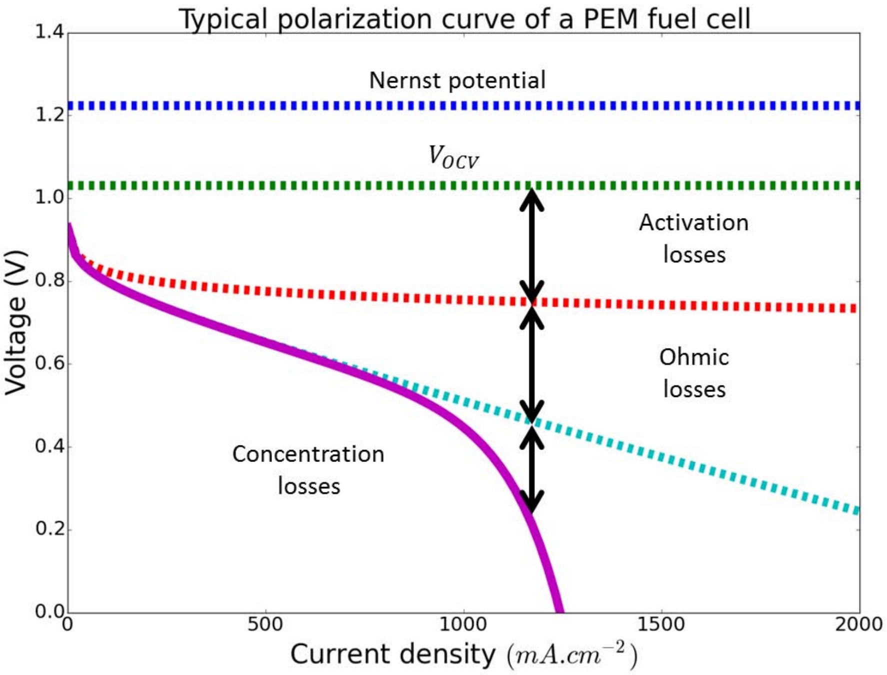

Figure 1.2 Typical polarization curve of a PEM fuel cell.

When current is generated, additional voltage losses occur. The voltage losses can be decomposed into activation polarization $\eta_{act}(i)$, ohmic polarization η_{IR} and concentration polarization η_{conc} [O'Hayre2009].

$$V_{cell}(i) = V_{OCV} - \eta_{act}(i) - \eta_{IR}(i) - \eta_{conc}(i)$$

Équation 1.4

The activation losses are related to the kinetic limits of the chemical reaction. For the reaction to occur, reactive species and intermediate species must overcome several energetic barriers. The electrical potential of the cell affects the ability of these species to overcome barriers, which leads to a relationship between cell potential and reaction rate. The relationship between current and resulting voltage can be described by the Tafel equation:

$$\eta_{act} = \frac{RT}{anF} ln\left(\frac{i}{i_0}\right)$$

Équation 1.5

Where F is the Faraday constant, R is the universal constant of the perfect gases, T is the reaction temperature, α is the electron transfer coefficient, n is the number of electrons transferred per reaction and i_0 is the exchange current density. The exchange current density depends on the activity of the catalysts and the concentration of reactants in the catalytic layers.

The ohmic losses η_{IR} are due to the ohmic resistance occurring during transfer of protons and electrons in materials. They are expressed by the following equation:

$$\eta_{IR} = i \times (R_1 + R_2 + \cdots)$$

Équation 1.6

where R_1, R_2, … are the ohmic resistances of the different materials. The largest ohmic losses are caused by the transport of protons in the membrane and the electrical contact resistances between the battery components.

The concentration losses are related to the fact that when the current density is high, the gas transfers through the electrode have difficulty in supplying the reactive gases sufficiently quickly. This leads to a reduction in the concentration of the reactants at the level of the catalysts, which results in a decrease in the local exchange current density and thus in additional activation losses. The current of the cell to which the reactive gas concentration reaches zero is called the limit current density, i_L. It depends on the effective diffusion coefficient of the dioxygen in the porous materials of the cathode and the concentration of dioxygen in the channel bringing the dioxygen to the surface of the cathode. The concentration overvoltage can be expressed by the following formula [Barbir2005]:

$$\eta_{conc} = \frac{RT}{\alpha n F} ln\left(\frac{i_L}{i_L - i}\right)$$

Équation 1.7

The transport of reactive gases through the electrodes is limited by several factors. The diffusion of oxygen is slower than that of dihydrogen, because on the one hand its concentration is generally lower because it is contained in the air and because on the other hand it is a heavier molecule therefore its binary diffusion coefficient is lower. The effective diffusion coefficient in the porous medium also depends on the microstructure of the electrodes. Finally, when much water is produced by the cell, the water tends to condense in the GDL and fill the pores, which limits the access of gases.

In this thesis, we concentrate on the concentration losses due to the transfer of species and the ohmic losses due to the transfer of electrons in a porous material of fuel cell, the gas diffusion layer.

1.1.3 Materials

The core of the cell is composed of two electrodes, anode and cathode, separated by a membrane. The electrodes are formed from several layers: catalytic layer and gas diffusion layers (GDL). Figure 1.3 illustrates schematically the exchanges between these different layers and the exchanges between the core of the stack and the bipolar plates situated on either side. The role of bipolar plates is to supply reactive gases to the core of the cell, to capture the electrons produced at the anode and to return them to the cathode, and to evacuate the heat and water produced in the core of the cell. Figure 1.4 shows a cross-sectional view of a real membrane-electrode assembly (MEA). We describe here in detail the materials constituting the MEAs.

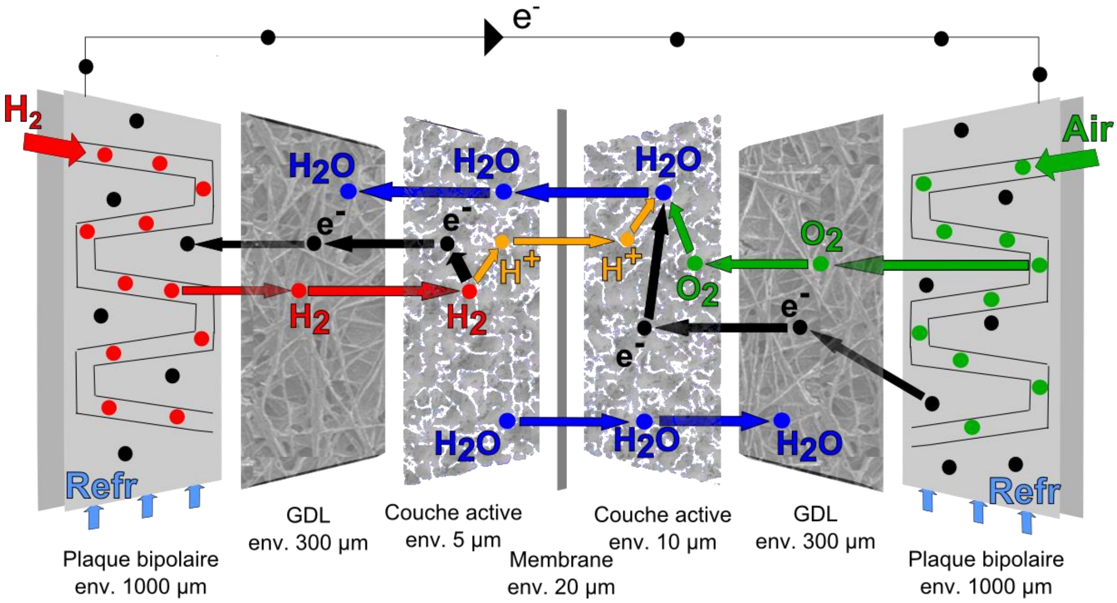

Figure 1.3 Diagram illustrating the operation of a PEMFC fuel cell cell and sectional view of its constituents. Figure extracted from [Robin2015].

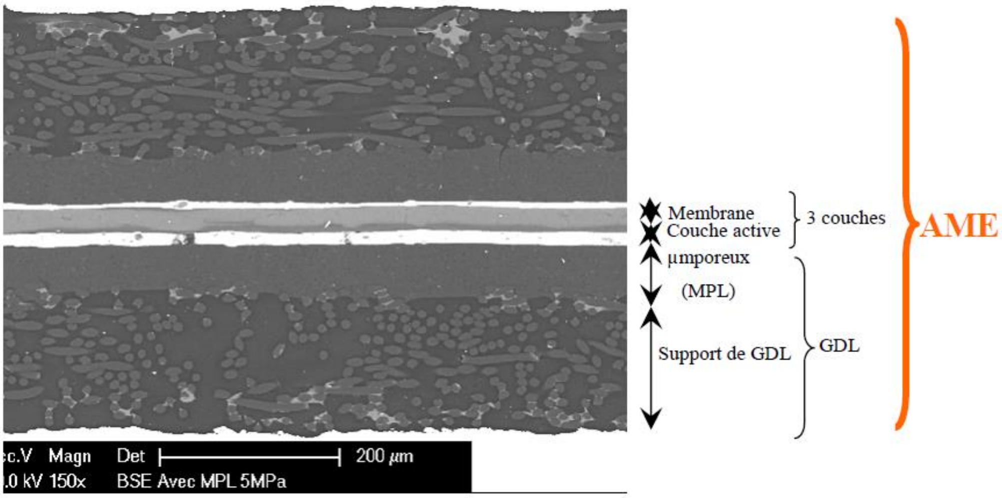

Figure 1.4 Sectional view of an electrode membrane assembly. Image made with a scanning electron microscope (SEM). Image from [CHAMEAU2010].

The role of the membrane is to be impermeable to the gases H_2 and 0_2, as far as possible, but to transport the H^+ ions. This selective permeability is obtained by the material of the membrane, which has different physical and chemical interactions with gas and protons. The membrane consists of a proton-conducting ionomer. This ionomer is often Nafion, a fluoropolymer, consisting of fluorine carbon chains, providing mechanical strength and resistance to acidity, and of hydrophilic SO_3H groups [Peighambardoust2010]. The Nafion has the possibility of nanostructuring to form nanometric conduits filled with water, through which the protons can circulate thanks to their affinity with the water molecule, by hoping or diffusion [Peighambardoust2010]. The level of hydration of the membrane has a significant impact on its effective proton conductivity. Therefore, it is necessary to maintain a certain humidity near the membrane [Ji2009]. Water can circulate through the membrane between the anode and the cathode, through electro-osmosis and diffusion [Kraytsberg2014].

Anodic and cathodic catalytic layers are the site of electrochemical reactions. These layers are located on either side of the membrane. The catalytic layers are composed of platinoid catalysts supported by carbon. Chemical reactions occur when the gases reach the surface of the catalysts. To maximize the chemical reaction rate, the catalytic layers have a microstructure that maximizes the developed surface area per unit volume. To reach high surfaces, the catalysts are formed of grains of a few nanometers in diameter. The carbon supports are made of grains of carbon black, which allows to reach specific surfaces of 10 to 1000 m² per gram. The role of the carbonaceous support is to mechanically support the catalyst and to conduct the electrons required for the oxidation-reduction reactions. Proton-conducting ionomer (often Nafion) is added to the catalytic layers to conduct the protons to or from the membrane. The catalytic layers are produced by coating an ink on the membrane or on the diffusion layers. Their thickness generally varies between 5 µm and 30 µm. Figure 1.5 a) shows SEM images of the microstructure of the catalytic layer. The exact microstructure of the catalytic layers is the product of complex interactions between carbons, Nafion, catalysts and chemical additives used in ink. It is a porous microstructure, the pores of which typically measure between 5 nm and 200 nm.

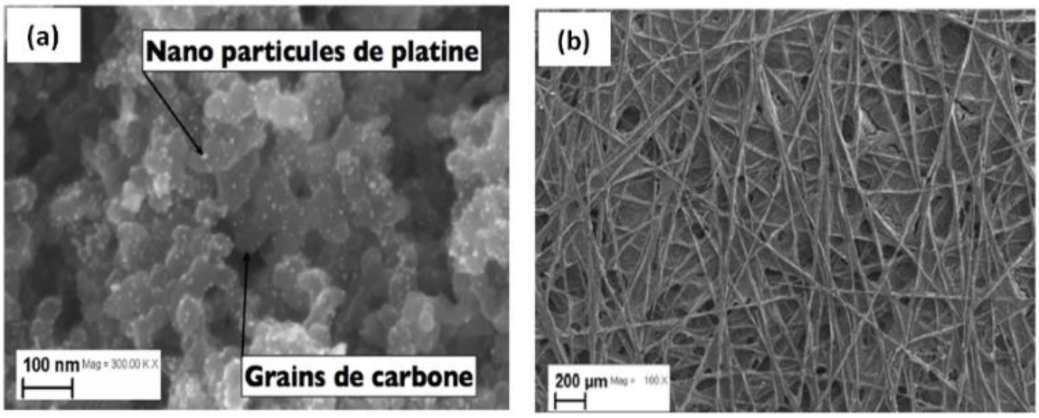

Figure 1.5 SEM image of porous materials used in PEM fuel cell electrodes. a) catalytic layer b) gas diffusion layer. Images from [CHAMEAU2010].

The diffusion layers are located between the bipolar plates and the catalytic layers. Figure 1.6 shows how a bipolar plate and a GDL are in contact. The role of the GDLs is to homogenize the transfers between the bipolar plate and the catalytic layer. Indeed, the GDLs allow the gases to reach the catalytic zones located under the ribs of the bipolar plate, leaving a thickness between ribs and catalytic layer. GDLs also have a mechanical role. They protect, by deforming, the catalytic layers and the membrane when the bipolar plates are compressed against the MEA to obtain good electrical contact.

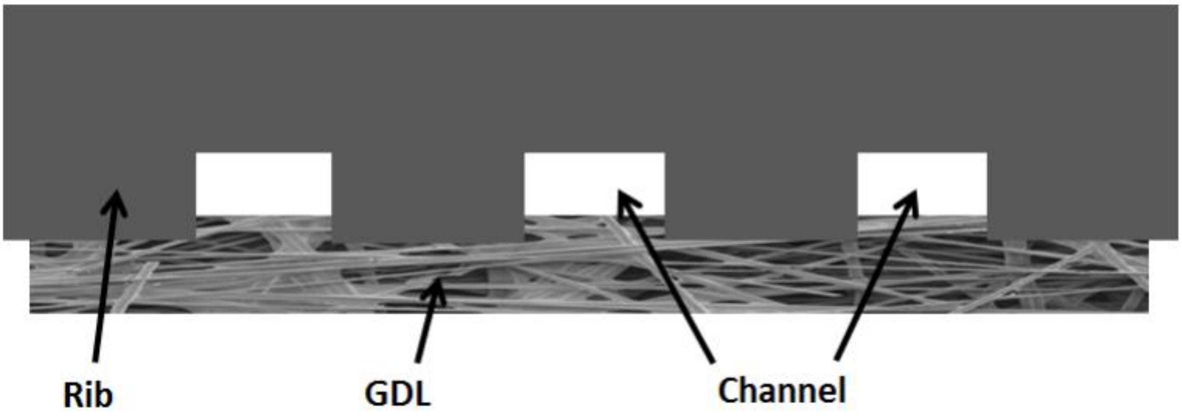

Figure 1.6 GDL in contact with a bipolar plate. Image from [Straubhaar2015].

The GDLs are crossed by flows of reactive gas, heat and electrons. To this are added the flows produced at the cathode. To allow these flows, GDLs are porous materials. The electrons circulate through the electrically conductive solid phase. Reactive gases and water circulate through the pores. The thickness of the GDL is very thin (~150-300 µm) so that the transport resistances through the thickness of the GDL (through-plane) are minimized. Transport in the plane of the GDL (in-plane) allow the gases to reach the areas beneath the teeth of the bipolar plates. Transfers in GDL to and from the bipolar plate take place in two distinct zones: electrons circulate through the rib of the bipolar plate, in contact with the GDLs, while the gases flow through the channels of the bipolar plate, in contact with the GDLs too. Figure 1.7 shows these transfers in GDL in the presence of a bipolar plate.

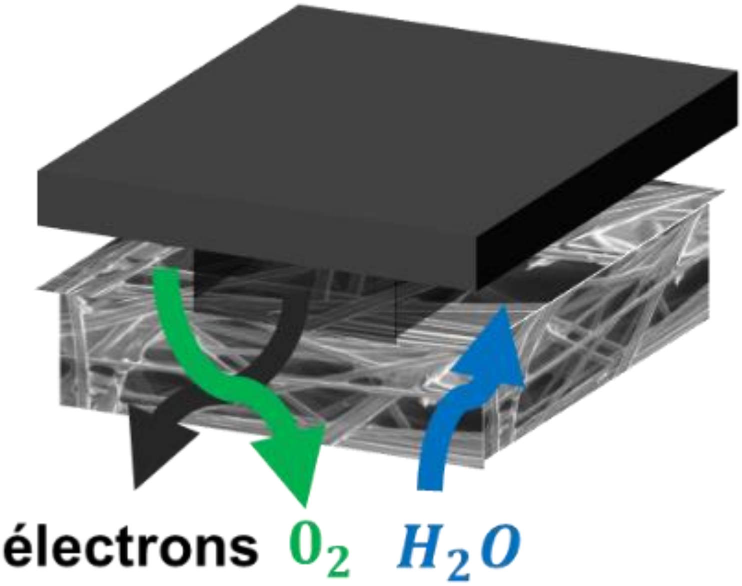

Figure 1.7 Transport of reactive gases, electrons and water vapor in a GDL inserted between a bipolar plate and a catalytic layer (the microporous layer is not shown).

Figure 1.5 b) shows a SEM image of the microstructure of a GDL. The GDLs are composed of carbon fibers whose diameter is between 6 and 10 µm. The fibers are held together by a carbon binder (carbonaceous binder). A hydrophobic treatment involving PTFE (Teflon) is often added to limit the accumulation of water in GDL. The distribution of this treatment is often non-uniform, as it is distributed mainly in the surface layers of the GDL.

The porosity of GDL is between 70 and 90% [Rashapov2015]. The pore diameters are of the order of a few tens of micrometers. The physical properties of GDL are anisotropic because of the microstructure is anisotropic.

A microporous layer (MPL) is often added between the diffusion layer and the catalytic layer. Figure 1.8 shows a sectional view of a MPL-GDL assembly. The MPL is formed from carbon grains mixed with PTFE. Its thickness generally varies between 20 µm and 60 µm. It serves as a diffusion layer for gases and a conduction layer for electrons and heat. As such, it is sometimes considered to be part of the gas diffusion layer. The sizes of its pores are like those of the catalytic layers. It therefore makes it possible to have a porosity gradient in the diffusion layer. It is found experimentally that the microporous layer improves the performance of the membrane-electrode assembly, but its exact role is still uncertain. It makes it possible to protect the catalytic layer from mechanical perforation by the fibers of the GDL. It adds resistance to thermal and gas diffusion, which changes the conditions in the catalytic layers and can have a beneficial effect on water management in the MEA.

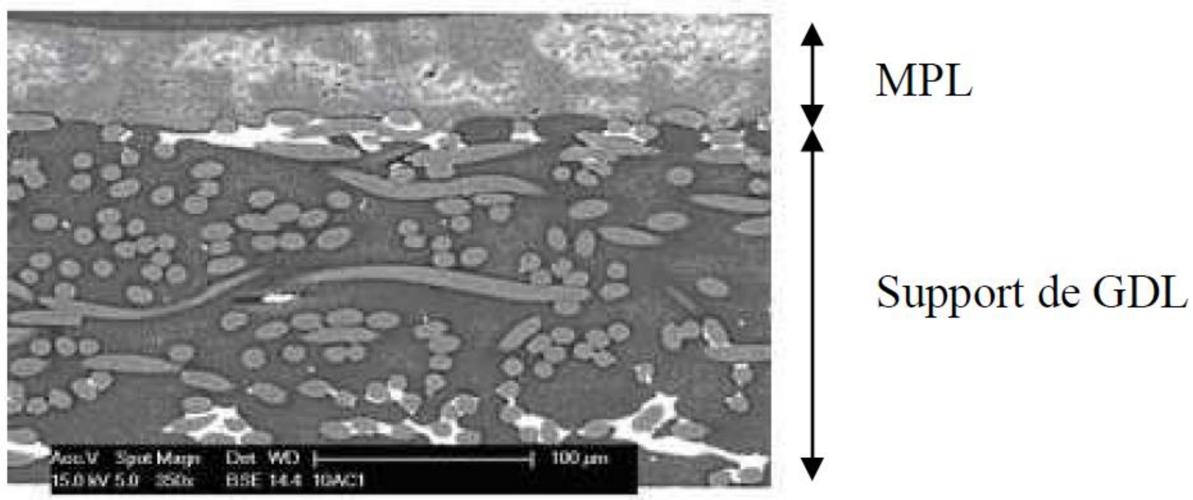

Figure 1.8 Sectional view of a GDL Freudenberg H2315T10A with MPL, obtained by scanning electron microscopy on a sample coated with epoxy resin and then polished [CHAMEAU2010].

1.1.4 Water management

Water is continuously produced by the chemical reaction at the cathode and must be evacuated from the AME. There is a balance to keep on the amount of water present in the pile. In fact, too much water in liquid form blocks the pores and prevents gases from reaching the catalytic layers at the reaction sites. On the other hand, not enough water dries out the membrane, which prevents the protons from circulating from the anode to the cathode. This is the issue of water management.

It is possible to vary the external conditions, for example the physical conditions of the injected gases (pressure, temperature, humidity), or the rate of water production. Optimum conditions are difficult to obtain, because local conditions are not the same throughout the stack. Indeed, each mm² of cell is a source of heat and water and consumes reactive gases. The temperatures, water contents and concentrations of reactive gases are homogenized by cooling circuits and gas circuits running through the stack. However, the efficiency of these fluid circuits is limited, so the temperatures, humidity and reactive gas concentrations vary spatially in the cell. On the other hand, the rate of water production depends directly on the current produced by the cell, which is subject to a variable load by the electric circuit, for example in the case of a car changing speed.

The water is transported in the porous electrodes by vapor diffusion and optionally in liquid form by capillary pressure, and passes through the membrane by diffusion and electro-osmosis. The wettability and microstructure of porous media (pore sizes for example) are parameters which can be used to tune water transfers. Information on two-phase transport in the electrode materials is given in section 2.2.

GDL has an important role in water management. Indeed, water often condenses in the GDL, which blocks its pores. A hydrophobic treatment (PTFE) is often applied to the GDL to prevent it from being drowned. However, the material added during this treatment may have the effect of blocking certain pores, and therefore of decreasing the effective diffusivity of the GDL. This treatment can also decrease the effective electrical conductivity of the GDL, as PTFE is a very poor electrical conductor. Besides, it has been found that the addition of a microporous layer changes the diffusion of water vapor and influences water management. The precise role of the microporous layer is still uncertain. The thermal conductivities of GDL and MPL also potentially play an important role in water management by changing the phase change conditions of the water.

1.1.5 Material issues

The goals to increase the competitiveness of fuel cells are to reduce their cost of production, increase their lifetime, and reduce their losses. The materials in the membrane-electrode assemblies have an essential role in achieving these objectives.

The platinum in the catalytic layers is the first cost source if the fuel cells are produced in large quantities, although now the membrane also represents a high cost. Mass production will greatly reduce the price of all materials except platinum [Moreno2015]. Indeed, the cost of platinum is linked to its rarity. The price of platinum may even increase if demand increases. An essential issue for fuel cells is therefore to reduce the amount of platinum used. The considered solutions are for example the nanostructuring of the platinum so that the platinum is better used, or the optimization of the material supporting the platinum [Debe2012]. In the longer term, the use of platinum-free catalysts is studied, but the performances of these catalysts are still much lower than those of platinum [Debe2012].

The durability of the materials has an impact on the total cost of a fuel cell over its lifetime. The lifetime of fuel cells is limited by the degradation of electrode materials [Dubau2014]. The electrode materials are subjected to demanding conditions: acidity, oxidation potentials, heat, humidity. Degradation phenomena are, for example, Oswald's maturation, which reduces the specific surface area of platinoid catalysts and the oxidation of the carbon support of the active layer. Carbone is widely used in fuel cells because it is resistant to corrosion, electrically conductive, and generally cheap. Carbon exists in many forms, such as carbon blacks having a very large specific surface area, carbon fibers having high mechanical strength, carbon nanotubes having high electrical conductivity, excellent mechanical strength and chemical stability. The considered solutions for increasing the lifetime of the materials are, for example, to use more resistant carbon supports, such as carbon nanotubes, and to play on the operating conditions and the design of the batteries to avoid unfavorable local scale physical conditions (hot spots, high oxidation potentials, etc.).

The optimization of the transfers in the materials makes it possible to reduce the losses. These transfers are of many types: transfers of protons in the membrane, transfers of gas, heat, electricity, water in the porous electrode materials. Transfers in porous materials depend on the microstructure and the intrinsic (bulk) properties of the constituents, as discussed in Chapter 2. It is therefore possible to play on one or the other parameter to improve transfers. The design choices of materials often result from compromises between opposing objectives. We are interested in this thesis to the transfers in the GDL. Optimizing the transfer of electrons and gas through the thickness of GDL is an example of opposing objectives. Having a high conductivity and a high diffusivity is contradictory because increasing porosity promotes diffusivity to the detriment of conductivity and vice versa. Under these conditions, improving transfers requires a clear understanding of the physical parameters driving these transfers, and the model we use should be precise enough to account for compromises between several properties.

1.2 Thesis work

1.2.1 Goals

Transports in porous electrodes play a crucial role in the operation of fuel cells. Improving transport efficiency in porous electrode materials reduces diffusion losses and ohmic losses. It is interesting to reduce losses for two reasons. Firstly, this reduces fuel consumption H_2. Secondly, this makes it possible to obtain a higher surface current, which makes it possible to reduce the catalytic surface required in the fuel cells and thus their cost. In this thesis, we concentrate on a porous material in the gas diffusion layers (GDL), because we have tomographic images of the GDL microstructure.

The goal of this thesis is to model the transport properties of GDL. The GDLs are crossed by gas, electron, heat and water flows. The transport properties of GDLs are often difficult to measure experimentally, due to their small thickness (300 µm). Figure 1.9 illustrates the various physical phenomena modeled and simulated in this document.

To allow these multiple transports, the GDLs are composed of a fluid phase and a solid phase, itself composed of several materials. The microstructure of GDL plays a key role in trade-offs between transports. It makes it possible to explain the anisotropies of the effective transport properties and to explain the changes of effective properties of the GDLs under compression. We take great care to develop simulation tools that are predictive of the effect of the microstructure.

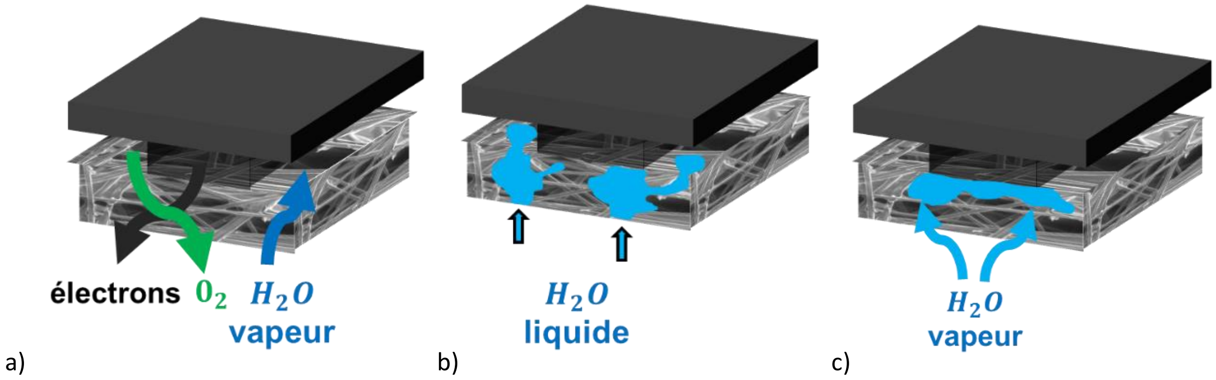

Figure 1.9 Diagram of transports in a GDL, for an in-situ fuel cell configuration. The GDL is inserted between a bipolar plate (in black) and a catalytic layer. a) diffusive transport of electrons or gases b) transport of water injected in liquid form into the GDL c) condensation of water coupled to a diffusive transport of water vapor.

The efforts made in this thesis to model physical phenomena and microstructures are justified first by the expected advances in the modeling of the behavior of water in porous electrode materials. This topic is crucial to better understand water management in GDL, which has a significant effect on the loss of concentration in the fuel cell. A second justification for this effort is to develop computer tools to help design porous fuel cell materials.

Note that designing materials by simulation is impossible without prior work in physics and applied mathematics, as we conduct during this thesis. The predominant physical phenomena must first be understood and put into equations before being simulated. Experiments and models complement each other at this stage, to better understand physical phenomena. Then, mathematical methods must be put in place to ensure the numerical precision of the simulations and to manage the complexity resulting from the complexity of the geometries, and possibly couplings between physical phenomena. The work on the numerical precision of the simulations, in turn, allows us to acquire new information tu study physical phenomena, for example by making it possible to exploit models based on tomographic images.

1.2.2 Implemented approach

To better understand the effect of the microstructure of porous materials on transport, we are taking advantage of advances in imaging techniques that allow us to know precisely the microstructure of fuel cell porous materials. Chapter 2 provides information on the use of imaging techniques for porous materials. We focus in this paper on a material, the GDL, because we have images of their microstructure. In fact, X-ray tomography images are more readily available for GDLs than for other electrode materials because the resolution constraint is lower for GDLs. This GDL study is a first step in setting up the methodology and the tools for analyzing tomographic images and performing simulations on images. These tools allow the quantitative exploitation of tomographic images of porous materials and may in future be applied to other porous materials than the GDL.

We develop processing tools for tomographic images and physical simulation tools that work on 3D images. Figure 1.10 and Appendix 9.1 provide a graphical overview of the various imaging and simulation tools used in this document. A first simulation tool used is an open source tool for direct simulation of diffusive transport on microstructures. A second simulation tool used is a pore network simulation code that we have developed. On the pore networks, we simulate diffusive transports such as gas diffusion, electrical conduction and thermal conduction, and biphasic phenomena such as the transport of liquid water in the capillary fingering regime and the condensation of water in the GDL. To use pore networks on tomographic images, we have developed a procedure for extracting pores from 3D images of porous microstructures.

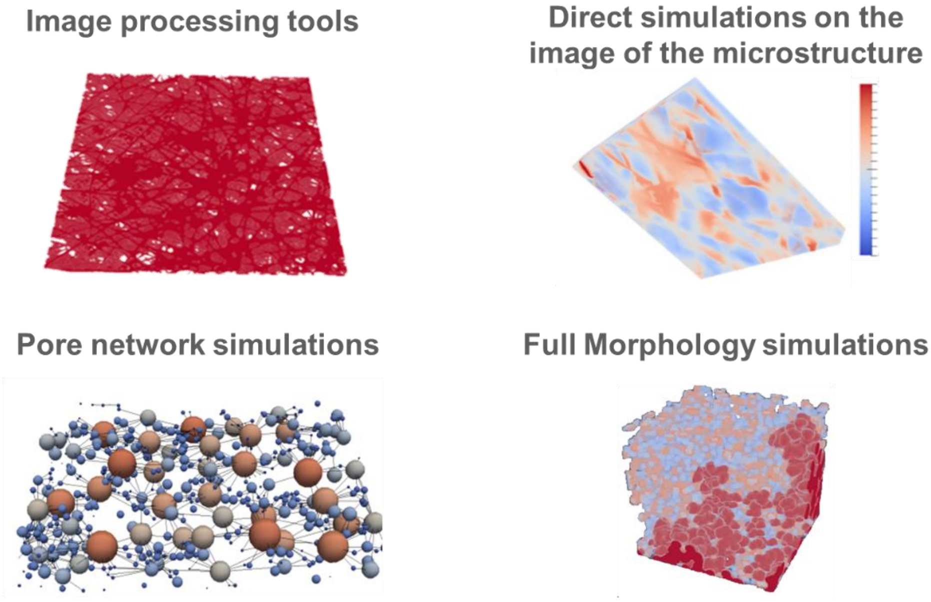

Figure 1.10 Tools used to process tomographic images and perform simulations on tomographic images.

The computer tools are introduced in several chapters of this document, in an arrangement that we describe in Tableau 1-1. Chapter 3 and Chapter 5 are the most important chapters to understand our simulation tools.

Tool	Introduced in chapter	Used in chapter
Tomographic image processing	Experimental validation of diffusive transport simulations (Chapter 4)	Experimental validation of diffusive transport simulations (Chapter 4)
Pore network extraction from a tomographic image	Injection of liquid water into a GDL (Chapter 5)	Injection of liquid water into a GDL (Chapter 5) Numerical verification of diffusive transport simulations (Chapter 3) Condensation (Chapter 6)
Simulation of diffusive transport by pore network	Numerical verification of diffusive transport simulations (Chapter 3)	Numerical verification of diffusive transport simulations (Chapter 3) Condensation (Chapter 6)
Two-phase pore network simulations	Injection of liquid water into a GDL (Chapter 5) Condensation (Chapter 6)	Injection of liquid water into a GDL (Chapter 5) Condensation (Chapter 6)
Simulation of diffusive transport by direct simulation	Numerical verification of diffusive transport simulations (Chapter 3)	Numerical verification of diffusive transport simulations (Chapter 3) Experimental validation of diffusive transport simulations (Chapter 4)
Two-Phase full morphology simulations	Injection of liquid water into a GDL (Chapter 5)	Injection of liquid water into a GDL (Chapter 5)

Tableau 1-1 List of the numerical tools used, chapters in which they are introduced and chapters in which they are used.

To develop predictive simulation codes, we quantitatively validate our models by comparison with the experiment. Experimental validation is essential is essential for models to be reliable, firstly for making recommendations on materials, secondly so that models can replace experimental measurements that are sometimes missing because they are difficult to carry out, thirdly to clarify the experimental characterizations. We also compare pore networks simulations with direct simulations, to ensure the numerical accuracy of the calculations. We have in fact implemented direct simulations in this thesis to validate the pore network simulations. We then realized that the direct simulations were very efficient, so we used them as reference in several chapters of this manuscript. Finally, we work on the consistency of the calculation procedures and try to limit the use of calibration parameters in the models and simulations, to increase the reliability and the ease of use of the models and simulations. Tableau 1-2 lists the various models and simulations developed and how we validate and exploit them.

Models and simulations	Validation and use	Microstructure
Pore network model: liquid water injection	Experimental validation	X-ray tomography
Pore network model : diffusive transport	Numerical verification	X-ray tomography Virtual microstructures
Direct simulation on microstructure : diffusive transport	Numerical verification Experimental validation Numerical study	X-ray tomography Virtual microstructures
Pore network model : condensation	Numerical study	X-ray tomography Virtual microstructures

Tableau 1-2 Implemented approach for the validation and exploitation of simulation tools that use images of porous microstructures.

We illustrate the possibility of virtually designing porous microstructures and characterizing them by simulation, with the aim of finding more efficient materials. We work on the generation of virtual microstructures close to real materials, to consider manufacturing constraints. This approach is likely to provide insight into the design of porous materials, complementary to the experimental approach.

1.2.3 Thesis outline

Chapter 1 is devoted to the introduction and Chapter 2 to the state of the art.

Chapter 3 and Chapter 4 are devoted to simulating diffusive transports in GDL. Chapter 3 presents the numerical methods used to simulate diffusive transport and the numerical verification of these methods. We develop a method for simulating diffusive transport using pore networks, and compare these simulations with direct simulations of diffusive transport on 3D images and analytical formulas. Chapter 4 is devoted to the experimental validation of diffusive transport simulations. We compare the simulations on several GDLs to experimental measurements of gas diffusivity and electrical conductivity. The goal is to check that the physics is well modeled and that the simulations allow to predict the properties of GDL with reliability.

Chapter 5 is devoted to the modeling of a water injection experiment in a GDL. We develop a pore network model extracted from tomographic images to simulate two-phase flows under capillary fingering conditions. The simulations are validated using a tomographic image which shows the water in the GDL at the micrometric scales.

This approach allows us to validate experimentally that the pore network simulations predict the proper water distribution. Simulations of capillary pressure curves in GDLs supplement this chapter.

Chapter 6 is devoted to modeling the condensation of water in GDL. The water vapor produced by the electrochemical reaction in the cathode catalyst layer cross the GDL and condensate in the cold regions of the GDL. A model of pore network coupling the diffusion of water vapor, phase change and capillary forces is developed. This model is illustrated with simulations performed on pore networks generated using Voronoi meshes.

Chapter 7 is devoted to the study of virtual microstructures. 3D images can depict experimental or virtual microstructures. We show that it is possible to produce virtual microstructures close to microstructures of real materials, to search for optimal microstructures and to study physical phenomena using simulation on virtual materials. Exploring virtually new material designs has advantages over the experimental approach, in terms of speed, cost and microstructure control.

Chapter 8 is devoted to the conclusion. The main results are recalled and perspectives are proposed.

Finally, appendices compiled in Chapter 9 supplement this document. They contain a presentation of simulation tools on tomographic images, theoretical reminders and analytical calculations.

1.3 Bibliography

- [Barbir2005] Frano Barbir, PEM Fuel Cells, Theory and Practice, Academic Press, 2005
- [CHAMEAU2010] “Rapport final de synthèse du projet PAN'H 2006 CHAMEAU”, 2010.
- [Debe2012] Mark K. Debe, Electrocatalyst approaches and challenges for automotive fuel cells, Nature 486, 43–51 (07 June 2012)
- [Dincer2015] Ibrahim Dincer, Canan Acar, Review and evaluation of hydrogen production methods for better sustainability, International Journal of Hydrogen Energy, Volume 40, Issue 34, 14 September 2015, Pages 11094–11111
- [Dubau2014] Laetitia Dubau, Luis Castanheira, Frédéric Maillard, Marian Chatenet, Olivier Lottin, Gaël Maranzana, Jérôme Dillet, Adrien Lamibrac, Jean-Christophe Perrin, Eddy Moukheiber, Assma ElKaddouri, Gilles De Moor, Corine Bas, Lionel Flandin, Nicolas Caqué, A review of PEM fuel cell durability: materials degradation, local heterogeneities of aging and possible mitigation strategies, Wiley Interdisciplinary Reviews: Energy and Environment, Volume 3, Issue 6, pages 540–560, November/December 2014
- [Durbin2013] D.J. Durbin, C. Malardier-Jugroot, Review of hydrogen storage techniques for on board vehicle applications, International Journal of Hydrogen Energy, Volume 38, Issue 34, 13 November 2013, Pages 14595–14617
- [EuropeEnergy2011] European Commission, Energy Roadmap 2050, 2011

- [Flynn2004] P. Flynn, et al., Meeting the Energy Needs of FutureWarriors, Tech. Rep., Committee on Soldier Power/Energy Systems, Board on Army Science and Technology, National Research Council of the Nation Academies, Ed. The National Academies Press, 2004
- [IEA2013] IEA, World Energy Outlook 2013, International Energy Agency, 2013.
- [IEA2014] IEA, CO2 emissions from Fuel Combustion, Highlights 2014, International Energy Agency, 2014.
- [IPCC2014] IPCC, 2014: Climate Change 2014: Synthesis Report. Contribution of Working Groups I, II and III to the Fifth Assessment Report of the Intergovernmental Panel on Climate Change [Core Writing Team, R.K. Pachauri and L.A. Meyer (eds.)]. IPCC, Geneva, Switzerland, 151 pp.
- [Ji2009] Mengbo Ji and Zidong Wei, A Review of Water Management in Polymer Electrolyte Membrane Fuel Cells, Energies 2009, 2, 1057-1106
- [Kraytsberg2014] Alexander Kraytsberg, Yair Ein-Eli, Review of Advanced Materials for Proton Exchange Membrane Fuel Cells, Energy Fuels 2014, 28, 7303−7330
- [Moreno2015] Nayibe Guerrero Moreno, Myriam Cisneros Molina, Dominic Gervasio, Juan Francisco Pérez Robles, Approaches to polymer electrolyte membrane fuel cells (PEMFCs) and their cost, Renewable and Sustainable Energy Reviews, Volume 52, December 2015, Pages 897–906
- [O'Hayre2009] R. O'Hayre, Fuel Cell Fundamentals, John Wiley & Sons Ltd, 2009
- [Paris2015] Accord de Paris, Paris, 12 December 2015, United Nations Treaty Collection
- [Peighambardoust2010] S.J. Peighambardoust, S. Rowshanzamir, M. Amjadi, Review of the proton exchange membranes for fuel cell applications, International Journal of Hydrogen Energy, Volume 35, Issue 17, September 2010, Pages 9349–9384
- [Rashapov2015] Rinat R. Rashapov, Jonathan Unno, and Jeff T. Gostick, Characterization of PEMFC Gas Diffusion Layer Porosity, Journal of The Electrochemical Society, 162 (6) F603-F612 (2015)
- [Robin2015] Christophe Robin, Développement d'un modèle prédictif de durée de vie d'une pile PEMFC pour une application aéronautique : étude des interactions entre le cœur de pile et les conditions d'opération du système, PhD Thesis, Univ. Grenoble Alpes, 2015
- [Tuot2007] TUOT Thierry, Grenelle de l'environnement : rapport général, La Documentation Française, 2007
- [USStorage2013] U.S. Department of Energy, Grid Energy Storage, report, December 2013
- [Vilekar2010] Saurabh A. Vilekar, Ravindra Datta, The effect of hydrogen crossover on open-circuit voltage in polymer electrolyte membrane fuel cells, Journal of Power Sources, Volume 195, Issue 8, 15 April 2010, Pages 2241–2247

Chapter 2 State of the art

Flows of reactive gases, water vapor and liquid water, heat and protons in GDL are essential to the operation of PEM fuel cells. This chapter is devoted to the state of the art of knowledge and models relating to these physical phenomena.

The transport of gas, heat and electrons have profound similarities. That is why they are referred to in this document using the term of diffusive transports. We present in the first section the diffusive transports in the GDL and the ways of modeling them. Phenomena involving liquid water and water vapor are termed two-phase phenomena. The two-phase transports differ from the diffusive transports by the presence of liquid-gas interfaces. These phenomena require specific modeling tools. We present in the second section the two-phase transports in GDLs and the ways of modeling them.

The microstructure of GDLs has an important effect on their transport properties. Imaging techniques are increasingly used to visualize the microstructure of porous materials and to model transport within these microstructures [Blunt2013]. We present in a third section the imaging techniques applicable to GDLs and the computer processings that make it possible to extract useful quantitative information from images. We explain how images can be useful to model the diffusive and two-phase transports in GDL.

2.1 Modeling of diffusive transport in GDL

The transports of gas, heat and electrons in porous materials play an important role in the operation of fuel cells. The diffusion of gases limits the maximum current that the fuel cell can provide. The heat has a decisive effect on the condensation and the evaporation of the water in the stack. The conduction of electrons and protons is responsible for ohmic losses. Thus, understanding and modeling these phenomena is important for increasing the electrical power and efficiency of fuel cells.

All these phenomena have profound similarities. The same mathematical framework can be used to model them. Therefore, they are referred to in this document using the term diffusive transports. In this section, we first present a physical analysis of the diffusive transports in GDL. This analysis includes a modeling of diffusive transports using a partial differential equation, a discussion of the effect of the microstructure on the effective transport properties in the material, and a presentation of the diffusive transports in a working cell. We then present the experimental characterizations used to measure the effective transport properties of GDLs.

Finally, we present the models and simulations that can be used to determine the effective transport properties of GDL when the experimental characterizations are not possible or not available. A first type of approach, which we are discussing, consists in using simplified microstructures to establish analytical formulas linking the effective properties of a material to its microstructure. A second type of approach, which we are discussing, consists in numerically simulating the transport properties from images of the real microstructures.

2.1.1 Physical analysis of diffusive transport in GDL

In this section, we present a physical analysis of the diffusive transport in GDL. This analysis includes a modeling of diffusive transport using a partial differential equation, a discussion of the effect of the microstructure on the effective transport properties in the material and a presentation of the diffusive transport in a fuel cell in operation.

2.1.1.1 Stationary heat equation

We assume that the heat fluxes can be modeled by the Fourier law, the electron fluxes by the local Ohm law and the diffusion fluxes by the Fick law. Under these hypotheses, whose limitations are discussed below, the stationary heat equation makes it possible to model the diffusion of dioxygen and water vapor in the gas phase, the conduction of heat in the solid and gas phases, the electrical conduction in the solid phase.

Let us recall how the equation of heat is obtained from the Fourier law. The Fourier law states that the heat flux $\vec{q}$ is proportional to the temperature gradient:

$$\vec{q} = \beta \vec{\nabla} T$$

Équation 2.1

where T is the temperature in K, $\beta(\vec{x})$ is the local thermal conductivity in $W.m^{-1}.K^{-1}$ at point $\vec{x} = (x_1, x_2, x_3)$ and $\vec{\nabla} \cdot$ is the divergence operator $\left(\frac{\partial}{\partial x_1}, \frac{\partial}{\partial x_2}, \frac{\partial}{\partial x_3}\right)$.

A balance of energy leads to the equation of heat in the material:

$$\vec{\nabla} \cdot \left(\beta \vec{\nabla} T\right) = \rho c \frac{\partial T}{\partial t}$$

Équation 2.2

Where ρ is the density of the material in $kg.m^{-3}$ and c is the specific heat of the material in $J.kg^{-1}.K^{-1}$. In steady state, the heat equation becomes :

$$\vec{\nabla} \cdot \left(\beta \vec{\nabla} T\right) = 0$$

Équation 2.3

Several simplifications are made when the diffusion of gas and the conduction of electricity and heat are modeled by the stationary heat equation. For diffusion, this is equivalent to modeling the relationship between flux and concentration by Fick's law rather than by Stefan-Maxwell's law. We thus neglect the diffusion effects in ternary gas mixtures. We assume that the binary diffusion coefficient does not depend on the concentration. For heat transfers, we consider only the conduction, not the transfers by radiation. We also neglect the effect of thermal expansion. Conducting effects appearing at the nanoscale are not considered, for example impedance mismatches for phonons in the case of heat transfer, or conduction of electrons on the surface for electrical transfers. These effects can reasonably be considered as negligible at the micrometric scales we are working on. Finally, we are interested in the steady state, not the transitional state. These different approximations seem reasonable for transports in GDL. They should be checked if we want to model other materials, especially if the characteristic dimensions are nanometric.

In this document, all diffusive transports are thus modeled by the stationary heat equation. We describe below the numerical methods used to solve this equation.

2.1.1.2 Effect of microstructure on effective transport properties

The microstructure of a porous material has an essential effect on the diffusive transports in this material. Let us explain this effect in the case of gas diffusion.

The diffusion coefficient of a gas in a porous medium is lower than in a space consisting only of gas. Indeed, the presence of solid materials limits the volume through which the gas can diffuse. The diffusion coefficient in a porous material, considering the effect of the microstructure, is called the effective diffusion coefficient, or effective diffusivity. In addition to the effect of the proportion of solid volume and gaseous volume in the material, in other words porosity, other microstructure effects influence effective diffusivity. For example, the solid microstructure can induce tortuous paths for the gas, extending the path it must travel. It must also induce constrictions and dead-ends. The effect of the microstructure on effective diffusivity can be summarized by the following equation:

$$D_{eff} = D_{bulk} \frac{\varepsilon}{\tau_{eff}}$$

Équation 2.4

Where D_{bulk} is the binary diffusion coefficient of the diffusing gas in the gas phase, ε is the porosity of the porous material and τ_{eff} is a factor called effective tortuosity. Note that the effective tortuosity defined here accounts for several geometric effects, and that we need to know the microstructure to be able to calibrate it.

Thus, the microstructure has an important effect on diffusive transport in porous media. The geometric properties of GDLs, such as anisotropy or deformation caused by the compression of the GDL by the ribs of the bipolar plate, influence the effective diffusivities and conductivities. We present in section 2.1.3 methods to quantify the effect of the microstructure on the effective properties of porous materials.

2.1.1.3 Layout of transports in a GDL in an operating fuel cell

The heat is produced in the catalytic layer and diffuses towards the ribs and channels of the bipolar plate. The heat flux flows through heterogeneous materials: the highly conductive carbon fibers that are aligned in the plane, the conductive binder between fibers, the insulating PTFE on the surface of the GDLs, the rather insulating gases in the pores of the GDL, and in some cases, some rather insulating liquid water in the pores.

The layout of electron transport is rather like the layout of heat transport. The electrons are produced in the catalytic layer and are conducted to the rib of the bipolar plate. The flow of electrons passes through heterogeneous materials: highly conductive carbon fibers aligned in the plane, conductive binder between the fibers, insulating PTFE on the surface of the GDLs, highly insulating gases in the pores of the GDL, and in some cases, some insulating liquid water in the pores.

The transport of gases occurs mainly by diffusion through the thickness of the electrodes, under the effect of a gradient of concentration in the thickness of the electrodes. This concentration gradient is because the reactive gases are consumed in the catalytic layer and are provided through the channels, which results in a higher gas concentration in the channels than in the catalytic layer. This induces a flow of reactive gases from the channels to the catalytic layer through the GDL. The effect is the reverse for the water vapor produced by the reaction, which is higher in the catalytic layer than in the channels. Note that in GDL, transport by diffusion in the plane are also important. Indeed, to access the channels, the water vapor produced must get around the rib of the bipolar plate, which is in contact with the GDL.

The transport of gas by convection through the thickness of the membrane electrode assembly is supposed to be negligible in this document, because the membrane prevents the gases from passing by convection and because we assume that the chemical reaction does not induce expansion or compression of the gas mixture in the catalytic layer. In contrast, the transport of gas by convection in the plane is possible, by imposing a pressure difference on either side of a rib of a bipolar plate. The advantage of the convective transport is that the gas flows may be greater than those resulting from diffusion. Thus, it would be possible to reduce the losses of the cell related to the transport of reactive gases, thanks to convection. The effective property which quantifies the convection in a porous material is called the effective permeability. Convective gas transport in GDL is modeled for example in [Bazant2010]. However, we suppose in this document that diffusion is the main gas transport mechanism in the membrane electrode assembly. We therefore do not discuss the permeability of GDL in this document. The reader interested in the permeability of GDL can read for example [Gostick2008-thesis].

2.1.2 Experimental characterizations

We have explained in section 2.1.1.2 that the effective properties of GDLs for diffusive transports differ from the bulk properties of their elementary constituents, gases, carbon fibers, binder, PTFE. Indeed, the effective properties of GDLs depend both on the properties of the elementary constituents of the GDLs and on the microstructure of the GDLs. Because of the small thickness of the GDLs, the experimental characterizations of the transport properties through the thickness of the GDL require elaborate methodologies. A state of the art of these methodologies is provided in [Zamel2013].

Several methods have been used to measure the effective diffusivity of GDL. A first type of method consists in imposing a gradient of concentration of gas on either side of the GDL and in measuring the evolution of the concentrations resulting from the return to equilibrium by diffusion. It is nevertheless difficult to impose a concentration gradient on either side of a GDL without obtaining a parasitic convection flux, because of the small thickness of the GDLs. A second type of method consists in filling the porous material with an ion-conducting liquid [Kramer2008]. A measure of the effective electrical conductivity of the ions makes it possible to determine the effective gas diffusivity, thanks to the mathematical similarity of these two phenomena of diffusion. In this method, the electrical conductivity of the ions can be separated from that of the electrons circulating in the solid phases of the GDL using impedance spectroscopy.

The general principle of measurements of the effective electrical conductivity of GDLs consists in injecting electrical currents in the GDLs and in measuring the induced voltage gradients. The effective conductivity can be determined from these measurements using Ohm's law. Several methods exist [Zamel2013]: the four-point method, the four-electrode method, the voltage drop method.

Several techniques have been used to measure the thermal conductivity of GDL [Zamel2013]. These techniques are based on the use of calorimeters or heat flux sensors.

2.1.3 Models and simulations to compute effective diffusive transport properties as a function of microstructure

We have seen that the microstructure of porous materials has an important effect on their effective diffusive transport properties. To determine the effective transport properties, the models and simulations provide complementary tools to the experimental characterizations. The models and simulations are useful especially when the experimental characterizations are technically difficult or not available for the materials studied.

A first type of approach consists in using simplified microstructures to establish analytical formulas linking the effective properties of a material to its microstructure. When the microstructures of the actual materials move away from the simplified microstructures on which the analytical formulas are based, it is interesting to numerically simulate the effective transport properties from the actual microstructures.

In this section, we first present analytic formulas that were established for simplified microstructures. We then present numerical simulation tools and methodologies used to compute the effective properties of porous materials from their microstructure.

2.1.3.1 Analytical formulas linking effective properties to microstructure

We present in this section analytical formulas allowing to calculate the effective properties as a function of geometrical parameters related to the microstructure. These formulas provide useful approximations for certain categories of materials. They also make it possible to forge an intuition of the most influential geometric parameters on diffusive transports.

A first type of analytical formulas is based on the study of simplified model microstructures. A second type of analytical formulas includes correlations between the effective transport properties and some geometrical properties of the real microstructures, which can be known, for example, by imaging. We begin by presenting examples of analytical formulas based on simplified model microstructures.

The most commonly used model for linking the microstructure of a porous material to its effective transport properties is the Bruggeman approximation [Bruggeman1935].

$$D_{eff} = D_{bulk}\varepsilon^{3/2}$$

Équation 2.5

where D_{eff} is the effective diffusivity, D_{bulk} is the binary diffusion coefficient of the gas and ε is the porosity. This model was originally established for media consisting of regular stacks of balls. Its validity for fuel cell materials is questionable [Tjaden2016].

Approaches based on the theory of percolation make it possible to consider more elaborate geometric effects, such as the existence of a percolation threshold for the conducting phase, below which transport through the sample cannot take place. An example of these approaches is given by the formula proposed in [Tomadakis1993]:

$$D_{eff} = D_{bulk}\left(\frac{\varepsilon - \varepsilon_p}{1 - \varepsilon_p}\right)^{\alpha}$$

Équation 2.6

where ε_p is the percolation threshold and α is an empirical constant. Values for ε_p and α are tabulated in [Zamel2013]. These percolation approaches are usually based on the study of infinite media. In the case of the fine media such as the GDL, the validity of these approaches is questionable. This is discussed in section 2.2.3.1.

In general, these analytical formulas have been developed for materials whose microstructure is different from those of GDL. They generally give imprecise estimates of the actual effective properties of GDL [Zamel2013]. To overcome these limitations, some authors have specifically developed analytical models for structures closer to those of GDL [Zamel2013]. These models are interesting for studying structures close to GDL, but their validity remains limited to restricted classes of microstructures.

A second type of analytical models is based on the use of tomographic images of real microstructures. These models make it possible to quantify the effect of the microstructure on the effective transport properties, using correlations between the effective transport properties and some geometric parameters measured in the tomographic image of the microstructure. An example of a method of this type is the equation of the constrictivity that was introduced in [Gaiselmann2014]. Annex 9.4 is devoted to this equation. This equation is a correlation between the effective diffusivity of a porous material and a small number of geometric parameters of the microstructure. These geometrical parameters are defined rigorously and can be computed on tomographic images. The equation giving the effective diffusivity as a function of these geometrical parameters is the following:

$$D_{eff} = D_{bulk} \times 2.03 \frac{\varepsilon^{1.57} \beta^{0.72}}{\tau_{geom}^{2}}$$

Équation 2.7

where ε is the volume fraction of the conducting phase, τ_{geom} is the geometric tortuosity and β is the constrictivity. Geometric tortuosity is defined as the average length of the shortest path between the inlet and the outlet. It can be calculated directly on a 3D image of the material. Le constrictivity parameter is defined as $\beta = \left(r_{constriction}/r_{pore}\right)^2$, where $r_{constriction}$ et r_{pore} are the average size of the constrictions and the average size of the pores, respectively.

The constrictivity equation sheds new light on the geometric parameters that have an impact on transport. Compared to the classical effective diffusivity model, where diffusivity is a function of porosity and of an effective tortuosity rather than the geometry tortuosity, this equation makes it possible to rigorously define the tortuosity and to calculate it on a tomographic image. Let us note that the equation of the constrictivity is only an approximation, obtained by calibrating the exponential parameters using direct numerical simulations on microstructures. This equation has been established for solid oxide fuel cell porous electrodes and for random graphs having a single connected component and no dead end. It is valid only for diffusive transports through one phase whose properties are uniform.

2.1.3.2 Calculation of effective transport properties using simulations on microstructures

The numerical simulation of the effective diffusive transport properties of a porous material from its microstructure is a complementary tool to experimental characterizations and analytical models. Numerical simulations are useful especially when experimental characterizations are technically difficult or unavailable, and when the microstructure of materials is far from the simplified structures on which the analytical models are based.

The methodology for simulating the effective properties of a porous material consists firstly in obtaining the microstructure of the material by imaging, and in a second step in simulating the physical transport on this microstructure. We are dealing here only with the simulation part. The problem of obtaining the microstructure using imaging techniques is dealt with in part 2.3.

In this section, we first deal with numerical methods used to simulate diffusive transports on microstructures of porous materials. In a second step, we discuss the boundary conditions and the notion of homogenized effective property.

2.1.3.2.1 Numerical simulation methods

We want to calculate the diffusive transport properties of porous materials. To do this, we simulate the diffusive transports modeled by the stationary heat equation. Numerous numerical methods exist to solve the stationary heat equation. These methods may vary in terms of the type of mesh used, sensitivity to the effects of discretization, sensitivity to the contrasts of properties of the different phases, computation time. A specificity of simulations on microstructures is that the mesh size must be sufficiently fine to capture the local geometry of the microstructure, and on the other hand the volume of material considered must be high enough to be representative. It results from this double constraint that the meshes have very many elements, often several hundreds of millions, which induces a challenge in terms of calculation time.

A quantitative comparison of several numerical methods is made in [Andrä2013-2], for the calculation of the effective diffusive transport properties of porous rocks, from tomographic images of their microstructure. Simulation of transport on microstructures of porous materials is widely used in the field called virtual rock physics [Andrä2013] [Blunt2013]. The methods compared in [Andrä2013-2] include the finite element method, the finite difference method, the explicit jump method (EJ-Heat). Note that some methods are not studied in this article, for example the Lattice-Boltzmann method and the Monte-Carlo method for diffusion simulation. The deviations found in [Andrä2013-2] between the different methods are, as a percentage of maximum deviation from the mean value, 11% for the elastic modulus, 38% for the permeability, 23% for the electrical formation factor, i.e. the inverse of the effective electrical conductivity. These results show that well-established numerical methods can show discrepancies when calculating on tomographic images. A second conclusion is that not all physical phenomena are solved with the same precision, depending on their sensitivity to the microstructure, for example. A third conclusion is that to calculate physical quantities such as electrical conductivity, the error coming from the numerical approximations is relatively moderate compared to other sources of potential errors, namely the precise determination of the microstructure by imaging, the spatial variability of the microstructures and the determination of the bulk properties of the constituents of the material.

In this thesis, we developed a method for calculating diffusive transport on a tomographic image, using a pore network method. The principle of these methods is to decompose the domain into two scales, the infra-pore scale and the scale of the network. The microstructure is decomposed into simple geometric elements called pores, transport between neighboring pores is approximated by analytical formulas based on the shape of the pores (infra-pore scale), and transport at the scale of the entire material are computed by an equivalent network formulation (network scale). More information on this method is given in section 3.1.1.1. The interest of this decomposition in two scales is to model complex physical phenomena taking place on the infra-pore scale using simple analytical models. Moreover, the computation time of the diffusive transports is reduced compared to the direct simulation because the resolution of the transports at the infra-pore scale is made by fast analytical formulas. Other numerical methods follow a similar approach, such as multiscale finite volume methods [Tomin2013], multiscale finite element methods [Taralova2015], variational multiscale methods [Weinan] [Bauer2012], and heterogeneous multiscale methods [Weinan2004]. These approaches are considered as multiscales and have been used to simulate many types of physical phenomena.

In addition to the pore networks, we use direct simulation using the explicit jump method (EJ-Heat). We use direct simulation as a reference to verify and validate pore networks. Direct simulation makes it possible to study the analytical formulas used to approximate the infra-pore scale in the pores networks, since direct simulation does not make such approximations and is therefore generally more accurate. However, this better accuracy is at the cost of a much higher computation time.

2.1.3.2.2 Numerical computation of effective properties: boundary conditions and homogenization

The theory of homogenization shows that, under certain conditions, a material can be characterized by an effective transport property. For diffusive transport, the material is then equivalent to a homogeneous material with the same effective transport property. We discuss in this section the notion of homogenized effective property of a material. We discuss the methodologies for calculating the effective properties by numerical simulation, and the criteria required for the framework of the homogenization theory to be applicable. We also discuss the limiting conditions to be applied to limit artifacts when the criteria of homogenization are not met.

Numerical simulation makes it possible to simulate diffusive transport in porous materials. Let us note that simulating a phenomenon of diffusive transport consists in seeking a solution of the stationary heat partial differential equation. This solution is a function of the bulk conductivities of the materials in the domain, a function of the microstructure, and a function of the boundary conditions used. When the conditions of applicability of the homogenization theory are satisfied, it can be shown that the boundary conditions no longer have any influence and that the transport properties are relative only to the microstructure and bulk conductivities of the material components. Simulated properties then depend only on intrinsic properties of the material.

Two criteria must be met in the context of homogenization: a criterion on the size of the simulation domain and a criterion on boundary conditions. First, the correlation length of the medium must be much smaller than the simulation domain, which makes it possible to speak of representative elementary volume. Second, the characteristic length of spatial variation of the boundary conditions must be large compared to the correlation length of the medium [Gibiansky1993]. If these conditions are fulfilled, we can speak of homogenized effective property tensor. This tensor depends only on the intrinsic properties of the material. If these conditions are not fulfilled, we speak of upscaled property or block property [Renard1997]. The block properties are not intrinsic to the material, they depend also on extrinsic boundary conditions. In addition, they may vary depending on the sample considered. Indeed, the microstructure of a real porous material generally varies as a function of the position. Two small volumes extracted from the same material do not necessarily have the same transport properties.

In the case of GDLs, which are thin porous media, the conditions of homogenization are not generally fulfilled, as we discuss several times throughout this document. The transport block properties of the GDL are therefore likely to vary spatially and to be sensitive to the boundary conditions used to measure them experimentaly or to simulate them numerically. Another case mentioned in this document is the diffusive transport between two pores inside a GDL, at the micrometer scale. In this case, the conditions of homogenization are not fulfilled, and the boundary conditions have an influence on the simulated transport properties.

We now discuss the choice of boundary conditions. To calculate an effective transport property in one direction, transport in this direction is generally simulated by imposing a temperature difference between two opposite boundaries of the simulation domain. Transport is solved using these boundary conditions and other boundary conditions on the other sides, detailed below. The simulation makes it possible to obtain the total flux flowing through the medium. The effective thermal conductivity is obtained with the formula [Renard1997]:

$$C_{eff} = -\frac{Q}{S}\frac{L}{\Delta T}$$

Équation 2.8

Where L is the distance between the two boundaries on which the temperature difference ΔT is imposed, S is the cross-section area and Q is the total flux crossing S. The effective conductivities in the other directions can be obtained by repeating this operation in the other directions.

Several choices are possible concerning the boundary conditions on the lateral edges of the simulation domain. The aim is to choose boundary conditions as close as possible to the boundary conditions to which the material would be subjected in real conditions, to limit artefacts coming from unrealistic boundary conditions. These artefacts have a negligible effect if the homogenization conditions are met, but can introduce a non-negligible error if the conditions of homogenization are not fulfilled.

A first option is to use zero-flow limit conditions on the sides. These limiting conditions being simple to implement, we use them in this document for the pore network simulations. Their disadvantage is that zero-flow on the sides is often unrealistic. A second option is to impose a temperature field varying linearly on the sides, proportionaly to the temperature gradient imposed to calculate the thermal conductivity. This has the effect of better approximating the actual boundary conditions. A third option is to enlarge the simulation domain by artificially adding margins on the edges of the domain, to be able to impose boundary conditions at greater distance from the sample. This normally means that the simulated field has had time to interact with the material when it arrives at the boundary of the initial domain, therefore it should be closer to a field to which a material is subjected in real situations. A method for adding realistic margins to the simulation domain is to take as margins the symmetric of the domain with respect to the edges of the domain, which represents six symmetries relative to plans for a three-dimensional domain. Finally, it is possible to impose periodic boundary conditions on the simulated temperature field.

2.2 Modeling of two-phase transports in GDL

Water management in PEM fuel cells has an important effect on their performance. GDL has an important role in water management. Indeed, water often condenses in GDL, which blocks its pores and limits transfers of reactive gas to the catalytic layers, thus limiting the current produced by the cell. Thus, the modeling of water transport in GDL and the interactions between liquid water and the solid phase of GDL have an important role to play in improving the performance of fuel cells.

Water transport is referred to as two-phase transport when it involves a liquid phase and a gas phase. These two-phase transports imply the presence of interfaces between the two phases. Specific forces apply to the interfaces and the interfaces are generally mobile. The modeling of these two-phase phenomena implies to model the phenomena related to the interfaces, in addition to the phenomena occurring within each of the two phases [Lemonnier2006].

We first present a state of the art of the experimental information available on water in GDL. We then present a physical analysis of the two-phase transports in the GDL. Finally, we present a state of the art of the models and simulations dedicated to two-phase transport.

2.2.1 Experimental information

Several types of experimental information can be used to understand and model two-phase transports in GDL. We first present the information obtained by imaging techniques, then experimental ex-situ characterizations of the two-phase properties of the GDL.

2.2.1.1 Water imaging in GDL

Several imaging techniques are used to visualize water in PEM fuel cells: optical imaging, X-ray imaging, magnetic resonance imaging (MRI), and neutron imaging. A state of the art of these techniques was realized in 2009 [Bazylak2009]. Tableau 2-1 provides a comparison of these different techniques.

Method	Spatial resolution	Temporal resolution	Advantages	Disadvantages
Optical imaging	10 µm	0.06 s	High spatial and temporal resolution	Transparent cell is required
X-ray imaging	680 nm	1 s	High spatial and temporal resolution	Low sensitivity to water content
MRI	50 µm	50 s	Sensitive to water	Incompatible with conductive materials
Neutron imaging	25 µm	1 min	Very high sensitive to water	Low spatial and temporal resolution

Tableau 2-1 Imaging methods used to visualize water in PEM fuel cells. Table adapted from [Kim2013]

The simplest technique for visualizing water is the direct optical observation of water drops on the surface of the GDLs or in the channels. This can be done in-situ using transparent cells, or ex-situ, for example by injecting water into a GDL and by visualizing the places where water flows out of the GDL. Another example of direct ex-situ visualization is the observation of water distributions in a transparent micro-model, i.e. an artificial structure representing a simplified porous microstructure intended to test the behavior of fluids in porous media. The micro-models have been used, for example, for fluid injection experiments in a porous medium [Lenormand1988], or for water condensation experiments in a porous medium [Straubhaar2015]. The results of these two experiments are briefly described in section 2.2.1.2.

X-ray imaging can be used to visualize water in GDL. The general principle of this technique is described in section 2.3.1. X-rays are useful for visualizing water in GDLs because they are sensitive to both water and carbonaceous materials, and because they allow to reach a micrometric resolution, which makes it possible to see the water at the pore scale. There are two X-ray imaging modalities: radiography, which consists of taking an image in one direction, and tomography, which consists in taking a series of images in different directions to reconstruct the three-dimensional internal structure of the object. A state of the art of X-ray water visualization in PEM fuel cells is provided in [Kim2013]. We describe here some information obtained with this technique. X-rays showed an eruptive ejection of water from the GDL to the channel [Manke2007] [Hartnig2008]. X-ray tomography made it possible to visualize water in a GDL during an ex-situ experiment of capillary pressure curve [Kim2012] [Lamibrac2016], to visualize an accumulation of water near the interface between GDL and catalytic layer

[Hinebaugh2015-Thesis] [Hinebaugh2012-tomo] [Lee2013], to visualize the percolation of water and the presence of several clusters of liquid water in GDL [Hinebaugh2015], and to visualize that the water condenses in the GDL under the rib of the bipolar plate [Straubhaar2015]. A series of other works were published, in which X-ray tomography is used to visualize water in PEM fuel cells [Sinha2006] [Becker2009] [Flückiger2011] [Gostick2010] [García-Salaberri2015] [Zenyuk2015] [Markötter2011] [Rosen2012] [Mayrhuber2015].

Magnetic resonance imaging has been used a few times to visualize water in fuel cells [Bedet2008] [Teranishi2006] [Tsushima2004] [Suzuki2011]. Its advantage is to be sensitive to water, but its disadvantage is that the presence of electrical conductive materials deteriorates the quality of the images. The resolution of this technique is about 50 µm [Kim2013].

Neutron imaging is an established technique for visualizing water in PEM fuel cells [Satija2004] [Kramer2005] [Zhang2006] [Yoshizawa2008] [Boilat2008] [Kim2009] [Spernjak2010] [Iranzo2014]. The advantage is that neutrons are sensitive almost exclusively to hydrogen atoms, which makes it possible to detect the presence of water without being disturbed by the other materials of the cell. The resolution of this technique is, however, smaller than that of X-rays (about 25 µm [Kim2009]). Note that the use of this technique is limited by the scarcity and the cost of the neutron beams.

2.2.1.2 Ex-situ experimental characterizations of the two-phase transports properties of GDL

We describe here two types of ex-situ experiments used to obtain information on the two-phase transports properties of GDLs: capillary pressure curve measurements and wettability measurements.

The capillary pressure curve makes it possible to collect a lot of information about the capillary forces which are exerted within a porous material. This curve represents the capillary pressure Pc (the pressure difference between the two fluids in the material) as a function of saturation. The fluid phase of the porous materials is composed of multiple pores that have different sizes. Each of these pores can be associated with a capillary pressure whose value is given by the Young-Laplace equation:

$$P_c = -\frac{2\gamma\cos\theta}{R}$$

Équation 2.9

where $\gamma = 7.2 * 10^{-2} N.m^{-1}$ at 25°C is the surface tension between air and water, θ is the contact angle and R is the radius of the pore. When water is injected into the porous material, the pores are gradually invaded, and the capillary forces exerted on the water vary as a function of the capillary pressure of the invaded pores. The capillary pressure curve can be measured by injecting water into the material. In the case of a hydrophobic material, it is necessary to impose a pressure on the liquid water to make it enter the material, because the capillary pressure in the material opposes the entry of the water. The level of pressure exerted on the water is varied, which makes it possible to scan the capillary pressures exerted in the material. At each pressure level, the amount of water injected into the material, i.e. the saturation of the material, is measured. Thus, the capillary pressure curves make it possible to have averaged access to the capillary forces, from which one can deduce pore size distributions and contact angles.

Several methods exist for measuring capillary pressure curves [Si2015]. Mercury intrusion porosimetry involves using mercury as an injection fluid. The mercury is strongly non-wetting with respect to carbon and PTFE, which means that it is not sensitive to the inhomogeneities of the contact angles in the GDL. It therefore makes it possible to measure the size of the pores. The standard porosimetry method, the volume control method, and the gas-controlled porosimetry are other examples. It should be noted that the use of water as an injection fluid is more representative of the actual conditions of use of GDL, but that is difficult because part of the water tends to evaporate, which distorts the saturation calculations [Gostick 2006]. To overcome this difficulty, water injection experiments are often carried out on a GDL enclosed in a sample holder, with a hydrophilic membrane and a hydrophobic membrane on either side of the GDL to control the inlets and outlets.

Capillary pressure curves are central in the theory of two-phase flows in homogenized porous media. Indeed, generalized Darcy models rely on capillary pressure curves to model capillary forces, as described in section 2.2.3.1. Section 5.2 provides information on the modeling of capillary pressure curves.

The wettability of GDL, the affinity of water with the surfaces of the solid materials of GDL, has a crucial effect on the two-phase properties of the GDL. If a GDL is hydrophilic, water will tend to spread along the internal surfaces of the GDL. On the contrary, if a GDL is hydrophobic, the water will tend to avoid contact with the solid surfaces internal to the GDL. The wettability of a material can be quantified by the contact angle between the air-liquid interface and the surface of the material, when a drop is placed on it. The contact angle depends on the chemical properties of the surface and its roughness. Treatments, generally based on PTFE (teflon), are applied to GDLs to make them hydrophobic, to prevent water from invading them and blocking the pores. The wettability of a GDL is generally not uniform since the hydrophobic treatment is not uniformly distributed in the GDL. The measurement of the contact angles in the GDL is thus essential to characterize its two-phase properties. External contact angle measurement techniques generally measure the contact angle of drops placed on the GDL surface. These techniques do not provide information on the wettability within the sample. Several techniques for measuring the average internal contact angle exist: the Washburn technique and the capillary rise technique. These methods unfortunately do not allow to characterize the inhomogeneities of the contact angle inside the GDLs. This lack of detailed information on the wettability of GDL induces some uncertainty on the two-phase simulations.

2.2.2 Physical analysis of two-phase phenomena in GDL

We analyze here two mechanisms of transport of water in the porous materials of PEM fuel cells. The first mechanism is a transport of water in liquid form from the catalytic layer through the GDL. The second mechanism is a transport of water in gaseous form through the GDL, with the condensation of some of the water in a cold region of the GDL.

2.2.2.1 Capillary fingering regime for the invasion of water in a GDL

We analyze here the forces that control the transport of water in liquid form in GDL. Experiments of drainage of two immiscible fluids have shown that the invasion pattern depends on the capillary number Ca and the viscosity ratio M [Lenormand1988], defined as :

$$Ca = \frac{\mu_l U}{\gamma}$$

Équation 2.10

$$M = \frac{\mu_l}{\mu_g}$$

Équation 2.11

where μ_l et μ_g are respectively the dynamic viscosities of the non-wetting and wetting fluids (in $Pa.s$), U is the displacement speed (in $m.s^{-1}$) and γ is the surface tension between the two fluids (in $N.m^{-1}$).

As indicated on the Figure 2.1, three characteristic invasion patterns of the non-wetting fluid in the wetting fluid are possible: stable displacements, characterized by a flat front, viscous digitations, characterized by relatively rectilinear advances, and capillary digitations, characterized by a random and arborescent appearance.

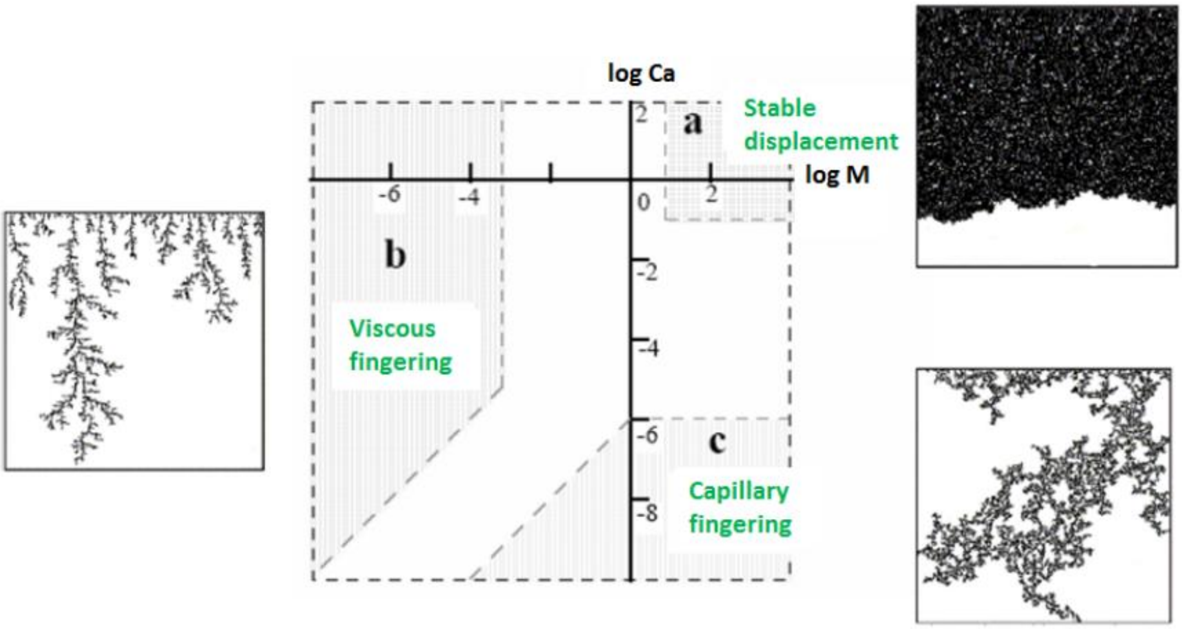

Figure 2.1 Classification of the invasion patterns during fluid drainage experiments in a porous media, as a function of the capillary number and the ratio of the viscosities of the wetting and non-wetting fluids. Taken from [Ewing2001].

Let us study the case of the displacement of water in the GDL. At 80 °C, the ratio of dynamic viscosities of water and air is $M \approx \frac{3.55\times10^{-4}}{2\times10^{-5}} \approx 17.5$. Suppose that all water produced by one square centimeter of fuel cell is transported in liquid form through the GDL on the cathode side, from the cathodic catalytic layer to a channel of the bipolar plate. Suppose also that the velocity of water corresponds to the displacement of this produced water in a medium uniformly constituted by water. Then the speed of water U and the capillary number Ca are [Straubhaar2015]:

$$U = \frac{iM_{H_2O}}{2F\rho_l}$$

Équation 2.12

$$Ca = \frac{\mu_l i M_{H_2O}}{\gamma \cos(\theta_w)\, 2F\rho_l}$$

Équation 2.13

where M_{H_2O} is the molar mass of the water (in $kg.mol^{-1}$), ρ_l is the water density (in $kg.m^{-3}$), θ_w is the contact angle of the wetting fluid with the solid, i is the produced current density (in $A.m^{-2}$) and F is the constant of Faraday ($F = 96487\ C.mol^{-1}$). If we assume $i = 1\ A.cm^2$, $\theta_w = 70°$, we get $Ca \approx 10^{-7}$. This corresponds to the regime of capillary digitations. Moreover, if part of the water is transported in vapor form or passes through the membrane to the anode, the flow of liquid water to the cathode is reduced, which decreases Ca and makes the flow remain it in the regime of capillary digitations.

Thus, capillary effects have a dominant effect on the transport of liquid water in GDL. We therefore neglect the viscous effects in this document and focus our efforts on the modeling of the capillary forces exerted on the liquid water in the GDL. Moreover, since capillary forces depend on the spatial distribution of water in the porous medium and not on the velocity of water, transient phenomena are neglected and we consider the invasion to be quasi-static.

Note that the dynamic effects associated with the eruption of drops from the GDL to the channel [Quesnel2015] are not considered in this model. Moreover, when we computed the water velocity we did not consider the volume occupied by the solid and the narrowing of the invasion patterns, which means that the water produced must evacuate through a smaller surface, so water velocity may be locally higher than we considered. In the case of GDL, this analysis should remain valid because on the one hand the narrowing of the digitations is moderate because the GDLs have only a few pores of thickness and on the other hand the volume occupied by the solid in GDL is low. However, in the case of thicker and less porous layers such as MPL or catalytic layers, it is possible that water flow is outside the capillary digitation regime and that the viscous forces are of importance.

2.2.2.2 Transport of water in vapor form and condensation of water in a GDL

The second mechanism studied for the evacuation of the water produced in the cathodic catalytic layer is a diffusion of water in gaseous form through the GDL with condensation of part of the water in a cold region of the GDL [Nam2003]. Since heat is produced in the catalytic layer, it is generally warmer than the GDL. The contact area between the rib of the bipolar plate and the GDL is generally the coldest place in the GDL, since the bipolar plate is often cooled by a cooling system. This region is therefore favorable to the condensation of water vapor. The vapor may also condense pointwise where the surface energy is favorable for a phase change, for example in hydrophilic zones or at places where liquid water is already present [Ceballos2011]. Because of this condensation, pores are blocked, which reduces the transfer of reactive gases to the cathodic catalytic layer.

This phenomenon of water transport in vapor form and of condensation in GDL therefore involves diffusive transport in GDL (gas diffusion, heat conduction) and capillary forces at the level of the condensed water droplets. The simulation of this phenomenon implies simulating diffusive and two-phase transports in a coupled way.

2.2.3 Models and simulations

We present here the models and simulation methods used to model the two-phase phenomena in the GDL. We begin by presenting models that treat porous media as homogenized media. We show some of their limitations in the case of water transport in GDL. Then we present models at the pore scale that we use to model more precisely the two-phase phenomena in the GDL.

2.2.3.1 Homogenized models

The generalized Darcy models [Darcy1856] are models consisting of partial differential equations (PDE) for the transport of liquid water at the homogenized level. The advantage of homogenized PDE is that they can be solved on a macroscopic scale without having to discretize the material at the pore scale, which is economical in computing time.

We describe here a generalized Darcy model. The water distribution is represented by local saturation. A mass balance for liquid water in the pores gives:

$$\frac{\varepsilon \rho_l}{M_{H_2O}} \frac{\partial}{\partial t}(s) + \nabla \cdot (J_l) = -\Gamma$$

Équation 2.14

where ε is the porosity, i.e. the void fraction, ρ_l is the water density, M_{H_2O} is the molar mass of water and Γ is the rate of phase change of the water.

The molar flow of liquid water is modeled by Darcy's law:

$$J_l = -\frac{\rho_l}{M_{H_2O}} \frac{K K_{rl}(s)}{\mu_l} \nabla P_l$$

Équation 2.15

where P_l is the pressure in the liquid water, K is the permeability of the porous medium and μ_l is the water viscosity. The relative permeability K_{rl} is modeled by the formula:

$$K_{rl} = s^3$$

Équation 2.16

The pressure in the liquid is related to the pressure in the gas through the notion of capillary pressure, P_c :

$$P_l = P_g - P_c$$

Équation 2.17

The capillary pressure depends on the saturation, the microstructure of the porous medium, the surface tension and the contact angle. To calibrate the two-phase homogenized models of the generalized Darcy type, it is necessary to know the capillary pressure curve of the porous material. In the absence of data, the following analytical formula is often used, called the Leverett-Udel correlation [Leverett1941]:

$$P_c(S) = \sqrt{\frac{\varepsilon}{K}}\gamma \cos(\theta)\, J(s)$$

Équation 2.18

Where γ is the surface tension of the water, θ is the contact angle of the water on the solid and $J(s)$ is a function of the saturation. To calibrate $J(s)$, the Leverett-Udel function [Udell1985] is often used:

$$J(s) = 1.417(1-s) - 2.120(1-s)^2 + 1.262(1-s)^3$$

Équation 2.19

The validity of the Leverett-Udel correlation for GDL has been studied in several articles [Si2015] [Gostick 2006] [Liu 2015] [Schulz 2007]. Most conclude that the Leverett-Udel curve is poorly adapted to GDL. Indeed, GDL are complex materials, whose microstructure is far away from the granular porous on which the Leverett-Udel correlation has been established.

The validity of these homogenized models is subject to caution. Indeed, there is no clear separation of scale between the pore scale and a macroscopic scale [Prat2015]. GDLs have in fact less than 10 pores in their thickness, because the GDLs have a thickness of approximately 300 µm and pores of 40 µm on average. Moreover, different water distributions are obtained with a homogenized Darcy model and a more precise pore network model, as shown in Figure 2.2. This raises the question of the representativeness of the Darcy-type simulations for the transport of liquid water in the GDL. The boundary conditions are also a subject of discrepancies between these simulations, as shown in Figure 2.2.

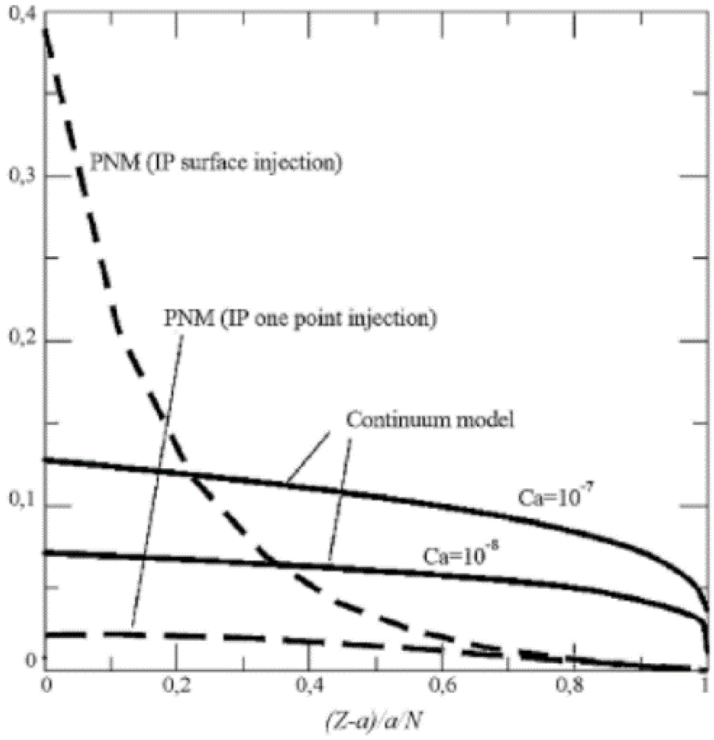

Figure 2.2 Comparison of saturation profiles obtained using a generalized Darcy model at the homogenized scale and a pore network model at the pores scale. Figure extracted from [Rebai2009].

2.2.3.2 Pore-scale models

We have seen that homogenized models have limitations for modeling the transport of liquid water in GDL. To better represent the two-phase phenomena, it is possible to model them on a finer scale, the pore scale [Blunt2013]. At this scale, simulations are made on the geometry of the pores, typically resolved on the micrometric or nanometric scale.

Pore-scale simulation methods can be divided into direct methods such as the Lattice-Boltzmann method, the volume of fluid method or interface tracking methods, and geometric (mesoscopic) methods such as the full morphology method and pore network models. Mesoscopic methods are preferred in this thesis due to their lower computational cost, which makes it possible to use microstructures large enough to be representative of the GDL structure.

2.2.3.2.1 Pore network models

The pore network models have been used many times in the field of PEM fuel cells. A state of the art of these studies has been done recently [Straubhaar2015].

In the pore network approach, the pore space of the GDL is represented as a network of pores and links. The links represent the constrictions, i.e. the narrower passages between the two neighboring pores. It is usual to distinguish structured pore networks from unstructured pore networks [Agaesse2016]. A structured pores network is constructed on a regular geometric lattice, typically a cubic lattice for 3D simulations. The pores are located on the nodes of the lattice and connected by links, which correspond to the constrictions of the pore space. In a simple cubic lattice, the links are aligned with the three main directions of a Cartesian coordinate system. In contrast, unstructured networks offer the possibility of more closely respecting the local geometry of a given microstructure. From a digital image of the actual microstructure, the network is constructed directly from the image using appropriate image analysis techniques.

Since water flow in the GDL is in the capillary digitation regime, water distribution in the network is simulated using the invasion percolation algorithm [Wilkinson1983]. This algorithm makes it possible to simulate the progressive invasion of a non-wetting fluid (liquid water here) in a wetting fluid (the gas phase here). The principle of the percolation invasion algorithm is as follows. A capillary pressure threshold is associated with each link. This threshold is given by the Young-Laplace equation, Équation 2.9. Physically, this threshold represents the maximum value of the water pressure that the capillary forces in the link can retain. The water invades one link (and its neighboring dry pore) after the other, selecting at each step the link at the liquid-gas interface that has the lowest capillary pressure threshold. This process is illustrated in Figure 2.3. This process mimics a quasi-static injection.

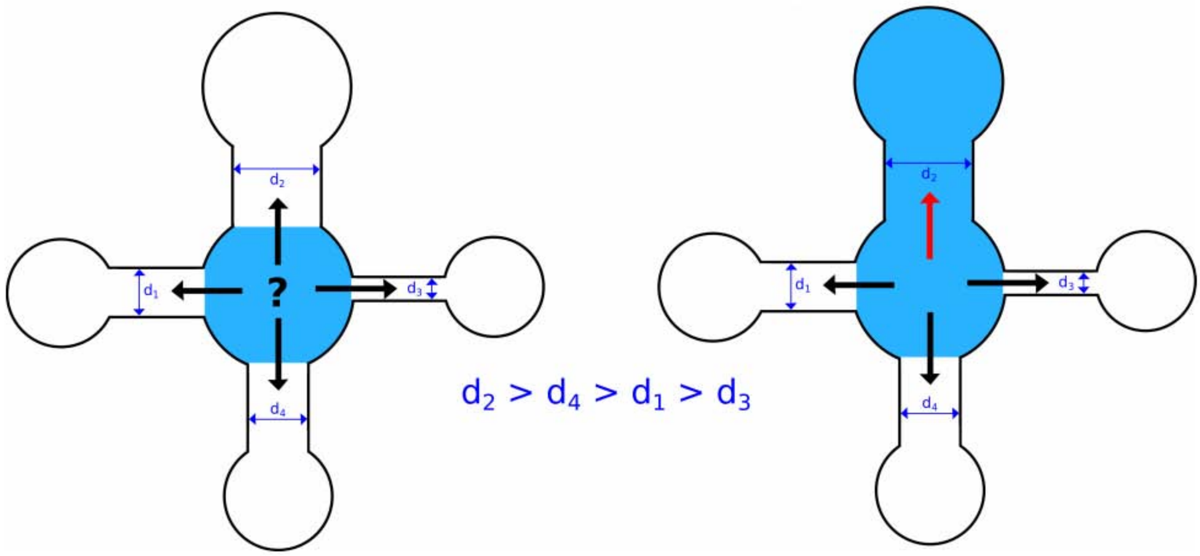

Figure 2.3 Explanatory diagram of the percolation invasion algorithm. At each stage, water invades the link which has the lowest capillary pressure threshold. When the network is uniformly hydrophobic, this leads to invading the broadest links first. Figure extracted from [Straubhaar2015].

Diffusive transport simulations are also possible with pore networks, using a method described in section 3.1.1.1.2. This makes it possible to simulate couplings between diffusive and two-phase transports using pore networks models. This is used in Chapter 6.

Percolation phenomena have been the subject of numerous works, notably in mathematics. The analogy between pure percolation and invasion percolation is as follows. In pure percolation, a random proportion of network links is randomly activated. In invasion percolation, at a fixed fluid pressure, the links whose capillary pressure thresholds are lower than the fluid pressure can potentially be invaded. The activated links are like the potentially invaded links. Increasing the fluid pressure has the effect of increasing the proportion of activated links. There is, however, a difference between invasion percolation and pure percolation. In invasion percolation, water can invade only the potentially invaded links that are connected to the injection face [Gostick2008-thesis]. This leads to rejecting certain potentially invaded links if they are not connected to the injection face, in contrary to pure percolation where no activated links are rejected. This difference is illustrated in Figure 2.4, where gray links in Figure 2.4 b) are activated but not invaded because they are not connected to the injection face.

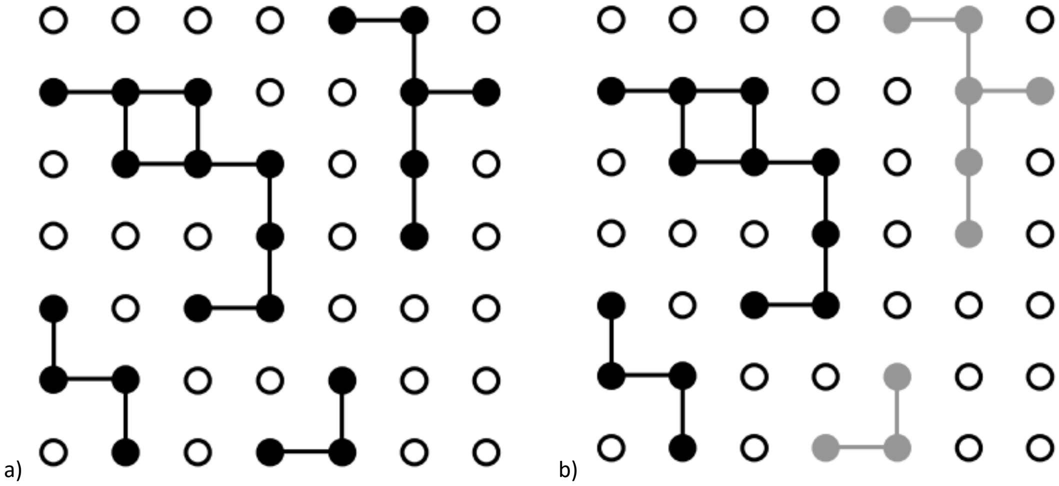

Figure 2.4 Comparison of percolation invasion and pure percolation on a square lattice. (A) Pure percolation. Black areas are active regions. B) invasion percolation. The black areas are invaded regions because they are active for pure percolation and because they are connected by a continuous path to the injection face, on the left. The gray areas are not invaded because they are not connected to the injection face. Figures from [Gostick2008-thesis].

Note that the results of the percolation theory are often not useful in the case of GDL. Indeed, these results are very often obtained on infinite networks, whereas the GDL is a thin medium which has only a few pores of thickness [Prat2015]. In addition, geometric effects, such as compression by the bipolar plate, induce that the pore sizes of the real GDL are spatially correlated, which reduces the relevance of the results obtained with uncorrelated networks. It is found experimentally that the actual percolation properties of GDL differ in many aspects from the theoretical results of percolation [Gostick2008-thesis].

2.2.3.2.2 Full morphology model

The full morphology model is based on an entirely geometric representation of the distribution of water in a porous medium. The full morphology algorithm is applied to a tomographic image of the microstructure of a porous medium. In addition to its simplicity and low cost in computing time, this approach has the advantage of considering in detail the microstructure of the porous medium.

In full morphology simulations, the shape of the region occupied by water is approximated by a union of balls of the same radius [Agaesse2016]. The radius of the balls is determined by the Young-Laplace equation, as it is assumed that the water has a uniform pressure, that the contact angle is uniform, and that the menisci are spherical. All the balls have the same radius because all meniscus bear the same capillary pressure under the conditions of capillary equilibrium which prevail during a quasi-static injection. Water invades regions to which a ball of this radius can access by following a continuous trajectory starting at the injection points. These regions are determined by a geometric analysis of the tomographic image of the porous microstructure.

More information on full morphology models is available in Chapter 5.

2.3 Imaging techniques to study fuel cell materials

2.3.1 Imaging techniques

Many techniques exist to obtain images of materials. Imaging techniques have made great progress in recent years [Yang2012]. Generally, the principle of imaging techniques is to use radiation to interact with the material. An image is reconstructed based on the information captured by detectors following this material-radiation interaction. The techniques differ by the type of radiation used, the type of interaction used and the modalities of the shooting. Figure 2.5, taken from [Cocco2013], presents a panorama of the different imaging techniques and their use in the various fields of materials for energy.

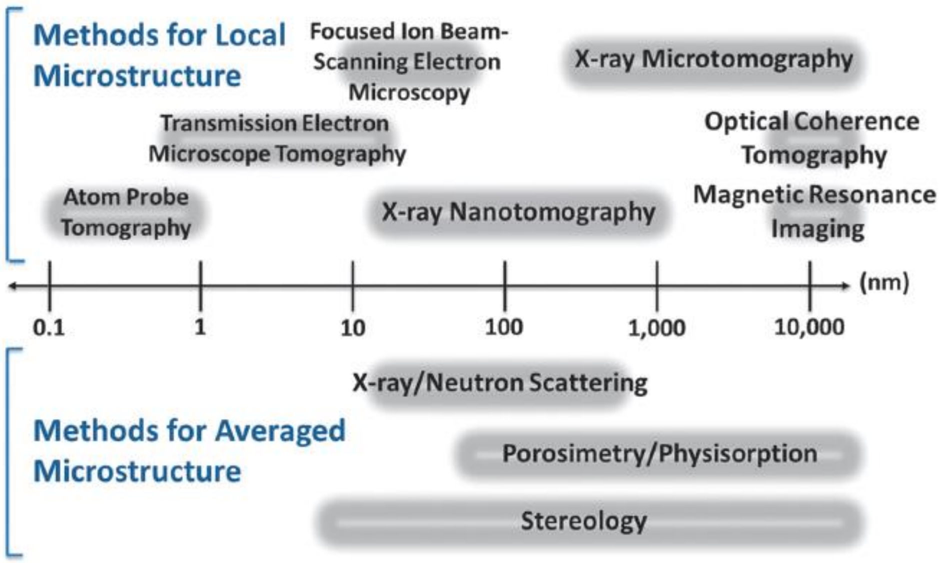

a)

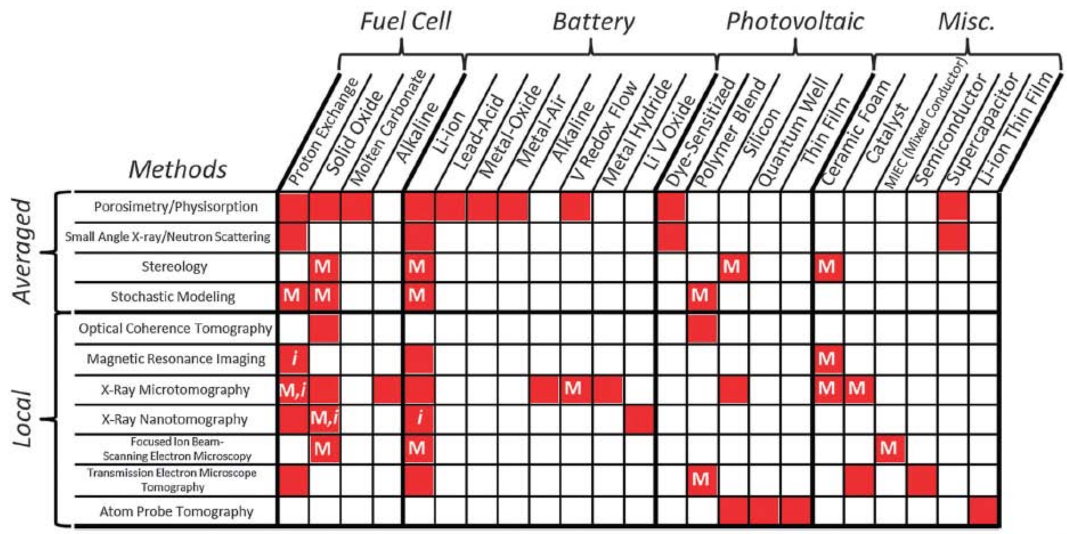

	Methods	Fuel Cell				Battery								Photovoltaic					Misc.					
		Proton Exchange	Solid Oxide	Molten Carbonate	Alkaline	Li-ion	Lead-Acid	Metal-Oxide	Metal-Air	Alkaline	V Redox Flow	Metal Hydride	Li V Oxide	Dye-Sensitized	Polymer Blend	Silicon	Quantum Well	Thin Film	Ceramic Foam	Catalyst	MIEC (Mixed Conductor)	Semiconductor	Supercapacitor	Li-ion Thin Film
Averaged	Porosimetry/Physisorption	■	■	■		■	■	■	■		■			■									■	
	Small Angle X-ray/Neutron Scattering	■				■								■									■	
	Stereology		M			M										M			M					
	Stochastic Modeling	M	M			M									M									
Local	Optical Coherence Tomography		■												■									
	Magnetic Resonance Imaging	*i*				■													M					
	X-Ray Microtomography	M,*i*	■		■	■				■	M	■				■			M	M				
	X-Ray Nanotomography	■	M,*i*			*i*							■											
	Focused Ion Beam-Scanning Electron Microscopy		M			M															M			
	Transmission Electron Microscope Tomography	■				■									M					■		■		
	Atom Probe Tomography															■	■	■						■

Fig. 2 Overview of works featured in this review. Each red box corresponds to one or more publications. M's denote sets of publications that, in addition to imaging/characterization, include modeling efforts using imaged microstructures. Similarly, i's represent *in situ* or *in operando* imaging.

b)

Figure 2.5 a) Classification of techniques used to image materials for energy, depending on the resolution and the spatially resolved or averaged nature b) state of the art in the use of these imaging techniques for different materials for energy. Figures from [Cocco2013]

In this thesis, we mainly use X-ray tomography to image the GDL. X-ray tomography makes it possible to obtain three-dimensional images of the internal structure of a sample. Figure 2.6 shows the diagram of an X-ray tomography device. The sample is traversed by a beam of X-rays emitted by a source. An X-ray detector picks up the radiation after it has passed through the sample. A radiography of the object is thus performed. The sample is rotated from many angles to obtain radiographies in many directions. A three-dimensional image of the internal structure of the sample is reconstructed by mathematical processing of all the radiographs. The interaction between matter and radiation is characterized here by the coefficient of attenuation of the X-rays during their crossing of the various materials constituting the sample. The level of attenuation depends on the physical properties of the material, the wavelength of the radiation and the energy of the radiation.

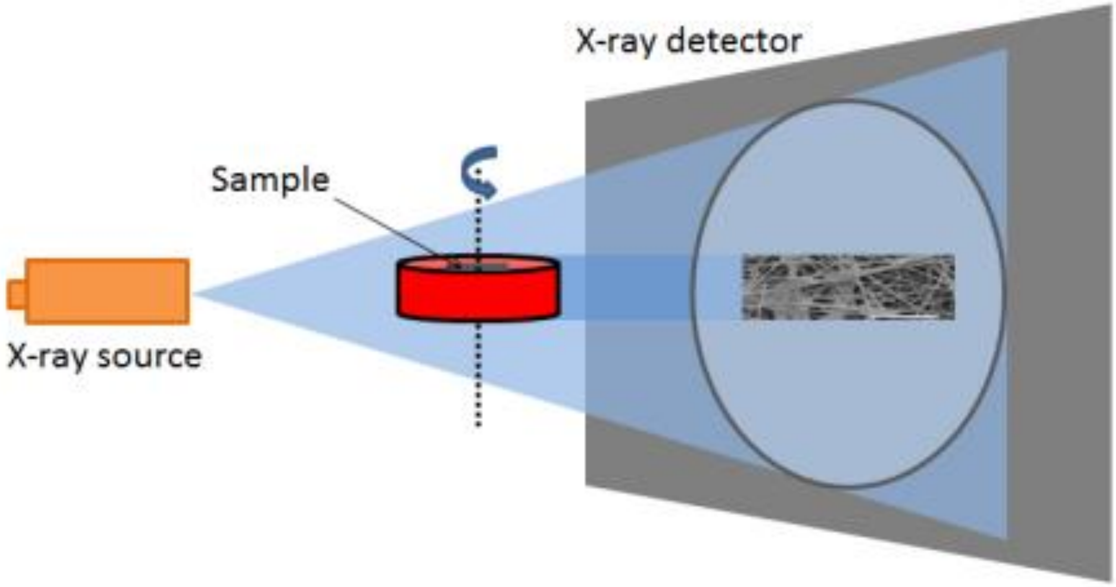

Figure 2.6 Diagram of an X-ray tomography device. Taken from [Straubhaar2015].

We sometimes use in this thesis scanning electron microscopy images (SEM). This technique makes it possible to obtain two-dimensional images of the surface of a sample, by using the interactions between matter and electrons. This technique makes it possible to produce images whose resolution can vary over several orders of magnitude, from millimeter to nanometer. It also makes it possible to obtain other contrasts between materials than using X-ray tomography, thus providing additional information. It should be noted that three-dimensional images can be obtained by the so-called FIB-SEM technique, which consists in taking SEM images of a sample which is cut layer by layer by a focused ion beam (FIB).

Numerous other imaging techniques exist [Cocco2013] [Thiele2015]: electronic transmission microscopy, neutron imaging, magnetic resonance imaging, tomographic atomic probe, atomic force microscopy, etc. Imaging techniques are experiencing strong progress, driven by the improvement of the quality of the beams and the detectors, the development of the devices to control the sample, the development of new imaging techniques, the progress of the image analysis algorithms and the increase in computing capacity [Yang2012].

2.3.2 Quantitative use of images

A possible first use of images is visual interpretation. Qualitative information is derived from this type of analysis. We are interested in quantitative analysis of images using computer-based tools.

The information contained in the images is not directly usable. Recall that an image is nothing more than an array of three-dimensional voxels (these elements are called pixels in 2D) containing gray levels. Specific algorithms must be used to extract relevant information that will increase our knowledge of materials. Let us note that the quantity of information that a tomographic image contains is counted in hundreds of Mo. Indeed, each voxel of an image contains a few bits of information on the local properties of interaction of the material with the radiation, and a 3D image usually contains several hundred million voxels. This wealth of information represents an opportunity to know precisely the materials, but also a challenge for computer processing, because of the computing time and the amount of RAM used.

2.3.2.1 Image processing and analysis tools

Quantitative analysis of images makes it possible to go beyond a simple visual analysis [Maire2014]. We describe in this section a certain number of usual analyzes applied to the images.

Computer codes are required for image analysis. A list of computer tools for image analysis of materials is compiled in [Cnudde2013]: Avizo, VGStudio Max, MAVI, Blob3D, Pore3D, 3DMA-Rock, Morpho +, Fiji. Let us also mention imorph [Imorph]. In this thesis, we have used open source libraries in python, mainly ITK and VTK, combined with the Paraview visualization software which serves as a graphical interface, as well as the ImageJ software. A brief graphical presentation of these tools is given in appendix 9.1. Note that the open source softwares 3D Slicer and Tomviz are also graphical interfaces for ITK and VTK libraries. The choice of computer tools has an important influence on the productivity of the developers and the users. The criteria that made us choose these tools are the high number of developers and users, the completeness of the toolbox and the ease of use.

2.3.2.1.1 Filtering

The images resulting from microscopy are often noisy, which means that the gray levels have random fluctuations superimposed on the value characterizing the material. To reduce the influence of these noises on the quantitative analysis of images, filters can be used.

The median filter consists in replacing each pixel by the median value of the grey level of the neighboring pixels. This in principle makes it possible to eliminate the random component of each pixel and to keep the non-random component, which varies less spatially.

The Gaussian filter consists in convolving the image by a Gaussian kernel. Each voxel is thus replaced by the average of the gray levels of the neighboring voxels, weighted by a Gaussian function depending on the distance between the voxels. This has the effect of smoothing gray levels. Let us note the analogy with the physical diffusion phenomenon, because the Gaussian function describes the resulting concentration of the diffusion of a point source in a homogeneous medium.

The anisotropic diffusion filter is a more elaborate version of the Gaussian filter. The principle of anisotropic diffusion is to reduce the noise while retaining the shape of the regions of the image. The gray levels in the image are smoothed by application of a diffusion process. The diffusion coefficient varies spatially: it is made dependent on the gradient norm of the gray levels of the image, so that it vanishes at the boundaries between regions of the image. Indeed, the norm of the gradient makes it possible to identify the edges between regions, because at the edges there is a jump of the gray level. Since the coefficient of diffusion vanishes on the edges, the shape of the regions is preserved. Elsewhere than on the edges, i.e. within the regions, the gray levels are smoothed, so the noise is removed.

2.3.2.1.2 Segmentation

Segmentating an image means identifying regions or objects in the image. This makes it possible to describe the content of the image in a more elaborate way. Identifying a region is equivalent to separating it from the surrounding regions. Several criteria can be envisaged for establishing a separation, for example a discontinuity of gray levels or a criterion on the shape of the object. Note that this operation is often complicated by the fact that the images are noisy.

We can classify the segmentation methods into several categories [Albregtsen]. Segmentation based on pixel values considers each pixel independently of the others. Thresholding is a method of this type. Region-based segmentation looks for similar pixels in the image to group and form regions. Region growth methods, split & merge, and watershed segmentation fall into this category. Edge-based segmentation is another category. The edges of the regions are sometimes simple to detect because they are zones of strong gray level change. In edge-based segmentation methods, the zones likely to be edges of regions are detected, then linked together, which makes it possible to find the regions.

2.3.2.1.3 Shape analysis

The regions in an image can be analyzed in terms of sizes and shapes. Size analyzes cover lengths, areas, volumes, and moments. In the context of microstructures, these analyzes can lead to pore and grain size distributions, volume fraction profiles, mean volume fractions, chord lengths [Torquato1993], tortuosities [Cecen2012]. The shapes can be measured by form factors, compactness, curvatures, moments, constrictivities, sphericities, roundness.

Note also that the shape of a region can be described by a cloud of points sampling its boundary. The advantage of point clouds is that geometric operations in space can be applied to points coordinates, such as rotations, translation, scaling. It is also possible to define distances between shapes from point clouds. This is used in the Procrustes analysis, a method for statistical shape analysis. Finally, the regions can be reduced to a skeleton formed of the median axes, which provides a simplified representation of the shapes.

Statistical analyzes of microstructures are also available. For example, the n-points spatial correlations [Cecen2014], and texture analyzes such as the Gray-Level Co-Occurrence Matrix (GLCM) (used for electro-catalysts as a measure of roughness [Artyushkova2012]).

In this thesis, we are interested in linking these measurements to physical phenomena, with the aim of capturing the effect of the microstructure on these physical phenomena.

2.3.2.1.4 Mathematical morphology

The mathematical morphology provides a toolbox of geometric operations allowing to modify the geometry of an image and to analyze it. Mathematical morphology algorithms are, among others, erosion and dilation, opening and closing, distance maps, local maxima, skeletons, watersheds.

These tools play a very important role in this thesis. Dilation was used to create balls representing water meniscii in Chapter 5. Opening was used to erase the fibers in a tomographic image of GDL, to distinguish them from the binder. Closure was used to add binder between the fibers of virtual GDL. Distance maps were used to calculate the constrictions sizes and to support the extraction of the pore networks. The local maxima of the distance map were used to indicate the locations of the pores. The watersheds were used to find constrictions and to set limits between the pores. The skeletons have not been used in this thesis but are often used in the literature to extract the pore networks.

The tools of mathematical morphology will be described in the different chapters as they are used.

2.3.2.1.5 Other algorithms

We cite here some of the other computer algorithms that have been used during this thesis. 3D geometry algorithms have been used to generate virtual microstructures: generation of meshes, conversion of meshes to images (voxelization) based on the intersection of meshes with rays. We also mention the surface extraction by the marching cube algorithm and the Sobol edge detector. Finally, let us emphasize that visualization and 3D rendering algorithms are essential for visualizing images.

2.3.2.2 Image-based models and simulations

Adding a physical model to images provides additional information to the image. Indeed, physical models often bring information from outside the images. The informations may be, for example, equations representing physical phenomena, physical properties of materials, information on the structure of the material at scales lower than the resolution of the image. All these informations are generally obtained by different methods than the method used to acquire the image. Conversely, an image can bring useful information to a physical model. It can for example make it possible to calibrate the geometrical parameters of the model [Maire2014].

A first approach for associating images and models is to calibrate the geometric parameters of the model with an image. An example is to calibrate a random network on an image [Thiedmann2011] [Stenzel2013]. A second approach is to use the image directly as a simulation domain. This is the case for example of direct simulations on microstructures obtained by X-ray tomography, using the voxel grid as discretization [García-Salaberri2015], or pore networks constructed directly on elements of the image. We describe these two methods in section 3.1.1. Note that the medical sector is at the forefront in the field of simulations based on images [Ayache2014].

2.3.3 Virtual models of microstructures

3D images can be created virtually, without computerized tomography. Virtual microstructures make it possible to design and test materials that do not yet exist. Microstructure models also provide a better understanding of existing microstructures. Chapter 7 is devoted to virtual microstructures.

This approach has been the subject of numerous publications in the field of PEM fuel cells. Virtual images have been developped for the GDL [Thiedmann2012] [Thiedmann2009] [Froning2014] [Becker2011] [Daino2012] [Gaiselmann2012] [El-Hannach2014] [Tayarani-Yoosefabadi2016], the MPL [Becker2011] [Zamel2012] [El-Hannach2015] and the catalytic layers [Mukherjee2006] [Kim2009] [Siddique2010] [Malek2011] [Lange2012] [Baker2012].

2.3.4 Limitations of accessible information using imagery

We list here a series of limitations of the imaging techniques: the presence of noise, the limited resolution, the lack of contrast between certain materials, the limited field of view and the discretization effect. These limitations impose constraints on the choice of imaging techniques and the type of information that we can access on materials. These constraints are at the origin of many design choices for image-based methodologies and image-based modeling of materials. In addition, specific techniques can be developed to overcome these limitations.

2.3.4.1 Noise

The images obtained using microscopy are often noisy, i.e. the gray levels have random fluctuations superimposed on the value characterizing the material. This is because images are obtained by using physical signals. The acquisition chain involves the radiation sources, the detectors, the sample holders, the sample itself ... Each element of the chain can undergo a fluctuation and contribute to a source of noise.

These noises have an influence on the quantitative analysis of images. To extract reliable information from the images, it is therefore necessary to reduce the noise level by using the appropriate imaging techniques and appropriate image processing filters.

2.3.4.2 Limited resolution and multi-scale structure of materials

An image gives information about the microstructure of a material at a certain length scale. However, the physical, chemical and geometric structure of the material at smaller length scales can have an impact on the properties of the material. Figure 2.7 shows the structure of a GDL at several length scales. The finer scales show that the binder is porous, which was not seen at larger scales. This may influence the diffusion properties of the GDL, but it can not be determined from the larger scale image only.

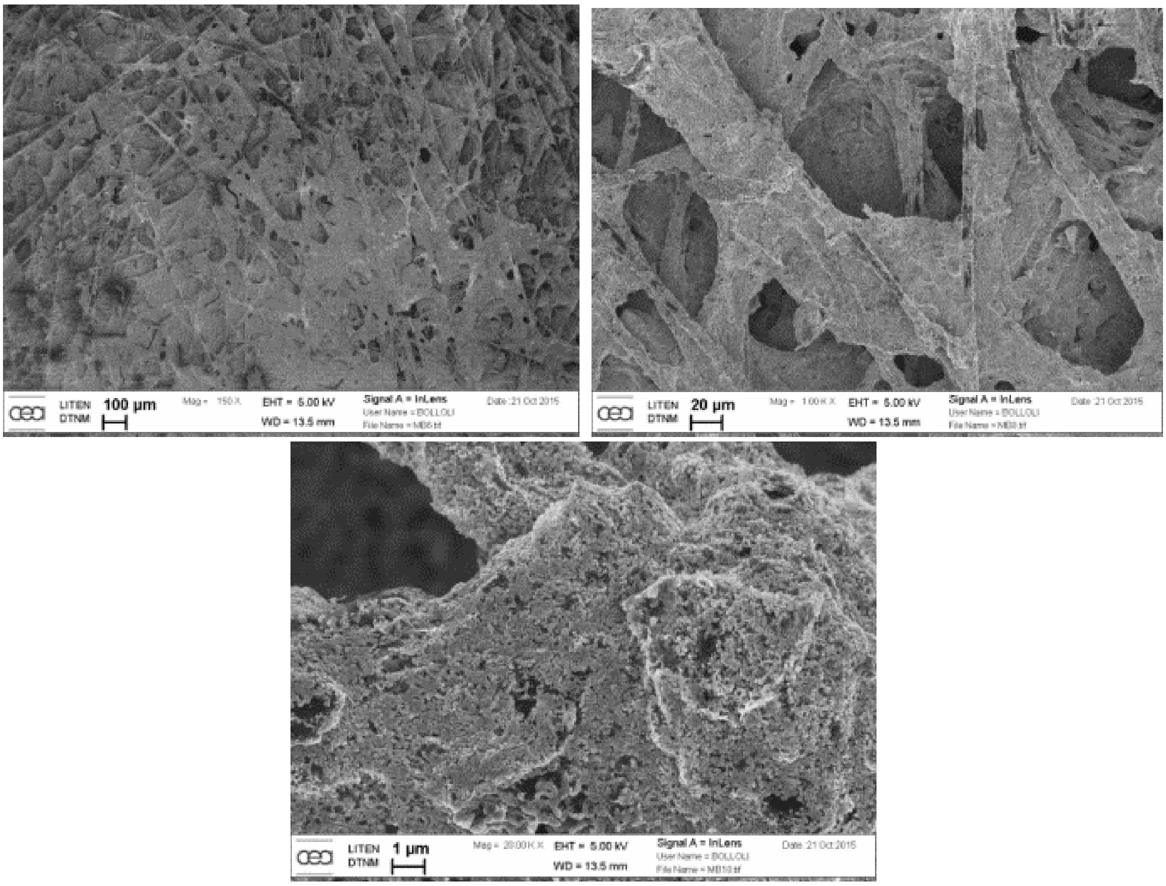

Figure 2.7 SEM images of GDL. From left to right and from top to bottom: increasing zoom. The characteristics of the microstructure are not the same at all scales. Images taken by Marco Bolloli, CEA.

An image therefore gives partial information on the materials. To model the physical properties of a material, it is often necessary to add the information that is missing in the images. It is often necessary to know non-geometric physical parameters, such as the bulk property of a phase. These parameters must be determined otherwise. This can be a challenge, for example if this leads to experimental measurements on microscopic samples. Note that in the absence of these non-geometric parameters, using images with models can be useful anyway. For example, a parametric study with fixed geometry can shed light on these non-geometric parameters. Conversely, varying the microstructure while maintaining non-geometric parameters can shed light on the effect of the microstructure on the properties of the material.

Multi-scale imaging has been developed to overcome the resolution limitation [Cnudde2013]. The principle of multi-scale imaging is to make high-resolution images of some sub-samples, and to associate them to their position in an image of the entire sample [Grader2009]. The image registration techniques make it possible to map the images taken at different scales in an automated manner. Thus, one can capture the microstructure on several scales in a coherent way, and develop models on each scale.

2.3.4.3 Lack of contrast between some materials

It is desirable to be able to distinguish on an image of a composite material the different constituent materials. This is useful for example in modeling the properties of the composite material - a porous material for example – as a function of the properties of its constituents.

The contrast between the gray levels of the different materials comes from the different interaction properties of these materials with the radiation. The contrast depends on the type of radiation used. For example, the contrast is very low between the fibers and the binder of the GDL on an X-ray tomography image, whereas on a SEM image the difference is very visible. This lack of contrast adds a constraint on the choice of imaging techniques.

To overcome this constraint, techniques have been developed to mix the information obtained with several techniques. This is the case, for example, for correlative tomography. Its principle is to use computer imaging tools to match images of the same sample obtained with different imaging techniques [Burnett2014]. This provides access to additional information about materials that would be inaccessible if only one imaging technique was used.

2.3.4.4 Limited field of view and spatial variability of microstructures

An image offers a limited field of view, allowing only a part of the microstructure to be seen. Microstructures often vary from one place to another [Cnudde2013]. Figure 2.8 illustrates the random variability of a GDL microstructure. If we are below the representative elementary volume, the spatial variability of the microstructure is reflected in the transport properties of the samples, which therefore vary from one region to another [Wargo2012].

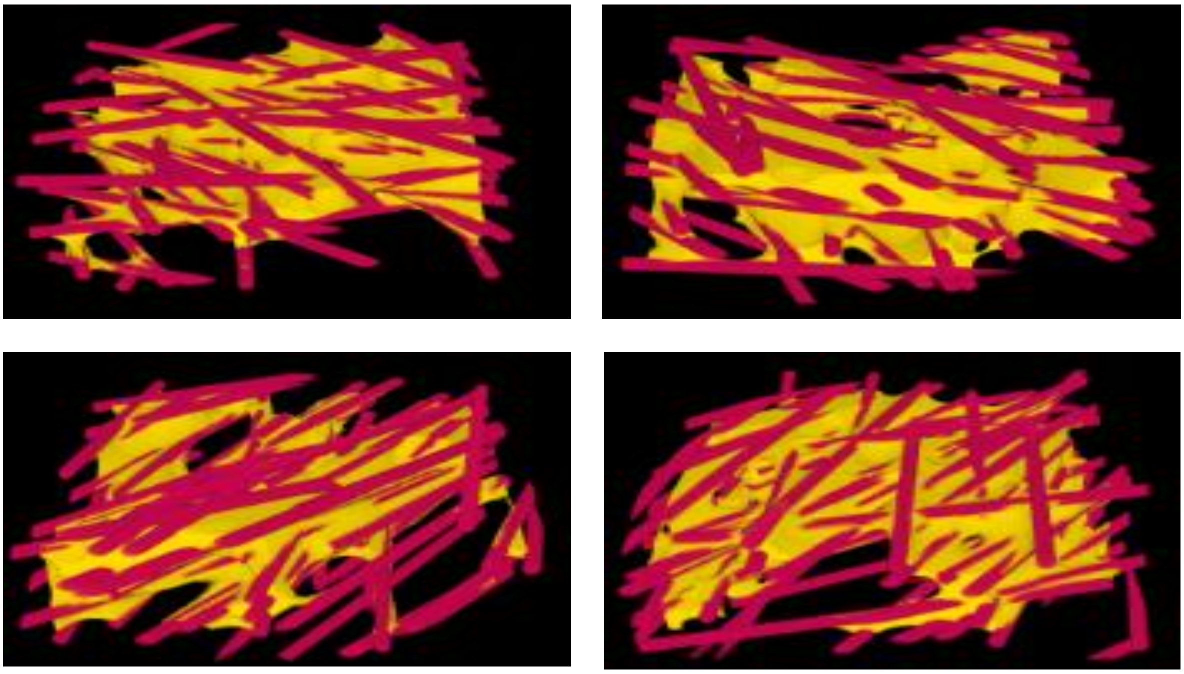

Figure 2.8 3D images of virtual GDL microstructures at the same zoom level, which vary randomly.

One way to overcome this limitation is to construct an image with a wide field of view, from a mosaic of images with a smaller field of view [Haberthür2010] [Mokso2012]. The disadvantages of this approach are the large number of small images to be taken and the large memory size of the image with a large field of view obtained. It is more interesting, rather than exhaustively sampling the sample, to perform a partial sampling to characterize the statistical properties of the microstructure. Once the data are collected on the variability of the microstructure, probabilistic models can be used to model the variability. An example of a probabilistic model of the spatial variability of GDL properties is given in Appendix 9.2.

2.3.4.5 Discretization effect

The discretization in voxels implies that the finest detail accessible in an image has the size of a voxel. For instance, the position of the interfaces between materials is known only up to a voxel. Indeed, the gray level of a voxel in which there is an interface between two materials does not indicate where the interface is in this voxel. The gray level of the voxel is generally the average of the gray levels of the two materials, weighted by the volume fractions of these materials in the voxel [Cnudde2013]. It follows from this that the exact volume of the regions is known only to a certain precision. This is generally an artifact that reduces the accuracy of quantitative analyzes [Ketcham2001], especially for small regions or regions that have a high surface to volume ratio. Another consequence is that the interfaces are represented by steps because of the discretization in voxels, an effect which is called aliasing. This involves difficulty in knowing surface areas, which is problematic for roughness calculations. Special algorithms can be used to interpolate regular surfaces through the discretized surfaces.

2.4 Bibliography

- [Agaesse2016] Tristan Agaesse, Adrien Lamibrac, Felix N. Büchi, Joel Pauchet, Marc Prat, Validation of pore network simulations of ex-situ water distributions in a gas diffusion layer of proton exchange membrane fuel cells with X-ray tomographic images, Journal of Power Sources, Volume 331, 2016, Pages 462–474
- [Albregtsen] Fritz Albregtsen, Digital Image Analysis course, Department of Informatics, University of Oslo
- [Andrä2013-1] Heiko Andrä, Nicolas Combaret, Jack Dvorkin, Erik Glatt, Junehee Hand, Matthias Kabel, Youngseuk Keehm, Fabian Krzikalla, Minhui Lee, Claudio Madonna, Mike Marsh, Tapan Mukerji, Erik H. Saenger, Ratnanabha Sain, Nishank Saxena, Sarah Ricker, Andreas Wiegmann, Xin Zhan, Digital rock physics benchmarks—Part I: Imaging and segmentation, Computers & Geosciences, Volume 50, January 2013, Pages 25–32
- [Andrä2013-2] Heiko Andrä, Nicolas Combaret, Jack Dvorkin, Erik Glatt, Junehee Hand, Matthias Kabel, Youngseuk Keehm, Fabian Krzikalla, Minhui Lee, Claudio Madonna, Mike Marsh, Tapan Mukerji, Erik H. Saenger, Ratnanabha Sain, Nishank Saxena, Sarah Ricker, Andreas Wiegmann, Xin Zhan, Digital rock physics benchmarks—part II: Computing effective properties, Computers & Geosciences, Volume 50, January 2013, Pages 33-43
- [Artyushkova2012] Kateryna Artyushkova, Svitlana Pylypenko, Madhu Dowlapallic, Plamen Atanassov, Use of digital image processing of microscopic images and multivariate analysis for quantitative correlation of morphology, activity and durability of electrocatalysts, RSC Advances, 2012, 2, 4304–4310
- [Ayache2014] Nicholas Ayache, Des images médicales au patient numérique, cours au Collège de France, Chaire annuelle Informatiques et Sciences numériques, 2014
- [Baker2012] Craig Baker, A MICROSTRUCTURAL MODEL FOR A PROTON EXCHANGE MEMBRANE FUEL CELL CATALYST LAYER, Master Thesis, Queen's University, Kingston, Ontario, Canada, 2012
- [Bauer2012] Georg Josef Bauer, A Coupled Finite Element Approach for Electrochemical Systems, PhD thesis TECHNISCHE UNIVERSITÄT MÜNCHEN, 2012
- [Bazant2010] Martin Bazant. 10.626 Electrochemical Energy Systems. Spring 2010. Massachusetts Institute of Technology: MIT OpenCourseWare, http://ocw.mit.edu. License: Creative Commons BY-NC-SA.
- [Bazylak2009] Bazylak, Liquid water visualization in PEM fuel cells: A review, Int. J. Hydrogen Energy. 34 (2009) 3845–3857. doi:10.1016/j.ijhydene.2009.02.084.
- [Becker2009] J. Becker, R. Flückiger, M. Reum, F.N. Büchi, F. Marone, M. Stampanoni, J. Electrochem. Soc. 156 (2009) B1175
- [Becker2011] Jürgen Becker, Christian Wieser, Stephan Fell, Konrad Steiner, A multi-scale approach to material modeling of fuel cell diffusion media, International Journal of Heat and Mass Transfer, Volume 54, Issues 7–8, March 2011, Pages 1360–1368
- [Bedet2008] J. Bedet, G. Maranzana, S. Leclerc, O. Lottin, C. Moyne, D. Stemmelen, P. Mutzenhardt, D. Canet, International Journal of Hydrogen Energy 33 (2008) 3146.
- [Blunt2013] Martin J. Blunt, Branko Bijeljic, Hu Dong, Oussama Gharbi, Stefan Iglauer, Peyman Mostaghimi, Adriana Paluszny, Christopher Pentland, Pore-scale imaging and modelling, Advances in Water Resources, Volume 51, January 2013, Pages 197–216
- [Boilat2008] P. Boillat, D. Kramer, B.C. Seyfang, G. Frei, E. Lehmann, G.G. Scherer, A. Wokaun, Y. Ichikawa, Y. Tasaki, K. Shinohara, Electrochem. Commun. 10 (2008) 546
- [Bruggeman1935] D.A.G. Bruggeman, Calculation of various physics constants in heterogenous substances I dielectricity constants and conductivity of mixed bodies from isotropic substances, Annalen der Physik (Leipzig), 24 (1935), pp. 636–664

- [Burnett2014] T. L. Burnett, S. A. McDonald, A. Gholinia, R. Geurts, M. Janus, T. Slater, S. J. Haigh, C. Ornek, F. Almuaili, D. L. Engelberg, G. E. Thompson & P. J. Withers, Correlative Tomography, SCIENTIFIC REPORTS, 4 : 4711, 2014
- [Cecen2012] A. Çeçen, E. A. Wargo, A. C. Hanna, D. M. Turner, S. R. Kalidindi and E. C Kumbur, 3-D Microstructure Analysis of Fuel Cell Materials: Spatial Distributions of Tortuosity, Void Size and Diffusivity, J. Electrochem. Soc. 2012, volume 159, issue 3, B299-B307
- [Cecen2014] A. Çeçen, T. Fast, E.C. Kumbur, S.R. Kalidindi, A data-driven approach to establishing microstructure-property relationships in porous transport layers of polymer electrolyte fuel cells, Journal of Power Sources 245 (2014) 144-153
- [Cnudde2013] V. Cnudde, M.N. Boone, High-resolution X-ray computed tomography in geosciences: A review of the current technology and applications, Earth-Science Reviews, Volume 123, August 2013, Pages 1–17
- [Cocco2013] Alex P. Cocco, George J. Nelson, William M. Harris, Arata Nakajo, Timothy D. Myles, Andrew M. Kiss, Jeffrey J. Lombardo, Wilson K. S. Chiu, Three-dimensional microstructural imaging methods for energy materials, Phys.Chem. Chem. Phys., 2013, 15, 16377
- [Daino2012] Michael M. Daino, Satish G. Kandlikar, 3D phase-differentiated GDL microstructure generation with binder and PTFE distributions, International journal of hydrogen energy 37 (2012) 5180-5190
- [Darcy1856] Darcy, H., 1856. Les Fontaines Publiques de la Ville de Dijon. Dalmont, Paris.
- [El-Hannach2014] Mohamed El-Hannach, Erik Kjeang, Stochastic Microstructural Modeling of PEFC Gas Diffusion Media, Journal of The Electrochemical Society, 161 (9) F951-F960 (2014)
- [El-Hannach2015] Mohamed El-Hannach, Randhir Singh, Ned Djilali, Erik Kjeang, Micro-porous layer stochastic reconstruction and transport parameter determination, Journal of Power Sources 282 (2015) 58-64
- [Flückiger2011] R. Flückiger, F. Marone, M. Stampanoni, A. Wokaun, F. N. Büchi, Investigation of liquid water in gas diffusion layers of polymer electrolyte fuel cells using X-ray tomographic microscopy, Electrochimica Acta 56 (2011) 2254.
- [Froning2014] Froning, D., Gaiselmann, G., Reimer, U. et al., Stochastic Aspects of Mass Transport in Gas Diffusion Layers, Transp Porous Med (2014) 103: 469. doi:10.1007/s11242-014-0312-9
- [Gaiselmann2012] Gerd Gaiselmann, Ralf Thiedmann, Ingo Manke, Werner Lehnert, Volker Schmidt, Stochastic 3D Modeling of Fiber Based Materials, Computational Materials Science, Volume 59, June 2012, Pages 75–86
- [García-Salaberri2015] P. A. García-Salaberri, G. Hwang, M. Vera, A.Z. Weber, J.T. Gostick, Effective diffusivity in partially-saturated carbon-fiber gas diffusion layers: Effect of through-plane saturation distribution, Int. J. Heat Mass Transf. 86 (2015) 319–333.
- [García-Salaberri2015] Pablo A. García-Salaberri, Gisuk Hwang, Marcos Vera, Adam Z. Weber, Jeff T. Gostick, Effective diffusivity in partially-saturated carbon-fiber gas diffusion layers: Effect of through-plane saturation distribution, International Journal of Heat and Mass Transfer 86 (2015) 319–333
- [Gibiansky1993] https://www.mat.uniroma2.it/~braides/ICTP93/ICTP93Gibiansky.pdf
- [Gostick 2006] Capillary pressure and hydrophilic porosity in gas diffusion layers for polymer electrolyte fuel cells, Jeffrey T. Gostick, Michael W. Fowler, Marios A. Ioannidis, Mark D. Pritzker, Y.M. Volfkovich, A. Sakars, Journal of Power Sources, Volume 156, Issue 2, 1 June 2006, Pages 375–387
- [Gostick2008-thesis] J. Gostick, Multiphase Mass Transfer and Capillary Properties of Gas Diffusion Layers for Polymer Electrolyte Membrane Fuel Cells, PhD thesis, Waterloo University, 2008
- [Gostick2010] J. Gostick, H. Gunterman, B. Kienitz, Tomographic Imaging of Water Injection and Withdrawal in PEMFC Gas Diffusion Layers, ECS Trans. 33 (2010) 1407–1412. doi:10.1149/1.3484632.
- [Grader2009] A.S. Grader, A.B.S. Clark, T. Al-Dayyani, A. Nur, Computations of porosity and permeability of sparic carbonate using multi-scale CT images, SCA2009-Temp Paper, International Symposium of the Society of Core Analysts, 2009

- [Haberthür2010] D. Haberthür, C. Hintermüller, F. Marone, J.C. Schittny, M. Stampanoni, Radiation dose optimized lateral expansion of the field of view in synchrotron radiation X-ray tomographic microscopy, Journal of Synchrotron Radiation, 17 (5), 2010, pp. 590–599
- [Hartnig2008] C. Hartnig, I. Manke, R. Kuhn, N. Kardjilov, J. Banhart, W. Lehnert, Cross-sectional insight in the water evolution and transport in polymer electrolyte fuel cells, Appl. Phys. Lett. 92 (2008) 134106.
- [Hinebaugh2012-tomo] Hinebaugh J, Lee J, Bazylak A. Visualizing Liquid Water Evolution in a PEM Fuel Cell Using Synchrotron X-ray Radiography. Journal of the Electrochemical Society 2012; 159 (12), F826.
- [Hinebaugh2015] J. Hinebaugh, J. Lee, C. Mascarenhas, A. Bazylak, Quantifying Percolation Events in PEM Fuel Cell Using Synchrotron Radiography, Electrochimica Acta, Volume 184, 1 December 2015, Pages 417–426
- [Hinebaugh2015-Thesis] James Thomas Hinebaugh, Pore Network Modeling and Synchrotron Imaging of Liquid Water in the Gas Diffusion Layer of Polymer Electrolyte Membrane Fuel Cells, PhD thesis, University of Toronto, 2015
- [Imorph] imorph open source software, http://imorph.fr/, contact: Jerome Vicente, IUSTI Laboratory, UMR CNRS 72343, Aix Marseille Université
- [Iranzo2014] Alfredo Iranzo, Pierre Boillat, Liquid water distribution patterns featuring back-diffusion transport in a PEM fuel cell with neutron imaging, International Journal of Hydrogen Energy, Volume 39, Issue 30, 13 October 2014, Pages 17240–17245
- [Ketcham2001] R.A. Ketcham, W.D. Carlson, Acquisition, optimization and interpretation of X-ray computed tomographic imagery: applications to the geosciences, Computers & Geosciences, 27 (4), 2001, pp. 381–400
- [Kim2009] S. Kim, MM. Mench. Investigation of temperature-driven water transport in polymer electrolyte fuel cell: phasechange-induced flow. Journal of the Electrochemical Society 156 (2009) B353.
- [Kim2009] Seung Hyun Kim, Heinz Pitsch, Reconstruction and Effective Transport Properties of the Catalyst Layer in PEM Fuel Cells, Journal of The Electrochemical Society, 156 (6) B673-B681 (2009)
- [Kim2012] Jongrok Kim, Junho Je, TaeJoo Kim, Massoud Kaviany, Sang Young Son, MooHwan Kim, Breakthrough/drainage pressures and X-ray water visualization in gas diffusion layer of PEMFC, Current Applied Physics, Current Applied Physics 12 (2012) 105e108
- [Kim2013] Seung-Gon Kim, Sang-Joon Lee, A review on experimental evaluation of water management in a polymer electrolyte fuel cell using X-ray imaging technique, Journal of Power Sources, Volume 230, 15 May 2013, Pages 101–108
- [Kramer2005] D. Kramer, J. Zhang, R. Shimoi, E. Lehmann, A. Wokaun, K. Shinohara, G.G. Scherer, Electrochim. Acta 50 (2005) 2603.
- [Kramer2008] Denis Kramer, Stefan A. Freunberger, Reto Flückiger, Ingo A. Schneider, Alexander Wokaun, Felix N. Büchi, Günther G. Scherer, Electrochemical diffusimetry of fuel cell gas diffusion layers, Journal of Electroanalytical Chemistry 612 (2008) 63–77
- [Lamibrac2016] A. Lamibrac, J. Roth, M. Toulec, F. Marone, M. Stampanoni, F.. Buechi, Characterization of Liquid Water Saturation in Gas Diffusion Layers by X-Ray Tomographic Microscopy, J. Electrochem. Soc. 163 (2016) F202–F209.
- [Lange2012] Kyle J. Lange, Pang-Chieh Sui, Ned Djilali, Determination of effective transport properties in a PEMFC catalyst layer using different reconstruction algorithms, Journal of Power Sources 208 (2012) 354–365
- [Lee2013] Lee J, Hinebaugh J, Bazylak A. Synchrotron X-ray radiographic investigations of liquid water transport behavior in a PEMFC with MPL-coated GDLs. Journal of Power Sources 2013; 227(0):123-30.
- [Lemonnier2006] Hervé Lemonnier, UNE INTRODUCTION AUX ECOULEMENTS DIPHASIQUES, 2006, http://herve.lemonnier.sci.free.fr/TPF/TPF.htm
- [Leverett1941] Leverett MC. Capillary behavior in porous solids. American Institute of Mining and Metallurgical Engineers -- Petroleum Development and Technology, 142 (152-168) 1941.

- [Liu 2015] Liquid water transport characteristics of porous diffusion media in polymer electrolyte membrane fuel cells: A review, Xunliang Liu, Fangyuan Peng, Guofeng Lou, Zhi Wen, Journal of Power Sources 299 (2015)
- [Mack2014] Florian Mack, Merle Klages, Joachim Scholta, Ludwig Jörissen, Tobias Morawietz, Renate Hiesgen, Dominik Kramer, Roswitha Zeis, Morphology studies on high-temperature polymer electrolyte membrane fuel cell electrodes, Journal of Power Sources, Volume 255, 1 June 2014, Pages 431–438
- [Maire2014] E. Maire, P. J. Withers, Quantitative X-ray tomography, International Materials Reviews, 59:1, 1-43, (2014)
- [Malek2011] Kourosh Malek, Tetsuya Mashio, Michael Eikerling Microstructure of Catalyst Layers in PEM Fuel Cells Redefined: A Computational Approach, Electrocatal (2011) 2:141–157
- [Manke2007] I. Manke, C. Hartnig, M. Grünerbel, W. Lehnert, K. Kardjilov, A. Haibel, et al. Investigation of water evolution and transport in fuel cells with high resolution synchrotron X-ray radiography. Applied Physics Letters 90 (2007) 174105.
- [Manke2007] I. Manke, Ch. Hartnig, M. Grünerbel, W. Lehnert, N. Kardjilov, A. Haibel, A. Hilger, J. Banhart, H. Riesemeier, Investigation of water evolution and transport in fuel cells with high resolution synchrotron x-ray radiography, Applied Physics Letters 90, 174105 (2007)
- [Markötter2011] H. Markötter, I. Manke, P. Krüger, T. Arlt, J. Haussmann, M. Klages, et al., Investigation of 3D water transport paths in gas diffusion layers by combined in-situ synchrotron X-ray radiography and tomography, Electrochem. Commun. 13 (2011) 1001–1004.
- [Mayrhuber2015] I. Mayrhuber, F. Marone, M. Stampanoni, T.J. Schmidt, F.N. Buechi, Fast X-ray Tomographic Microscopy: Investigating Mechanisms of Performance Drop during Freeze Starts of Polymer Electrolyte Fuel Cells, ChemElectroChem (in Press. (2015).
- [Mokso2012] R. Mokso, L. Quaroni, F. Marone, S. Irvine, J. Vila-Comamala, A. Blanke, M. Stampanoni, X-ray mosaic nanotomography of large microorganisms, Journal of Structural Biology, 177 (2), 2012, pp. 233–238
- [Mukherjee2006] Partha P. Mukherjee, Chao-Yang Wang, Stochastic Microstructure Reconstruction and Direct Numerical Simulation of the PEFC Catalyst Layer, Journal of The Electrochemical Society, 153 (5) A840-A849 (2006)
- [Nam2003] J. H. Nam et M. Kaviany, Effective diffusivity and water-saturation distribution in single- and two-layer PEMFC diffusion medium, International Journal of Heat and Mass Transfer, vol. 46, n°. 24, p. 4595-4611, Nov. 2003.
- [Prat2015] M. Prat, T. Agaësse, Thin Porous Media, Chapter in book: Handbook of Porous Media, Edition: Third Edition, Chapter: 4, Publisher: CRC Press, Editors: Kambiz Vafai, pp.89-112, 2015
- [Quesnel2015] Charles Quesnel, Ren Cao, Jorge Lehr, Anne-Marie Kietzig, Adam Z. Weber, and Jeff T. Gostick, Dynamic Percolation and Droplet Growth Behavior in Porous Electrodes of Polymer Electrolyte Fuel Cells, J. Phys. Chem. C, 2015, 119 (40), pp 22934–22944
- [Rebai2009] Rebai M, Prat M. Scale effect and two-phase flow in a thin hydrophobic porous layer. Application to water transport in gas diffusion layers of PEM fuel cells. J Power Sources, 2009, 192,534-543.
- [Renard1997] Ph. Renard, G. de Marsily, Calculating equivalent permeability: a review, Advances in Water Resources, Volume 20, Issues 5–6, October–December 1997, Pages 253–278
- [Rosen2012] T. Rosen, J. Eller, J. Kang, N.I. Prasianakis, J. Mantzaras, F.N. Buchi, Saturation Dependent Effective Transport Properties of PEFC Gas Diffusion Layers, J. Electrochem. Soc. 159 (2012) F536–F544.
- [Satija2004] R. Satija, D. Jacobson, M. Arif, S. Werner, In situ neutron imaging technique for evaluation of water management systems in operating PEM fuel cells. Journal of Power Sources 129 (2004) 238.
- [Schulz 2007] Modeling of Two-Phase Behavior in the Gas Diffusion Medium of PEFCs via Full Morphology Approach Volker Paul Schulz, Jürgen Becker, Andreas Wiegmann, Partha P. Mukherjee, and Chao-Yang Wangb, Journal of The Electrochemical Society, 154 4 B419-B426 2007

- [Si2015] Chao Si, Xiao-Dong Wang, Wei-Mon Yan, and Tian-Hu Wang, *Review Article: A Comprehensive Review on Measurement and Correlation Development of Capillary Pressure for Two-Phase Modeling of Proton Exchange Membrane Fuel Cells,* Hindawi Publishing Corporation Journal of Chemistry Volume 2015, Article ID 876821, 17 pages
- [Si2015] Chao Si, Xiao-Dong Wang, Wei-Mon Yan, Tian-Hu Wang, A Comprehensive Review on Measurement and Correlation Development of Capillary Pressure for Two-Phase Modeling of Proton Exchange Membrane Fuel Cells, Hindawi Publishing Corporation, Journal of Chemistry, Volume 2015, Article ID 876821, 17 pages
- [Siddique2010] N.A. Siddique, Fuqiang Liu Process based reconstruction and simulation of a three-dimensional fuel cell catalyst layer, Electrochimica Acta 55 (2010) 5357–5366
- [Singh2008] H. Singh, A.M. Gokhale, S.I. Lieberman, S. Tamirisakandala, Image based computations of lineal path probability distributions for microstructure representation, Materials Science and Engineering: A, Volume 474, Issues 1–2, 15 February 2008, Pages 104–111
- [Sinha2006] P.K. Sinha, P. Halleck, C.-Y. Wang, Electrochem. Solid State 9 (2006) A344.
- [Spernjak2010] Dusan Spernjak, Partha P. Mukherjee, Rangachary Mukundan, John Davey, Daniel S. Hussey, David Jacobson, Rodney L. Borup, Measurement of Water Content in Polymer Electrolyte Membranes Using High Resolution Neutron Imaging, ECS Trans. 2010 volume 33, issue 1, 1451-1456
- [Stenzel2013] O Stenzel, D Westhoff, I Manke, M Kasper, D P Kroese, V Schmidt, Graph-based simulated annealing: A hybrid approach to stochastic modeling of complex microstructures, Modelling and Simulation in Materials Science and Engineering, Volume 21, Number 5, 2013
- [Straubhaar2015] Benjamin Straubhaar, Pore network modelling of condensation in Gas Diffusion Layers of Proton Exchange Membrane Fuel Cells, PhD thesis, INP Toulouse, 2015
- [Suzuki2011] T. Suzuki, Y. Tabuchi, S. Tsushima, S. Hirai, Measurement of water content distribution in catalyst coated membranes under water permeation conditions by magnetic resonance imaging, International Journal of Hydrogen Energy 36 (2011) 5479.
- [Taralova2015] Vasilena Taralova, Upscaling Approaches for Nonlinear Processes in Lithium-Ion Batterie, PhD thesis Technischen Universität Kaiserslautern, 2015
- [Tayarani-Yoosefabadi2016] Z. Tayarani-Yoosefabadi, D. Harvey, J. Bellerive, E. Kjeang, Stochastic microstructural modeling of fuel cell gas diffusion layers and numerical determination of transport properties in different liquid water saturation levels, Journal of Power Sources 303 (2016) 208-221
- [Teranishi2006] K. Teranishi, S. Tsushima, S. Hirai, J. Electrochem. Soc. 153 (2006) A664.
- [Thiedmann2009] Ralf Thiedmann, Christoph Hartnig, Ingo Manke, Volker Schmidt, Werner Lehnert, Local Structural Characteristics of Pore Space in GDLs of PEM Fuel Cells Based on Geometric 3D Graphs, Journal of the Electrochemical Society 156, B1339 - B1347 (2009)
- [Thiedmann2011] Ralf Thiedmann, Ingo Manke, Werner Lehnert, Volker Schmidt, Random geometric graphs for modelling the pore space of fibre-based materials, Journal of Materials Science, December 2011, 46:7745
- [Thiedmann2012] Ralf Thiedmann, Gerd Gaiselmann, Werner Lehnert, Volker Schmidt, Stochastic Modeling of Fuel-Cell Components, in book Fuel Cell Science and Engineering: Materials, Processes, Systems and Technology, editors Detlef Stolte, Bernd Emonts, Wiley-VCH Verlag & Co. KGaA, 2012
- [Thiele2015] Simon Thiele, Severin Vierrath, Matthias Klingele, Roland Zengerle, Tomographic Analysis of Polymer Electrolyte Fuel Cell Catalyst Layers: Methods, Validity and Challenges, ECS Transactions, 69 (17) 409-418 (2015)
- [Tjaden2016] Bernhard Tjaden, Samuel J Cooper, Daniel JL Brett, Denis Kramer, Paul R Shearing, On the origin and application of the Bruggeman correlation for analysing transport phenomena in electrochemical systems, Current Opinion in Chemical Engineering, Volume 12, May 2016, Pages 44–51

- [Tomadakis1993] M.M. Tomadakis, S.V. Sotirchos, Ordinary and transition regime diffusion in random fiber structures, AIChE Journal, 39 (1993), pp. 397–412
- [Tomin2013] Pavel Tomin, Ivan Lunati, Hybrid Multiscale Finite Volume Method for Two-Phase Flow in Porous Media Article in Journal of Computational Physics · May 2013 DOI: 10.1016/j.jcp.2013.05.019
- [Torquato1993] S. Torquato, B. Lu, Chord-length distribution function for two-phase random media, PHYSICAL REVIEW E VOLUME 47, NUMBER 4 APRIL 1993
- [Tsushima2004] S. Tsushima, K. Teranishi, S. Hirai. Magnetic resonance imaging of the water distribution within a polymer electrolyte membrane in fuel cells. Electrochemical and Solid State Letters 7 (2004) A269.
- [Udell1985] Udell KS. Heat transfer in porous media considering phase change and capillarity - The heat pipe effect. International Journal of Heat and Mass Transfer, 28 (485-495) 1985.
- [Wargo2012] E.A. Wargo, A.C. Hanna, A. Çeçen, b, S.R. Kalidindi, E.C. Kumbur, Selection of representative volume elements for pore-scale analysis of transport in fuel cell materials, Journal of Power Sources, Volume 197, 1 January 2012, Pages 168–179
- [Weinan] Weinan E, Principles of Multiscale Modeling
- [Weinan2004] The Heterogeneous Multiscale Method: A Review, Weinan E, Bjorn Engquist, Xiantao Li, Weiqing Ren, and Eric Vanden-Eijnden
- [Wilkinson1983] D. Wilkinson et J. Willemsen, Invasion percolation - a new form of percolation theory, Journal of Physics A, vol. 16, p. 3365-3376, 1983.
- [Yang2012] Judith C. Yang, Matthew W. Small, Ross V. Grieshaber, Ralph G. Nuzzo, Recent developments and applications of electron microscopy to heterogeneous catalysis, Chem. Soc. Rev., 2012, 41, 8179–8194
- [Yoshizawa2008] K. Yoshizawa, K. Ikezoe, Y. Tasaki, D. Kramer, E.H. Lehmann, G.G. Scherer, J. Electrochem. Soc. 155 (2008) B223.
- [Zamel2010] N. Zamel, N.G.C. Astrath, X. Li, J. Shen, J. Zhou, F.B.G. Astrath, et al., Experimental determination of effective diffusion coefficient of oxygen-nitrogen mixture in carbon paper, Chemical Engineering Science, 65 (2010), pp. 931–937
- [Zamel2012] Nada Zamel, Jürgen Becker, Andreas Wiegmann, Estimating the thermal conductivity and diffusion coefficient of the microporous layer of polymer electrolyte membrane fuel cells, Journal of Power Sources 207 (2012) 70– 80
- [Zamel2013] Zamel & Li, Effective transport properties for polymer electrolyte membrane fuel cells – With a focus on the gas diffusion layer, (review), PECS 2013
- [Zenyuk2015] I. V Zenyuk, D.Y. Parkinson, G. Hwang, A.Z. Weber, Electrochemistry Communications Probing water distribution in compressed fuel-cell gas-diffusion layers using X-ray computed tomography, Electrochem. Commun. . 53 (2015) 24–28.
- [Zhang2006] J. Zhang, D. Kramer, R. Shimoi, Y. Ono, E. Lehmann, A. Wokaun, K. Shinohara, G.G. Scherer, Electrochim. Acta 51 (2006) 2715.

Chapter 3 Numerical verifications of diffusive transport simulations

Transport in porous materials plays an important role in the operation of fuel cells. Indeed, part of the limitations of the performances of the stacks are linked to the transport loss. The use of reliable methods to simulate the transport properties of PEMFC porous materials would be very useful in optimizing the use of current materials and in guiding the development of new materials.

The aim of this chapter is to present and verify numerically simulation methods for diffusive transports in GDL. We designate by the term “numerical verification”, tests of the reliability of calculations realized with a numerical method. These tests are carried out on test cases for which the physical phenomena and the microstructure are fixed. The only errors result from the numerical methods used to simulate and solve physical phenomena. We are interested here in these errors. Note that 3D images are well suited for these comparisons because they allow to specify the microstructure of the test cases. In addition, images are a computer standard on which both direct simulation tools and pore network extraction tools work.

The microstructure of a porous material has a decisive influence on its effective transport properties. This is the case, for example, of a GDL which diffusion properties are modified when the GDL is deformed by the compression imposed by the bipolar plate [Rashapov2016]. We developed simulation tools based on tomographic images. 3D microscopy, for example X-ray tomography and FIB-SEM, gives access to detailed information on the microstructure of a wide variety of porous materials. It can also be used to visualize in-situ and ex-situ two-phase experiments. This makes this methodology useful for many applications.

We have also studied another way of representing porous microstructures, regular pore networks. This has the advantage of simplicity. It has been used for many years in our laboratory. We verify if it makes it possible to model reliably the transport mechanisms in the GDL, and compare these regular pore network to the data available by tomography X on the microstructure of the GDL.

Our contributions to the advance of the state of the art are as follows. We proposed a novel method for extracting the pore network. We have interpreted the problem of computing the conductances of pore networks as a multi-scale problem and a shape analysis problem. We used a novel method to evaluate the effective properties of regular pore networks, using the Wiener bounds. Finally, less novel but nevertheless useful in practice, we conducted a review of open source codes allowing to set up powerful tools for simulations on images of microstructures. We have also developed a new software for pore network simulations. These computer works proved that simulations on tomographic images can be carried out in reasonable time and cost, and pave the way for a more systematic use of image based models.

The outline of the chapter is the following. A first section presents the methodology used. The pore network and Ej-Heat simulation methods are described. We detail the method for calculating the conductances for pores of very disparate shapes extracted from images. We also describe the test cases used to rigorously validate the simulations on images. The regular pore network model is also presented. A second section presents the results of numerical verification for image-based simulations, as well as a comparison of the properties of regular pore networks and a GDL. Finally, a section of perspectives and a concluding section conclude this chapter.

3.1 Methodology

3.1.1 Simulation methods

As stated in section 2.1.1.1, we assume in this document that the stationary heat equation allows to model different diffusive transport phenomena in the GDL, such as the diffusion of oxygen or water vapor in the gas phase, the conduction of heat in the solid and gas phases and the electrical conduction in the solid phase. We present in this section the numerical methods used to solve the stationary heat equation and to compute the effective transport properties of GDL from these numerical simulations.

We first present image based pore networks, where pores are extracted from tomographic images by image analysis. Since tomographic images are large data, typically several hundred mega-bytes, the computer performance of numerical methods is critical. Pore networks make it possible to reduce the computing times by several orders of magnitude compared to direct simulations. This is essential to develop simulations coupling several physical phenomena, such as condensation simulations in Chapter 6. We then present a direct simulation method, that we use as a reference to verify the pore network simulations. Finally, we present a regular pore network approach.

3.1.1.1 Pore network extracted from images

In this section, we present the image based pore network approach for diffusive transports simulations. We present first the image analysis methods that extracts the pores from a tomographic image of a porous microstructure. Then we present the modeling of diffusive transports used by pore networks, the conductance model for transport between two pores. We present the numerical resolution of the transport at the network scale. We present the shape analysis problem consisting in calibrating the conductances on the 3D geometry of the pores. Then we present the different options we studied to solve the problem of conductances calibration.

3.1.1.1.1 Network extraction

Our method for extracting a pore network from a 3D image is described in detail in an article inserted in section 5.1. We present here the main steps of this method, which are illustrated in Figure 3.1. An image segmentation technique is first used to identify pores in the image, or other regions of the image having a physical significance, such as fibers. From this segmentation of the image into multiple regions, a network consisting of nodes and links - the pore network - is created per the following rules. A node of the network is created for each of the regions segmented in the image and is positioned at the center of this region. Two nodes of the network are then connected by a link if the regions to which they correspond have neighbor voxels (section 5.1.2.4.3). Finally, scalar geometric properties on the shape of the regions are extracted by shape analysis and are associated with the nodes and the links to which these regions correspond (section 5.1.2.4.3 and table 1 of section 5.1). These geometric properties are used to quantify the local characteristics of the microstructure and are used to calibrate transport conductances, as explained in section 3.1.1.1.3.

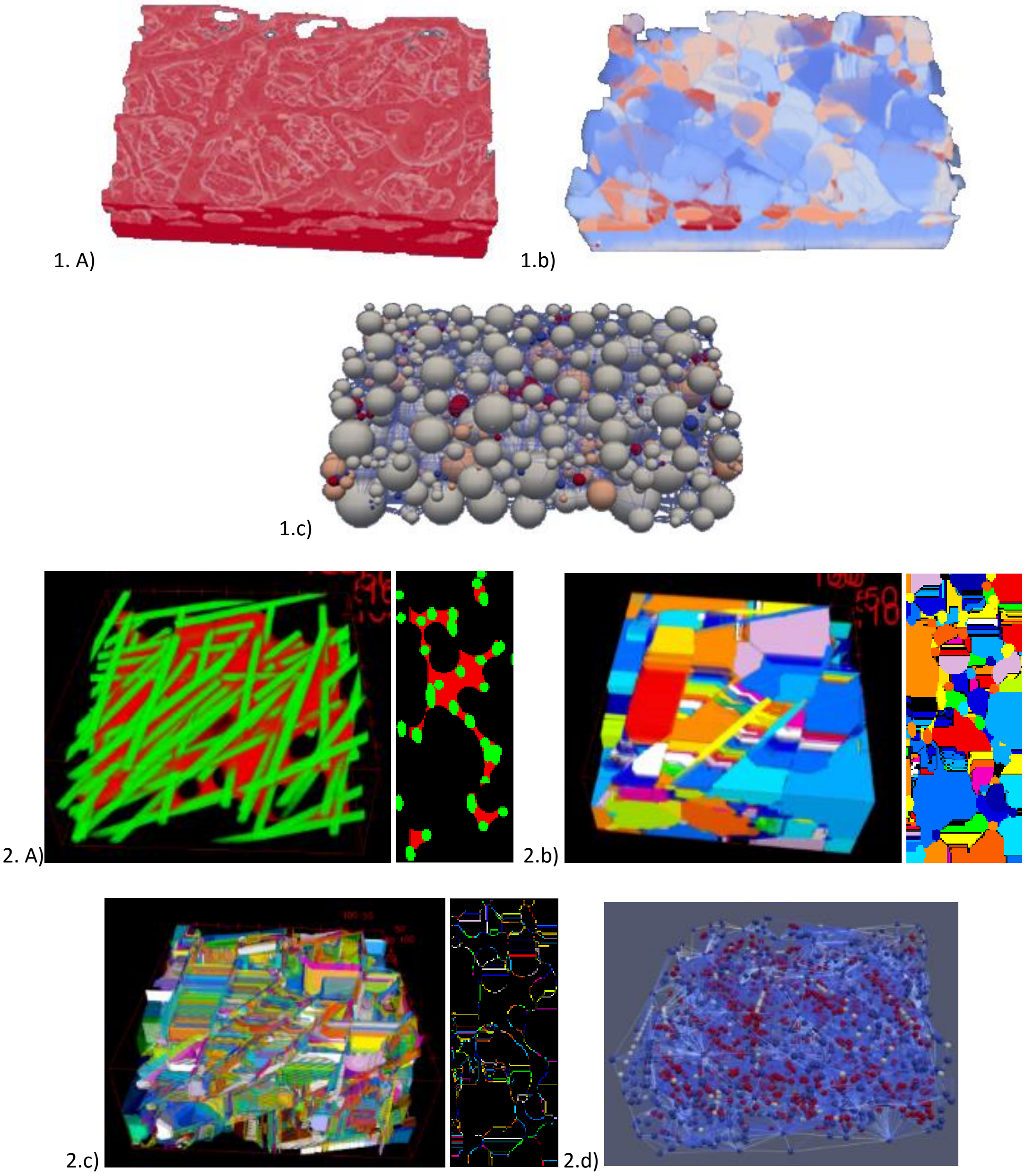

Figure 3.1 Illustration of the pore network extraction method on two types of GDL images. A-1) tomographic image of a GDL b-1) pores extracted from the porous phase of this image, one color per pore c-1) extracted pore network. The pore network is shown in the form of balls, although the pores are volumes of any shape. A-2) virtually generated GDL image: fibers in green, binder in red, air in black. B-2) Pores extracted from the image. One color per pore, 4500 pores in total. The pores are extracted independently for the air, fibers and binder phases. C-2) Links extracted from the image. One color per link, 17000 links in total. A link is a region at the boundary between two pores. D-2) Extracted network. Pore are represented as balls, with a color depending on the phase. Blue: air, white: fibers, red: binder. The links are represented by lines.

Many image segmentation algorithms exist in the literature. Here, we use a watershed segmentation algorithm to identify the pores. The essential advantage of this algorithm is to find the constrictions in the image and to separate the pores at the level of the constrictions. The constrictions have a physical importance, because they are the places where the capillary forces are the highest. It is therefore essential to identify them accurately in the image. The pores obtained by watershed segmentation have variable, complex shapes, as can be seen in Figure 3.1. The details of the segmentation procedure are given in section 5.1.2.4.2. Note that we initially used watershed segmentation to extract pores from the porous phase, with a focus on capillary forces. We then extended its use, to identify elements in the solid phase. For example, we use it in this chapter to calculate the properties of the solid part of the GDL by decomposing the fibers. Applied to a fuel cell catalyst layer image, watershed segmentation could make it possible to decompose the solid phase into agglomerates. Other segmentation methods may be more appropriate on a case-by-case basis, depending on the typical shape one seeks to identify in a microstructure.

3.1.1.1.2 Diffusive transports simulations on pore networks

In this section, we describe the formulation used to calculate a temperature field in a pore network. As explained in section 482.1.1.1, we assume that the temperature field T is a solution of the stationary heat equation. Gas diffusion and electrical conduction can be calculated using the same method. Indeed, these fields are also solutions of the stationary heat equation.

For diffusive transport simulations, the pore network method is a finite volume method, where each pore is a control volume. Finite volume methods have the advantage of ensuring that the material and energy balances are respected, and of being applicable to any geometrical elements. The temperature field is discretized at the centers of the pores. We therefore have an unknown temperature T_i for each pore. In all the pores, the balance of energy gives:

$$\sum_{links\ of\ this\ pore} Q_{link} = 0$$

Équation 3.1

where Q_{link} is the flux of heat exiting through a link of the pore in which the energy balance is made. We have assumed here for simplicity that there are neither sources of heat nor accumulation of energy in the pores.

A linear relationship is postulated between the difference between the average temperatures of the two pores and the heat flux passing from one pore to the other:

$$Q_{ij} = G\left(T_j - T_i\right)$$

Équation 3.2

G is called conductance of the link which is between the pores i and j. We suppose that G depends only on the geometry of the two pores and the link. Note that this method is like an equivalent network formulation used for example for electrical circuits.

These equations give us for each pore a linear equation whose unknowns are the temperatures. To solve this system of equations, all energy balance linear equations are put into a matrix linear system.

$$\begin{bmatrix} \cdots & \cdots & \cdots & \cdots & \cdots \\ \cdots & \sum_j G_{i,j} & \cdots & -G_{i,j} & \cdots \\ \cdots & \cdots & \cdots & \cdots & \cdots \\ \cdots & \cdots & \cdots & \cdots & \cdots \\ \cdots & \cdots & \cdots & \cdots & \cdots \end{bmatrix} \times \begin{pmatrix} \cdots \\ T_i \\ \cdots \\ T_j \\ \cdots \end{pmatrix} = \begin{pmatrix} \cdots \\ Q_i^{Neumann} \\ \cdots \\ \cdots \\ \cdots \end{pmatrix}$$

Équation 3.3

Where j denotes the pores neighboring the pore i and Q_i^{Neuman} denotes the flux exiting a boundary pore I that is imposed by a Neuman boundary condition. We have assumed that the boundary conditions here are of the Neumann type, i.e. that a flow is imposed on the inlet and outlet pores. Q_i^{Neuman} is zero if the pore i is not in contact with the input or the output. This linear system is solved using Matlab™ linear system resolution functions, either direct matrix inversion or an iterative method such as GMRES or MINRES [Matlab].

To calculate the effective thermal conductivity C_{eff} of a material, the temperature field is solved by imposing a temperature T_{inlet} in the pores of the inlet boundary and a temperature T_{outlet} in the pores of the opposite boundary. The total flux Q passing through the links of the inlet boundary is then calculated from the simulated temperature field. Note that the flux which passes through the links of the outlet boundary is also equal to Q by conservation of the energy. C_{eff} is obtained with the following formula :

$$C_{eff} = \frac{Q}{T_{outlet} - T_{inlet}}$$

Équation 3.4

The pore network method has the advantage of being economical in computing time because the discretization in pores is wider that a discretization in voxels. The network's discretization element, the pore, usually contains several tens or hundreds of voxels. In comparison, the Ej-Heat simulation method presented in the next section uses the voxels as discretization elements. The quantity of unknowns in the pore network is therefore much lower. Figure 3.2 illustrates the discretization of a microstructure using pores or voxel as discretization elements.

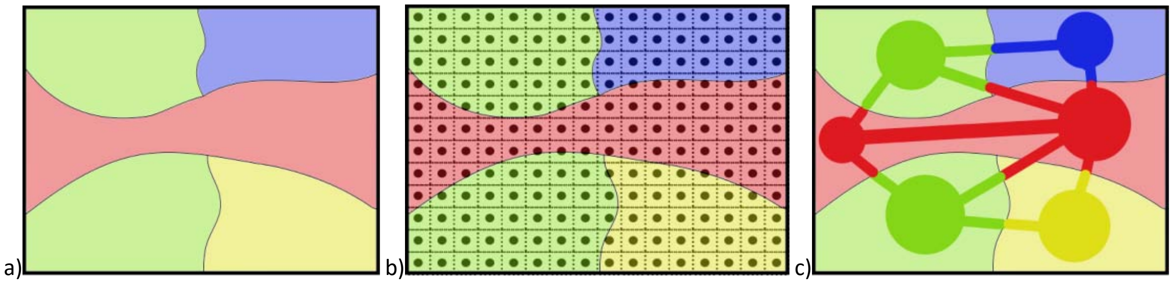

Figure 3.2 Several discretizations for the same microstructure. A) microstructure composed of 4 distinct phases, indicated by different colors. B) discretization of the microstructure on a grid of voxels c) diagram of a pore network extracted from the microstructure. Each pore corresponds to a region of the image. Two pores are connected by a link if the regions of the pores in the image have a common boundary.

3.1.1.1.3 Calibration of the conductances on the pores and link geometries

In this section, we present first the problem of the calibration of the conductances, then we propose a solution to this problem consisting of analytical models of a conductance dependent on the geometry, and a methodology to calibrate these models on the 3D image of each pore and link.

3.1.1.1.3.1 Presentation of the problem of conductance calibration

Modeling a diffusive transport between two pores by an equivalent conductance amounts to approximating the flux between the two pores in the presence of a temperature difference. Let's start with a simple case study to get an idea. Figure 3.3 presents the geometry conventionally used for links and pores in pore networks. The pores are supposed to be cubic and the links are supposed to be parallelepiped aligned with the pores.

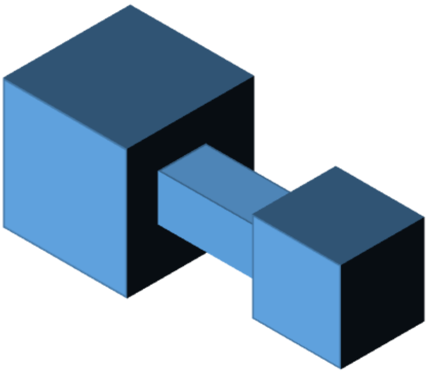

Figure 3.3 Pores and cubic links conventionally used in pore networks.

The conductance for this configuration is obtained taking the harmonic mean of the conductances of each element:

$$G = \left[\frac{L_1}{2L_1^2} + \frac{L_{link}}{S_{link}} + \frac{L_2}{2L_2^2}\right]^{-1}$$

Équation 3.5

where $L_1$and L_2 are the lengths of the sides of the two cubic pores, L_{link} is the length of the link and S_{link} is the area of the link section.

The actual shape of the pores is more complex than on this simplistic case. Figure 3.4 shows pores extracted by watershed segmentation from an image of a GDL 24BA. We have represented in each case two neighboring pores, between which we must approximate the flux. We see that there are many different configurations and shapes. The size ratio between two pores and their relative position can be very variable. Some pores have an extreme shape, for example a flat part or a very small size.

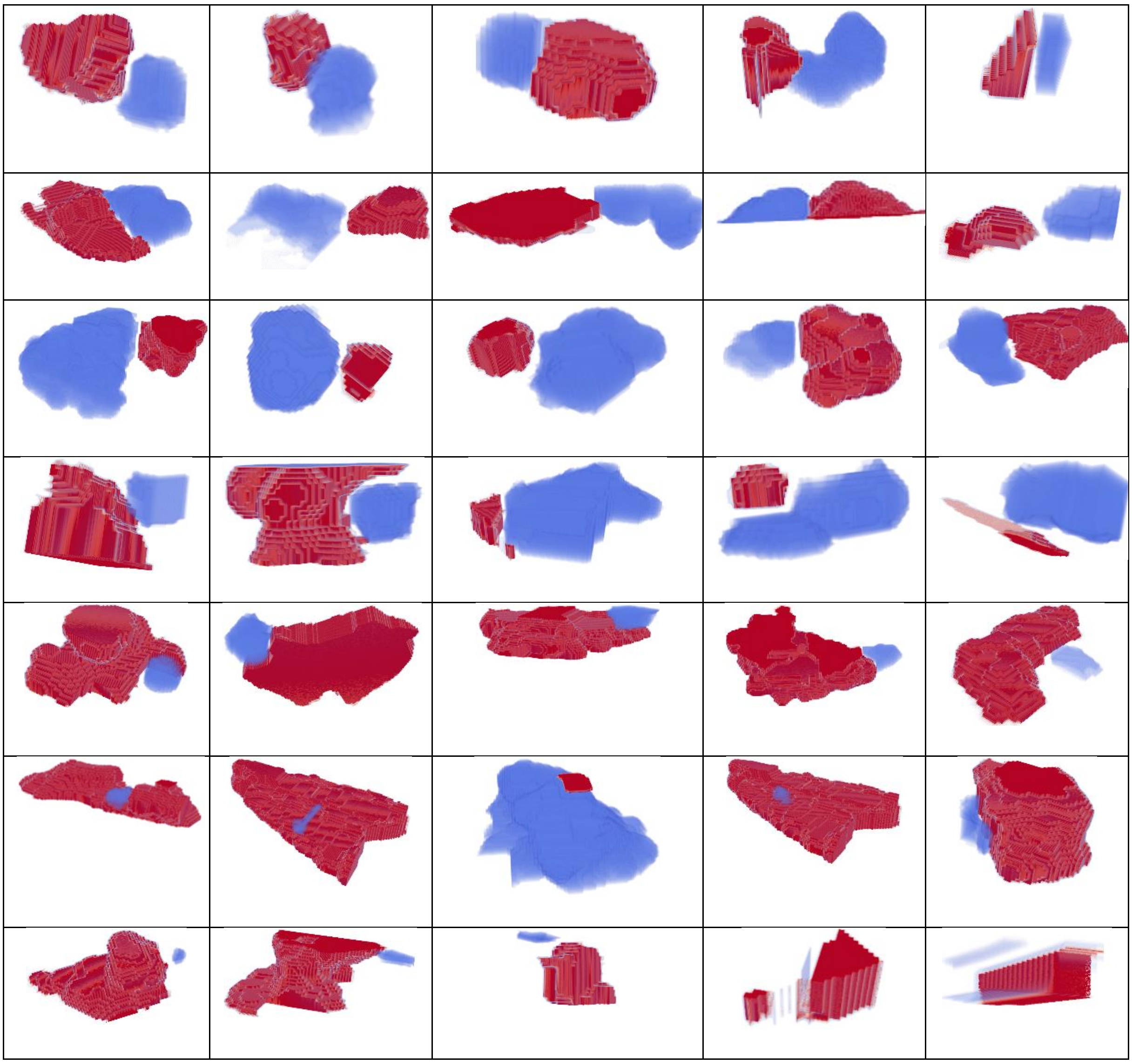

Figure 3.4 3D visualizations of pore extracted by watershed segmentation from an image of a GDL 24BA. Blue and red pores are pairs of pores linked by a link. Links are not shown on these images.

The conductances must be calibrated on the geometry of each pore. The choice of a calibration procedure which considers the essential features of the geometry and the simulated physical phenomemon is crucial for the pore network simulations to give sufficiently precise results. We present in the remainder of this section the approach followed to solve this problem.

3.1.1.1.3.2 Geometry-dependent conductance model

Calculating the conductances for pores of variable geometry requires to use a model approximating the transport as a function of the geometry. We use an analytical formula to calculate the transport at the pore scale. Analytical formula can be computed very fast, which is essential to the speed of pore network simulations.

We introduce a formula giving the conductance for a relatively wide category of geometries. Then we make a series of simplifying assumptions to reduce the number of parameters describing the geometry.

Approximation 1. We call x-axis the axis that connects the center of the link with the center of the neighboring pore. We approximate the link geometry by a series of cylinders along the x-axis, having a thickness dx and a surface section $S(x)$. These cylinders being in series, the conductance of the link G is the harmonic mean of the conductances of the cylinders:

$$G^{-1} = \int_0^L \frac{dx}{S(x)}$$

Équation 3.6

We assumed here that the boundary conditions are zero flux at the lateral boundaries of the link. Let us note that the formula used for the conductance of an elementary cylinder has been established for cylinders, where the current lines are parallel to the x-axis and where the potential depends only on x. Note that approaches based on the analysis of the median axis or the skeleton extracted from the image (briefly described in section 3.3) use a curved axis that follows the center of the porous phase. x is then a curvilinear abscissa along this curve.

Approximation 2. We assume that the shape of the link is invariant by rotation around the x-axis. The surface of each section of the link at the point x, $S(x)$, is then :

$$S(x) = \pi R^2(x)$$

Équation 3.7

Where R (x) is the radius of the link at the point x. We call the R function, the longitudinal profile of the link.

Approximation 3. We parameterize the longitudinal profile R(x) using an analytic function with some geometric parameters. Tableau 3-1 lists the longitudinal profile shapes we used, as well as the conductances and volumes corresponding to these profiles.

	Constant profile	**Linear profile**	**Step profile**
Profile shape	$R(x) = R_0$	$R(x) = \frac{x}{L}(R_L - R_0) + R_L$	$R(x) = \begin{cases} R_0 \; si \; x \leq \alpha L \\ R_L \; si \; x > \alpha L \end{cases}$
Parameters	R_0	$R_0 = R(0)$ $R_L = R(L)$	$R_0 = R(0)$ $R_L = R(L)$ α
Conductance	$G = \pi \frac{{R_0}^2}{L}$	$G = \pi \frac{R_L R_0}{L}$	$G = \left(\frac{\alpha L}{\pi {R_0}^2} + \frac{(1-\alpha)L}{\pi {R_L}^2} \right)^{-1}$
Volume	$V = \pi L {R_0}^2$	$V = \pi L {R_L}^2 \frac{1 + \frac{R_0}{R_L} + \left(\frac{R_0}{R_L}\right)^2}{3}$	$V = \pi L \left(\alpha {R_0}^2 + (1-\alpha){R_L}^2 \right)$

Tableau 3-1 Profile shapes of the links, used for conductance calculation.

The profiles are thus parameterized by a small number of parameters which we calibrate on the 3D geometry of the pores, in the tomographic image. For the step profile, the location of the boundary between the two step, $x = \alpha$, is a parameter to be calibrated. In the following, for simplicity, we fix it as a function of the ration of the pore diameter R_0 and the link diameter R_L : $\frac{\alpha L}{(1-\alpha)L} = \frac{R_0}{R_L}$.

We observe that the calibration of the conductances with this method is done by calibrating one or two parameters per link, which describe in a very simplified way the geometric profile of the link. This approximation is very limited, especially as we see in Figure 3.4 that the actual link or pore shapes are far from a cylindrically symmetric profile. To go further, we could classify the pores into categories and use a different type of profiles for each category. This would make it possible to adapt the geometric model in a more personalized way. A more ambitious perspective is to look for solutions to the transport problem on a larger class of geometries, using analytical or numerical solutions of the stationary heat equation, as discussed in Section 3.3 of this chapter.

We proposed in this section a parametrization of the geometry of the links and a formula for the conductance in these geometries. We derive in the following section the method used to calibrate these model geometries on the real geometries of the pores.

3.1.1.1.3.3 Calibration of the conductance model on the pores and links geometries

We describe here the methodology used to calibrate conductances on 3D pore images. The conductances were calculated on simplified geometries presented in the previous section. We want to calibrate the parameters of these simplified geometries from the shape of the pores and links extracted from the 3D image. The parameters we calibrate are the radii of the pores and the links and the lengths of the links.

We compute these parameters on the image as follows. The center of the pore is chosen as the center of mass of the pore. The center of the link is chosen as the position of the maximum of the distance map in the voxels of the constriction, which corresponds to the location of the constriction furthest from the non-conductive phase. The length of the link is the Euclidean distance between the center of the link and the center of the pore. The radius of the pore R_0 and the radius of the bond R_L are calculated using the formula $R_0 = V_{pore}^{1/3}$ and $R_L = S_{lien}^{1/2}$.

Thus, to calibrate the conductances, we must extract from each pore and link a small number of geometric quantities: the position of the center of mass and the maximum of the distance map, the volume (obtained by counting the number of voxels in the region), the area of the surface (obtained as the area of a mesh of the surface, which is extracted from the voxels of the pore or link by a marching cube algorithm).

Thus, we used very simple shape descriptors for the pores and constrictions. Many other shape descriptors exist. To find which shape descriptors are the most relevants, it would be useful to determine which geometric quantities have the most influence on the physical phenomenon studied. A sensitivity analysis of the solution of the stationary heat equation on a simplified geometry would be useful from this perspective.

In summary, we have implemented a method to extract geometric shape descriptors from real pore images. We used these parameters to calibrate a simplified geometric model of the links, on which the equivalent conductance for diffusive transport is given by an analytical formula. At this stage, we used the same conductance formula for all links, adapting the geometric parameters for each link. This allowed us to calculate a conductance adapted to the geometry of each link. This method has the advantage of being economical in computing time, simple to implement, and can be extended to other physical phenomena by adapting the physical model and by adapting the shape descriptors calculated on the image. However, several approximations are made successively on geometry and physics. It is therefore necessary to pay attention to the precision of the conductances obtained and to carefully validate the results.

3.1.1.2 Direct simulations using the explicit jump method, EJ-Heat

We present in this section the explicit-jump direct simulation method for heat transport, referred to in this document as EJ-Heat. We outline the formulation of the heat transport problem and its resolution by the EJ-Heat method. A complete description of the method can be found in [Wiegmann2006].

We used direct simulation because we needed a reference method to validate the pore network diffusion simulations. We chose EJ-Heat rather than other direct simulation methods for several reasons. First, this method has been validated experimentally for GDL [Becker2009]. Second, it is a numerical method that has been studied mathematically [Wiegmann2006] [Wiegmann2000] [Wiegmann1999], so we expect numerically reliable results. Third, it is available in the commercial code GeoDict [Geodict] and in open source [Wiegmann2006].

3.1.1.2.1 Stationary heat equation

The Ej-Heat method solves the stationary heat equation in the material,

$$\nabla \cdot (\beta \nabla T) = 0$$

Équation 3.8

where T is the temperature, $\beta(\vec{x})$ is the local conductivity at point $\vec{x} = (x_1, x_2, x_3)$ and $\nabla \cdot$ is the divergence operator $\left(\frac{\partial}{\partial x_1}, \frac{\partial}{\partial x_2}, \frac{\partial}{\partial x_3}\right)$. We assume that β does not depend on T.

The stationary heat equation is discretized directly on the regular grid of voxels. Each voxel has a value of beta, given by the user as a parameter, and an unknown value of T, resolved numerically. Figure 3.5 illustrates the discretization of a microstructure on a voxel grid.

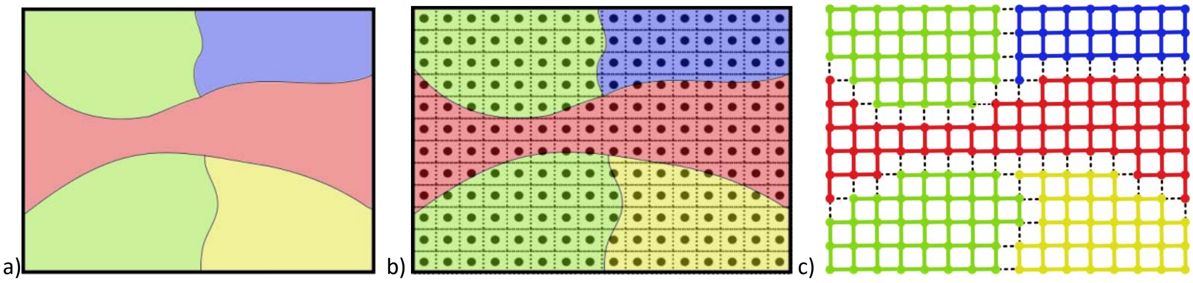

Figure 3.5 Illustration of the discretization of a microstructure on a regular grid of voxels. A) microstructure composed of 4 phases (one color per phase). B) superposition of the voxel grid and the microstructure. Each voxel is assigned the conductivity of the dominant phase in the volume of this voxel. C) voxel grid obtained. The relation with a network representation is illustrated by connecting the neighboring voxels by edges. At the interfaces between the phases (in dotted lines), the value of the conductivity generally undergoes a jump.

To calculate the effective conductivity in a direction l, a temperature gradient is imposed in the direction l. The temperature is decomposed into a component varying linearly in the direction l, corresponding to the temperature field in a uniform medium, and a deviation T_l about this linear component. The numerically resolved field is in fact the deviation T_l. When the imposed temperature gradient is equal to $\vec{e_l}$, the unit vector in the direction l, T_l follows the following equation:

$$\nabla \cdot \left(\beta(\vec{x})(\nabla T_l + \vec{e_l})\right) = 0, \vec{x} \in \Omega$$

Équation 3.9

Where T_l is the deviation field from the average temperature field simulated when computing the effective conductivity in the direction $l = x, y \; or \; z$.

The boundary conditions are assumed to be periodic for the deviation field T_l.

$$T_l(\vec{x} + id_1\vec{e_1} + jd_2\vec{e_2} + kd_3\vec{e_3}) = T_l(\vec{x}), i, j, k \in \mathbb{Z}$$

Équation 3.10

Once T_l is computed, the effective conductivity tensor β^*, normalized by the dimensions of the domain, is obtained by integrating the flux over the entire domain using the following formula [Wiegmann2006].

$$\beta^* = \begin{bmatrix} \beta_{11}^* & \beta_{12}^* & \beta_{13}^* \\ \beta_{21}^* & \beta_{22}^* & \beta_{23}^* \\ \beta_{31}^* & \beta_{32}^* & \beta_{33}^* \end{bmatrix}$$

Équation 3.11

$$\beta^*_{ml} = \frac{1}{d_1 d_2 d_3} \int_{\Omega} \langle \overrightarrow{e_m}, \beta(\vec{x})(\nabla T_l + \overrightarrow{e_l}) \rangle \, \overrightarrow{dx}, \qquad l = 1,2,3; \quad m = 1,2,3$$

Équation 3.12

where d_1, d_2, d_3 are the dimensions of the domain in the directions x, y, z.

3.1.1.2.2 Discretization and solving

This section describes the method used by the Ej-Heat method [Wiegmann2006] to solve the equations presented in the previous section.

The discretization of the equations is done with a numerical scheme of finite differences. Attention is paid to the discretization of the conductivity jumps at the interfaces between the phases. Indeed, the conductivities can vary by several orders of magnitude between two phases of the same material. This can induce digital artefacts. At the interfaces between materials, the limited development goes up to order 2 to be more precise and additional variables, called jump variables, are introduced to compensate for the digital artefacts related to the conductivity jumps. This method is like the immersed boundary methods (IBM) [Wiegmann2006]. The consideration of the interfaces by an IBM type method makes it possible to get rid of the meshing of the surfaces between the phases, which is a costly step in computation time. It makes it possible to consider curved interfaces between the materials in a numerically reliable manner.

The linear system is solved by combining the Fast Fourier Transform (FFT) and an iterative BiCGStab method. The Fourier transform is used to solve the deviation around the mean temperature field, whose boundary conditions are periodic, by assuming the value of the jump variables. The use of the fast Fourier transform accelerates the calculations. The exact value of the jump variables is determined by an iterative method, to obtain a coherent value with the temperature field. Indeed, these jump variables are related to the temperature flux at the interfaces, which is proportional to the harmonic mean of the conductivities. The numerical precision of the method is largely due to the considering of the jump variables. We verify in this chapter whether it is numerically reliable.

3.1.1.3 Regular pore networks

Regular pore networks represent in a simplified manner the microstructure of a porous material. The porous phase is represented by a series of pores having simple geometries, distributed on a cartesian grid. Links connect the neighboring pores, making it possible to form a continuous porous phase. Although simplified, the microstructure is calibrated on data extracted from the actual microstructure to consider the essential geometrical characteristics of the actual porous material. For example, the pore size used in the regular pore network is calibrated on the pore size distribution of the actual material, which can be measured for example by a porosimetry experiment.

We consider in this chapter regular cubic pores networks such as the one shown in Figure 3.6. The unit cells of these networks are composed of a cubic pore and 6 parallelepipedic links. The size of the pores varies from one unit cell to the next, following a random distribution.

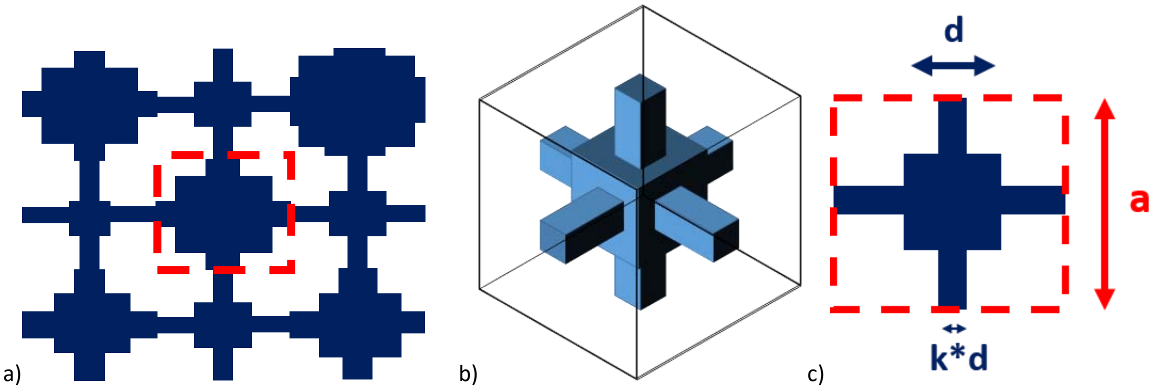

Figure 3.6 Diagrams of a regular cubic pore network, composed of cubic pores and parallelepiped links distributed on a regular 3D grid. A) 2D section of a 3D cubic pore network. B) 3D representation of a unit cell. C) slice view of a unit cell.

Pore networks are mainly used for two-phase simulations. Indeed, they make it possible to represent the capillary forces in a precise and economical way in computation time. In addition, diffusive transport can be simulated with a regular pore network. This is what we are interested in, in this chapter. To calculate the diffusive transport properties of random regular pore networks, we propose an approach based on analytical formulas. We begin by calculating the diffusive transport properties of the unit cells forming the network, using analytic formulas valid for simple geometric elements such as cubes and cylinders. Then we estimate the diffusive transport properties of networks composed of multiple unit cells, whose geometric properties follow a random distribution. We use analytical formulas called Wiener bounds, rather than numerical simulations. The Wiener bounds have the advantage of providing bounds for the effective transport properties of the network, whatever the random distribution of the unit cells in the network.

3.1.1.3.1 Properties of the unit cells

We compute here the effective properties of a unit cell of the cubic regular pore network shown in Figure 3.6 b) and c). The transport properties of this unit cell can be analytically calculated by simple geometric considerations. We present these formulas below. Their demonstration is in the appendix 9.3.

Let d be the diameter of the pore, a be the step of the network, k*d be the diameter of the bonds. Let $\mathbf{u}=\boldsymbol{d/a}$ be the pore size normalized by the network step. The relative effective diffusive transport property of the gas phase of a unit cell, $D_{eff:gaz}$, is given by the following formula:

$$D_{eff:gaz} = u\left(1+\frac{\frac{1}{u}-1}{k^2}\right)^{-1}$$

Équation 3.13

The relative effective diffusive transport property of the solid phase of a unit cell, $D_{eff:solide}$, is given by the following formula:

$$D_{eff:solide} = \left(\frac{1-u}{1-u^2k^2} + \frac{ku}{1-2ku+u^2(2k-1)} + \frac{(1-k)u}{1-u^2}\right)^{-1}$$

Équation 3.14

Note that the transport properties of a unit cell are also the effective transport properties of a network composed of multiple cells identicals to this unit cell. This is the reason why we use the notation $D_{eff:\ldots}$ for the properties of the unit cells, by analogy with the notations of the effective properties of the networks.

The porosity of a mesh, ε, is given by the following formula.

$$\varepsilon = \frac{1}{a^3}(d^3 + 3(a-d)(kd)^2) = \frac{d^3}{a^3}(1-3k^2) + \frac{d^2}{a^2}3k^2 = u^3(1-3k^2) + 3u^2k^2$$

Équation 3.15

Note that these properties depend only on k and $\mathbf{u}=\boldsymbol{d/a}$.

These formulas will allow us to study the relationship between the microstructure and the effective transport properties of regular cubic pore networks, using analytical formula.

3.1.1.3.2 Properties of regular pore networks with random pore sizes

We consider regular pore networks composed of many cubic unit cells. The geometry of the unit cells varies randomly. We want to calculate the effective properties of this network for diffusive transport.

More precisely, we vary the adimensionned pore size parameter, $\mathbf{u} = \boldsymbol{d} / \boldsymbol{a}$, randomly from one unit cell to another. The statistical distribution of $\mathbf{u}$ is calibrated on the pore size distribution of a real material. This can be measured, for example by porosimetry, or calculated from a tomographic image. Another option is to model the pore size distribution with a continuous probability distribution. The Weibull distribution is often used. The probability density function of the Weibull distribution is given by the following formula:

$$f(x,\beta,\lambda) = \frac{\beta}{\lambda}\left(\frac{x}{\lambda}\right)^{\beta-1} e^{-(x/\lambda)^{\beta}}$$

Équation 3.16

Where $\beta > 0$ is the shape parameter and $\lambda > 0$ is the scale parameter of the Weibull distribution. It should be noted that the pore sizes distribution is truncated in the regular pore networks to comply with criterion $0 \leq u \leq 1$. The ratio parameter between link size and pore size, k, is considered constant from one unit cell to the other, for simplicity.

Note that considering a varying pore size is justified especially for the two-phase simulations. Indeed, capillary flow usually found in GDL follow percolation patterns. Percolation phenomena result here from a random distribution of invasion potential. It is typically modeled with varying pore sizes in the network. On the other hand, for diffusive transports, the theory of homogenization shows that the properties of materials can be represented by a deterministic effective parameter. A random modeling is therefore not essential for diffusive transport, if we want to use a homogenized model.

Several approaches are possible to determine the effective properties of the network. A first approach is to solve the Équation 3.3 directly by linear system resolution, as presented in section 3.1.1.1.2. A second approach consists in bounding the effective properties by analytically computable bounds. This is the approach we use in this document for regular pore networks. Indeed, this approach has the advantage of making it possible to study analytically the effect of the calibration parameters used in the regular pore networks.

The Voigt-Reuss-Wiener bounds make it possible to bound the effective properties of a material, knowing the properties of the materials constituting it. Let $\boldsymbol{D}_0$ be the effective property of the regular cubic network. Let $\boldsymbol{D}_i$ be the effective property of each elementary cell.

The Voigt bound is defined as the arithmetic mean of the transport properties of the components.

$$\langle \, \boldsymbol{D}(\boldsymbol{x}) \, \rangle = \sum_i m_i \boldsymbol{D}_i$$

Équation 3.17

The Reuss bound is defined as the harmonic mean of the transport properties of the components.

$$\langle \, \boldsymbol{D}^{-1}(\boldsymbol{x}) \, \rangle^{-1} = \left[\sum_i m_i \boldsymbol{D}_i^{-1} \right]^{-1}$$

Équation 3.18

These quantities are lower and upper limits on the effective transport properties of the composite material.

$$\langle \, \boldsymbol{D}^{-1}(\boldsymbol{x}) \, \rangle^{-1} \leq \boldsymbol{D}_0 \leq \langle \, \boldsymbol{D}(\boldsymbol{x}) \, \rangle$$

Équation 3.19

The demonstration of these bounds is presented in [Gibiansky1993].

The Wiener bounds generally give too broad bounds for the effective properties of porous media, when they are applied directly to the properties of the constituents of porous media, i.e. an insulating void phase and a conductive solid phase. However, we apply here the Wiener bounds to the transport properties of the unit cells, which are neither totally insulating nor totally conductive. This allows us to obtain more precise bounds of the properties of the material. Note that there are other types of theoretical bounds for the effective properties [Renard1997], which give more or less precise bounds depending on the case. Particularly noteworthy are the Cardwell and Parson [Renard2000] bounds, which are conceptually like the Wiener bounds but can give more accurate results when the network dimensions are fixed.

The advantage of using Wiener bounds is that the arithmetic and harmonic means are analytically computable for a random pore size distribution. We can therefore evaluate the effect of a statistical distribution without the need for complex computer code. The averaging effect of the disorder can be evaluated simply. Indeed, if the exact value of the effective property depends on the exact distribution of the pores, which is unknown, the bounds still allow be computed with a certain approximation.

3.1.2 Test cases for simulations

This section presents the test cases used to verify the numerical methods, pore networks extracted from an image, regular pore networks, and EJ-Heat direct simulation. These test cases consist of 3D images of two virtual microstructures and a tomographic image of a real GDL.

The simulations with pore networks extracted from images and direct EJ-Heat simulations are carried out directly on the 3D images that define each test case. We calculate numerically the effective diffusive transport properties of these microstructures. For the first two test cases, an analytical formula gives the theorical effective diffusive transport properties of the microstructures. This allows us to check whether the simulations calculate the theoretical value. The third test case is a real tomographic image of GDL, for which there is no analytical solution. This case allows us to study the pore networks extracted from images using direct simulation as a reference.

The simulations by regular pore networks are carried out only on the real GDL tomographic image. The pore size and link size distributions of this GDL are extracted from the tomographic image by image analysis, like in section 5.1. These size distributions are used to calibrate the regular pore network. We compare the effective transport properties calculated by the regular pore network with the effective transport properties calculated by the direct EJ-Heat simulation, which serves as a reference here.

This methodology allows us to verify the numerical methods, or to identify some of their limitations.

3.1.2.1 Test case: layered medium

In this test case, we study the microstructure shown in Figure 3.7. This microstructure is composed of 5 superimposed layers which have 20 voxels of thickness and are perpendicular to an axis of the voxel grid. The layers have two different conductivities, alternating from one layer to the other. The sample is a cube which edges are 100 voxels long.

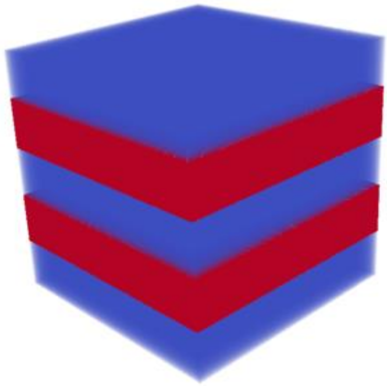

Figure 3.7 3D rendering of the microstructure used for the test case layered medium.

The effective conductivity of this sample is given by two analytical formulas. In the direction which is perpendicular to the layers, the conductivity is the harmonic mean of the conductivities of the two phases, weighted by the thicknesses of the layers:

$$\frac{1}{k_{eff}}=\frac{3/5}{k_1}+\frac{2/5}{k_2}$$

Équation 3.20

In both directions which are parallel to the layers, the effective conductivity is the arithmetic mean of the phase conductivities, weighted by the thicknesses of the layers:

$$k_{eff}=\frac{3}{5}k_1+\frac{2}{5}k_2$$

Équation 3.21

This case makes it possible to test if the geometry of the layers is correctly considered by the numerical methods and if the fluxes from one layer to the other are considered correctly.

3.1.2.2 Test case: regularly spaced cylinders in a continuous medium

The microstructure of this test case is shown in Figure 3.8. The sample is a parallelepiped which edges are 200 voxels long in the x-direction, 150 voxels long in the y-direction, 200 voxels long in the z-direction. Six cylinders parallel to the z axis and having the same radius are spaced regularly in the x and y directions, every 50 voxels. The conductivity of the cylinders is k_1. The remainder of the sample is filled with a homogeneous medium of conductivity k_m.

Radius of cylinders (in voxels)	2	5	10
Images	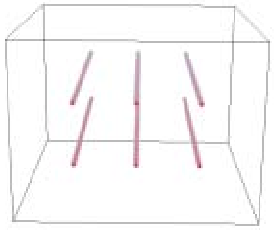	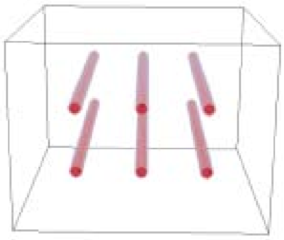	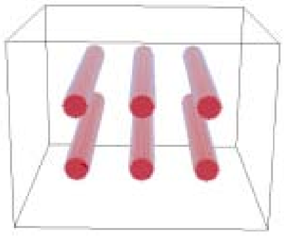
Radius of cylinders (in voxels)	20	30	40
Images	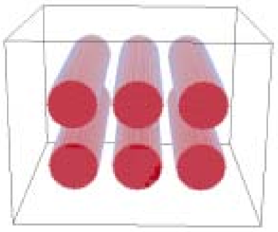	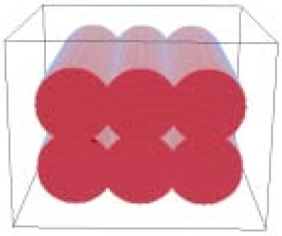	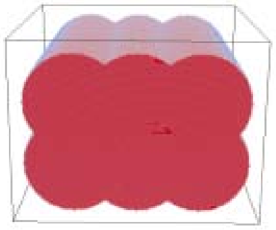

Figure 3.8 Microstructures used for the test case: cylinders regularly spaced in a continuous medium.

The effective conductivity of this material is given by analytical formulas. In the directions perpendicular to the cylinders, the Rayleigh formula gives the value of the effective conductivity [Pietrak2015]:

$$\frac{k_{eff}^{\perp}}{k_m} = 1 + \frac{2\phi}{C_1 - \phi + C_2(0.30584\phi^4 + 0.013363\phi^8 + \cdots)}$$

Équation 3.22

where ϕ is the volume fraction of cylinders, $C_1 = \frac{k_1+k_m}{k_1-k_m}$, and $C_2 = \frac{k_1-k_m}{k_1+k_m}$.

In the direction parallel to the cylinders, the effective conductivity is given by an arithmetic mean. This case is like the layered media case, so we're not considering it again.

This test case is interesting because additional effects are tested compared to the previous test case, such as the deformation of the current lines by cylindrical inclusions. The discretization of the medium into pores by the pore network extraction method can also be verified.

3.1.2.3 Test case: GDL tomographic image

The microstructure used for this test case is a tomographic image of a compressed GDL 24BA, which is described in more details in 4.1. This image is shown in Figure 3.9. There is no analytical formula for the effective transport properties of this microstructure.

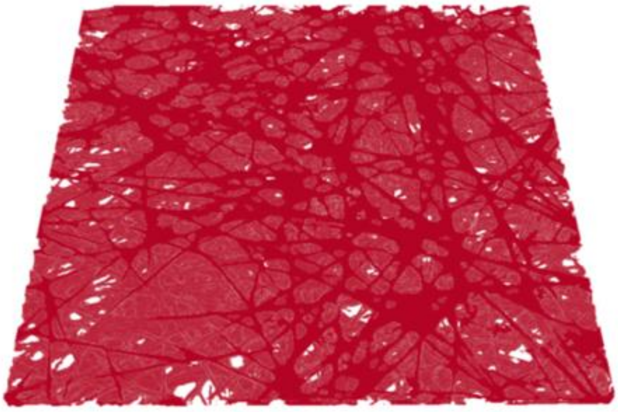

Figure 3.9 Tomographic image of a compressed GDL 24BA.

We compare the Ej-Heat direct simulation with pore network simulations on this case, for diffusive transports in the solid and fluid phases. This case makes it possible to check these numerical methods on a real microstructure. The new elements compared to the previous test cases are the large size of the image, the complexity of the microstructure and the limited resolution (the fibers in the image are less than 5 voxels thick). We can evaluate the speed of the numerical methods, their ability to consider complex geometries, and their sensitivity to the poor resolution of the image.

The simulations using regular pore networks are carried out only on this test case. The pore size and link size distributions of this GDL are extracted from the tomographic image by image analysis, like in section 5.1. These size distributions are used to calibrate the regular pore network. We compare the effective transport properties calculated by the regular pore network with the effective properties calculated by direct EJ-Heat simulations, which serve as a reference here.

3.2 Results

3.2.1 Numerical verification of direct EJ-Heat simulations and simulations on pore networks extracted from images

Ej-Heat simulations and simulations on pore networks extracted from images are carried out on test microstructures to verify their reliability. This section presents the verification results for the three tests defined in the methodology section: an image composed of parallel layers, an image composed of parallel cylinders inserted in a homogeneous medium, and a tomographic image of a real GDL.

3.2.1.1 Test case: layered medium

The superimposed parallel layers microstructure used for this test case and the extracted pore network are shown in Figure 3.10.

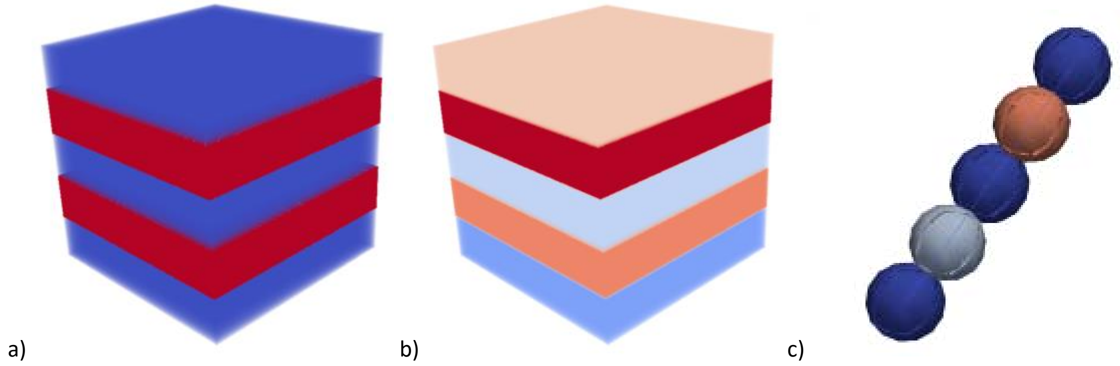

Figure 3.10 A) microstructure used for the test case array of cylinder b) pores extracted from the image c) pore network extracted. Pore are represented as balls, although the pores shapes considered in the conductances are not balls.

Figure 3.11 shows the comparisons of the pore network and Ej-Heat simulations with the theoretical conductivity value in the direction parallel to the layers. We find that Ej-Heat calculate very precisely the theorical value. The accuracy of simulations with pore network extracted from the image depends on the conductance formula used. The best formula considers a constant link profile which radius is calibrated on the surface of the images of the links. With this formula, the right trend is predicted for the variation of the effective conductivity as a function of the bulk conductivity of the phases. This formula makes it possible to consider correctly the size of the rectangular interfaces between pores. The step profile overestimates the conductivity while the linear profile underestimates the conductivity. The problem is that these two formula are calibrated using the pore radius, which is poorly estimated because the radius is estimated from the pore volume with the assumption that the pores are either cubic or spherical, whereas in this geometry the pores are parallelepipeds.

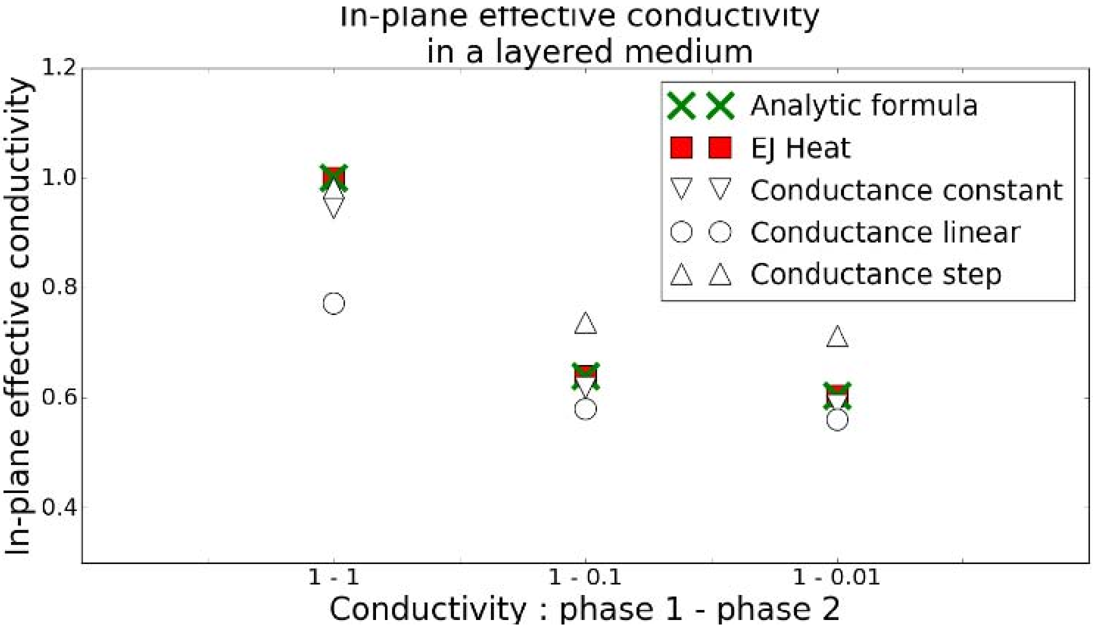

Figure 3.11 Comparison of numerical methods on the case test layered medium, for the effective conductivity in the direction parallel to the layers. The bulk conductivity of one phase is set to 1, the bulk conductivity of the other phase is either 1, 0.1 or 0.01.

These results show that the EJ-Heat method is validated on this test case. The pore network extracted from the image makes it possible to find the right trends. Nevertheless, there is some imprecision which is due to the way in which the geometry is considered in the calculation of the conductances.

3.2.1.2 Test case: regularly spaced cylinders in a continuous medium

The microstructure composed of parallel cylinders used for this test case, the extracted pores and a diffusive transport field computed with EJ-Heat are shown in Figure 3.12.

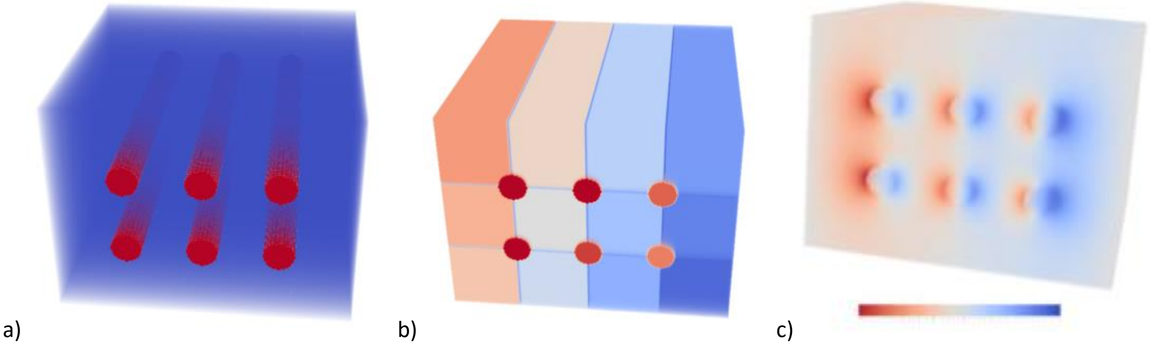

Figure 3.12 A) microstructure used for the test case array of cylinder b) pores extracted from the image c) deviation around the mean temperature field calculated by EJ-Heat.

Figure 3.13 shows the comparisons of the pore network simulations and Ej-Heat simulations with the theoretical conductivity value in the direction perpendicular to the cylinders. We find that Ej-Heat calculates precisely the theoretical value. The results of the pore network are not very accurate. The best choice of conductance is the constant profile, which allows to find the good trend but underestimates the conductivity by 40%.

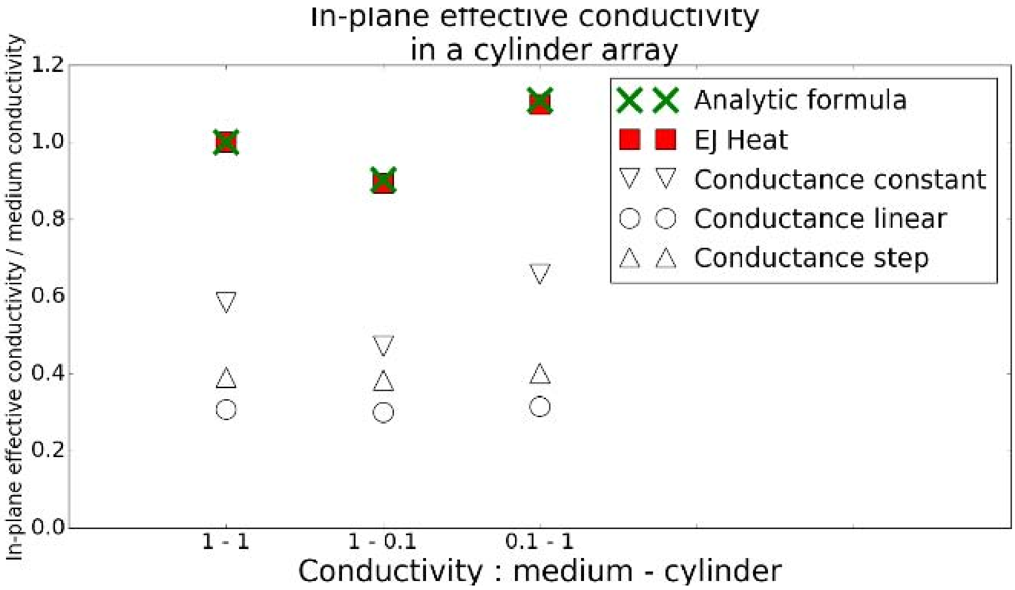

Figure 3.13 Comparison of numerical methods on the case test cylinder array, for the effective conductivity in the direction perpendicular to the cylinders. The bulk conductivity of the homogeneous medium is set to 1, the bulk conductivity of the cylinders is either 1, 0.1 or 0.01.

We now study the results of the EJ-Heat simulations on a larger number of cylinder radii and bulk conductivities to better illustrate the good performance of this simulation method. Figure 3.14 shows comparisons between EJ-Heat and the theoretical Rayleigh formula obtained by varying the radius of the cylinders and the conductivities of the phases. The relative error between the analytic formula and Ej-Heat simulation is less than 1% for cylinders whose radii are less than 10 voxels. For an average cylinder of 20 voxels thickness, the difference is always less than 4%. For cylinders with a radius greater than 30 voxels, the cylinders interpenetrate, so the analytical formula is not valid and the EJ-Heat simulations cannot be verified.

These results make it possible to verify that the Ej-Heat method calculates very precisely the theoretical effective transport properties of these microstructures. This indicates that the Ej-Heat method is numerically reliable.

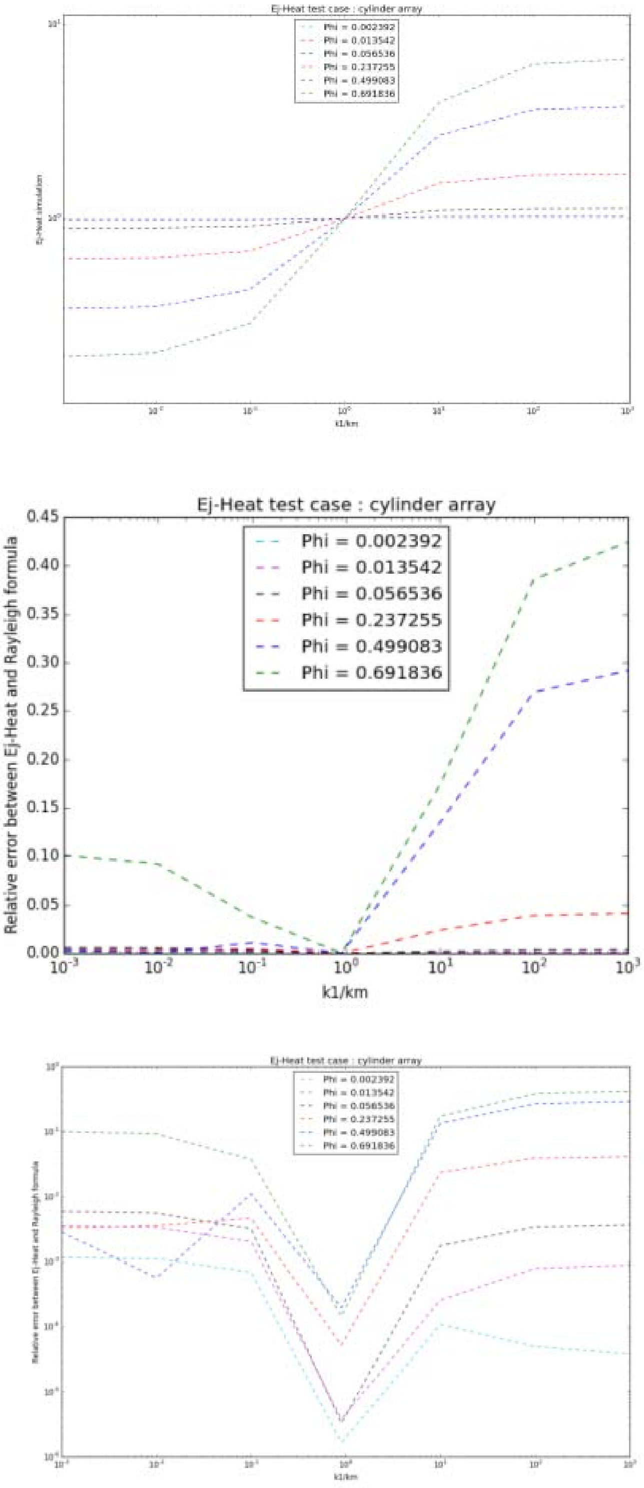

a)

b)

c)

Figure 3.14 A) Effective conductivity values calculated by EJ-Heat. B) and c) relative deviations between the effective conductivities calculated with Ej-Heat and with the Rayleigh formula.

3.2.1.3 Test case: GDL tomographic image

The pore network extracted from the compressed 24BA image used for this test case is shown in Figure 3.15. The pore network is extracted either from the fluid phase only, or from the solid phase only, or from both the fluid and the solide phases. The effective diffusive transport properties calculated with these different networks are compared below. Note that the extraction parameters (value of the H-contrast) were taken identical for the fluid and the solid phases for the sake of simplicity.

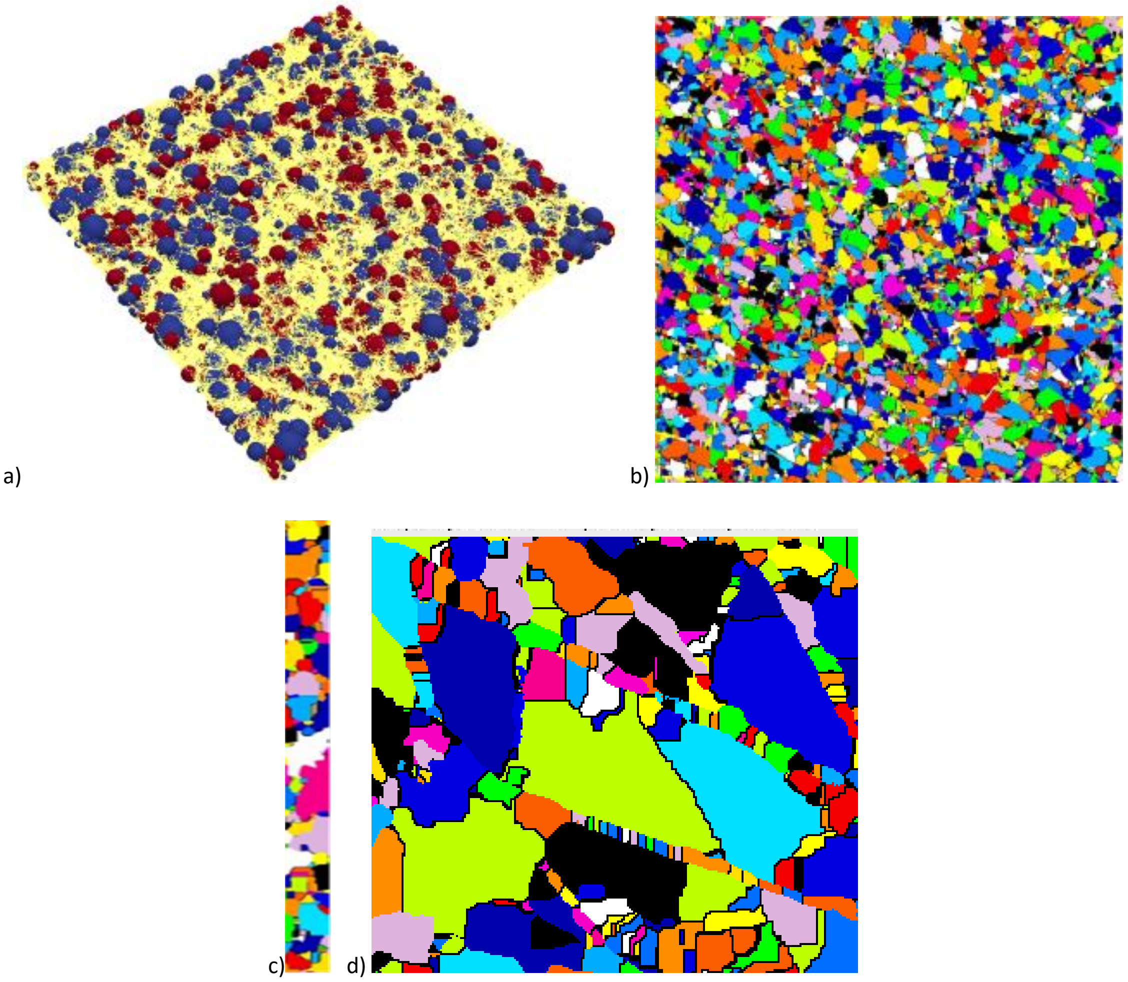

Figure 3.15 Pore network extracted from fluid and solid phases of a compressed 24BA image. A) "stick and balls" representation of the pore network. The red balls represent the pores of the fluid phase, the blue balls the pores of the solid phase, the yellow segments the links. B) and c) Sectional view of the extracted pores. D) zoom on a part of the view in section b.

We perform three types of tests on these images. The first test consists in calculating the effective conductivity of the microstructure if the conductivities of the two phases are equal. This is a physically unrealistic case, but for which we know the exact solution: the effective conductivity is equal to the bulk conductivity of the two phases. The second test consists in calculating the effective diffusivity of the fluid phase. The third test consists in calculating the effective conductivity of the solid phase. We do not have the exact values for these last two test cases, so we only compare the pore network simulations with Ej-Heat simulations.

The computational times for these simulations are as follows. Extraction of the pore network takes 10 min if we only extract it from the fluid phase, 20 min if we extract the network from both the solid and fluid phase, on an Intel Xeon 5 2.2Ghz CPU. The calculation of the pore shape parameters from the segmented pore takes only 1% of this time. The computing time to solve a diffusive transport on the extracted pore network takes about 2s with our Matlab code. It is 10,000 times faster than EJ-Heat simulations, which takes 5 hour and 30 min to solve the diffusive transport in one direction, on 1 CPU.

3.2.1.3.1 Diffusive transport in the fluid phase and in the solid phase

The results of the diffusive transport in the fluid and the solid phase with the bulk properties of the two phases being the same, is shown in Figure 3.16. We find that Ej-Heat manages to calculate exactly the theoretical value. The pore network simulations give good results in the in-plane direction, but underestimate the through-plane effective property. The best result is achieved with the conductance formula corresponding to a constant profile whose radius is calibrated on the surface of the constrictions. Other conductances give more inaccurate results. This is an indication that the error is related to the calibration of the conductances. The difference in both directions may be related to an anisotropy of the pore geometry and constrictions, or to a size effect because the through-plane direction is much thinner because it has only a few pores of thickness.

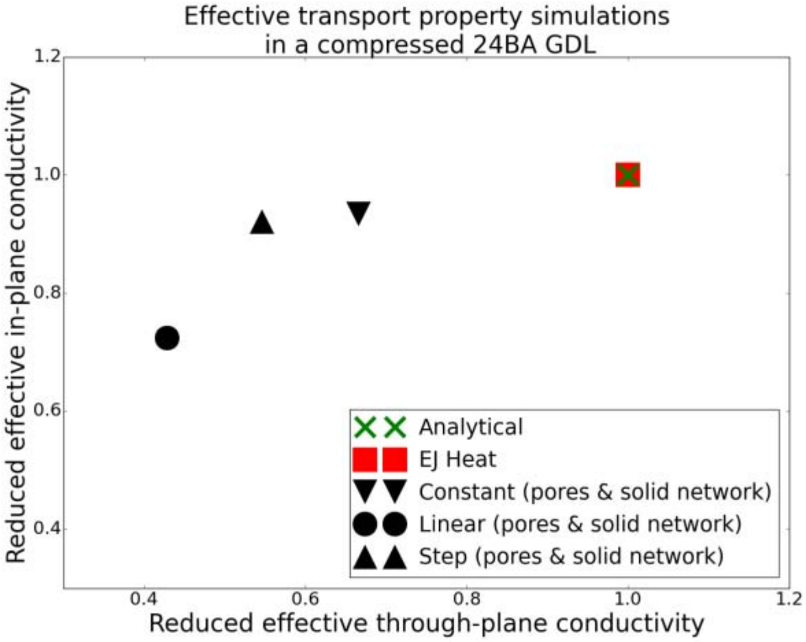

Figure 3.16 Simulation results on a tomographic image of 24BA. The conductivity of the two phases is assumed to be the same.

We conclude from this test case that the Ej-Heat method is numerically reliable on such cases. The simulations with pore networks extracted from the image give good results in one direction but are imprecise in the other direction.

3.2.1.3.2 Diffusive transport in the fluid phase

The simulation results for the effective diffusivity of the fluid phase are shown in Figure 3.17. We do not have a theoretical value for this property. Since the Ej-Heat simulations proved to be numerically reliable in all other test cases, we take the Ej-Heat result as a reference to verify the pore network simulations.

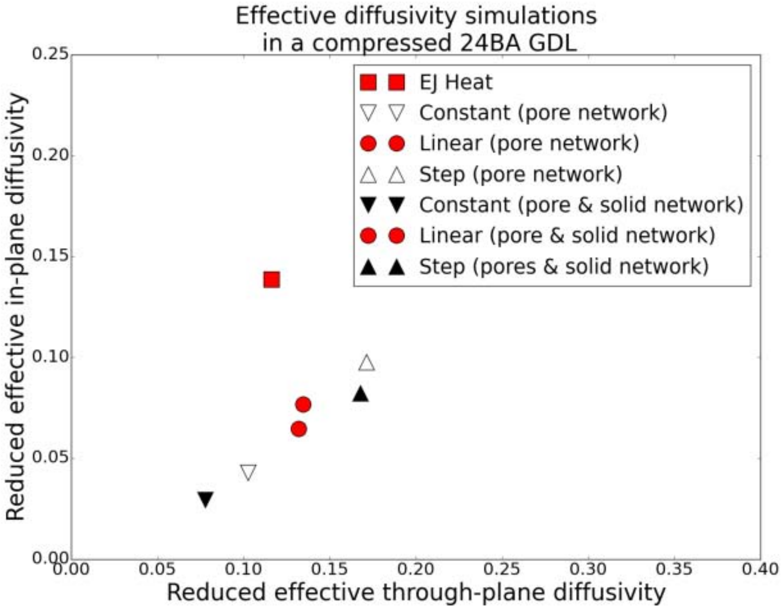

Figure 3.17 Simulation of effective diffusivity on a tomographic image of a GDL 24BA. The bulk diffusivity of the fluid phase is assumed to be non-zero, that of the solid phase is assumed to be zero.

The pore network results were obtained for two different networks. One was extracted from the fluid phase only, the other from both the fluid and solid phases. In principle, both should give the same results, since the simulated transport occurs only in the pores of the fluid phase. Indeed, we see in Figure 3.17 that the results are close in both cases. There is, however, a small decrease of the effective diffusivity when the network is extracted from both the fluid and the solid phases. The explanation for this numerical phenomenon is as follows. To link the pores of the solid and fluid phases, we consider that the regions in contact with both fluid and solid phases are links. These regions are surfaces of two voxels in thickness, located at the boundaries between the two phases. The volumes of these regions are subtracted from the pore volumes. This reduces the volume of the pores, therefore decreases their estimated effective radius. This is not an important effect if the volumes of the pores are much greater than the volume of their voxelized surface, but this can become important for small pores.

The different formula used for conductances give different results, although it is not clear which one is the best. Indeed, all these simulations underestimate the in-plane effective diffusivity by a factor of 2 to 3. The through-plane effective diffusivity is better predicted, with a margin of error of 50%.

We conclude from this test case that it is essential to verify the pore network simulations. These are relatively imprecise on this test case, with a factor 2 to 3 error on the in-plane effective diffusivity. This suggests improving the formulas used to calibrate the conductances on the pores geometry, or introducing adjustment parameters into the conductance formula to calibrate the pore network model on reference effective transport properties.

3.2.1.3.3 Diffusive transport in the solid phase

The simulation results for the effective conductivity of the solid phase are shown in Figure 3.18. We have no theoretical value for this case. For the same reasons as in the previous test case, we take the Ej-Heat result as a reference to verify the pore network simulations.

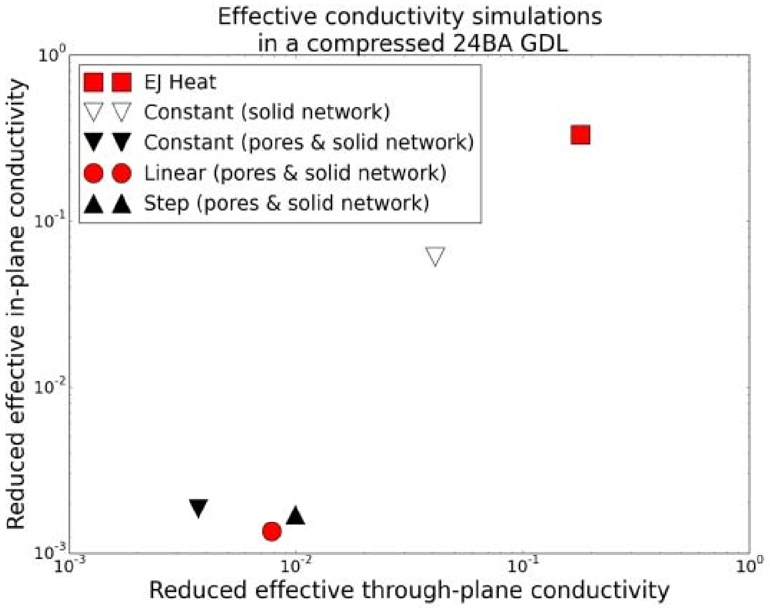

Figure 3.18 Simulation of effective conductivity on a tomographic image of a GDL 24BA. The bulk conductivity of the fluid phase is assumed to be zero, that of the solid phase is assumed to be non-zero.

The best pore network result was obtained with a conductance formula corresponding to a constant profile whose radius is calibrated on the surface of the links, on a pore network extracted from the solid phase only. However, this result is not satisfactory, because it differs from the reference value by a factor of 5 for the effective conductivities in both directions. This may be due to the over-segmentation that can be seen in Figure 3.15. Indeed, the over-segmentation creates a multitude of small pores and constrictions, for which the transports are perhaps not very well approximated by the conductances. The pore segmentation process should be re-examined for such weakly resolved straight fibers. Note that several specific methods of segmentation of fibers exist in the literature. The literature indicates that segmentation methods often must be adapted to the type of shape studied.

Simulations with pore networks extracted from both the fluid and the solid phases give much too low effective conductivities, with a one or two orders of magnitude error. This is probably because we wrongly considered the surface voxels between the two phases, as described for the previous test case. Here the effect is particularly important because the pores are small, so removing a voxel over their entire surface decreases their volume considerably. We could mitigate this effect by considering the volume of these surfaces in the pore volume, without significantly changing the methodology.

We conclude from this test case that our pore network simulations have difficulty in calculating diffusive transports in fibers. The segmentation of fibers into distinct elements by watershed segmentation is made complicated by the poor resolution of the fibers, which are less than 5 voxels thick. A 5-fold error with respect to the reference Ej-Heat was found for the effective conductivities.

In all these test cases, the conductance which gave the best results is that calculated with a constant profile calibrated on the surfaces of the constrictions. We therefore recommend to calibrate conductance using this formula.

3.2.1.4 Conclusion

The Ej-Heat simulation method and the image based pore network method were tested on a series of microstructures to verify their reliability. The proposed test cases cover a wide range of microstructures, ranging from simple geometries to real GDL geometries.

The Ej-Heat method could predict very precisely the theoretical effective diffusive transport properties for cases where an analytical formula was available. The limited resolution of the images did not prevent the correct calculation of these theoretical values [Hutzenlaub2013]. This validates the Ej-Heat simulations from a numerical point of view. Moreover, we could verify that these simulations were simple to perform since they do not require geometry adjustment by the user. The duration of the calculations is reasonable, since 5h are sufficient to compute the tensor of effective properties in one direction. This time is significantly shorter than the time required by other commercial multi-purpose direct simulation codes.

A pore network simulation code extracted from images has been developed. Simulations of diffusive transport can be carried out on images with multiple phases representing complex geometries such as those of GDL. The calculations are extremely fast: on a GDL image, the computation time is decreased by 4 orders of magnitude compared to the Ej-Heat simulations. Nevertheless, the calculated effective diffusive transport properties are inaccurate at this stage. In all the test cases studied except one, the error on the effective property was less than a factor 3. Diffusive transport in weakly resolved fibers gave a 5-fold error. Progress is still desirable to better consider the geometry. There remains a potential for significant improvement in view of the coarse geometric approximations we used. Despite these numerical inaccuracies, the pore networks remain relevant because of the speed of the calculations, which allow simulating couplings between diffusive transports and two-phase phenomena, such as the condensation phenomenon presented in Chapter 6.

3.2.2 Study of the diffusive transport properties of regular cubic pore networks

This section is devoted to the diffusive transport properties of regular cubic pore networks. We want to verify if they can accurately calculate the real GDL diffusive transport properties. In a first section, we estimate the effective diffusive transport properties of a pore network whose pore sizes are calibrated on a pore size distribution extracted from a tomographic image of a 24BA GDL. We compare the effective transport properties of this network with the effective transport properties calculated by direct simulation on the 24BA GDL tomographic image. In a second section, we study all the effective diffusive transport properties accessible by regular networks, for the solid and gas phases. We check whether correlations between the solid and gas phases transport properties of real GDLs can be obtained with regular networks.

3.2.2.1 Regular cubic pore network model calibrated on the pores size distribution of a GDL

In this section, we verify a regular pore network model for diffusive transports in a compressed GDL 24BA. We first present the calibration of the regular pore network model from the pore size distribution of a GDL 24BA obtained by image analysis. We then compare the transport properties calculated with the regular network with the transport properties of the 24BA calculated by direct EJ-Heat simulations on the tomographic image.

3.2.2.1.1 Calibration of the network

First, we want to ensure that the porosity of the pore network is equal to the porosity calculated on the tomographic image. The porosity calculated on the image is $\varepsilon_{macropores} = 0.51$. More information on the porosity of this image is given in section 4.1.3.1. The porosity ε of the pore network is calculated with the formula:

$$\varepsilon = (1 - 3k^2)\langle u^3 \rangle + 3k^2 \langle u^2 \rangle$$

Équation 3.23

where $\langle \quad \rangle$ denotes the volume average over the entire network and u is the dimensionless pore size.

Figure 3.19 shows the pore size distributions and the constrictions size distributions extracted from the compressed GDL 24BA tomographic image. Note that for pore networks constructed on regular grids, the choice of the pore size distribution must be supplemented by the choice of the regular grid step. This step has the effect of truncating the pore sizes distribution, because pores larger than the step of the network cannot be considered. Thus, it often happens that the pore sizes distributions of regular networks are modified compared to the experimental pore sizes distribution.

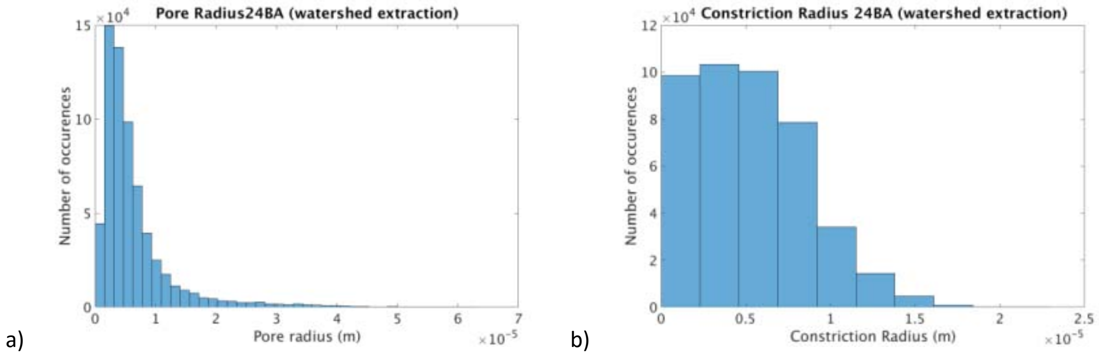

Figure 3.19 Distributions of pore sizes (a) and constriction sizes (b) based on a compressed 24BA tomographic image. The pores and constrictions are extracted from the image by watershed segmentation with h-Maxima markers, h = 4 voxels.

The image analysis allows us to know the average values of the pore sizes and constrictions sizes. We calibrate the constrictivity parameter k as the ratio between these average sizes:

$$k = \frac{mean(constrictionRadius)}{mean(poreRadius)} = \frac{5.31\mu\mathrm{m}}{6.35\mu\mathrm{m}} = 0.84$$

We take the same value of k for constrictions oriented in the plane and in the thickness directions. Indeed, the image analysis did not detect a significant difference in the constrictions sizes in the plane and in the thickness. This fact is not confirmed by [Lamibrac2016], so this choice of constrictivity must be taken with caution. Nevertheless, we believe that the choice of constrictivity does not change the conclusions of the study of the regular pore networks presented here.

3.2.2.1.2 Effective diffusive transport properties of the regular network

Figure 3.20 presents a sensitivity analysis of the Wiener bounds of the effective diffusive transport properties of the gas and solid phases. The dimensionless pore size distribution is modeled with Weibull distribution whose shape and threshold parameters are varied, while maintaining a network porosity equal to the porosity calculated on the image.

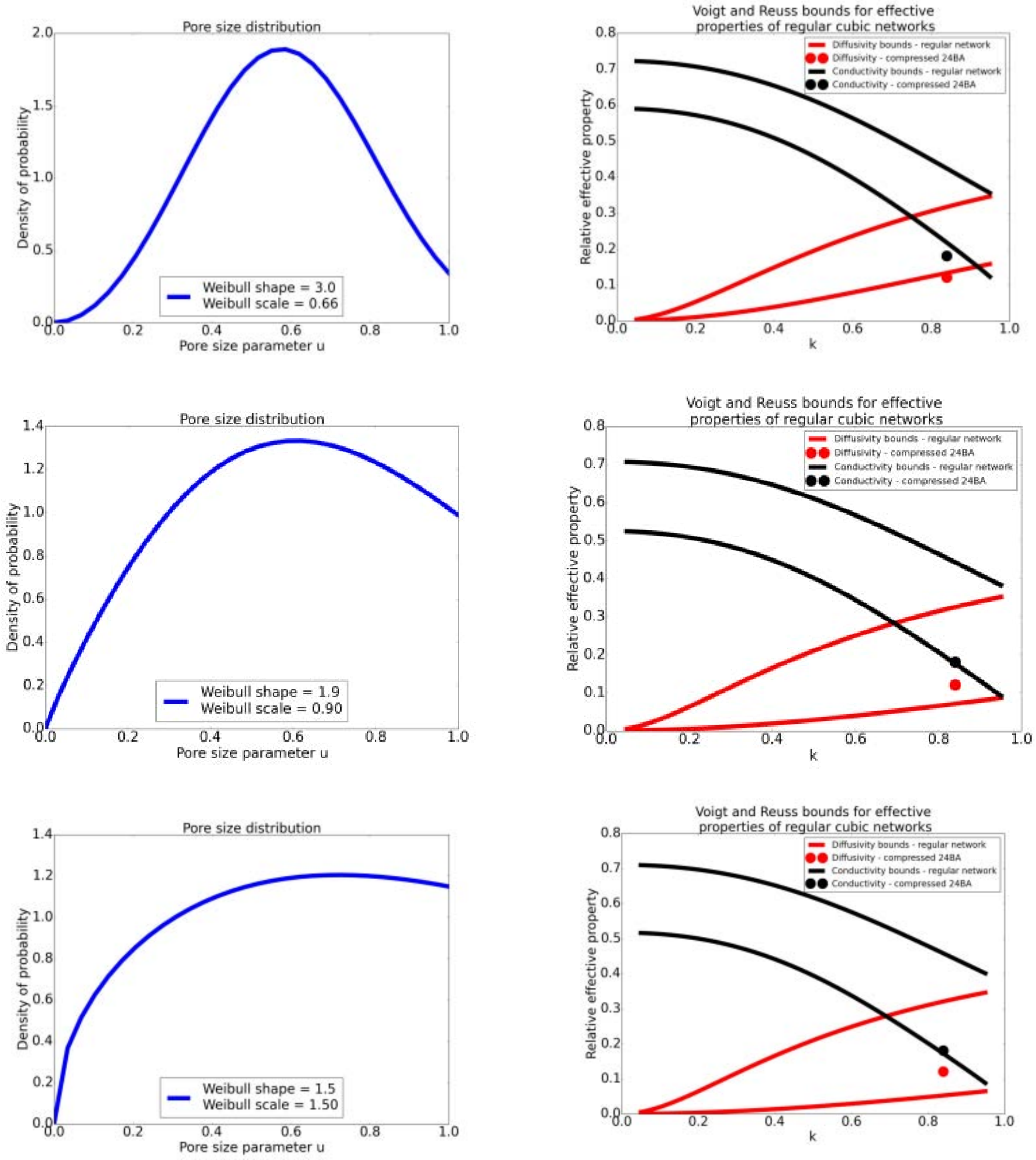

Figure 3.20 Sensitivity study of the effective transport properties of regular networks. On the left, dimensionless pore size distribution. Three Weibull distributions are studied, with different shape parameters and thresholds. On the right, the Wiener bounds on the effective diffusivity in the gas phase and the effective conductivity in the solid phase as a function of k. EJ-Heat simulations of the effective properties of a compressed GDL 24BA are shown as points for comparison.

We see in Figure 3.20 that the effective diffusivity of the compressed GDL 24BA is within the Wiener bounds of the regular network, but it requires to take highly truncated pore size distributions. On the other hand, the effective conductivity of the compressed 24BA is very difficult to obtain. In the best case, it is close to the lower Wiener bound, which corresponds to an unrealistic pore distribution as discussed in the following paragraphs.

Figure 3.21 shows the effective diffusivities of the GDL 24BA calculated by the different simulation methods, as well as some experimental values. The simulations methods studied are the Ej-Heat simulation, the pore network extracted from the image and the regular pore network calibrated on the pore size distributions.

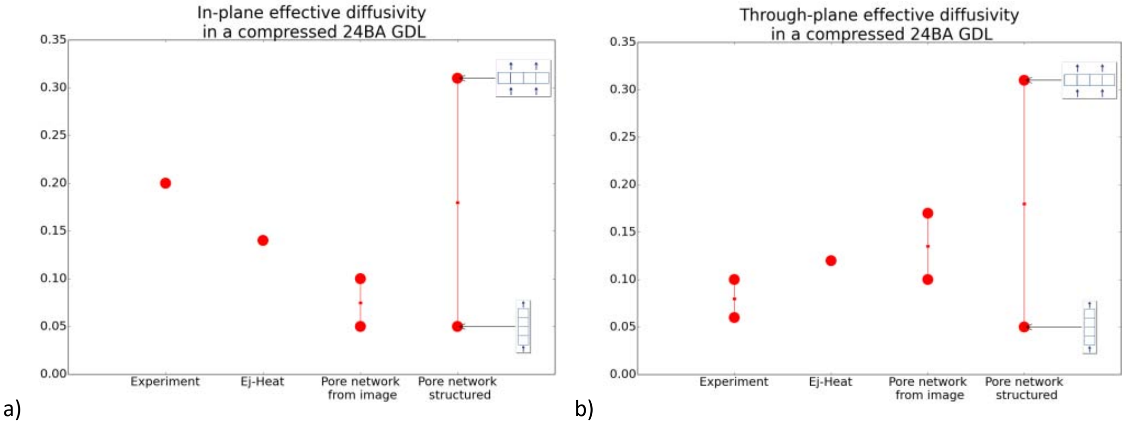

Figure 3.21 Comparison of numerical methods for the effective diffusivity of compressed GDL 24BA. A) effective diffusivity in the plane. B) Effective diffusivity through the thickness.

Some results in Figure 3.21 are given with margins of error. These margins of error have different origins. For the pore network extracted from the image, these are the values obtained with different geometric formulas for the conductances. The margin of error for the regular pore network comes from the gap between the two Wiener bounds. Note that the Wiener bounds are reached for microstructures having either a single pore thickness or a single pore width. It would probably be possible to narrow the width of the Wiener bounds by imposing a specific number of pores in the thickness and width, to be closer to the actual dimensions of the GDLs. The margin of error for the experimental value through the thickness comes from the scattering of experimental values given in [Zamel2013] for GDL 24AA and 24DA. These GDLs have the same structure as the 24BA but the 24AA has less PTFE whereas the 24DA has more. Other uncertainties affect the experimental values: uncertainty on compression level and binder bulk diffusivity as well as variability of values from one sample to another. For further details on experimental values, please refer to Chapter 4.

The upper Wiener bound for relative diffusivity is the same in all three cases, 0.31. This corresponds to a network in which the pores are aligned in the direction of transport. Note that this value is close to the value predicted by the Bruggeman formula, $D_{eff}^{Bruggeman}(\varepsilon = 0.5) = 0.35$. The lower Wiener bound varies between 0.05 and 0.13, depending on the pore size distribution chosen. We considered the value 0.05 for Figure 3.22, which provides the broadest diffusivity range.

In this section, we verify that the numerical methods correctly consider the microstructure. The pore network extracted from the image gives a value close to Ej-Heat simulations in the trough-plane direction. This indicates that the conductances capture the essential characteristics of the pore geometry in this direction. On the contrary, in the in-plane direction, the pore network extracted from an image gives values significantly lower than Ej-Heat simulations. This indicates that the calibration of conductances misses an essential element of geometry. It is therefore necessary to find a more robust formula to calibrate the conductances, to be predictive of the diffusion anisotropy of GDL.

We now study the effective diffusivities calculated by the regular pore network. In the in-plane direction, the experimental value and the Ej-Heat value are close to the middle of the range of values accessible with regular pore networks. There are thus some network parameters which make it possible to correctly simulate the experimental value with a regular pore network. Note that the Wiener bounds are wide: 0.05-0.31. This indicates that the spatial distribution of the pores has some uncalibrated degrees of freedom, which have an important influence on the effective diffusivity. To go further, thorough simulations would be interesting to verify if the spatial distribution of pores corresponding to this value is realistic of a GDL.

In the trhough-plane direction, the experimental value is close to the lower Wiener bound. This corresponds to the effective property of pores in serie, i.e. the diffusion would take place through a line of aligned pores. This configuration is not representative of the low thickness of the GDLs. The actual configuration of the pores in a GDL is closer to pores in parallel. There is therefore a difficulty in calibrating the regular pore network in the direction of the thickness. This is because we aim to have a low effective diffusion (0.05-0.10) with a high porosity (0.5). The diffusion resistance of the regular pore network is here caused by small pores located in the gas path. However, for real GDL, geometrical tortuosity is the source of additional resistance to gas transport, as discussed in Appendix 9.4. To represent the geometric tortuosity, the regular pore networks must use additional calibration parameters.

These simulations of the effective diffusivity through the thickness of the GDL show that additional calibration parameters are required for the regular pore networks. The pore sizes and constriction sizes distributions alone do not make it possible to properly calibrate the regular pore network. The tortuosity of the microstructures is a degree of freedom that is not considered in the sizes distributions. The calibration procedure for regular pore networks needs to be improved. One solution consists in calibrating the conductances directly on effective transport properties obtained experimentally or obtained by direct simulations on microstructures. As mentioned previously, the limit of this approach is that then simulations by regular pore networks no longer make it possible to predict the effective diffusion properties, if they are unknown. On the other hand, the advantage of this approach is that it makes it possible to calibrate the regular pore networks to simulate two-phase transports coupled with diffusive transports, as presented in the Chapter 6.

Tableau 3-2 gives some values of relative effective transport properties for other GDLs, simulated with the EJ-Heat method. These data can be used to replicate this verification of regular pore network for other GDLs.

	Relative diffusivity in thickness	**Relative diffusivity in-plane**	**Relative conductivity in thickness**	**Relative conductivity in-plane**
Compressed 24BA	0.12	0.14	0.18	0.33
Uncompressed 24BA	0.27	0.46	0.037	0.19
Compressed TGP-H-060	0.10	0.21	0.17	0.32
Uncompressed TGP-H-060	0.26	0.43	0.028	0.19

Tableau 3-2 Effective properties of several GDL calculated by direct simulation Ej-Heat on the tomographic images used in Chapter 4. The effective diffusivities are normalized by the bulk diffusivity of the gas, the effective conductivities by the bulk conductivity of the solid (fibers and binder are indiscriminated).

3.2.2.2 Correlations between effective transport properties of solid and fluid phases

We study in this section the values accessible by a regular cubic pore network model for the effective diffusivity in the gas phase and the effective conductivity in the solid phase. We are particularly interested in the correlations between these two properties, to determine if there is a parametrization of the regular pore network models that can represent the real GDL properties.

We limit the study here to regular pore networks whose size of elements is not random. Under these conditions, the pore network is composed of many times the same unit cell. The normalized effective properties of such pore networks are those of their unit cell. For unit cells, the transport properties in the solid and gas phases can be calculated jointly by analytical formulas. It is thus possible to study the correlations between the transport properties in these two phases, which makes it possible to study with a good level of detail the effect of the geometry of the unit cell on the effective transport properties. We thus provide additional insight into the main issue of this section, which is to verify whether the microstructure of the GDLs is sufficiently well described by regular pore networks. It should be noted that for pores networks composed of random size pores, the effective transport properties are bounded by the harmonic and arithmetic means of the transport properties of the unit cell, per the Wiener bounds. Because these means are within the convex bulk of the unit cells properties, it may be possible to extend some results of this section to random pore networks.

Figure 3.23 shows the values of the gas phase diffusivity and the solid phase conductivity for all cubic unit cells. We denote by D_{eff} the diffusivity of the unit cell, which is also equal to the effective diffusivity of a network with all its unit cells identical to this cell. We find that D_{eff} and the porosity are not correlated. They can be chosen independently below an upper limit of D_{eff}. This lack of correlation is due to the constrictivity which adds a degree of freedom in addition to the porosity, as discussed in Appendix 9.4. On the other hand, the correlation between the porosity and the conductivity is strong for the solid phase. This is because the constrictivity of the solid phase depends very strongly on the porosity in these unit cell geometries, so the constrictivity is not a free parameter.

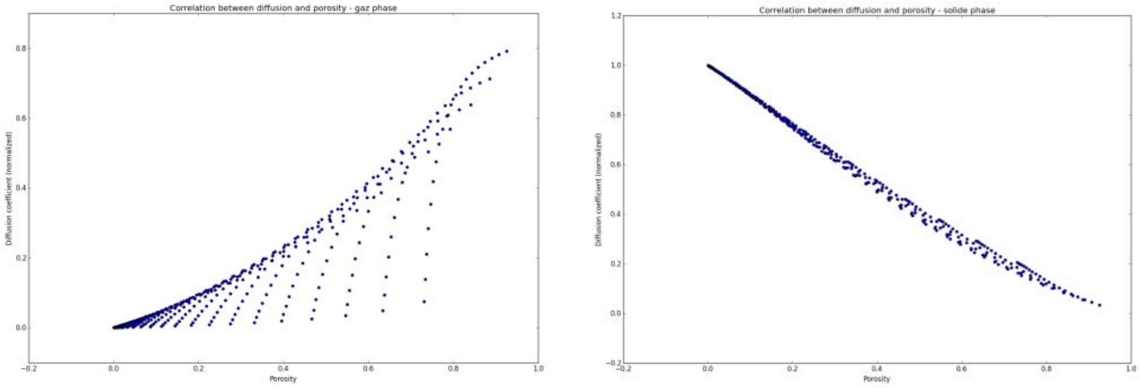

a) b)

Figure 3.23 A) relative effective diffusivity as a function of porosity, calculated for the whole range of u and k. B) relative effective conductivity as a function of porosity. Relative means adimensioned by the bulk transport property of the phase.

Note that the pore size is not the relevant parameter for calculating the effective diffusivity of a unit cell. The influent parameter is the dimensionless pore size $\mathbf{u} = \frac{\boldsymbol{d}}{\boldsymbol{a}}$, where a is the step of the network. Indeed, the effective diffusivity of these cells is a function of the dimensionless pore size $\mathbf{u}$ and the constrictivity parameter k, rather than the pore size d, per Équation 3.13.

Let us now study the correlations between the effective transport properties of the solid and gas phases. The goal is to verify if we can find a regular pore network that represents the actual GDLs for both transport in the solid phase and the gas phase. Figure 3.24 shows the set of conductivity-diffusivity values that can be obtained with cubic unit cells. We find that the accessible values occupy only a part of the set of possible values. The properties of some sub-samples of the compressed 24BA GDL are outside the values accessible by the cubic unit cells. The properties of the subsamples correspond to cubic unit cells with extreme geometries, such that u is close to 1 (low solid volume) and k is close to 0 (low gas diffusion). Thus, the cubic unit cells are not adapted to represent all the microstructures. This is particularly the case for microstructures having both low effective conductivity and low effective diffusivity.

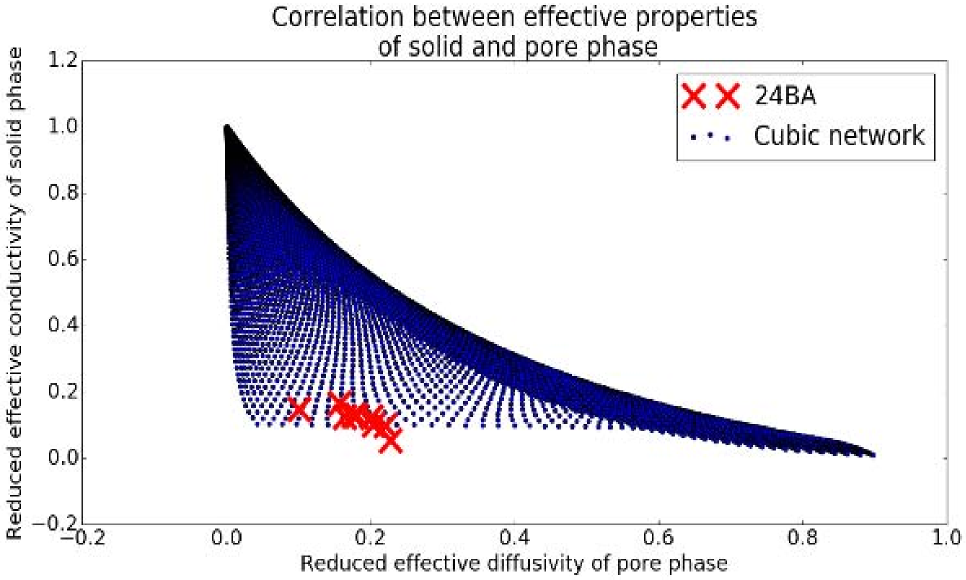

Figure 3.24 Correlation between the effective conductivity of the solid phase and the effective diffusivity of the gas phase. In blue: cubic mesh. In red: Ej-Heat simulations on a 24BA GDL 3D image.

Let us note that this conclusion is dependent on the geometry of the unit cells used for the regular pore network. It is possible to introduce additional calibration parameters to calibrate the simulated effective properties on reference effective properties. These reference effective properties can come for example from experimental measures or from direct simulations on microstructures. Let us note that with such a calibration, the simulations by regular pore networks no longer make it possible to predict the effective diffusive transport properties of new microstructures. On the other hand, this can make it possible to simulate two-phase transports coupled to diffusive transports, as presented in Chapter 6.

3.2.2.3 Conclusion

This part is devoted to the effective diffusive transport properties of regular pore networks. Regular pore networks model in a simplified manner a porous microstructure, using a set of unit cells having a simple geometry. Multiple physical phenomena can be simulated on these geometries, such as diffusive transport. The use of analytical formulas to model these phenomena in pores of simple geometries allows to carry out the simulations in an economical way in computation time. These networks can in principle be calibrated on real porous microstructures by adjusting the geometry of the unit cells, the size distribution and the spatial distribution of the pores and the links.

In this chapter, we verified whether the usual calibration methods of the regular pore networks allow to predictively simulate the diffusive transport properties of GDL. To do this, we studied the effective conductivity and effective diffusivity of regular cubic pore networks and compared it to the effective properties of a GDL 24BA. We have found that regular cubic pore networks overestimate conductivities and diffusivities of compressed GDL, such as a GDL 24BA. GDL are actually tortuous microstructures whereas regular pore networks are non-tortuous because all their pores are aligned. This tortuosity effect must be considered specifically in the models, as discussed in Appendix 9.4.

We therefore recommend to introduce a tortuosity parameter in the pore networks. A promising solution to this is to use morphological pore networks rather than regular pore networks. Indeed, they retain the advantages of regular networks in terms of simulation capabilities, while exceeding their geometric limitations. For example, they may have some tortuosity. The extraction of a pore network from a tomographic image is another reason for using morphological networks, because this procedure makes it possible to calibrate a pore network on a real microstructure.

3.3 Perspectives

We describe in this section perspectives to improve the caibration of conductances for pore networks extracted from images. The calibration of the conductances is indeed the main source of error in the test cases that we studied. We propose two approaches: the first consists in introducing non-geometric calibration parameters into the conductances, the second to better consider the microstructures in the formulas giving the conductances.

The first approach consists in using fields computed by direct simulations, for example concentration or temperature fields, and in introducing an adjustment parameter in the conductance of each link. A global optimization procedure could make it possible to calibrate these adjustment parameters by minimizing the difference between the fields calculated by direct simulation and the fields calculated by pore network. The pore network once calibrated could be used to perform new simulations.

The second approach consists in better considering the pores and constrictions geometries. We propose two ways of improvement: first, extending the range of geometries on which we can calculate the exact conductances for diffusive transports, secondly, better calibrating the model geometries on the actual geometries of the pores.

A first axis of improvement is to improve the geometry-dependent transport model. The geometries on which we know how to solve diffusive transport in an analytical way are few. A direct simulation of diffusive transport on more varied pore geometries [Combaret2013] would allow to extend the range of geometries for which we know how to accurately calculate the conductance. Microscopic simulation in pores would also make it possible to extend the number of physical phenomena that we can model at the pore scale, which would be interesting, for example, for physical phenomena in catalytic layer agglomerates.

This approach of solving transport on two scales is also used in the methods multiscale finite volume [Tomin2013], and heterogeneous multiscale [Weinan2004]. These methods are analyzed mathematically in the literature to make the two scales coherent and to ensure the accuracy of the calculations. Here we try to identify some ideas for which we could draw inspiration from these methods. The boundary conditions of the microscopic calculation are a first question. To increase the coherence between the micro and macro scales, one option would be to use boundary conditions depending on the macroscopic field, such as a temperature gradient. The conductance may then depend on the macroscopic field. The conductance between two pores is assumed to be localized, i.e. it depends only on the geometry of the two pores, not on that of the pores around. The boundary conditions used to solve a localized microscopic problem are studied in the multiscale literature. One option is to take the microscopic field equal to zero outside the two pores.

For the calculations to be faster than a direct calculation over the whole domain, it would be ideal not to recalculate the transport between two pores by direct simulation each time. A perspective for this purpose consists in constructing a database of geometries for which the conductance has been determined precisely. From this database, a fast model approximating the conductance of new geometries would be constructed, for example using a model reduction methodology. An essential step for this purpose is to evaluate the proximity of a new geometry to the geometries in the database. For this purpose, scalar shape descriptors or a procustian analysis could be used. A procustian analysis is a computer technique used to compare shapes, considering the invariance of shapes by translation, rotation and scaling.

A second way of improvement is to better calibrate the conductances on the pore geometry.

We applied to all the pores the same formula for the conductance. A first improvement would be to classify the pores into several geometric categories, to use a different formula for each category of pores. Using a unique type of longitudinal profile for all geometries seems inappropriate. Indeed, let us consider the case of large pore having a much smaller constriction. A constant link profile adjusted to the size of the constriction overestimates the resistance to transport in this geometry. However, this type of profile is well suited for other configurations, since it is the one that gives the best results on our test cases. Several methods can be used to find classification criteria, including automatic or statistical classification methods.

The shape descriptors that we used to parameterize 3D pore geometries are simplistic. We mention here two more sophisticated tools for shape analysis. The skeleton is used in the pore network literature to extract networks and compute conductances [Bauer2011]. This consists of extracting from the 3D image the median axis of the transport phase. At each point of the median axis, the width of the transport phase is given. This provides a detailed information on the transport phase shape, and it is well adapted to compute conductances using the simplified model of transport that we used. Nevertheless, on complex 3D geometries, the median axis is not defined uniquely, it can become a two-dimensional median surface. Another methodology consists in representing the shape by their surface. The surface is discretized by a set of points, which gives the possibility to work on points coordinates in 3D. This makes it possible to use other algorithms, such as a Procrustes analysis.

Porosity is an essential geometric feature. However, we did not specifically consider it when we defined the conductances. For the equivalent network to have the right porosity, the most rigorous method would be to ensure that the profiles of links used for computing the conductances respect the volume of each pore. We present here a balance of volume of each pore intended to define profiles of links respecting the porosity. We have the following relation between the volume of the pore and the volume of the linksof this pore:

$$V_{pore} = \sum_{links} V_{links} - n_{links} \frac{V_{sphere}}{2}$$

Équation 3.24

We assumed that the links only overlap at a central sphere embedded in the pore. Volumes of links V_{links} can be calculated based on link profiles. Unfortunately, we were unable to correctly correlate the pore volume with other useful geometric data, such as pore-link lengths. This has prevented us from defining the profiles with this constraint of conservation of the pore volume. This may explain some of the numerical errors in our pore networks. The problem probably came from the geometric descriptors used, not precise enough. More detailed geometric analyzes would be required to define the conductances coherently with the total porosity.

3.4 Conclusion

The aim of this chapter is to present and verify numerically several simulation methods for diffusive transport in GDL. The challenge is to have reliable methods to simulate the transport properties of PEMFC porous materials.

We developed simulation tools based on tomographic images. Indeed, 3D microscopy gives access to detailed information on the microstructure of porous materials. We have also studied another way of representing porous microstructures, regular pore networks. This approach has been used for many years in the laboratory.

The explicit-jump direct simulations (Ej-Heat) and simulations on pore network extracted from images were tested on a series of microstructures to ensure their reliability. The test cases cover a wide range of microstructures, ranging from simple geometries to real GDL geometries.

The Ej-Heat method could predict very precisely the theoretical values for several microstructures for which an analytical formula was available. This validates the relevance of EJ-Heat simulations from a numerical point of view. The calculation time is reasonable to calculate the effective properties. The next step is to compare Ej-Heat simulations with experimental results to validate the physical modeling of GDL. This is done in Chapter 4.

A code to extract pore networks from 3D images of porous materials has been developed. Simulations of diffusive transport can be performed on extracted pore networks representing real geometries such as those of GDL and involving multiple phases. Pore network calculations are faster than direct simulation by several orders of magnitude. Nevertheless, the calculated values are relatively imprecise. Progress is still desirable to better take geometry into account. Despite these numerical inaccuracies, the pore networks remain interesting because of the speed of the calculations, for example to simulate couplings between diffusive and two-phase transports, such as the one presented in Chapter 6.

We have found that regular cubic pore networks overestimate the effective conductivities and diffusivities of compressed GDL, such as a GDL 24BA. The GDL are in fact tortuous structures through which the diffusive transports follow paths longer than in a regular pore network that has all pores aligned. This tortuosity effect must be considered specifically in the models.

3.5 Bibliographie

- [Bauer2011] D. Bauer, S. Youssef, M. Han, S. Bekri, E. Rosenberg, M. Fleury, and O. Vizika, From computed microtomography images to resistivity index calculations of heterogeneous carbonates using a dual-porosity pore-network approach: Influence of percolation onthe electrical transport properties, PHYSICAL REVIEW E 84, 011133 (2011)

- [Becker2009] Jürgen Becker, Reto Flückiger, Mathias Reum, Felix N. Büchi, Federica Marone, Marco Stampanonic, Determination of Material Properties of Gas Diffusion Layers: Experiments and Simulations Using Phase Contrast Tomographic Microscopy, Journal of The Electrochemical Society, 156 10 B1175-B1181 2009

- [Combaret2013] Nicolas Combaret. Construction d’un modèle de réseau de pores à partir d’une image 3D pour l’estimation de la perméabilité. PhD thesis, Université Sciences et Technologies - Bordeaux I, 2012.

- [Geodict] A. Wiegmann. GEODICT virtual micro structure simulator and material property predictor. 2001–2010. http://www.geodict.com.

- [Gibiansky1993] L.V. Gibiansky, Bounds on the Effective Moduli of Composite Materials, School on Homogenization ICTP, Trieste, September 6–17, 1993, https://www.mat.uniroma2.it/~braides/ICTP93/ICTP93Gibiansky.pdf

- [Hutzenlaub2013] T. Hutzenlaub, J. Becker, R. Zengerle and S. Thiele, How Coarsening the 3D Reconstruction of a Porous Material Influences Diffusivity and Conductivity Values, ECS Electrochem. Lett. 2013, Volume 2, Issue 2, Pages F14-F17.

- [Lamibrac2016] A. Lamibrac, J. Roth, M. Toulec, F. Marone, M. Stampanoni, F.. Buechi, Characterization of Liquid Water Saturation in Gas Diffusion Layers by X-Ray Tomographic Microscopy, J. Electrochem. Soc. 163 (2016) F202–F209.

- [Pietrak2015] Pietrak et al., A review of models for effective thermal conductivity of composite materials, Journal of Power Technologies 95 (1), 2015

- [Rashapov2016] Rashapov, R and J.T. Gostick, In-Plane Effective Diffusivity in PEMFC Gas Diffusion Layers, Transp Porous Med (2016). doi:10.1007/s11242-016-0648-4

- [Renard1997] P. Renard, G. de Marsily, Calculating equivalent permeability: a review, Advances in Water Resources, 1997, vol. 20, no. 5-6, p. 253-278

- [Renard2000] Philippe Renard, Gaëlle Le Loc'h, Emmanuel Ledoux, Ghislain de Marsily, Rae Mackay, A fast algorithm for the estimation of the equivalent hydraulic conductivity of heterogeneous media, Water Resources Research, Volume 36, Issue 12, Pages 3567–3580, 2000

- [Wiegmann1999] Andreas Wiegmann, The explicit jump immersed interface method and integral formulas, Lawrence Berekeley National Laboratory Technical Report, 1999
- [Wiegmann2000] Andreas Wiegmann and Kenneth P. Bube, The Explicit-Jump Immersed Interface Method: Finite Difference Methods for PDEs with Piecewise Smooth Solutions, SIAM J. Numer. Anal., 37(3), 827–862.
- [Wiegmann2006] A. Wiegmann, A. Zemitis, EJ-HEAT: A Fast Explicit Jump Harmonic Averaging Solver for the Effective Heat Conductivity of Composite Materials, Berichte des Fraunhofer ITWM, Nr. 94 (2006)
- [Zamel2013] Zamel & Li, Effective transport properties for polymer electrolyte membrane fuel cells – With a focus on the gas diffusion layer, (review), PECS 2013

Chapter 4 Experimental validation of diffusive transport simulations

The transports of gas, heat and electrons in porous materials play an important role in the operation of fuel cells. The diffusion of gases limits the maximum current that can be supplied by the fuel cell. The heat has a decisive effect on the condensation and evaporation of the water in the cell. Thus, understanding transport in porous materials is important to increase the electrical power and efficiency of fuel cells.

Diffusive transports in porous materials are often characterized by effective properties, such as the effective diffusivity and the effective electrical and thermal conductivities. Knowing these properties is important for understanding and improving materials. They are also indispensable for models of fuel cells modeling porous materials as homogenized media.

The aim of this chapter is to validate that the simulations on tomographic images of GDL make it possible to calculate in a predictive way the properties of diffusive transports measured experimentally. Numerical simulations have several advantages over experimental measurements. Experimental measurements of the properties of GDL are often difficult due to the low thickness of the GDL. It is often easier to produce a tomographic image of a porous material than to characterize experimentally its physical properties. Tomographic images are available for a large number of porous materials, used for example in PEMFCs, SOFCs, electrolysers and batteries. In addition, numerical simulations allow the study of microstructures designed virtually. This opens the way to a numerical optimization of porous materials. Validating the relevance of image-based models is an important step in providing a reliable method for studying porous materials and guiding the development of new materials.

The microstructure of a porous material directly impacts the effective properties of this material. Knowing the precise microstructure of a GDL is therefore important in determining its properties. The microstructure of the GDL is different from the simplified microstructures for which analytical formulas or correlations exist, such as the Bruggeman formula [Tjaden2016]. Moreover, changes in the microstructure of the GDLs, such as the presence of binder or the deformation due to compression by the bipolar plate, modify the GDL transport properties. This is why we use tomographic images to model the GDL microstructure. Numerical simulations are carried out on these 3D images to calculate the effective transport properties from the solving of the partial differential equation modeling the diffusive transports.

The simulations in this chapter are performed using direct simulations on microstructure images with the explicit-jump method. This method is referred to as EJ-Heat. This method has been used several times in the literature to calculate porous material transport properties [Becker2009]. It was analyzed mathematically [Wiegmann2006] [Wiegmann2000] [Wiegmann1999] and we verified that it gives the correct numerical results on several test cases in Chapter 3. We therefore consider in this chapter that this method is numerically reliable. We use it as a reference to develop other numerical methods such as pore networks. We use an open source version of Ej-Heat [Wiegmann2006].

In this chapter, we use experimental measurements from the literature to validate Ej-Heat simulations on tomographic images. This validation work requires additional work compared to numerical verification. It is necessary to collect data to calibrate the bulk transport properties, to check that the resolution of X-ray tomography images, typically a few microns, is sufficient. It must also be verified that the physical modeling is sufficiently rich, in the sense that it allows to capture the preponderant physical phenomena to estimate these effective transport properties. This work of validation has already been partially carried out in [Becker2009].

Our contribution to the advance of the state of the art is as follows. We studied in detail the complications due to the lack of contrast between the binder and the fibers in the images obtained by X-ray tomography, which led us to design an algorithm to reconstruct the fibers and binder phases. Once these two phases were identified, we could work with the bulk transport properties of standard materials, not artificially calibrated bulk properties [Becker2009], which made our study more rigorous. In adition, an original study of the effect of PTFE located between two fibers is presented in Section 7.2.3.

The outline of the chapter is the following. A first section describes the methodology: the materials we studied, the image acquisition and segmentation, the simulation method we used and the bulk transport properties we used. A second section presents the comparisons between the simulations and the experimental data of the literature for the effective diffusivities and the electrical conductivities, as well as some additional simulations, notably the spatial variability of the properties of the GDL. Finally, a discussion section and a conclusion section conclude this chapter.

4.1 Methodology

We describe in this section the GDLs studied, the acquisition of tomographic images, the image processing necessary to distinguish the different phases. Then we detail the numerical simulations and the parameters chosen for the transport properties of the constituents.

4.1.1 Materials

The materials studied in this chapter are GDL SGL 24BA (without MPL) with 5 wt% PTFE (SGL, Meitingen, Germany) and GDL Toray TGP-H-060 (without MPL, Toray Industries, Japan) with 10 wt % PTFE.

The GDLs have a porous structure for the gases to diffuse through the pores and for the solid phase to conduct the electrons. The porosity of GDL is between 70 and 90% [Rashapov2015]. The GDLs are composed of carbon fibers with a diameter between 6 and 10 µm. The fibers are held together by a carbonaceous binder. A hydrophobic treatment comprising PTFE (Teflon) is often added to limit the accumulation of water in GDL. In this chapter, we refer to all non-fiber solid materials as binders. The criteria that guide the design of GDLs are chemical stability, mechanical strength, conductivity and effective diffusivity. Having high conductivity and high diffusivity is contradictory and requires optimizing the porous and solid phases, as discussed in section 7.1.1. The thickness of the GDL is very thin (~150-300 µm) so that the transport resistances through the thickness of the GDL (through-plane) are minimized. Transport in the plane of the GDL (in-plane) allow the gases to reach the areas beneath the rib of the bipolar plates. The properties of GDL are anisotropic because of its microstructure.

4.1.2 X-ray tomography

In this section, we describe the acquisition of GDL images by X-ray tomography. Images of uncompressed GDL were performed at CEA Grenoble on an industrial tomography system, images of compressed GDL were performed on a synchrotron at the Paul Scherrer Institute (PSI) in Switzerland. The power of the X-ray beam of the synchrotron makes it possible to obtain images that are less noisy than those produced on an industrial tomography system.

The device used at CEA is a Phoenix Nanotom. The images of GDL were realized with a resolution of 1.1 µm. The adjustment parameters of the X-ray source are a voltage of 120kV and a current of 140µA. The offset and gain of the sensor are calibrated to be sensitive to the response peaks of the X-ray material. 2550 images are made by rotating the sample. The acquisition of images takes 90 min. The reconstruction of the 3D image is then carried out automatically by the software of the device. Figure 4.1 shows the images obtained at the CEA.

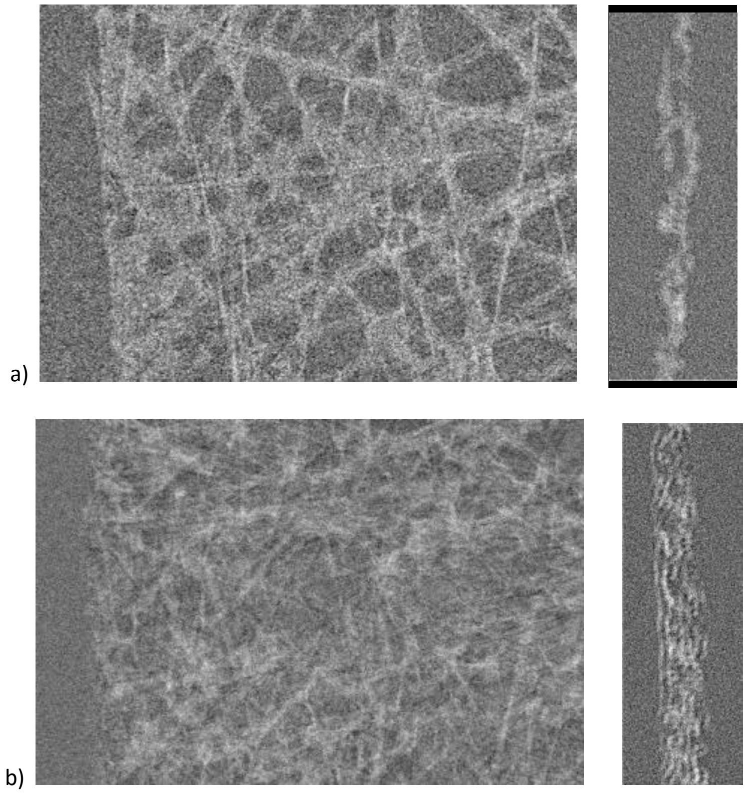

Figure 4.1 Tomographic images of GDL obtained on a CEA industrial tomography system. A) image of uncompressed GDL 24BA (slices). B) GDL image TGP-H-060 uncompressed (slices).

At the Paul Scherrer Institute, images were made on the Tomcat beam of the Swiss Light Source (SLS). The energy of the beam is 13.5 keV, the exposure time is 15 ms per projection and 2001 projections are made by tomography [Lamibrac2016]. The resolution is 2.2 µm for 24BA and TGP-H-060. The image size of 24BA is 1500 * 1500 * 55 voxels, so its physical dimensions are 3.3mm * 3.3mm * 120µm. The image size of TGP-H-060 is 1700 * 1700 * 51 voxels, so its physical dimensions are 3.7mm * 3.7mm * 110µm. The images were made on samples compressed by two membranes [Lamibrac2016] because the initial goal was to visualize an ex-situ water injection experiments. The two membranes described in section 5.1, which penetrate the outer layers of the GDLs, are visible on the images. We cropped the image to keep only the central GDL regions, to remove the upper and lower membranes. The PSI having provided us with images already processed, we can not show here the raw images.

4.1.3 Image segmentation

We describe in this section the methodology used to transform grey scale raw tomographic images into segmented images where each voxel belongs to a well-defined phase: void, fibers or binder. In a first part, we explain the noise filtering and the thresholding process. In a second part, we explain how to differentiate the fibers from the binder, despite the lack of contrast between these two materials in X-ray tomographic images.

4.1.3.1 Segmentation of air and solid

The raw tomographic images are in gray level, so the contrast between two phases is not discrete but continuous. Simulations on 3D images require that each pixel be assigned to a distinct phase, for example air or solid. To change gray levels to a binary value, we use a threshold on gray levels. Indeed, since the gray level represents the absorption level of X-rays in each elementary volume (voxel), we expect that a critical value will make it possible to distinguish the different phases. Nevertheless, the presence of measurement noise and possibly artefacts impose an additional step of cleaning the images.

The procedure for differentiating the air from the solid is similar for the images made by the Paul Scherrer Institute [Lamibrac2016] and the CEA. The noise correction is carried out by an anisotropic diffusion filter, the principle of which is described in the following paragraph. Once the noise is removed, the image is binarized by a threshold. Figure 4.2 illustrates this procedure. We see in the initial image the presence of a noise, that is to say that the gray levels have random fluctuations superimposed on the value related to the absorption of the X-rays by the material. We also see that the anisotropic diffusion filter manages to effectively attenuate the noise while preserving the shape of the regions.

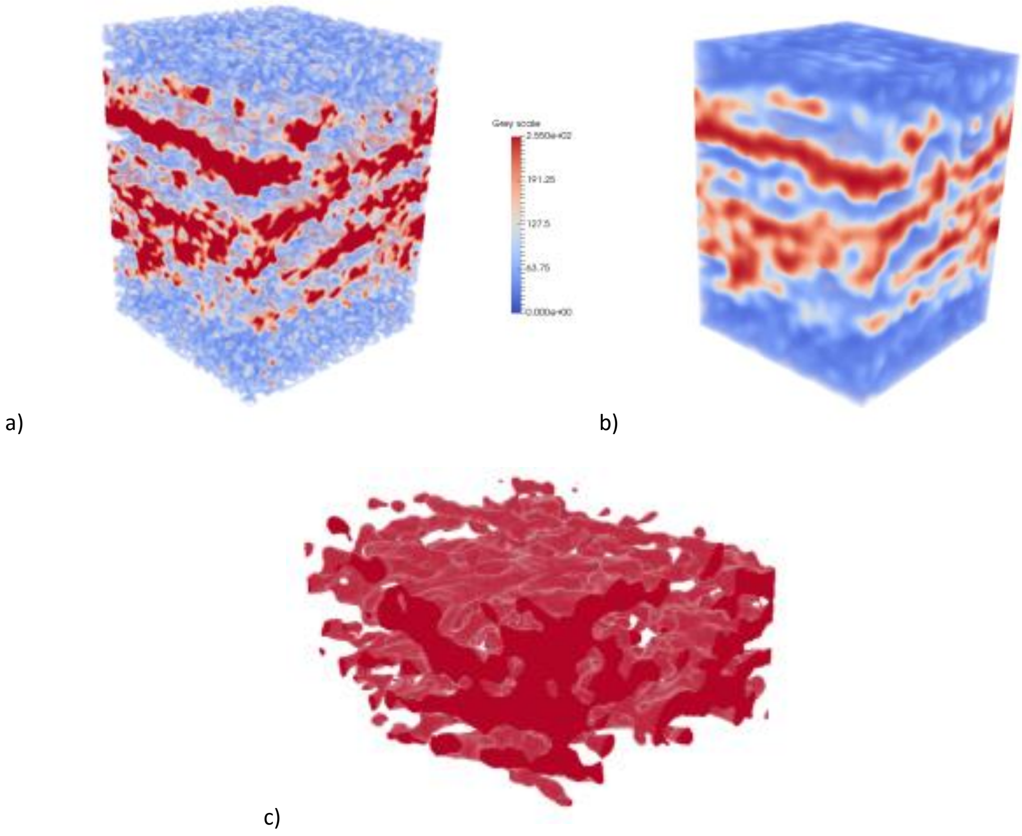

Figure 4.2 X-ray tomographic image of uncompressed TGP-H-060 taken at CEA. A) raw image, with adjusted contrast b) 3D anisotropic diffusion filter applied to the image a. C) solid phase obtained after thresholding of the image b.

The principle of anisotropic diffusion is to reduce the noise while preserving the shape of the regions of the image. The gray levels in the image are smoothed by application of a diffusion process. The diffusion coefficient varies spatially: it is made dependent on the norm of the gradient of the gray levels of the image, so that it vanishes at the boundaries between regions of the image. Indeed, the norm of the gradient makes it possible to identify the boundaries, because at the level of the boundaries there is a jump of the level of gray. As the coefficient of anisotropic diffusion vanishes on the boundaries, the shape of the regions are preserved. Elsewhere than on the borders, that is to say within the regions, the gray levels are smoothed, so the noise is removed. We use the GradientBasedAnisotropicDiffusion function of the ITK python open source library.

Figure 4.3 shows the images used in this chapter after distinguishing between air and solid. The surfaces of the compressed images are not visible in Figure 4.3 because they have been cropped, as explained in the previous section.

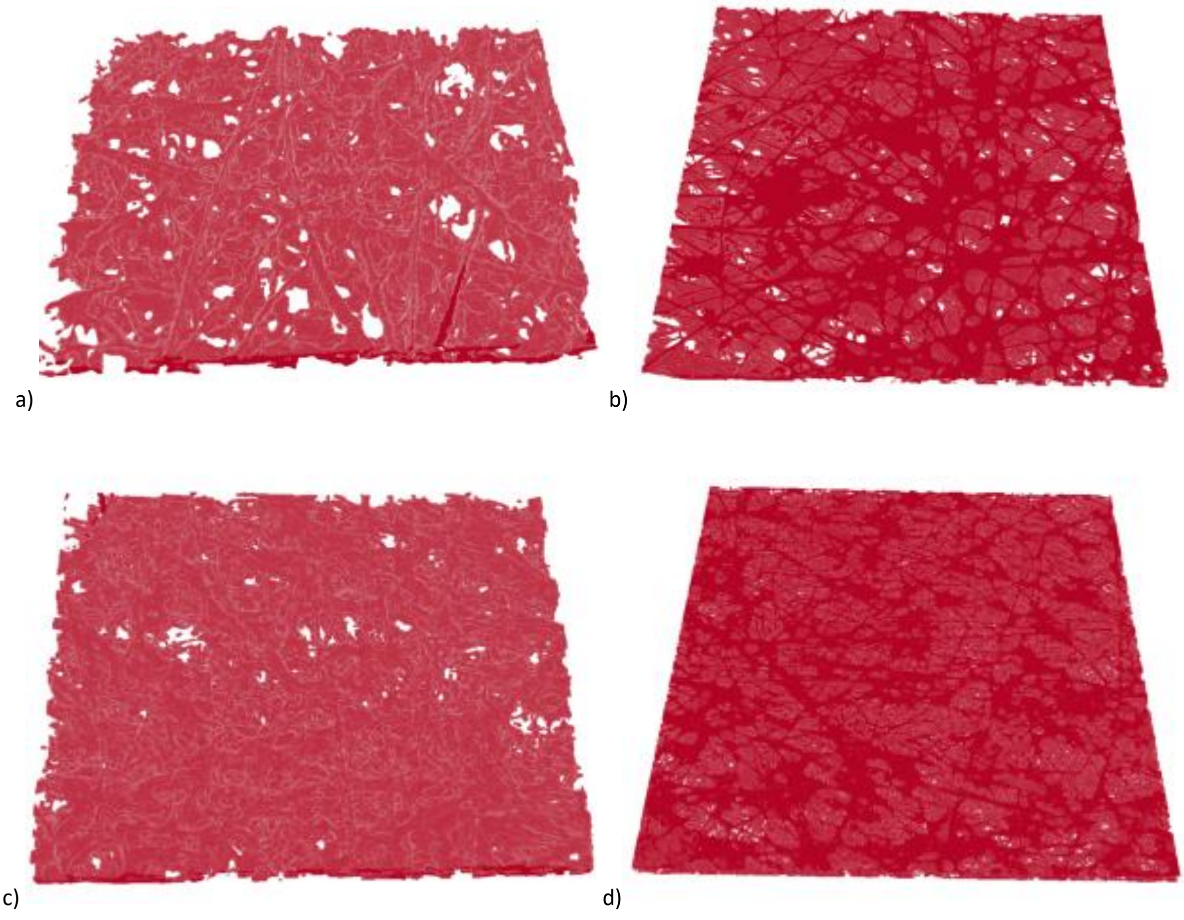

Figure 4.3 Images of GDL after segmentation of air and solid. A) Uncompressed 24BA image b) Compressed 24BA image C) Uncompressed TGP-H-060 image d) Compressed 24BA image. The images a and c were carried out by the CEA on an industrial tomography system. The b and d images were taken by the Paul Scherrer Institute on a synchrotron.

The proportions of solid phase and air obtained after thresholding are listed in Tableau 4-1. Note that the threshold level used can vary the proportion of the phases in the final image. The selection of the threshold can be easy if the gray levels of the two phases are well separated. Unfortunately, the gray scale histograms of the uncompressed GDL images made at CEA did not make it easy to distinguish the different phases. The gray levels of compressed GDL images are published in [Lamibrac2016]. We find that for the images of the uncompressed GDL, the phase proportions obtained do not correspond to the porosities measured experimentally by the GDL manufacturers. Part of this error can be explained by the presence of micropores in the binder, which are not visible on the raw tomographic images because the resolution is too low. However, microporosity alone is not sufficient to explain the error in GDL TGP-H-060 cases. In this cases, the choice of the threshold level and the presence of a strong measurement noise during the acquisition of the images are all sources of errors likely to distort the results. Obtaining binarized images sufficiently close to the real microstructures of GDL on the CEA industrial tomography device therefore requires additional tests.

	Porosity calculated on the image	**Porosity measured experimentally**	**Volume fraction of micropores in the binder**
Uncompressed 24BA	66%	~85%	Significant
Uncompressed TGP-H-060	61%	~80%	Negligible
Compressed 24BA	51%	?	Significant
Compressed TGP-H-060	52%	?	Negligible

Tableau 4-1 Porosity of GDL calculated on images and experimentally measured. The experimental measurements given here are data provided by the manufacturers of GDL.

4.1.3.2 Distinction of binder and fibers

We want to distinguish the binder and fibers phases from the images. Indeed, we want to attribute different transport properties to the voxels of these two phases for the simulations. However, the contrast between these two phases is very low with X-ray tomography. It is very difficult to distinguish them from gray levels.

We try to artificially reconstruct the fibers and the binder using a geometric criterion to distinguish these two phases. We assume that the fibers are thin while the binder is thick. To distinguish the thick regions from the thin regions in the image, we use a tool of mathematical morphology: the morphological opening. The morphological opening consists in consecutively applying an erosion and a morphological dilation of length L. Morphological erosion make disappear all voxels of the solid phase which are located less than L voxels away from of the air phase. We thus make the fibers completely disappear, whereas only a superficial layer of binder is eroded. The morphological dilation then makes the remaining solid phase thicken by a thickness of L voxels. Thus, the binder will regain its initial thickness, but the fibers will have disappeared.

The parameter L is related to the limiting thickness of the elements that we want to make disappear from the image. It is a free parameter, which we will try to calibrate using several methods, depending on the data available on the GDL. One method is to calibrate L from the experimental volume fractions of binder and fibers. Another method is to check visually that the distribution of fibers and the binder is realistic. Another method is to correlate the L parameter to the experimental diameter of the fibers.

Figure 4.4 shows the segmentation obtained by visual analysis. We can see that thin and thick regions can be distinguished. In addition, the binder is located at the intersection of the fibers, which is consistent with the actual microstructure of the GDLs. The result is not perfect nevertheless. The fibers are stopped at the level of the binder packages, whereas in reality they pass through them and measure up to several centimeters in length.

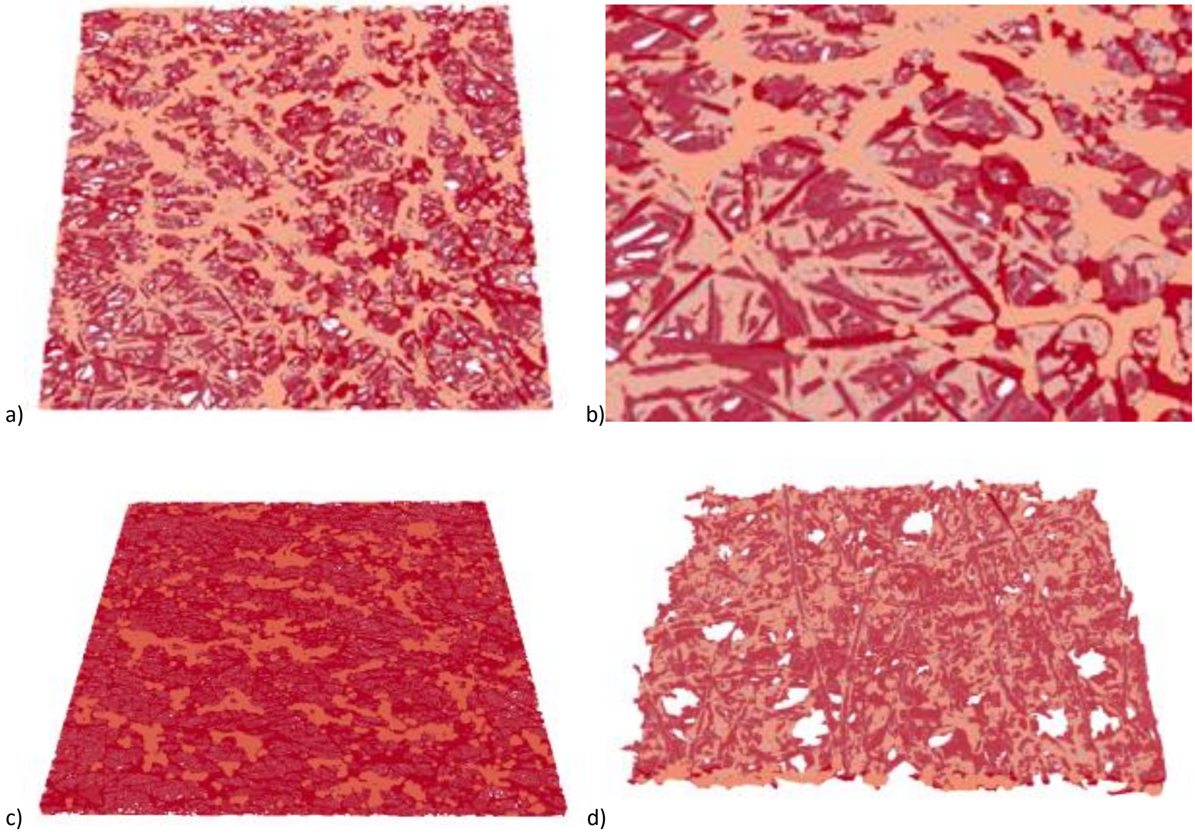

Figure 4.4 A), b): Compressed 24BA images with binder identified by morphological segmentation. Fibers in red, binder in pink salmon. (A) complete sample. B) zoom on the surface of the GDL. C) Images of TGP-H-060 with segmented binder. D) uncompressed 24BA with segmented binder.

The limiting thicknesses that we used to separate fibers and binder are 7 voxels (~ 15µm) for compressed 24BA, 12 voxels (~ 13µm) for uncompressed 24BA, 9 voxels (~ 20µm) for compressed TGP-H-060, 18 voxels (~ 20 µm) for uncompressed TGP-H-060. These limiting thicknesses were determined by visual analysis. The volume proportions of binder in the solid obtained with these limiting thicknesses were 31% for the compressed 24BA, 71% for the uncompressed 24BA, 23% for the compressed TGP-H-060, 41% for the uncompressed TGP-H-060. Experimental data on the volume fraction of binder and fibers in the GDLs would make it possible to better parameterize the limiting thickness parameter of this algorithm of artificial reconstruction of the fibers and of the binder in the solid phase of the GDLs.

To compare the transport simulations on these microstructures with experimental measurements of porosity-dependent transport properties, it is necessary to know the total porosity of the sample. The porosity of the binder is an important parameter for determining the total porosity of the sample. In fact, only the porosity due to the macropores is visible on the image, the microporosity of the binder is invisible. For the uncompressed 24BA, the porosity was taken equal to the porosity measured experimentally, 85% [Rashapov2016]. The total porosity is unknown for the compressed 24BA sample. It depends on the level of compression, which we do not know precisely. In this image, the porosity due to the macropores represents 51% of the volume, the binder (see FIG. 4.4) represents 34% of the volume, the fibers 15%. This is consistent with the results of [Fluckiger2008 ElecActa], estimating that 70% of the solid of the 24BA is composed of binder. The microporosity of the binder therefore represents between 0% and 20% of additional porosity, if the porosity of the binder is between 0% and 60%. [Fluckiger2008 ElecActa] evaluates the porosity of the binder at 31%. That is the value we have chosen. We assumed that the binder of the GDL TGP-H-060 is weakly porous. Thus, we have neglected its effect on diffusion and porosity [Rashapov2016]. The porosity of the uncompressed GDL TGP-H-060 was taken equal to the value given by the manufacturer 78% [TorayDataSheet]. The porosity of the compressed GDL TGP-H-060 was taken equal to the volume fraction of air phase in the tomographic image, 52%.

More sophisticated image analysis methods [Gaiselmann2012] could be developed to overcome the limitations of this approach. For example, segmentation by searching the local orientations is conceivable, since there are no a priori preferential orientations of the binder unlike fibers. Nevertheless, morphological opening has the advantage of being a classical tool immediately available. In addition, it is a very fast procedure that takes only 40 seconds, on a single CPU, for the 24BA image. Thus, the morphological opening allows us to distinguish fibers and binder on the GDL image in a simple way and visually conform to the real microstructure.

4.1.4 Ej-Heat direct simulation of diffusive transports

We use in this chapter direct simulations on the microstructures to calculate the effective diffusivities and effective conductivities of GDL from their 3D images. The numerical method used, direct simulation with explicit jumps (EJ-Heat), is described in section 3.1.1.2. We recall that this numerical method consists in solving the stationary heat equation (Équation 2.3), in which the thermal conductivity is supposed independent of the temperature. The temperature is decomposed into a mean value varying linearly in the sample, linked to an imposed temperature gradient, and a deviation around this mean value, for which periodic boundary conditions are imposed. The equation is discretized by finite differences on the voxel grid and resolved numerically. The effective conductivities of the microstructure are then calculated from the simulated temperature field.

We perform simulations on the images of GDL 24BA and TGP-H-060 shown in Figure 4.4 a) d). GDL images being much thiner than wide, it is interesting to also look at the properties of sub-samples. Therefore, we performed additional simulations on subsamples of the compressed GDL 24BA.

4.1.5 Bulk transport properties of materials constituting the GDL

As described in the previous sections, we want to calculate the effective conductivities and diffusivities of 3D images of GDL by EJ-Heat simulation. The bulk conductivities and diffusivities of the materials of each phase are required parameters for these simulations. This section is devoted to determining these bulk properties.

We recall that a voxel is a cubic volume, whose size is equal to the resolution of the tomography. We assume in this chapter that each voxel is filled by one of the three phases: gas, fiber or binder. It is therefore sufficient to determine the bulk properties of these three phases. For example, to calculate the diffusion of dioxygen or water vapor in the gaseous phase, the required parameter is the intrinsic diffusivity (bulk) of oxygen or water vapor in air. For electrical conductivity, the required parameters are the bulk electrical conductivities of the fibers and of the binder.

4.1.5.1 Binary diffusion coefficients of several gases

The diffusion properties of usual gases are tabulated in the literature. Table 4.1 lists the binary diffusion coefficients of the main gases that may be in a GDL [DeWitt]. The diffusion in ternary mixtures is not taken into account in our model.

Diffusion of substance A into substance B	**H20 in Air**	**H2 in Air**	**02 in Air**	**H2 in O2**	**H2 in N2**	**02 in N2**
Binary diffusion coefficient $m^2.s^{-1}$ (at 1 atm)	$0.26{\times}10^{-4}$ (at 298K)	$0.41{\times}10^{-4}$ (at 298K)	$0.21{\times}10^{-4}$ (at 298K)	$0.70{\times}10^{-4}$ (at 273K)	$0.68{\times}10^{-4}$ (at 273K)	$0.18{\times}10^{-4}$ (at 273K)

Table 4.1 Binary diffusion coefficients of gases likely to be present in GDL [DeWitt].

We parameterize the diffusion in the binder by a parameter, the effective diffusivity of the binder. There is also a microporosity in the GDL binder, but the resolution of the image is too coarse to see these micropores. Indeed, we estimate that the size of the micropores is about 0.05 µm. These pores are much smaller than the macropores visible in the image, but since the effective diffusivity is related to the porosity and not to the pore size, the effective diffusivity of the binder is potentially not negligible if its porosity is high. The diffusivity and porosity of the binder are unknown at this stage. They depend on the type of GDL. It is conceivable to experimentally measure the diffusivity of the binder. Another possibility would be to image the binder microstructure by X-ray or FIB-SEM tomography and then simulate the diffusion of gas in these 3D images. A resolution of a few tens or hundreds of nanometers is required for this.

The Knudsen effect is not considered in our model because it is negligible in the pores of the GDL visible on the image. Let us justify this point. The importance of the Knudsen effect can be evaluated by the ratio between the pore diameter D and the mean free path of oxygen λ. At standard temperatures and pressures, $\lambda = 0.07\mu\mathrm{m}$. The molecular diffusion is dominant at $D > 100\lambda$, the diffusion of Knudsen is dominant at $D < 0.1\lambda$, whereas these two types of diffusion occur between the two [He2014]. Thus, Knudsen diffusion does not occur for macropores of GDL ($D > 10\mu\mathrm{m}$) which are the pores that can be seen on tomographic images. In the absence of data on the pore size of the binder, we assume that they are micropores whose sizes D are between 0.5 µm and 0.05 µm. A mixture of molecular diffusion and Knudsen diffusion can occur in these micropores. This mixed diffusion effect can be taken into account in the effective diffusivity parameter of the binder [Becker2011].

4.1.5.2 Electrical conductivity of bulk materials

The bulk electrical conductivities of some common materials are tabulated in the literature. Table 4.2 lists bulk electrical conductivities of the usual GDL materials.

Material	**Carbon fibers (based on PAN) before graphitization**	**Air**	**PTFE**
σ bulk (300K) $S.m^{-1}$	61 000 ([Walsh])	10^{-15} ([Kamsali2009])	$> 10^{-20}$ ([DuPontPTFE])

Table 4.2 Bulk electrical conductivities of some materials composing a GDL.

However, the manufacturing processes applied to the material can significantly alter their conductivity. The electrical conductivities of solids depend on the exact nature of the material. This is particularly the case for the carbon fibers used in GDLs. A graphitization treatment is applied to the carbon materials of the GDLs to increase their electrical conductivity. Chemical treatments can also affect the electrical properties of fibers. The data in the literature thus give only an imprecise estimate of the actual bulk conductivity of the fibers in the GDL.

The conductivity of the binder is completely unknown at this stage. The exact composition of the binder is not well known. It depends on the type of GDL and is often an industrial secret of the manufacturer. It is nevertheless reasonable to assume that the binder is less electrically conductive than the carbon fibers because it is a more amorphous material containing less conductive chemical species.

At this stage, there is therefore considerable uncertainty as to the electrical properties of the fibers and of the binder. More detailed data on the materials used in GDL are therefore required. A perspective is to measure the conductivities of materials directly extracted from a GDL.

4.2 Results

4.2.1 Experimental validation of simulations

This section presents the comparisons between the effective properties of GDL obtained by experimental characterizations published in the literature and calculated by direct simulations on tomographic images. The aim is to validate whether the simulations succeed in predicting the experimental values.

All the values of the effective properties given in this section are normalized by the lengths of the sample and by the intrinsic conductivity of a phase - the effective diffusivity of the oxygen in the GDL is normalized by the binary diffusion coefficient of oxygen in air, the effective electrical conductivity is normalized by the intrinsic conductivity of the fibers.

4.2.1.1 Effective diffusivities

We compute by direct simulation, with the EJ-Heat method, the effective diffusivity of the GDL images shown in Figure 4.1. Figure 4.5 shows the deviation around the mean simulated concentration field on the microstructure of a compressed 24BA sample. The effective through-plane diffusivity is calculated from this field.

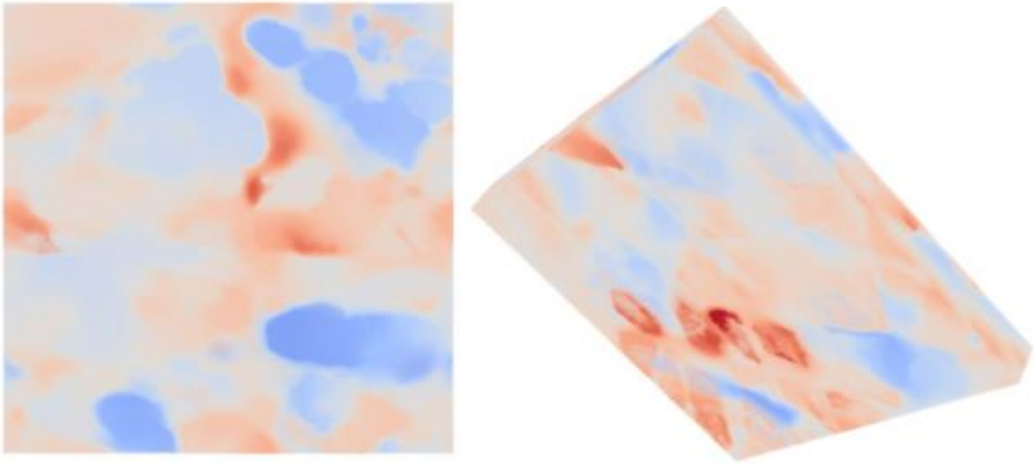

Figure 4.5 Images of the deviation around the mean concentration field, simulated on the microstructure to calculate the through-plane diffusivity. The microstructure is obtained by X-ray tomography on a compressed 24BA subsample. The colors represent the deviation from the average concentration field. Color code: dark red = high value, dark blue = low value.

4.2.1.1.1 GDL TGP-H-060

Figure 4.6 a) shows simulated values of the in-plane effective diffusivity of GDL TGP-H-060. We neglected the effect of the binder on the diffusion and the porosity of the sample [Rashapov2016]. The results obtained show that the simulations are close to the experimental results. The simulated through-plane diffusivity is very close to the experimental value. The simulated in-plane diffusivity is 20% lower than the experimental value. This is considered a good agreement because the difference can be explained by the spatial variability of properties (see the section of this chapter and the appendix devoted to this point).

Figure 4.6 b) shows the sensitivity of the effective diffusivity of GDL TGP-H-060 to the bulk diffusivity of the binder. On this curve, the diffusivities are normalized by the bulk diffusivity of the macropores. We find that the diffusivity of the binder can vary the effective diffusivity by about 50%.

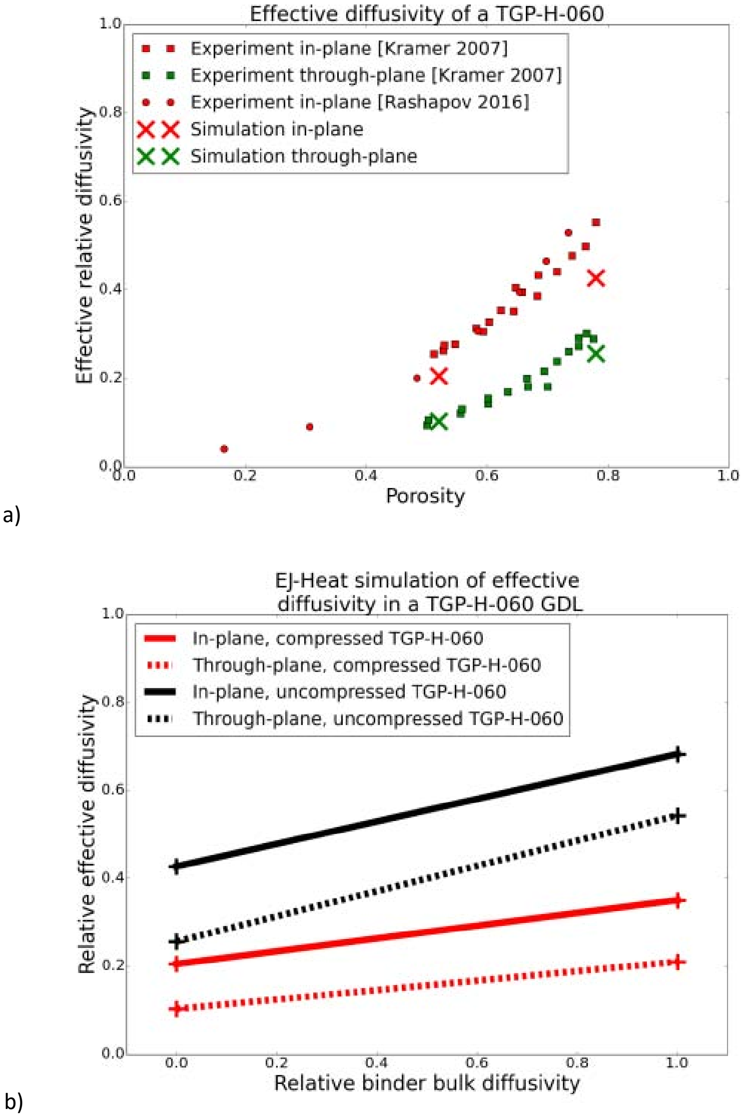

Figure 4.6 Effective relative diffusivity of a Toray H-060. A) Comparison between experiment and simulation for in-plane and through-plane effective diffusivities Figure created by the author from data in [Rashapov2016], [Kramer2008] b) Sensitivity of the simulations to the bulk diffusivity of the binder.

These results suggest that EJ-Heat simulations on tomographic images correctly predict the effective diffusivity of TGP-H-060 GDLs. These results also tend to indicate that the binder of this type of GDL has negligible bulk diffusivity. However, more data is required to ensure the reliability of these findings. Indeed, the properties of the binder had to be calibrated based on very few data from the literature.

4.2.1.1.2 GDL 24BA

Figure 4.7 a) shows comparisons between simulations and experimental characterizations for the effective diffusivity of GDL 24BA. For these simulations, two parameters are unknown: the porosity of the binder and its bulk diffusivity. We have taken the normalized bulk diffusivity of the binder equal to 0, according to [Rashapov2016], according to which the contribution of the binder to the total diffusivity is negligible.

Under these assumptions, Figure 4.7 a) shows the simulated values of diffusivity. The simulations are close to experimental results for in-plane diffusivity. The simulations for the two compression levels deviate from the experimental value by less than 25%. This is considered a good agreement, given the uncertainty about the diffusivity of the binder and the statistical variability of the samples. The uncompressed sample in particular is small therefore its properties are sensitive to the random variability of the microstructure. The through-plane diffusivity of 24BA could not be compared to experimental characterizations due to lack of experimental data. The simulations indicate that the ratio between through-plane and in-plane diffusivities is 0.8 for the compressed sample and 0.6 for the uncompressed sample. This suggests that the in-plane diffusivity decreases more than the through-plane diffusivity during the compression.

Nevertheless, there is a fairly large uncertainty due to the lack of data on the porosity and the bulk diffusivity of the binder. Figure 4.7 b) shows the sensitivity of the effective diffusivity of the compressed 24BA to the bulk diffusivity of the binder. On this curve, the diffusivities are normalized by the bulk diffusivity of the macropores. We note that the diffusivity of the binder can vary the simulated effective diffusivity from one to two. This leads to considerable uncertainty in the simulations. It is therefore important to have reliable information on this bulk diffusivity. Another consequence of these simulations is that it is possible to significantly increase the effective diffusivity of the GDL by increasing the diffusivity of the binder.

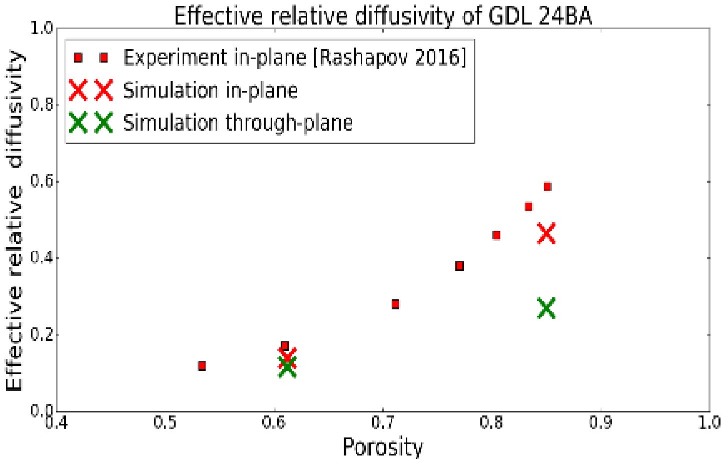

a)

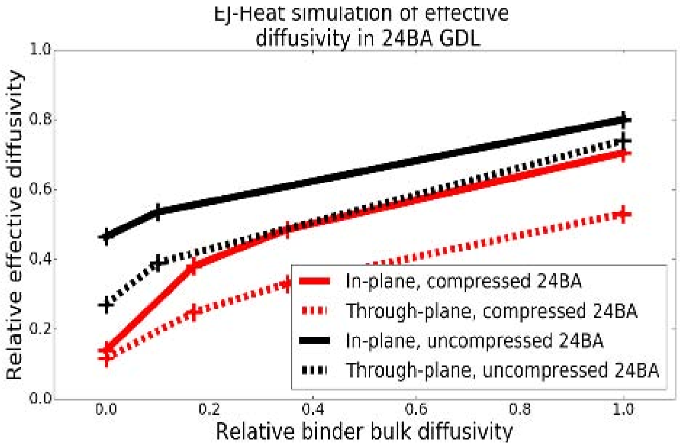

b)

Figure 4.7 Relative effective diffusivity of a GDL 24BA. A) Comparison between experiment and simulation for in-plane and through-plane effective diffusivities Figure created by the author from data in [Rashapov2016] b) Sensitivity of the simulations to the bulk diffusivity of the binder.

These results tend to indicate that the EJ-Heat simulations on tomographic images make it possible to predict the effective diffusivity of the GDL 24BA with an error of less than 25%. These results also tend to indicate that the binder has a significant porosity but a low bulk diffusivity. Low diffusivity may be due to poorly connected pores, high tortuosity or constrictivity. These indications could be verified by experimentally measuring the properties of the binder: its volumic fraction, its porosity and its bulk diffusivity.

In conclusion, the Ej-Heat simulation on tomographic images makes it possible to reliably calculate the effective diffusivities of GDL 24BA and TGP-H-060. We were able to evaluate the bulk diffusivity of the binder by comparing the simulation results and the experimental characterizations of effective diffusivity. The properties of the binder induce a moderate uncertainty in the simulations which could be decreased by collecting more data on the binder. Thus, this methodology has an important potential to study the properties of the GDL and the materials that compose them.

4.2.1.2 Effective electrical conductivities

We compute by EJ-Heat simulations the effective electrical conductivity for the GDL images shown in Figure 4.1. Figure 4.8 shows the deviation around the mean electrical potential field simulated on the microstructure of a compressed 24BA sample, and from which the effective electrical through-plane conductivity is calculated.

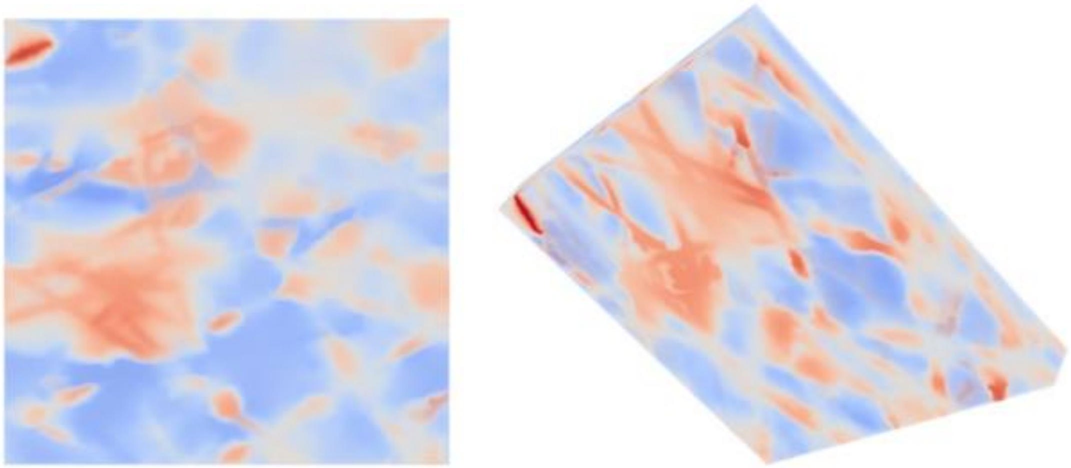

Figure 4.8 Images of the deviation around the mean electric potential field simulated on the microstructure to calculate the through-plane electrical conductivity. The microstructure is obtained by X-ray tomography on a compressed 24BA subsample. The colors represent the deviation from the mean electrical potential. Color code: dark red for high values, dark blue for low values.

Electrical conduction occurs in the solid phase, composed of fibers and binder. Two parameters must be fixed: the bulk conductivity of the fibers and the bulk conductivity of the binder. The conductivity of the fibers is taken to be 61000 S/m, per section 4.1.5.2. The conductivity of the binder is unknown, so a sensitivity study is made on this parameter.

4.2.1.2.1 GDL TGP-H-060

Figure 4.9 (a) shows comparisons between simulations and experimental characterizations for the effective in-plane and through-plane electrical conductivities of GDL TGP-H-060. The simulation results are given for two binder conductivities: a binder as conductive as the fibers and a fully insulating binder. We note agreements but also discrepancies between simulations and experience.

The calculated in-plane effective conductivity is compatible with the experimental values, with a deviation of less than 20% if the binder is as conductive as the fibers. Note that this difference is decreased if the conductivity of the fibers is taken higher, which is realistic knowing that we did not consider the graphitization of the fibers. The segmentation of the fibers and the binder may also reduce the simulated in-plane conductivity because the algorithm used cuts the fibers at the level of the binder clusters. In order to conclude more precisely on the validity of these simulations, priority should be given to reducing the uncertainty on the properties of the binder and the fibers.

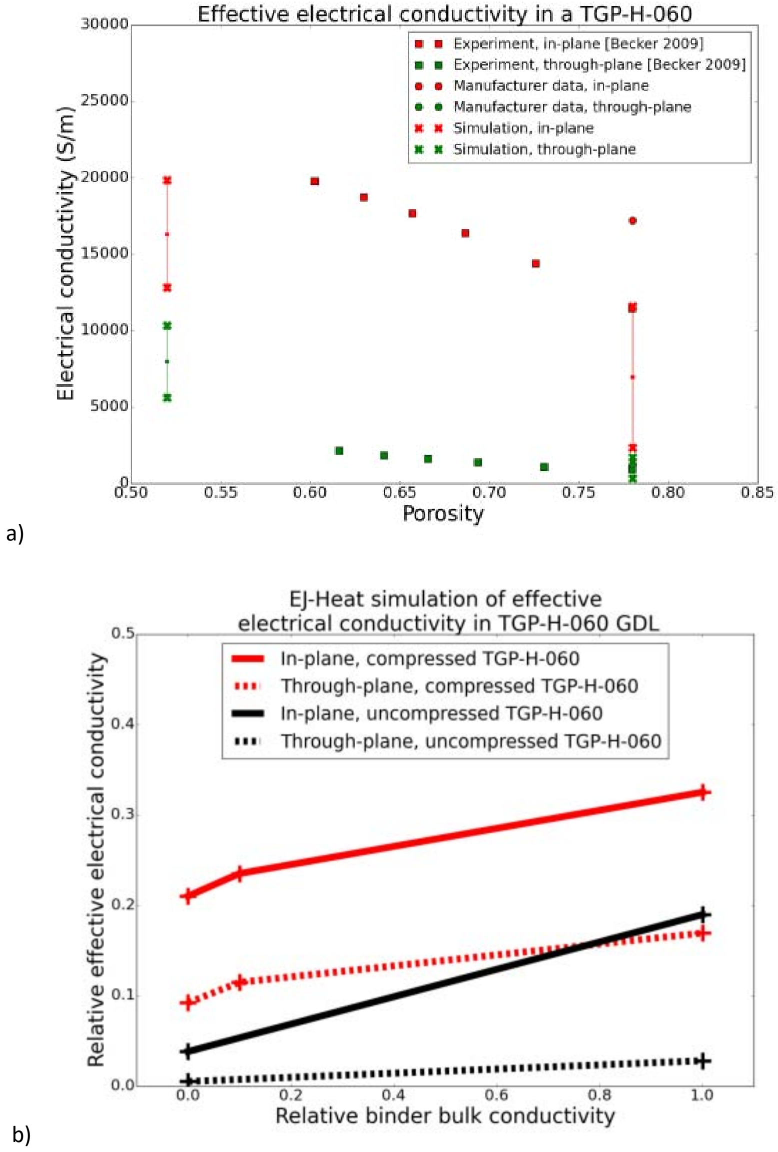

Figure 4.9 Effective electrical conductivity of GDL TGP-H-060. A) Comparison between experiment and simulation for in-plane and through-plane effective electrical conductivities. Figure created by the author from data in [Becker2009] b) Sensitivity of the simulations to the bulk conductivity of the binder.

The effective through-plane conductivity is overestimated by simulations, for compressed GDL. The simulated values are 2 to 3 times higher than the experimental values. The origin of this divergence is unknown. These could be differences in the boundary conditions between experience and simulation. Indeed, the electrical conductivity is measured by pressing electrodes on the GDL. The deformations of the fibers and the points of contact with the electrode may have an important influence on the electrical measurement. This point could be evaluated by simulations on tomographic images of GDL compressed by electrodes [Tötzke2014]. Another hypothesis is that additional electrical resistances should be introduced into the model. A model of contact resistance between fibers and binder is presented in section 7.1.3. The error on the through-plane conductivity is less pronounced for uncompressed GDL. This could come from different electrical contacts for simulations. These contacts depend on the cropping level of the upper and lower layers of the image.

Figure 4.9 b) shows the sensitivity of the effective conductivities to the bulk conductivity of the binder. On this curve, the conductivities are normalized by the conductivity of the fibers. We observe that the anisotropy of the simulated electrical tensor is between 0.4 and 0.5, whatever the conductivities of the fibers and the binder. In contrast, experimental anisotropy is about 0.1. This confirms the conclusions of the previous paragraphs on the limitations of electrical simulations.

These results suggest that direct simulations on tomographic images make it possible to predict reasonable values for the in-plane electrical conductivity of TGP-H-060 GDLs. Better knowing the properties of the binder and the fibers would make it possible to more precisely validate these simulations. However, the simulations give a significant error on the effective through-plane conductivity. We should improve our physical understanding of the through-plane electrical conductivity.

4.2.1.2.2 24BA GDL

Figure 4.10 a) shows comparisons between direct simulations on the microstructure and experimental characterizations for the effective in-plane and through-plane electric conductivity of GDL 24BA. Characterizations were made at the CEA in a previous project (CHAMEAU), using the 4-point measurements method.

The bulk electrical conductivity of the binder is an unknown parameter. Thus, simulation results are given for two binder bulk conductivities: a binder as conductive as fibers and a fully insulating binder. We find that the simulated effective conductivities can vary by a factor of 20 depending on whether we are in either case. This is also visible in Figure 4.10 b), which shows the sensitivity of the effective conductivities to the bulk conductivity of the binder. On this curve, the conductivities are normalized by the conductivity of the fibers. It is therefore essential to characterize experimentally the bulk conductivity of the binder in order to reduce this uncertainty.

Experimental in-plane conductivity is at the center of the range of simulated conductivity for both compression levels. This suggests that in-plane simulations are consistent with the experimental measurements. Nevertheless, it is essential to reduce the uncertainty on the electrical properties of the binder and the fibers in order to be able to conclude more precisely on the validity of these simulations.

The through-plane conductivity is overestimated by the simulations. For the compressed 24BA, the simulated values are 2 times higher than the experimental values in the most favorable case, consisting of a fully insulating binder. The difference increases to a factor of 30 if we consider a moderately conductive binder. This indicates that this model does not adequately estimate the through-plane electrical conductivity, or that the experimental characterization is defective. This is confirmed by the examination of the anisotropies. We find that the simulations give a ratio between in-plane conductivity and through-plane conductivity between 0.1 and 0.3, whatever the conductivities of the fibers and the binder. In contrast, the experimental measurements give a ratio between 0.01 and 0.05. It should be noted that the through-plane conductivity is very sensitive to electrical contacts between measuring electrodes and GDL. This can be seen, for example, during the experimental measurement: the GDL must be compressed by the electrodes so that the current flows. This is the reason why the experimental point corresponding to the minimum compression level was realized with a compression of 1 MPa.

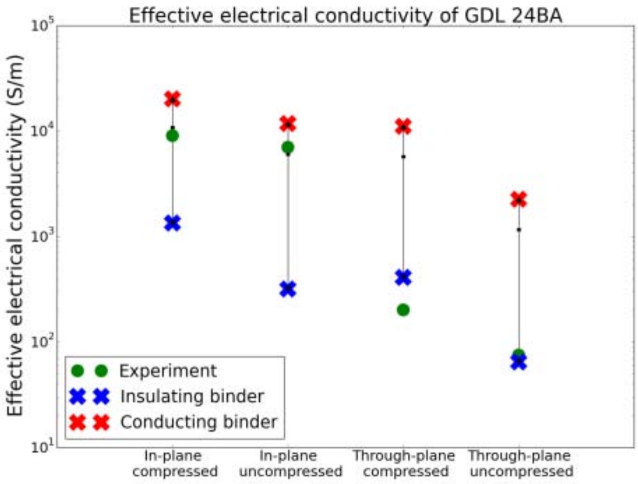

a)

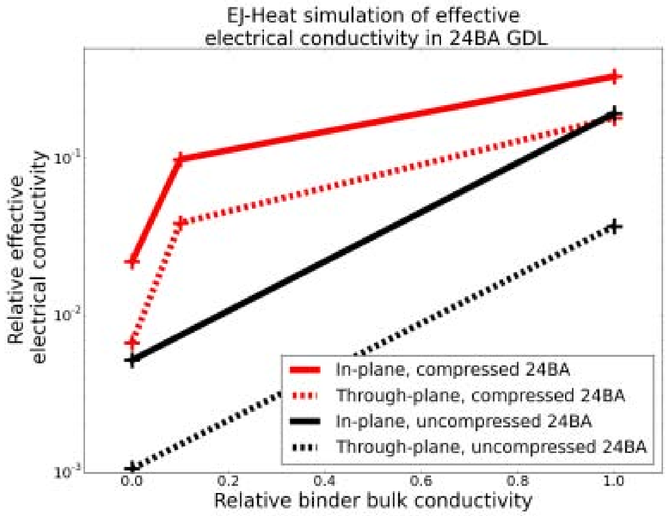

b)

Figure 4.10 Effective electrical conductivity of GDL 24BA. A) Comparison between simulations and experimental measurements. The experimental points were carried out at the CEA at 1 MPa and 5 MPa. The simulations were carried out with a binder conductivity either equal to zero or equal to the conductivity of the fibers (61000 S / m). B) Sensitivity of the simulations of effective electrical conductivity with respect to the bulk conductivity of the binder.

These results indicate that EJ-Heat electrical simulations on 24BA tomographic images are subject to a high uncertainty related to the properties of the binder and fibers. The in-plane conductivities are in the correct order of magnitude, but strongly depend on the conductivity of the binder. On the other hand, the simulations give an important error on the through-plane conductivity. We should improve our physical understanding of the through-plane conductivity, for example by studying the effect of GDL / electrode contacts and the effect of PTFE..

In conclusion, the direct simulation on tomographic images makes it possible to calculate the in-plane effective electrical conductivities of the GDL 24BA and TGP-H-060 with a correct order of magnitude. The properties of the fibers and the binder should be determined more precisely in order to reduce the margin of error. However, the simulations of through-plane electrical conductivities give values very different from the experimental measurements. We provide additional information on this point in the discussion section.

4.2.2 Additional simulation results

4.2.2.1 Spatial variability of GDL transport properties

We study in this section the spatial variability of the microstructure and the effective transport properties of a GDL 24BA, to characterize the inhomogeneities of the material. This is important because the notion of representative elementary volume is doubtful for GDL. Indeed, the GDL have less than a dozen pores in thickness. Moreover, these are thin media produced on very high surfaces, so local variations are likely during manufacturing.

Figure 4.11 shows the porosity of compressed 24BA sub-samples as a function of their in-plane width. The samples are parallelepipeds centered on the center of the overall sample. Their thickness is equal to the complete thickness of the GDL (120 µm) and their two in-plane dimensions are equal. We observe that the porosity varies with the width of the sample, even for larger samples. This variability of the porosity shows that 3.3 mm of width is not sufficient to have a representative elementary volume.

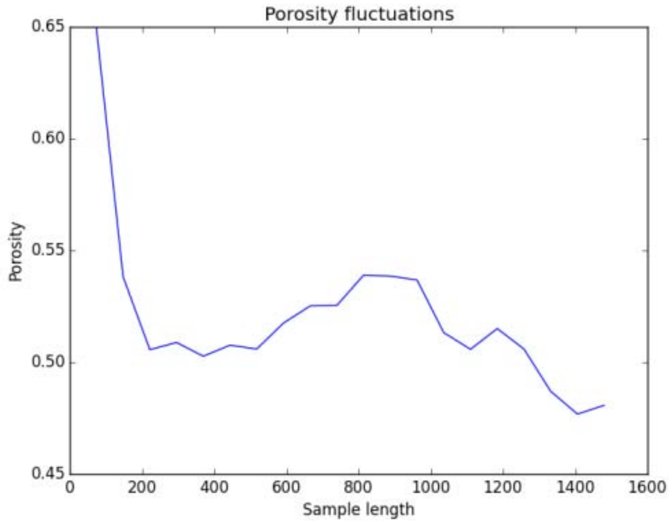

Figure 4.11 Porosity of sub-samples of 24BA whose size varies. The width of the sample on the abscissa is given in number of voxels. The size of a voxel on this image is 2.2µm.

We study the spatial variability of effective diffusivity and electrical conductivity. These properties are calculated by EJ-Heat simulations on 9 sub-samples of the compressed GDL 24BA. Figure 4.12 shows how these samples are obtained from the complete image.

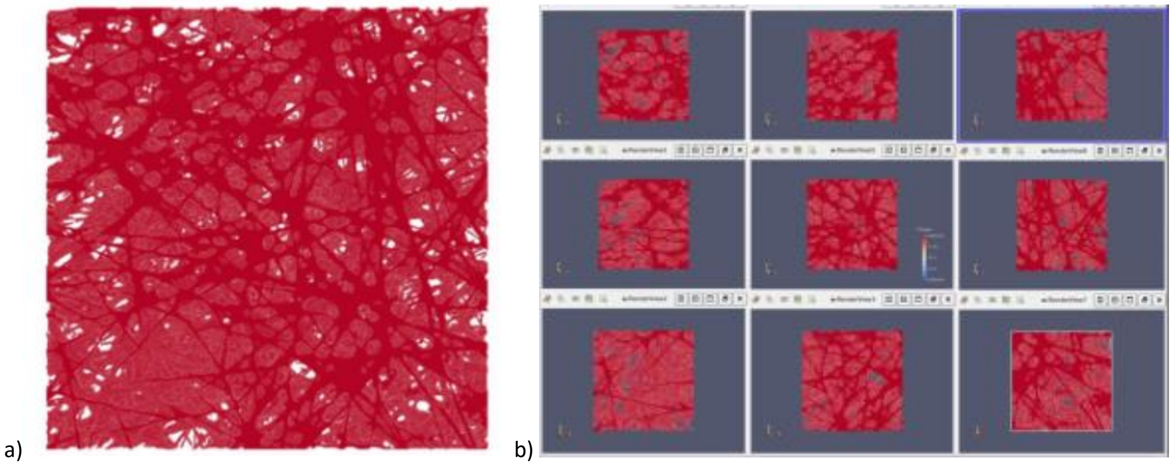

Figure 4.12 a) Image of GDL 24BA. B) 9 sub-samples of this image, decomposed per a 3 * 3 grid.

Figure 4.13 a) shows the effective electrical diffusivities and electrical conductivities of the sub-samples. We find that variability is important. Indeed, the relative diffusivity varies by a factor 3, the relative conductivity varies by a factor 2. The samples are however relatively large: they are parallelepipeds of 1.1mm of side and 120µm of thickness. Their ratio between width and thickness is greater than 10.

Figure 4.13 b) and c) show correlations between effective properties and the porosity of the sample. The aim is to test if the porosity alone makes it possible to explain the effective properties, which would allow to have a reduced model to calculate the transport properties as a function of the porosity. The linear correlation between conductivity and solid fraction makes it impossible to explain some conductivity values (for example for the solid fraction sample 0.47). The linear correlation between diffusivity and porosity is better than that for conduction. Nevertheless, there are fluctuations unexplained by this correlation (differences of 20% to 30% for the pairs of samples whose porosity is 0.5, 0.53, 0.55). The porosity is thus not a sufficient parameter to explain the effective transport properties of the GDLs.

In conclusion, simulations on tomographic images make it possible to study the spatial variability of the transport properties of GDL. The effective properties of conductivity and diffusivity can vary by a factor 3 from one sample to another, even for samples as large as 1mm². It would be interesting to study the effect of this variability on the performance of the fuel cells. Appendix 9.2 presents a simple theoretical framework for modeling the spatial variability of GDL transport properties and its effect on fuel cells performance.

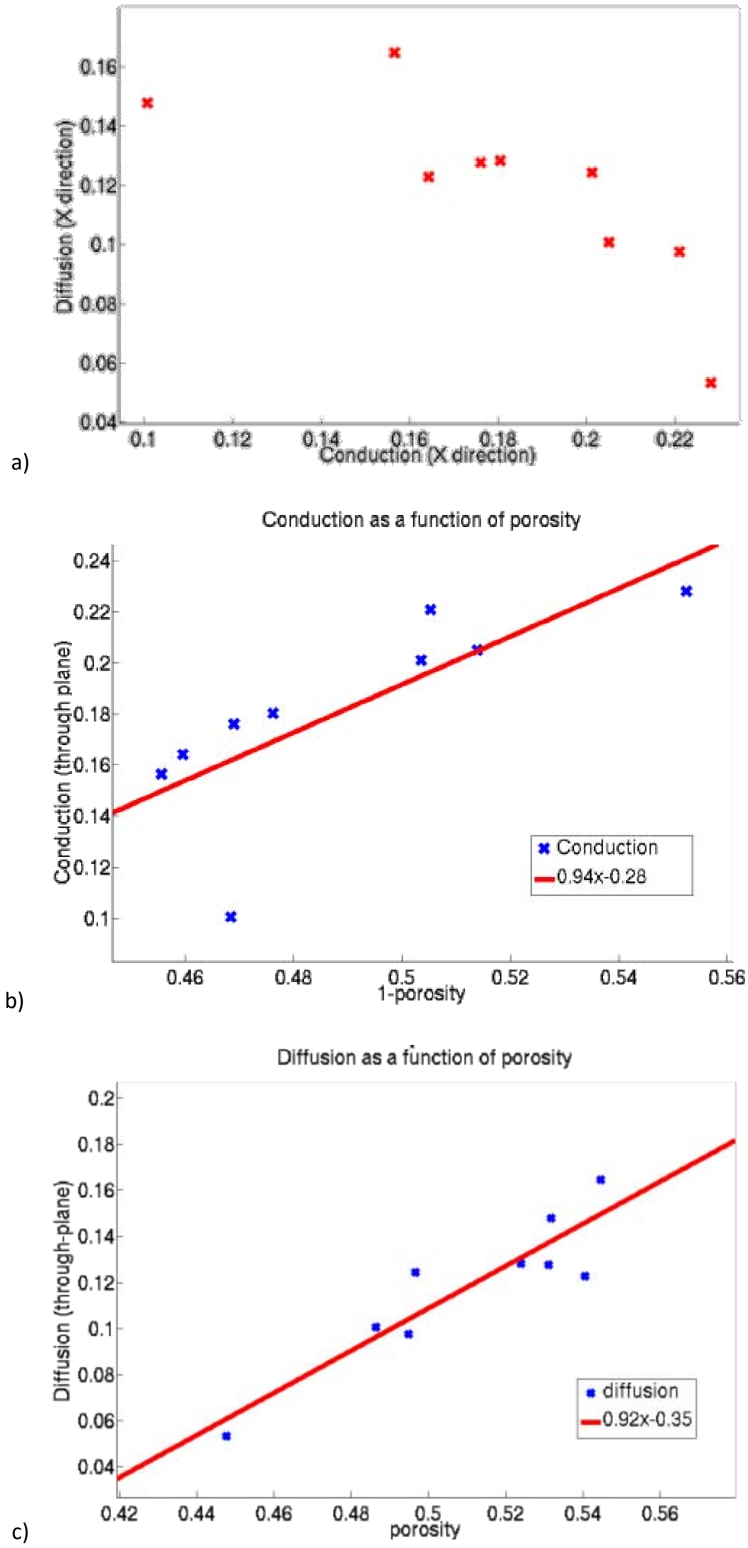

Figure 4.13 Effective through-plane properties of compressed GDL 24BA subsamples. A) effective diffusivity as a function of the effective conductivity. B) effective conductivity as a function of the solid fraction in the sample. C) effective diffusivity as a function of the gas fraction of the sample.

4.2.2.2 Diffusivity of a GDL completely invaded by liquid water

The aim of this section is to illustrate the flexibility of simulations on tomographic images. We simulate diffusivity on compressed GDL images, assuming that the macropores of the GDL are filled with water. We thus want to model a GDL invaded by liquid water. Flooding can occur when a lot of water is produced by the battery (i.e. with high current density) and the air is very wet.

We suppose that the micropores of the binder are not filled with water because they are hydrophobic and smaller than the macropores. The diffusion of gas into the GDL invaded by liquid water thus takes place only in the pores of the binder. The diffusivity of the voxels of the macropores and of the solid phase is taken equal to 0.

For the compressed TGP-H-060, the diffusion simulations give: $\frac{D_{eff}^{through-plane}}{D_{binder}} = 7 * 10^{-3}$, $\frac{D_{eff}^{in-plane}}{D_{binder}} = 0$

For the compressed 24BA, the diffusion simulations give: $\frac{D_{eff}^{through-plane}}{D_{binder}} = 6 * 10^{-2}$, $\frac{D_{eff}^{in-plane}}{D_{binder}} = 8 * 10^{-2}$

We find that effective diffusivity is very low in this extreme case where all the macropores are filled with water. Thus, diffusion in the binder alone does not make it possible to ensure the operation of a fuel cell when the GDL macropores are completely invaded by liquid water.

Note that assuming that the macropores of the GDL are totally filled with water is an extreme case that is unlikely in practice. A more in-depth study of the effect of liquid water on the transport properties of GDL was carried out in [Zamel2011].

4.3 Discussion

The simulations of the effective transport properties of GDL provide results comparable to the experimental characterizations except for the effective through-plane conductivities. We discuss here what might explain this difference.

A first hypothesis concerns the effect of electrical contact resistances between the GDL and the measuring electrodes. It is possible that this effect is considered differently in the experimental measure and the model based on a tomographic image. This contact resistance effect is particularly important for batteries in operation: the contact resistance between the GDL and the bipolar plate is greater than the through-plane resistance of the GDL. The level of compression of the bipolar plate on the GDL greatly influences this contact resistance. This effect was studied experimentally in [Nitta2007]: the contact resistance and the through-plane conductivity of GDL SGL 10BA were distinguished by varying the thickness of GDL measured. The electrical anisotropy measured in this article is 3 or 4, which is compatible with our simulations. Another approach would be to image by X-ray tomography the interface between the GDL and the bipolar plate to make simulations with the right boundary conditions and the correct deformation of the fibers. The contacts between the bipolar plate and the fibers were modeled in [Avasarala2008], [Zhou2007], considering the roughness of the bipolar plates.

The issue of boundary conditions also arises in image simulations. Indeed, some thickness of the images must be cropped so that the fibers touch the edge of the image, to prevent a layer of insulating air from decreasing the effective conductivity.

A second hypothesis is that the PTFE deposited on the surface of the GDLs would be responsible for an additional electrical resistance in the through-plane direction [Sadeghifar2014]. PTFE is a highly insulating material, so a layer of PFTE on the surface of the fibers could have an important effect. Note that the surface of the image of the compressed GDL 24BA had to be removed, as discussed above. PTFE is therefore not visible in this image. We study numerically in Section 7.1.3 the effect of PTFE located between the GDL fibers.

4.4 Conclusion

In this chapter, we simulated the effective diffusivity and the effective electrical conductivity of several GDLs using EJ-Heat simulations on 3D tomographic images. We compared the results with experimental data from the literature to validate the modeling. Two different types of GDL and two compression levels were studied.

The bulk transport properties of the materials constituting the GDL are essential parameters for calculating the effective properties. Bulk transport of the porous phase is the simplest to model because the diffusion properties of the gases are well known. On the other hand, the bulk electrical properties of the fibers and of the binder must be better characterized experimentally. The transport properties of the solid materials depend on the nature of the materials and possibly their microstructure at scales lower than the resolution of the image. They vary from one type of GDL to another.

The lack of contrast between the fibers and the binder is a critical problem in determining the effective electrical properties of the solid phase. We proposed a morphological algorithm to artificially reconstruct these two materials using a simple geometric criterion. This algorithm gives a good first approximation of the spatial distribution of binder and fibers. More elaborate geometric segmentation algorithms are desirable for processing more complex materials.

The effective properties of the porous phase, i.e. effective diffusivity, could be reliably simulated. Indeed, diffusion is controlled largely by macropores, which are well solved by X-ray tomography. The simulations of in-plane electric conductivities in the solid phase have given reasonable results although they are subject to a margin of error due to the uncertainties about the electrical properties of solid materials. On the other hand, simulations of through-plane electrical conductivities systematically overestimate the conductivity compared to the experiments. Indeed, the through-plane electrical conductivity seems to be controlled largely by the contacts between the phases, which are poorly visible by X-ray tomography. A better understanding of the contacts between GDL and measuring electrodes and possibly electrical contact resistances in the GDL core is required to model the electrical through-plane conductivity.

These results show that simulations based on tomographic images are relevant tools for determining the diffusive transport properties of a GDL. Used in conjunction with experimental characterizations, they provide a detailed understanding of transports in GDL. The simulations on 3D images thus have an important potential to understand and improve the porous materials of PEMFC.

4.5 Bibliography

- [Avasarala2008] Effect of surface roughness of composite bipolar plates on the contact resistance of a proton exchange membrane fuel cell B. Avasarala, P. Haldar, J. Power Sources (2008)

- [Becker2009] Jürgen Becker, Reto Flückiger, Mathias Reum, Felix N. Büchi, Federica Marone, and Marco Stampanoni, Determination of Material Properties of Gas Diffusion Layers: Experiments and Simulations Using Phase Contrast Tomographic Microscopy, Journal of The Electrochemical Society, 156 10 B1175-B1181 (2009).

- [Becker2011] Jürgen Becker, Christian Wieser, Stephan Fell, Konrad Steiner, A multi-scale approach to material modeling of fuel cell diffusion media, International Journal of Heat and Mass Transfer 54 (2011) 1360–1368

- [DeWitt] Fundamentals of Heat and Mass Transfer, 5th edition, Incropera & DeWitt

- [DuPontPTFE] DuPont©, Teflon PTFE fluoropolymer resin, Properties Handbook, http://www.rjchase.com/ptfe_handbook.pdf

- [Fluckiger2008 ElecActa] Anisotropic, effective diffusivity of porous gas diffusion layer materials for PEFC Reto Flückiger, Stefan A. Freunberger, Denis Kramer 1, Alexander Wokaun, Günther G. Scherer, Felix N. Büchi * Electrochimica Acta 54 (2008) 551–559

- [Gaiselmann2012] Gaiselmann, G., Manke, I., Lehnert, W. & Schmidt, V. (2012). Extraction of curved fibers from 3D data. Image Anal. Stereol., 32, 57-63.

- [Geodict] A. Wiegmann. GEODICT virtual micro structure simulator and material property predictor. 2001–2010. http://www.geodict.com.

- [He2014] He, Weidong, Lv, Weiqiang, Dickerson, James, Gas Transport in Solid Oxide Fuel Cells, SpringerBriefs in Energy, 2014

- [Kamsali2009] Nagaraja Kamsali, B.S.N. Prasad, Jayati Datta, Atmospheric electrical conductivity measurements and modeling for application to air pollution studies, Advances in Space Research, Volume 44, Issue 9, 2 November 2009, Pages 1067–1078

- [Kramer2008] Denis Kramer, Stefan A. Freunberger, Reto Flückiger, Ingo A. Schneider, Alexander Wokaun, Felix N. Büchi, Günther G. Scherer, Electrochemical diffusimetry of fuel cell gas diffusion layers, Journal of Electroanalytical Chemistry 612 (2008) 63–77

- [Nitta2007] Iwao Nitta, Tero Hottinen, Olli Himanea, Mikko Mikkola, Inhomogeneous compression of PEMFC gas diffusion layer: Part I. Experimental, Journal of Power Sources, Volume 171, Issue 1, 19 September 2007, Pages 26–36

- [Rashapov2015] Rinat R. Rashapov, Jonathan Unno, and Jeff T. Gostick, Characterization of PEMFC Gas Diffusion Layer Porosity, Journal of The Electrochemical Society, 162 (6) F603-F612 (2015)

- [Rashapov2016] Rashapov, R and J.T. Gostick, In-Plane Effective Diffusivity in PEMFC Gas Diffusion Layers, Transp Porous Med (2016). doi:10.1007/s11242-016-0648-4

- [Sadeghifar2014] Hamidreza Sadeghifar, Ned Djilali, Majid Bahrami, Effect of Polytetrafluoroethylene (PTFE) and micro porous layer (MPL) on thermal conductivity of fuel cell gas diffusion layers: Modeling and experiments, Journal of Power Sources 248 (2014) 632-641

- [Tjaden2016] Bernhard Tjaden, Samuel J Cooper, Daniel JL Brett, Denis Kramer, Paul R Shearing, On the origin and application of the Bruggeman correlation for analysing transport phenomena in electrochemical systems, Current Opinion in Chemical Engineering, Volume 12, May 2016, Pages 44–51

- [TorayDataSheet] Toray Carbon Fiber Paper “TGP-H” datasheet, http://fuelcellsetc.com/store/DS/Toray-Paper-TGP-H-Datasheet.pdf

- [Tötzke2014] Three-dimensional study of compressed gas diffusion layers using synchrotron X-ray imaging, C. Tötzke, G. Gaiselmann, M. Osenberg, J. Bohner, T. Arlt, H. Markötter, A. Hilger, F. Wieder, A. Kupsch, B.R. Müller, M.P. Hentschel, J. Banhart, V. Schmidt, W. Lehnert, I. Manke, Journal of Power Sources, Volume 253, 1 May 2014, Pages 123–131

- [Walsh] Paul J. Walsh, Carbon Fibers, ASM Handbook Volume 21, Composites, (ASM International), 35 - 40 (6), 2001

- [Wiegmann1999] Andreas Wiegmann, The explicit jump immersed interface method and integral formulas, Lawrence Berekeley National Laboratory Technical Report, 1999

- [Wiegmann2000] Andreas Wiegmann and Kenneth P. Bube, The Explicit-Jump Immersed Interface Method: Finite Difference Methods for PDEs with Piecewise Smooth Solutions, SIAM J. Numer. Anal., 37(3), 827–862.

- [Wiegmann2006] A. Wiegmann, A. Zemitis, EJ-HEAT: A Fast Explicit Jump Harmonic Averaging Solver for the Effective Heat Conductivity of Composite Materials, Berichte des Fraunhofer ITWM, Nr. 94 (2006)

- [Zamel2011] Nada Zamel, Xianguo Li, Jürgen Becker, Andreas Wiegmann, Effect of liquid water on transport properties of the gas diffusion layer of polymer electrolyte membrane fuel cells, international journal of hydrogen energy 36 (2011) 5466-5478

- [Zamel2013] Zamel & Li, Effective transport properties for polymer electrolyte membrane fuel cells – With a focus on the gas diffusion layer, (review), PECS 2013

- [Zhou2007] Y. Zhou, G. Lin, A.J. Shih, S.J. Hu, A micro-scale model for predicting contact resistance between bipolar plate and gas diffusion layer in PEM fuel cells, Journal of Power Sources, Volume 163, Issue 2, 1 January 2007, Pages 777–783

Chapter 5 Injection of liquid water into a GDL

This chapter is devoted to the modeling of liquid water flows in GDL of PEM fuel cells. We are interested in capillary pressure experiments, which involve injecting water into a GDL to characterize its capillary properties. This type of experiment is described in section 2.2.1.2. We develop two-phase simulations to simulate these experiments, and we validate these simulations using experimental data. This is also a first step in developing the simulation tools used in Chapter 6 to model the condensation of water in a GDL under actual operating conditions of a fuel cell.

The first part of this chapter is an article published in the Journal Of Power Sources (JPS). This paper presents two two-phase models based on tomographic images of a GDL, a pore network model and a full morphology model. These methods allow to simulate liquid water flows in the capillary digitating regime, using a geometric analysis of the microstructures. These models are experimentally validated using tomographic images of the distribution of water in the GDL during the capillary pressure experiment. It should be noted that all the experimental results that we use in this chapter were obtained by the team of F. Buechi (PSI, Switzerland) in the framework of the European project IMPALA.

The second part of the chapter presents additional results on the simulation of capillary pressure curves for two different types of GDL. These results allow to validate the full morphology method on experimental measurements.

5.1 Validation of pore network simulations of ex-situ water distributions in a gas diffusion layer of proton exchange membrane fuel cells with X-ray tomographic images

Journal of Power Sources 331 (2016) 462–474

Contents lists available at ScienceDirect

Journal of Power Sources

journal homepage: www.elsevier.com/locate/jpowsour

Validation of pore network simulations of ex-situ water distributions in a gas diffusion layer of proton exchange membrane fuel cells with X-ray tomographic images

Tristan Agaesse [a], Adrien Lamibrac [d], Felix N. Büchi [d], Joel Pauchet [a], Marc Prat [b, c, *]

[a] CEA, LITEN, LCPEM, F-38054 Grenoble, France
[b] Université de Toulouse, INPT, UPS, IMFT, Avenue Camille Soula, F-31400 Toulouse, France
[c] CNRS, IMFT, F-31400 Toulouse, France
[d] Electrochemistry Laboratory, Paul Scherrer Institut, CH-5232 Villigen PSI, Switzerland

HIGHLIGHTS

- X-ray tomographic images of liquid water in a GDL are compared to simulations.
- Pore network and full morphology simulations reproduced well the water distribution.
- Pore network extraction parameters were benchmarked using full morphology.

GRAPHICAL ABSTRACT

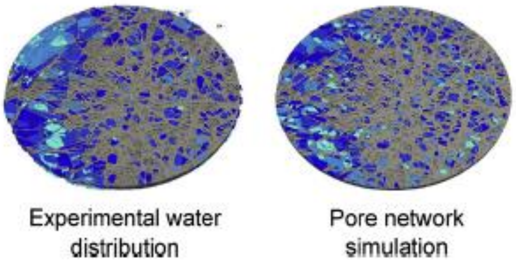

ARTICLE INFO

Article history:
Received 6 July 2016
Received in revised form
24 August 2016
Accepted 13 September 2016

Keywords:
Polymer electrolyte membrane fuel cell
Gas diffusion layer
X-ray tomographic microscopy
Pore network
Full morphology
Liquid water

ABSTRACT

Understanding and modeling two-phase flows in the gas diffusion layer (GDL) of proton exchange membrane fuel cells are important in order to improve fuel cells performance. They are scientifically challenging because of the peculiarities of GDLs microstructures. In the present work, simulations on a pore network model are compared to X-ray tomographic images of water distributions during an ex-situ water invasion experiment. A method based on watershed segmentation was developed to extract a pore network from the 3D segmented image of the dry GDL. Pore network modeling and a full morphology model were then used to perform two-phase simulations and compared to the experimental data. The results show good agreement between experimental and simulated microscopic water distributions. Pore network extraction parameters were also benchmarked using the experimental data and results from full morphology simulations.

1. Introduction

Water management is a crucial aspect of Polymer Electrolyte Membrane Fuel Cells (PEMFC) operation. Water produced in excess by the oxygen reduction reaction needs to be removed from the cell to prevent flooding while the polymer membrane must stay well

---

* Corresponding author. Université de Toulouse, INPT, UPS, IMFT, Avenue Camille Soula, F-31400 Toulouse, France.
E-mail addresses: felix.buechi@psi.ch (F.N. Büchi), Joel.pauchet@cea.fr (J. Pauchet), mprat@imft.fr (M. Prat).

http://dx.doi.org/10.1016/j.jpowsour.2016.09.076
0378-7753/

hydrated to conduct protons. Gas diffusion layers (GDL) are one of the electrodes porous layers [1] and a key component with respect to the water management. During fuel cell operation, liquid water can also appear in GDLs as a result of condensation [2]. Its effect is to impede the gas flux towards the catalyst layer where the electrochemical reactions take place, decreasing the fuel cell performance. The biphasic, electrical, thermal and mechanical behaviors of GDLs must be therefore understood and well characterized in order to optimize fuel cell performance. In this respect, it is desirable to develop efficient and accurate numerical tools to simulate two-phase flows in GDLs.

Biphasic simulations in PEMFCs porous media have been widely investigated [3,4]. The simulation methods can be divided into direct methods such as Lattice-Boltzmann and (mesoscale) geometry based methods like the full morphology [5] and pore networks models [6–8]. Mesoscale methods are preferred here in order to keep the computational cost low to allow for using images large enough to be representative of the GDL structure. It should be noted that the pore network models (PNM) have been frequently used to investigate two-phase flows in GDL, e.g. Refs. [2,9–22]. Therefore, it is particularly important to confirm that PNM are well adapted to describe two-phase flows in fibrous materials, especially for the case of the capillarity driven regime that is expected to prevail in GDLs [9]. This is not obvious a priori because the microstructure of fibrous materials is quite different from the structure of granular materials or porous rocks mostly considered in previous applications of PNM, e.g. Refs. [23,24].

It is usual to distinguish the structured pore networks from the unstructured ones. A structured pore network is constructed on a given lattice, typically a cubic lattice for 3D simulations. The pores are located on the nodes of the lattice and connected by narrower channels, also referred to as links, corresponding to the constrictions of the pore space. In a simple cubic network the channels are aligned with the three main directions of a Cartesian coordinate system. By, contrast, the unstructured networks offer the possibility to respect much more closely the local geometry of a given microstructure. Starting from a digital image of the "real" microstructure, the network is directly constructed from the image using appropriate numerical techniques. It is the approach taken in the present paper.

In this context, the main objective of the present paper is to investigate the capabilities of image based unstructured pore network and full morphology models to predict water distributions in fibrous materials such as the ones used in GDL. These simulation methods have already been successfully used to predict capillary pressure curves and saturation levels, e.g. Ref. [10] where a simple structured cubic network is used. The novelty in the present effort is to develop an image based unstructured pore network and to look at the three dimensional water distributions and not only to slice averaged saturation levels.

Extracting an unstructured pore network from a 3D digital image of a microstructure is described in a number of publications [25–29]. Most methods are based on medial axis analysis or the consideration of maximal balls. Several articles reviewed and discussed these methods [30–33]. As far as we are concerned, we develop a method based on watershed segmentation. Watershed segmentation [34,35] or similar methods [36,37] are used in several articles as an image analysis tool to segment pores without doing pore network extraction [38–40]. Recently a few approaches use watershed segmentation or similar methods as part of a pore network extraction procedure [26,28,29,41,42]. The principle of watershed segmentation is to find constrictions, defined in a robust way as watershed lines. It has several advantages: it is a well-known tool in image analysis, it is robust and off-the-shell open source codes are available. It also offers an explicit degree of freedom regarding the pore merging, thanks to pore markers defined by the user.

In order to validate our pore network extraction procedure and to study the impact of the pore merging degree of freedom, we compare pore network simulations with experimental data and full morphology simulations. Full morphology simulations are in fact suggested as a useful benchmark to test pore network extraction procedures.

The experimental data are 3D microscopic liquid water distributions from water injection experiments obtained by X-ray tomographic microscopy [11]. X-ray tomography has been used in several works to visualize liquid water in GDLs [23,24,43–49]. Liquid water distributions in GDL obtained by X-ray tomography have also been used in some previous works in conjunction with numerical simulations, e.g. Ref. [9]. However, the present work is the first one, to the best of our knowledge, to propose a detailed comparison between PNM simulations and X-ray tomography images of the liquid water distribution in a GDL.

The aim of this article is thus to assess the predictability of pore network and full morphology models to simulate capillarity dominated biphasic flows in GDLs and to study a pore network extraction procedure based on watershed segmentation.

Regarding two-phase flows in GDL, one can distinguish in situ two-phase flows from ex-situ two phase flows. In situ refers to GDL in an operating fuel cell whereas ex situ refers to GDL typically used in characterization experiments involving the sole GDL (as opposed to the GDLs in the membrane electrode assembly (MEA) for the in-situ case). A typical objective of ex-situ experiments is to characterize the capillary pressure curve, an important parameter of the porous media classical two-phase flow model. In situ two-phase flows are a priori more complex than the ones observed in typical ex-situ experiments because of the coupling with heat transfer and the significance of phase change phenomena. Also, obtaining images of in situ liquid distribution from X-ray microscopy is more challenging. For these reasons, it is natural to first develop comparisons between simulations and experiments for the simpler ex-situ conditions. In this paper, an ex-situ configuration is considered.

2. Methodology

2.1. Material

Gas diffusion layer material of the type SGL™ 24BA (SGL Carbon, D) is chosen for this study. SGL™ gas diffusion layer materials are composed from carbon fibers and a micro-porous carbonaceous binder. The pore size of the binder is typically less than 1 μm. SGL™ 24 has an uncompressed thickness of 190 μm and an uncompressed porosity of 84%. The suffix "BA" means that the material is hydrophobized with 5% (w/w) of PTFE and that there is no microporous layer (MPL).

2.2. X-ray tomographic microscopy

Experimental water distributions of a SGL™ 24BA (SGL Carbon, D) gas diffusion layer is determined by X-ray tomographic microscopy. The imaging methodology developed for ex-situ [44,50] and operando environments [47,48] is described in detail in Ref. [49] and is applied to an ex-situ water invasion experiment. Similar set-ups are used in Refs. [23,24]. Throughout the paper, water injection denotes the process in which liquid water is injected into an initially dry capillary structure and gradually invades it.

A circular GDL sample (6 mm in diameter) is placed in the sample holder between two porous membranes. The membrane at the bottom (water side) is hydrophilic whereas the one on top (air side) is hydrophobic. The hydrophilic membrane promotes a homogeneous water distribution at the bottom side of the GDL. The hydrophobic membrane is used as a barrier for liquid water to gradually saturate the GDL after the breakthrough capillary pressure has been reached (the breakthrough capillary pressure is the minimum pressure between the two fluids, air and water, allowing liquid water to cross the GDL). As discussed in Ref. [49], this choice of synthetic, homogeneous boundary conditions is not representative of in-situ conditions but is well adapted to the determination of the capillary pressure curve. It also simplifies interpretation and modeling studies. The water injection protocol involves a stepwise increase of the liquid pressure. For each imposed liquid pressure, a capillary equilibrium distribution of the liquid water is reached within the GDL. A 3D X-ray tomographic image corresponding to each capillary equilibrium is acquired. Imaging conditions are given in Ref. [49].

Experiments are performed at 25 °C. The voxel size of the 3D image is 2.2 μm. The solid, the liquid and the void phase in the sample are obtained by segmentation of the greyscale image [49]. The voxel resolution of the images does not allow segmenting the pores in the binder of the SGL™ 24BA material. Therefore the binder is considered as a solid. As a consequence the image based porosity of the sample is less than the real porosity.

Global and local saturations can be computed from the images to derive the saturation profile across the GDL thickness and the overall saturation vs. capillary pressure relationship Pc(S). The capillary pressure Pc is the pressure difference between the imposed liquid phase pressure and the gas phase (supposed to be constant and equal to atmospheric pressure). The imaging data are used for comparison with the modeling results.

2.3. Pore network simulations

Pore network simulations have been developed in collaboration between Commissariat à l'Énergie Atomique et aux Énergies Alternatives (CEA) and Institut National Polytechnique de Toulouse (INPT). A pore network is first extracted from the tomographic image of the dry GDL. The extraction procedure is described in the next section. Then the extracted network is used in a Matlab™ pore network code to perform the two-phase simulations. The computed water distributions are displayed and analyzed on images using a mapping between network elements and image regions.

2.3.1. Invasion percolation algorithm

As mentioned before, the GDL pore space is represented as a network of pores and links in the pore network approach. The links represent the constrictions, i.e. the narrower passages between two neighbor pores. Because the GDL is considered as hydrophobic, the water distribution is simulated using the invasion percolation algorithm [9], which is well adapted to describe the very slow displacement of a wetting fluid (the gas phase here) by a non-wetting one (liquid water here). An invasion critical capillary pressure threshold is associated with each link. Physically, this is the maximal value of water pressure the link can hold back (it can be regarded as the link breakthrough pressure). Water invades the GDL one link (and its adjacent pore still free of liquid) after the other, selecting at each step the link on the liquid – gas interface having the lowest invasion critical capillary pressures. This process imitates a quasi-static injection.

2.3.2. Invasion capillary pressure threshold

Each constriction is associated with one critical capillary pressure threshold given by the Young-Laplace equation:

$$P_c = -\frac{2\gamma \cos\theta}{R} \tag{1}$$

where $\gamma = 7.2*10^{-2} N.m^{-1}$ is the water/air surface tension at 25 °C, θ is the contact angle and R is the constriction radius.

Constrictions are given as image regions by our pore network extraction procedure. We can thus compute their size on the image. The constriction radius is computed as the size of the largest inscribed ball whose center is located in the constriction.

Modeling the contact angle requires making an assumption. Indeed there are little, if any, detailed experimental data on contact angle heterogeneities within GDLs. Depending on the quality of the hydrophobic treatment or because of aging [51], GDLs can have locally different contact angles. Fine tuning the wettability is an approach to increase GDL performances. However in this work we assumed that the contact angle is uniform. More refined models taking into account variations of the contact angle are left for a future work.

2.3.3. Boundary conditions

In order to impose boundary conditions in the simulations we need to know accurately the location of the elements of the experimental set-up: the GDL, the hydrophobic and hydrophilic membranes and the lateral gasket (Fig. 1). The latest is identified by a cylindrical mask using the software ImageJ [52]. Knowing the shape of the hydrophilic membrane is critical for inlet injection conditions. Hydrophilic and hydrophobic membranes tend to penetrate in the GDL because of the compression. We use a morphological criterion to distinguish between GDL and membranes: GDL fibers are thinner than the membrane. A threshold on the covering radius map is used to set a limit between thin regions and thick ones.

A reservoir inlet boundary condition is applied for the simulation. This means that we assume that the whole inlet face is in contact with a water reservoir at uniform pressure. Because the membrane which is in contact with the inlet face is hydrophilic, the water fills it completely before entering the GDL during the simulations. The interaction of water with the hydrophobic membrane is assumed to be the same as the interaction with the hydrophobic GDL, i.e. we use the same contact angle and water cannot penetrate this membrane. No-flux wall condition is applied between the GDL and the lateral gasket. The water distribution is computed for 5 injection pressures: 14, 22, 28, 39 and 53 mbar.

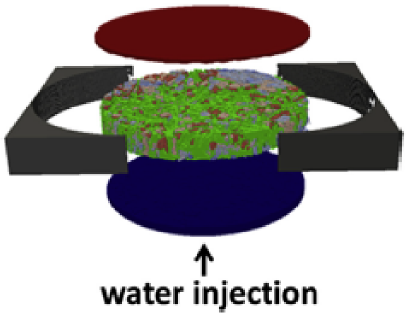

Fig. 1. Experimental set-up elements identified on the image. Green: GDL. Gray: lateral gasket. Blue: hydrophilic membrane. Red: hydrophobic membrane. Colored regions inside the GDL are liquid water at several pressures. (For interpretation of the references to colour in this figure legend, the reader is referred to the web version of this article.)

2.4. *Pore network extraction procedure*

We develop a pore network extraction method based on watershed segmentation. Our implementation of pore network extraction relies on open sources python libraries such as Scipy and ITK [53,54]. The open source functions used are listed in Table 1.

This section details the steps of the extraction procedure.

2.4.1. *Constriction search*

It is crucial to identify the constrictions in the pore space in order to model the capillary pressures since the constrictions control the invasions. Indeed, invasion capillary pressure thresholds are the highest where distances between solid parts are the lowest, i.e. at constrictions.

In this work, we define constrictions as being ridges of the distance map. A formal discussion of this definition can be found in Ref. [29]. The geometric reasoning is the following. The distance map is the map giving for each voxel of the pore space the minimum distance to a solid voxel. Fig. 2 illustrates this for a simple 2D geometry. The values in the distance map can be interpreted as depths. The voxels at the edges of the pores have a depth equal to 0 and the points in pores located the farthest from the pore walls correspond to maximum depth points. The center of a constriction is a saddle point, i.e. one can find two paths with an opposite curvature which intersect at this point. Indeed, a longitudinal path, connecting one pore to the pore located across the constriction, reaches its highest point at the constriction center. While a transversal path, connecting one solid edge of the constriction to the opposite solid edge, takes its maximum depth at the constriction center. The constriction is the transversal 2D surface located on the ridge of the distance map. It is also the watershed surface that the watershed algorithm finds.

Watershed segmentation is a common image analysis algorithm, used for example to separate objects at constrictions. Its principle is the following. The distance map is explored starting from marker voxels using a so-called flooding algorithm. Voxels around the markers are in the explored region if they are below a given depth according to the distance map. Then the depth is gradually decreased. Think of it as a flooding of the depth map from the bottom to the top by gradually increasing the water level. When a sufficiently high level is reached, two neighbors regions eventually meet at the ridges of the distance map. So the watershed surfaces search is a two steps process. In the first step markers are defined giving approximate locations of pores. This step is described in the next section. The second step is the ridges search using the flooding algorithm. At the end of this step, watershed surfaces are found between markers. They delimit distinct image regions, the pores. Each pore is then labeled using a connected-component labeling function.

The location and shape of constrictions are thus directly available. Then we can extract the constriction sizes which are directly linked to capillary pressures.

2.4.2. *Markers choice*

Markers are used to define the approximate location of pores and initialize the watershed segmentation process.

The basic idea is to locate markers at the widest locations (the locations the farthest from pore walls), i.e. at local maxima of the distance map. The problem with taking all local maxima is over-segmentation: the number of local maxima is sensitive to geometry noise like surface roughness. Several approaches have been used to prevent over-segmentation: direct filtering of the distance map [26], pore merging as a post-processing step [29], marker choice based on the medial axis analysis to prevent topology defects [28]. We explore two other methods to reduce the over-segmentation:

- The first method is to impose a minimal distance between two local maxima.
- The second method is to use H-maxima instead of local maxima.

The notion of H-maxima makes it possible to merge local maxima according to a contrast criterion on the distance map [40]. H-maxima are defined as the local maxima of the reconstruction by dilation of the distance map. Reconstruction by dilation [55] is an algorithm which truncates the peaks of the distance map by a height H voxels, so that peaks are replaced by plateaus. The truncation parameter H is a free parameter. Its meaning is the following. Suppose that a noise is superimposed on the distance map, so that the value of each voxel can change by plus or minus H/2. One such noise could come from the stairs-like discretization of surfaces in the image. Then truncating the peaks by H voxels makes it possible to erase the effect of noise on the peaks.

2.4.3. *Pores and links connectivity and shape analysis*

The connectivity is analyzed after the watershed surfaces are found and the pores are labeled. Each watershed voxel neighborhood is analyzed to list its neighbor pores. Voxels connectivity is defined in this work, so that a voxel is connected with its 26 neighbors voxels, i.e. diagonals included. Watershed voxels having exactly two different neighbor pores are assigned to the link between these two pores. After this analysis, labeled link voxels and connectivity tables between pores and links are available.

The geometry of pores and links are then analyzed. The exact geometry of pores and links is available as voxel regions in the image. Shape descriptors are used to take into account this geometry in the pore network simulations. The shape descriptors we use are the location of the center of mass, the location of the widest point, the inscribed sphere radius and the volume.

Table 1
List of open source functions.

Distance map	SimpleITK.DanielssonDistanceMap
Local maxima search	skimage.feature.peak_local_max
Reconstruction by dilation	skimage.morphology.reconstruction
Watershed search	SimpleITK.MorphologicalWatershedFromMarkers
Connected components labelling	scipy.ndimage.measurements.label
Morphological dilation	SimpleITK.BinaryDilate
Center of mass location	scipy.ndimage.measurement.center_of_mass
Widest point location	scipy.ndimage.measurement.labeled_comprehension (numpy.argmax (distanceMap))
Inscribed sphere radius	scipy.ndimage.measurement.labeled_comprehension (numpy.max (distanceMap))
Volume	scipy.ndimage.measurement.labeled_comprehension (numpy.size)

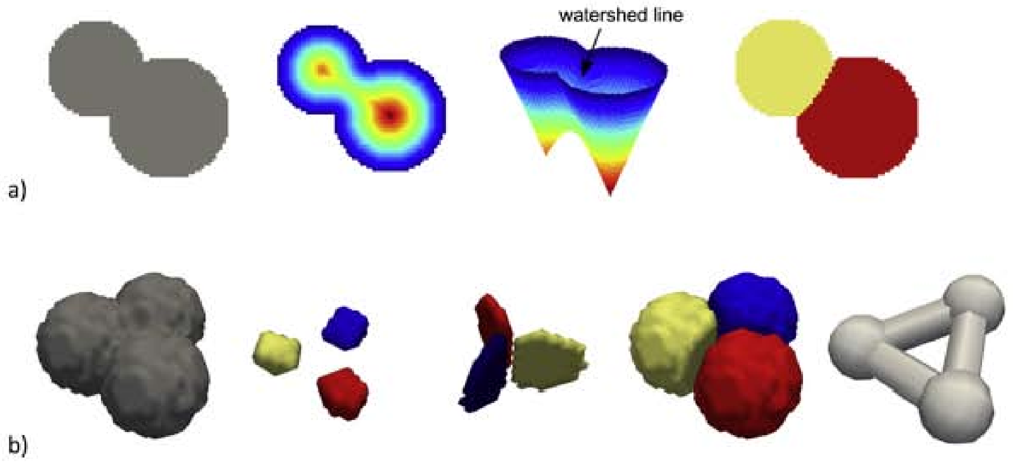

Fig. 2. Watershed segmentation and pore network extraction algorithms illustrated on two simple geometries. a) Watershed segmentation explained on a 2D geometry. From left to right: pore space, distance map, distance map interpreted as a depth map, pores separated by a watershed line. b) Pore network extraction explained on a 3D geometry. From left to right: pore space, markers chosen as H-maxima of the distance map, watershed surfaces, pores separated by watershed surfaces, extracted network.

2.5. *Full morphology simulations*

In the full morphology simulations, the shape of the region occupied by water is approximated as a union of balls of a constant radius. This is to take into account that all menisci have the same radius under capillary equilibrium condition. Assuming that water has a uniform pressure, that the contact angle is uniform and that menisci are spherical, then the radius is fixed by the Young-Laplace equation. Water invades regions that a ball of radius R can access following a continuous path from the injection points.

Our implementation of the full morphology model is the following. Regions where the distance map is greater than R are selected as ball centers candidates. Centers which are connected to injection points are found using a connected-component labelling algorithm. Non-connected centers are rejected. Then a morphological dilation of radius R is applied to the centers to form water balls.

The open source functions used to implement the full morphology model are listed in Table 1.

2.6. *Anisotropy characterization*

GDL are anisotropic structures with openings typically greater on average in the in-plane direction compared to the through plane direction. This can have an important consequence on the two-phase flow with the formation of preferential paths in the through plane direction [49]. Characterizing the GDL microstructure anisotropy is therefore of particular interest.

The chord length is a geometric measure which can be used to quantify the geometric anisotropy of regions in a 3D image [56]. Its principle is the following. The intersections of image regions with a series of straight lines parallel to a given direction are computed. These intersection lengths give a measure of the regions size in this direction. By varying the directions of straight lines, we can study the anisotropy of the regions sizes. Implementation details can be found in Ref. [56].

We also characterize the anisotropy of constriction sizes. Our method is as follows. Constrictions are found during the construction of the pores network. The direction of a constriction is computed as the direction of the segment joining the centers of its two neighboring pores. We classify the constrictions in two categories, in-plane and trough-plane, depending on whether they form an angle less than 45° with the through-plane direction. The sizes of constrictions in the in-plane and through-plane directions are compared.

3. Results

3.1. *Benchmarking network extraction parameters against full morphology results*

As mentioned before pore network extraction from an image is a complex procedure which involves making a choice regarding the definition of pores. We discuss in this section the consequences of the choice of the pore merging parameter. We also suggest that comparing pore network two-phase simulations with full morphology simulations can help verify that the extracted pore network is valid.

The extracted pore network is not unique because the markers choice gives a degree of freedom on pore definition. Two pores can be merged into one or be further divided depending on the markers choice. This degree of freedom is unavoidable because the notion of pore is not uniquely defined. Because there is no absolute criterion to decide whether two pores should be merged or not, the extracted networks are tested from the simulation results they produce rather than from using an intrinsic criterion.

We compare water distributions simulated with the pore network model with those simulated with the full morphology model. Indeed those two simulation methods have many points in common. Capillary forces are computed as a function of radii of maximal ball inscribed in constrictions. The porous medium is invaded from an injection side, the lowest capillary pressure threshold regions first. In the end, provided that boundary conditions are the same, water patterns for a given pressure should be the same.

The main source of information loss between the pore network model and the full morphology model is pore merging because information on the constrictions located inside pores are not taken into account. The possible water bifurcations caused by these constrictions are lost. Thus comparing water patterns given by pore network and full morphology models is one way to assess if a pore network extraction procedure correctly captures the water bifurcations associated with constrictions.

We use the following quantity to measure the degree of agreement between images of an experimental water distribution and of a numerical water distribution:

$$VoxelMatch(numerical|experimental) = \frac{Sat(numerical \cap experimental)}{Sat(experimental)} \quad (2)$$

where "numerical" and "experimental" denote the voxels filled with water in the two images and Sat is the number of voxels filled with water divided by the total number of pore space voxels, i.e. the overall saturation.

This quantity can be understood as the relative saturation of the numerical water distribution in the experimental water distribution. From a probability point of view, it is also the probability of a voxel to be filled with water in the numerical simulation knowing that it is filled with water in the experimental image. When compared with the overall saturation obtained in the simulation, it gives information on the correlation between the two water distributions. Indeed, the VoxelMatch is one if the two distributions are perfectly correlated. If they are statistically independents, the definition of statistical independence of two events involves the following property:

$$VoxelMatch(numerical|experimental) = Sat(numerical). \quad (3)$$

Thus, the closer to 1 is the VoxelMatch index, the better is the correlation between the experimental and numerical distributions.

Fig. 3 presents the Voxel Match index (Eq. (2)) of pore network water distributions with respect to full morphology water distributions for the five experimental pressures. Several network extraction parameters are benchmarked.

As can be seen from Fig. 3, the least successful choice is to take all local maxima for markers. The voxel match is almost perfect at low pressure, so it indicates that inlet boundary conditions are close. But it decreases as the pressure is increased from 14 mbar to 53 mbar, while the overall saturation increases up to 0.7. This indicates a correlation loss between the results of the two models. This is expected to happen when the impact of constrictions is not taken into account the same way in the two simulation methods. Indeed, let's consider a model of water interacting with random constrictions, as it is the case here where water must choose bifurcations according to constrictions. If constrictions in the two simulations are two uncorrelated random fields, water distributions which are initially correlated because of boundary conditions will lose their correlation because of the impact of different paths taken in the constrictions.

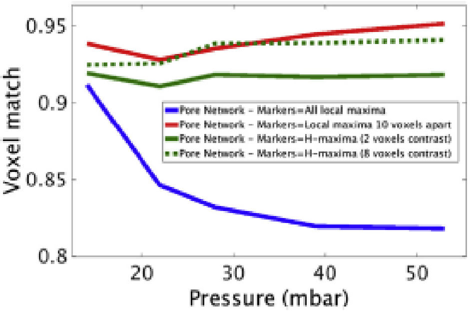

Fig. 3. Voxel matches of pore network water distributions with respect to full morphology water distributions, for 14, 22, 28, 39 and 53 mbar pressures. Simulations are run on the whole GDL sample with uniform wettability $\theta = 115°$.

On the contrary, the pore network and full morphology models give almost the same water distributions with around 95% voxel match when the markers are specified using the H-maxima procedure. This is almost a complete match, as the 5% difference could be explained by the following remarks. Firstly, because the pores are either fully invaded or fully dry in the pore network images, small water regions below the pore scale can differ, such as spherical menisci in full morphology or small roughness which are invaded at high pressure only. Secondly, we left link voxels (1 voxel thick surfaces) blank in PNM images.

This is an interesting result because it shows that these two geometry based methods have the same basis. The full morphology model is completely parameter free, so it can be used to benchmark the pore network complex extraction procedure.

This result also validates the capability of the watershed based extraction procedure to detect constrictions.

Since merging the local maxima clearly increases the match with the full morphology simulations, we recommend using a merging step.

3.2. Comparison between experimental and computed water distributions

We present here a comparison between experimental and computed water distributions. Firstly we look at the voxel by voxel agreement between the water patterns. Secondly we look at the overall saturation and at slice averaged saturation curves. Thirdly we study the water distribution anisotropy using chord length.

3.2.1. Voxel by voxel match

Fig. 4 shows 3D rendering of experimental and simulated water patterns in the whole GDL. We show on the same image the water distribution at several water injection pressure levels: 14, 22, 28, 39 and 53 mbar. The increments in the water presence between one pressure and the next are shown with different colors. Because the water occupied region grows when the pressure is increased, the water distribution at a given pressure is the union of the distributions corresponding to the increments at lower pressures.

Visually, the simulated patterns are close to the experimental ones. The most apparent difference is at the lowest pressure. This probably indicates that the injection conditions are not perfectly well reproduced. The shape of the hydrophilic membrane is probably not sufficiently accurately estimated.

Fig. 5 shows the sample averaged voxel match for the five experimental pressures. It is lowest at low pressure, between 0.4 and 0.6 depending on the simulation method. This noticeable difference with the experiment is probably due to the inlet boundary condition. When increasing pressure the voxel match increases up to 0.8–0.9. This increase is mostly a saturation effect, the average saturation increasing from 0.2 to 0.8. This saturation effect can be evaluated from total saturation levels (shown in dot lines in Fig. 5), representative of the voxel match in the case of statistical independence.

The fact that the voxel match is higher than the total saturation for the middle and high pressures is due to the preservation of initial correlation during the water injection, that is to say the relevance of the capillary model. These results are considered as good since there is only one free parameter, the uniform contact angle. The value $\theta = 115°$ gives the best results. This is consistent with the expected value of contact angle of water on PTFE.

Causes for disagreement are discussed further in the last section.

3.2.2. Averaged saturation curves

A more concise way to characterize the water distributions is to compute the overall saturation and the slice average saturation

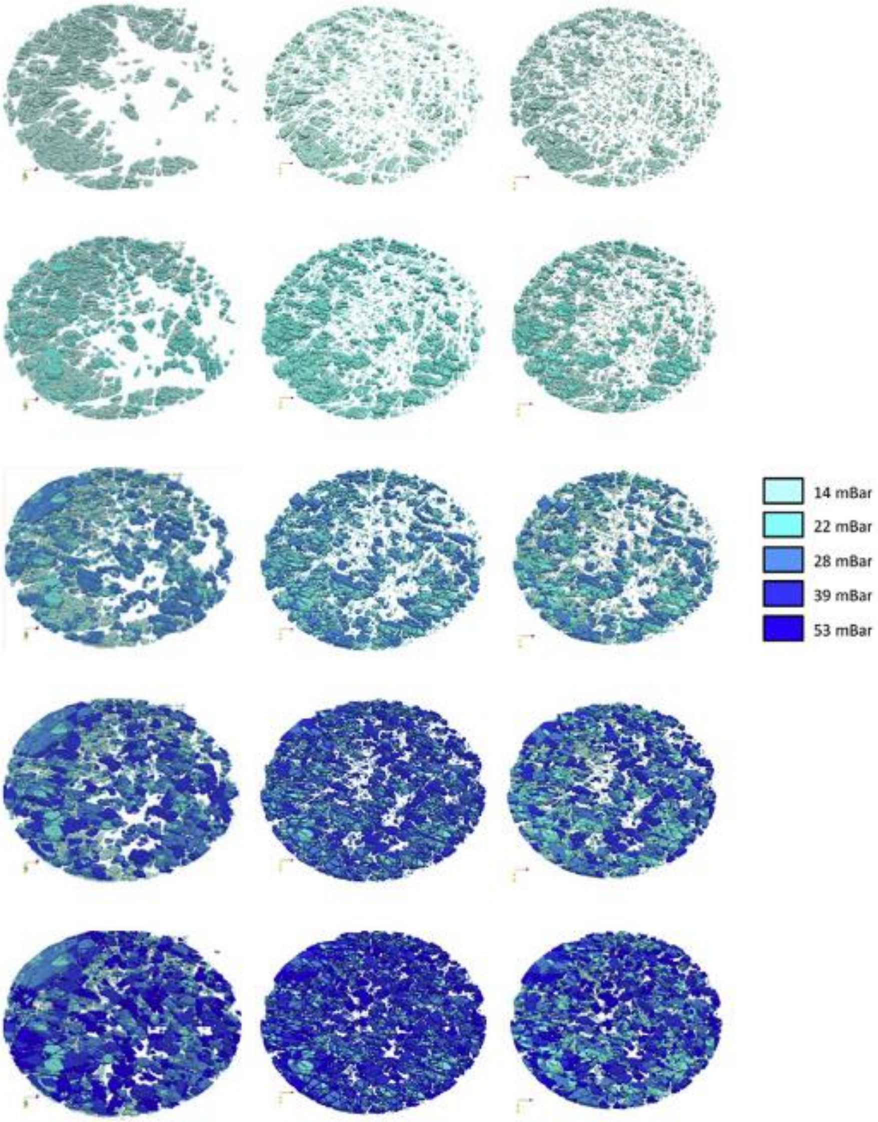

Fig. 4. 3D rendering of water patterns in the GDL at 14, 22, 28, 39 and 53 mbar. From left to right: experiment, full morphology simulation, pore network simulation with H-maxima markers (H-contrast = 8 voxels). Simulations are run on the whole GDL sample with uniform wettability $\theta = 115°$. Each color corresponds to the water distribution increment at a given pressure. (For interpretation of the references to colour in this figure legend, the reader is referred to the web version of this article.)

profile in the through-plane direction for the different pressure levels.

Fig. 6 shows comparisons between the experiment and the simulations as regards the through-plane saturation profiles and the capillary pressure curves. Saturation profiles are x-y slice averaged water saturations as a function of the z-axis, where z is the through plane direction. The five solid line curves represent the simulated saturation profiles at the five experimental pressures. The five dashed lines are the experimental saturation profiles. The capillary pressure curves show the sample averaged saturation as a function of the pressure level. The dashed curves represent the experimental data and the solid curves the simulations. All saturations are computed for the slices 15 to 85. The 0 to 15 slices correspond to the hydrophilic membrane, the 85 to 110 slices to the hydrophobic membrane.

As discussed in Ref. [14], the convex shapes of the experimental saturation profiles at low and middle pressure are different than the ones usually predicted using traditional continuum model based on the generalized Darcy's law and Leverett functions.

The full morphology and pore network simulations both give results quite consistent with the experiment. The capillary pressure curves are almost perfectly reproduced. The global shapes of saturation profiles are also nicely predicted although there remain some inaccuracies regarding the water distribution in the through plane direction. The effect of pressure on saturation profiles is well predicted.

The lowest accuracy was obtained with a pore network extracted without merging the local maxima. Therefore, as in the

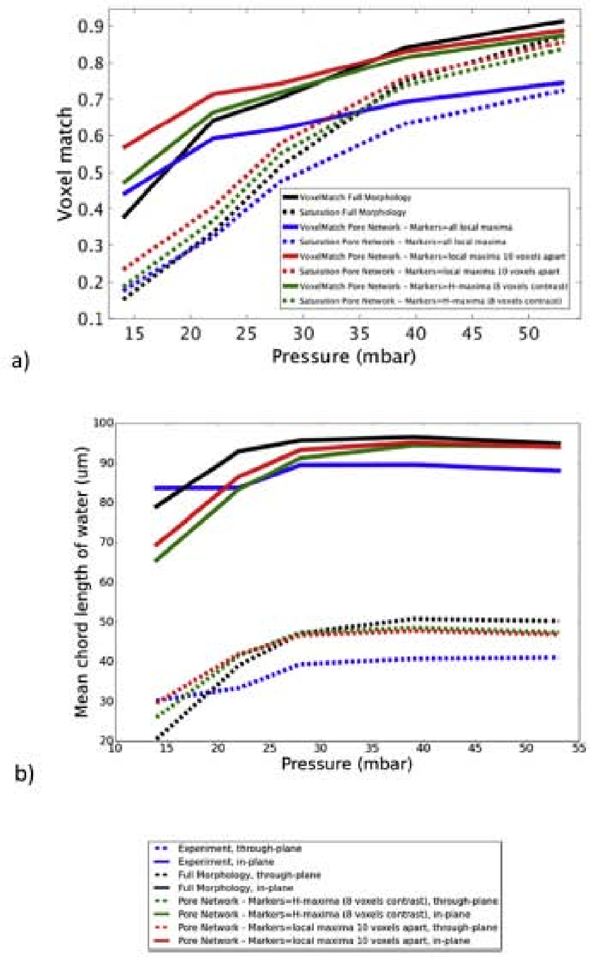

Fig. 5. Quantitative comparison of experimental water distribution with water distribution simulated with full morphology and pore networks. a) Full lines: sample averaged voxel match of simulated water distributions with respect to experimental water distributions. Voxels matches are computed for five pressure levels. Dotted lines: saturation levels of simulations. b) Mean chord lengths of water distributions, as a function of water pressure. Full lines represent in-plane chord lengths, dotted lines represent through-plane chord lengths.

previous section, it is recommended to merge local maxima in the pore network extraction procedure.

3.2.3. Chord lengths

Chord lengths are used to characterize the size of water clusters and the anisotropy. Fig. 5b shows the mean chord lengths of experimental and simulated water distributions.

The mean chord lengths for the experimental water distribution at high capillary pressures are 85 μm in the in-plane direction and 40 μm in the through-plane direction. The mean chord lengths of simulated water distribution are close: 92 μm for in-plane, 48 μm for through-plane. Thus, simulations are able to reproduce the anisotropy. This is another element showing the good match of simulations with the experiment.

The mean chord lengths of the dry pore space are respectively 81 μm and 37 μm. This is not exactly the values found for water distributions, although we could expect that the pore space is filled with water at high pressures. The difference can be explained by the small pores: they reduce the value of the mean chord length of the dry pore space, but not the mean chord length of water. Indeed, small pores are not filled with water, since the GDL is a hydrophobic material.

For comparison, the mean chord lengths of the solid area of the GDL are 74 μm and 33 μm respectively.

3.3. Quantitative analysis of the pore networks

The properties of the extracted networks can be studied in order to compare the extraction procedures. Fig. 7 provides quantitative information on the extracted networks.

The markers selection is a characteristic of our extraction method. The markers choice influences the properties of the resulting networks, such as the number of network elements. Fig. 7a illustrates this point by showing several networks extracted from the same microstructure with different choice of markers. Over-segmentation is illustrated when choosing all the local maxima of the distance map for markers. The number of pores decreases when choosing H-maxima for markers or imposing a minimal distance between markers.

We further characterize the network by the pores sizes distribution, the constrictions sizes distribution, the connectivity (number of neighboring pores of each pore), and the constrictivity (size ratio between neighboring pores and constrictions). Fig. 7b shows these data for three markers choices: no filtration of local maxima, a minimum distance imposed between two markers, and H-maxima.

The pore size distributions (Fig. 7b1) for the "H-maxima" and "unfiltered" networks have shapes reminiscent of the Weibull distribution. This is a standard shape for pore networks. A phenomenon of over-segmentation in the "unfiltered" network can be inferred from the high number of small pores, between 3 and 5 μm. We consider it to be detrimental, because the shape of pores which are only a few voxels wide cannot be precisely resolved. The shape of the pore size distribution obtained with the "minimum distance between markers" network is different from a Weibull distribution. It has two humps, with a cutoff around 3 voxels. This distortion indicates that this marker choice introduces an artificial cutoff between small pores and large pores.

Constriction size distributions (Fig. 7b.2) have similar shapes for the different networks. The distribution of links between the in-plane and the through-plane categories is as follows: 16% of constrictions are through-plane for the "unfiltered" network, 8% for the "minimum distance between markers" network, 10% for the "H-maxima" network. Overall, the through-plane sizes are close to the in-plane sizes, except for more frequent through-plane constrictions between 5 and 8 μm in the "minimum distance between markers" network. However, the pore space was found to be anisotropic in Ref. [49], using the notion of continuous pore size distribution [57]. More precise analysis of the constrictions geometry might be necessary in order to ascertain the anisotropy of constrictions.

Fig. 7b.3 shows the connectivity distributions. The "unfiltered" network has greater connectivity than other networks. This can be explained by the over-segmentation. The "H-maxima" network has fewer pores with 1 neighbor only compared to the "minimum distance between markers" network. It is considered positive because the pores with only one neighbor make inert dead-ends.

The constrictivity distributions are shown in Fig. 7b.4. For the "unfiltered" network, the most common ratio between pore radius and constriction radius, is 1. This is considered detrimental, because the constrictions are expected to be smaller than the pores. It is an indication of over-segmentation. As stated in Section 2.4.2, in the "H-maxima" network a constriction width is lower than the width

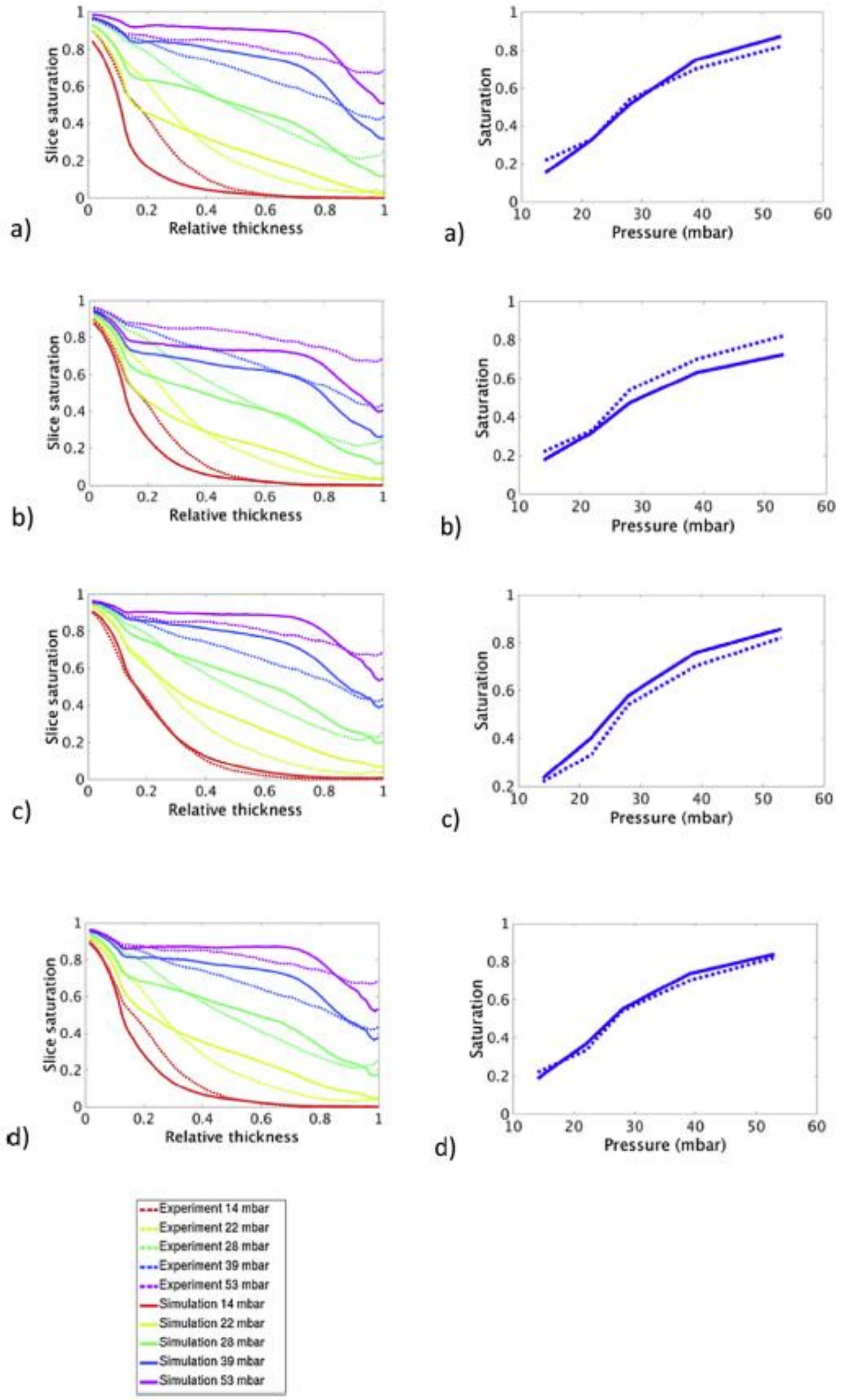

Fig. 6. Averaged saturations of simulated water distributions compared with experimental ones. Left: saturation profiles in the through-plane direction. Experimental curves are in dotted lines, simulations curves are in full lines. Right: capillary pressure curves. Simulation methods: a) Full morphology b) Pore network, markers = all local maxima c) Pore network, markers = local maxima at least 10 voxels apart, d) Pore network, markers = H-maxima (H-contrast = 8 voxels). Simulations are run on the whole GDL sample with uniform wettability $\theta = 115°$.

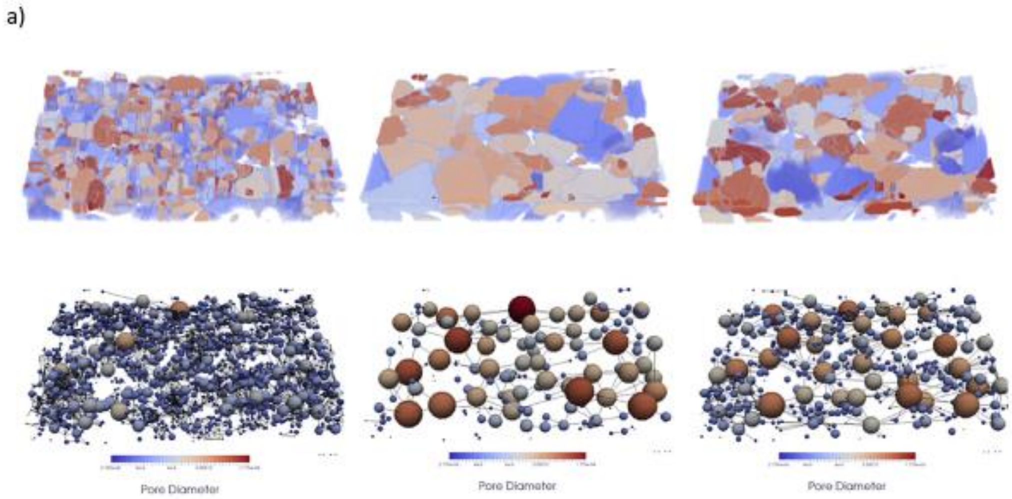

1) Markers = all local maxima.
2775 pores, 8095 links

2) Markers = local maxima at least 10 voxels apart.
181 pores, 310 links

3) Markers = H-maxima with H-contrast=8 voxels
559 pores, 1314 links

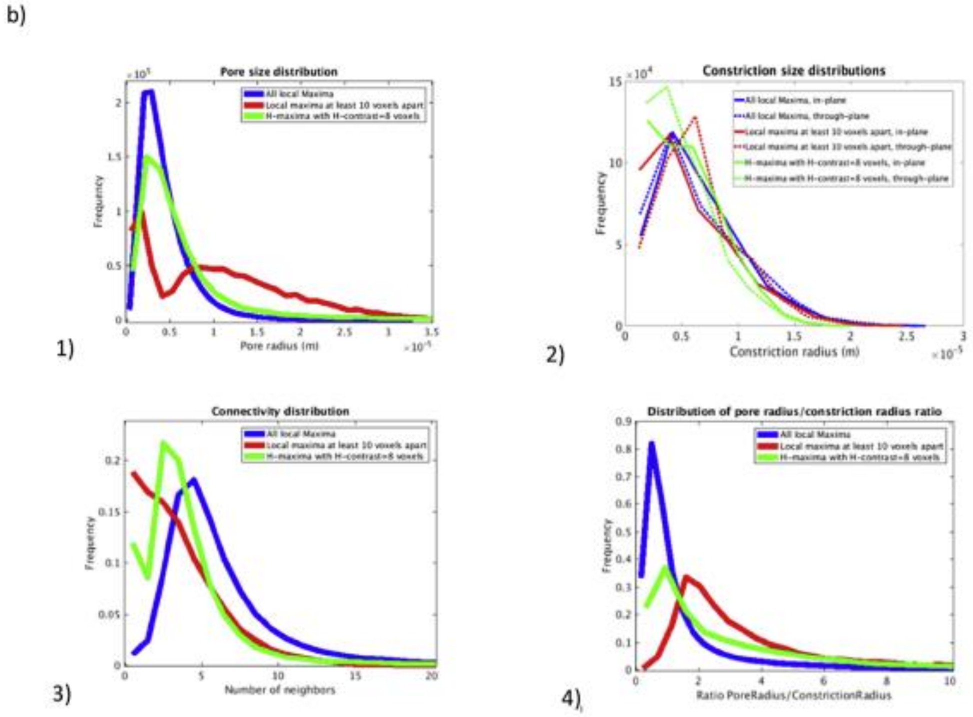

Fig. 7. Pore network extracted from a GDL subsample. a) 3D rendering of pores (top) and networks (bottom). Network elements are displayed with reduced size to increase readability. Criteria for markers choice are, from left to right a1) all local maxima, a2) local maxima at least 10 voxels apart, a3) H-maxima with H-contrast = 8 voxels. b) Quantitative data on the pore network. b.1) Pore size distributions. b.2) Constriction size distributions, in-plane and through-plane. b.3) Connectivity distribution. b.4) Constrictivity distribution.

of the smallest of its two neighboring pores minus H voxels. This relationship between pore size and constrictivity could explain why the constrictivity distribution of the "H-maxima" network has a shape similar to the shape of the pore size distribution.

3.4. Computation performances

The number of voxels in the tomography image is around 700 millions. Extracting the pore network from such an image takes

40 min and 40 Gb Ram on one Intel Xeon 5 2.2 Ghz CPU. Pore network simulations on the extracted pore network take 1 min. Full morphology simulations for the five pressure levels take 25 min.

4. Discussion

The agreement between the experiments and the simulations is considered as good but is not perfect. Possible model improvements are briefly discussed in this section.

Uncertainties regarding the inlet conditions are considered as a major cause of discrepancies between the simulations and the experiment. In this work we imposed inlet boundary conditions considering the hydrophilic membrane as a water reservoir. Accordingly, water enters the GDL where the fibers in contact with the membrane correspond to the lowest capillary pressure threshold. This method does not give a good accuracy on the water distribution near the hydrophilic membrane because it is too sensitive to the membrane geometry which is difficult to distinguish from the GDL. Another approach would be to use experimental water locations near the hydrophilic membrane, at the lowest pressure level, to define injection points and thus the initial conditions for the simulation. It boils down to simulating a water increment knowing the previous water distribution, in order not to be disturbed by injection conditions.

The capillary model could be improved taking into account the possible wettability heterogeneities. Curved menisci are visible in the experimental water images. The constriction size at the menisci may give an indication on the local contact angles using (Eq. (1)). These contact angles could be used as input for the pore network simulations. Another approach would be to estimate local contact angles from a model mixing fibers and binder contact angles. Assuming that fibers and binder could be distinguished on the image, the pore network extraction procedure makes it possible to extract the chemical composition, i.e. fiber or binder, of the vicinity of each constriction from the images.

GDL constrictions in the in-plane direction are more elongated than in the through plane direction. Inscribed balls radii do not take properly this effect into account. A better estimator of the invasion capillary pressure threshold in elongated constrictions is the hydraulic radius [58,59].

We recommended using a pore merging procedure before the watershed segmentation in order to prevent over-segmentation. Further studies are needed to check whether the H-maxima procedure recommended in our paper also apply to other fibrous materials than the GDL SGL™ 24BA.

5. Conclusion

Pore network and full morphology simulations of quasi-static two-phase flow in a gas diffusion layer were performed. A pore network extraction method based on watershed segmentation was developed. The geometry of the tomographic image was analyzed to identify pores and constrictions. A comparison between full morphology and pore network two-phase simulations was performed. This validated the extraction procedure. The extraction computations are fast (40min for a 700 million voxels image) and were developed using open source libraries. Hence the comparison with the full morphology approach provides a way to optimally specify the pore network extraction parameters and make the pore network approach more predictive than when only the microstructure is available.

Tomographic microscopy images of water imbibition into a GDL material (SGL™ 24BA) were used as reference data for comparison with numerical simulations. Full morphology and pore network simulations produced capillary pressure curves and saturation profiles reasonably similar to the experimental data. The results were obtained using a uniform wettability assumption. The voxel by voxel agreement between the experimental and simulated water distributions was analyzed. It also showed a good overall agreement. Experimental and modeling uncertainties were discussed to explain the remaining discrepancies between the experimental and numerical results.

Even if some improvements in the modeling are still desirable, the main conclusion is that full morphology and image based pore network models are quite reliable methods to simulate water distributions in GDLs. This is good news since pore network models have been used in many previous investigations to simulate two-phase flows in ex-situ as well as in-situ GDLs and will certainly be used in future work. They permit computationally cheaper and faster simulations than direct simulations and are more appropriate than continuum models because a GDL is a thin porous medium with very few pores over its thickness, thus characterized by a lack of length scale separation between the pore scale and the sample scale.

One can wonder, however, why developing pore network models since practically identical results are obtained with the full morphology model with fewer assumptions. A first point is that the pore network simulations are faster (not considering the pore network extraction step but only the two phase flow simulations). More importantly, pore network models make it possible to simulate more advanced biphasic phenomena than the full morphology model, such as for instance two-phase flows in systems of mixed wettability or in the presence of viscous effects for instance. From a more general point of view, the present work shows that pore network models are well adapted to simulate two-phase flow, at least in the quasi-static limit only considered in the present work and in fibrous materials: an important class of materials encountered not only in fuel cells but also in many other applications such as filter media and dewatering felt. It should be emphasized that the applicability of pore network modeling to this particular class of porous systems has frequently been a subject of questions owing to the particular features of fibrous media microstructures. It was by no means obvious that a technique developed initially for simulating two-phase flows in porous rocks and granular materials is also applicable to fibrous media.

This work opens up the route to model real structures with image based pore networks with consideration of more complex but more realistic in situ processes such as evaporation and condensation and to derive effective properties as a function of GDL local properties (structure, wettability) which will be important steps to analyze the influence of modifications of GDL and thus suggest design recommendations.

Acknowledgements

The authors gratefully acknowledge the funding from the EU project IMPALA ("IMprove Pemfc with Advanced water management and gas diffusion Layers for Automotive application", project number: 303446) within the Fuel Cells and Hydrogen Joint Undertaking (FCHJU), and SGL Carbon for the supply with gas diffusion layer materials.

References

[1] L. Cindrella, A.M. Kannan, J.F. Lin, K. Saminathan, Y. Ho, C.W. Lin, et al., Gas diffusion layer for proton exchange membrane fuel cells—A review, J. Power Sources 194 (2009) 146–160, http://dx.doi.org/10.1016/j.jpowsour.2009.04.005.

[2] B. Straubhaar, J. Pauchet, M. Prat, Water transport in gas diffusion layer of a polymer electrolyte fuel cell in the presence of a temperature gradient. Phase change effect, Int. J. Hydrogen Energy 40 (2015) 2–9, http://dx.doi.org/

10.1016/j.ijhydene.2015.04.027.

[3] P.P. Mukherjee, Q. Kang, C.-Y. Wang, Pore-scale modeling of two-phase transport in polymer electrolyte fuel cells—progress and perspective, Energy Environ. Sci. 4 (2011) 346–369, http://dx.doi.org/10.1039/b926077c.

[4] H.-J. Vogel, J. Tölke, V.P. Schulz, M. Krafczyk, K. Roth, Comparison of a lattice-Boltzmann model, a full-morphology model, and a pore network model for determining capillary pressure–saturation relationships, Vadose Zo. J. 4 (2005) 380, http://dx.doi.org/10.2136/vzj2004.0114.

[5] V.P. Schulz, J. Becker, A. Wiegmann, P.P. Mukherjee, C.-Y. Wang, Modeling of two-phase behavior in the gas diffusion medium of PEFCs via full morphology approach, J. Electrochem. Soc. 154 (2007) B419, http://dx.doi.org/10.1149/1.2472547.

[6] M.J. Blunt, M.D. Jackson, M. Piri, P.H. Valvatne, Detailed physics, predictive capabilities and macroscopic consequences for pore-network models of multiphase flow, Adv. Water Resour. 25 (2002) 1069–1089, http://dx.doi.org/10.1016/S0309-1708(02)00049-0.

[7] M. Blunt, Flow in porous media—pore-network models and multiphase flow, Curr. Opin. Colloid Interface Sci. 6 (2001) 197–207, http://dx.doi.org/10.1016/S1359-0294(01)00084-X.

[8] J. Hinebaugh, A. Bazylak, Pore network modeling to study the effects of common assumptions in GDL liquid water invasion studies, in: ASME 2012 10th Int. Conf. Fuel Cell Sci. Eng. Technol., ASME, 2012, pp. 479–484, http://dx.doi.org/10.1115/FuelCell2012-91466.

[9] O. Chapuis, M. Prat, M. Quintard, E. Chane-Kane, O. Guillot, N. Mayer, Two-phase flow and evaporation in model fibrous media, J. Power Sources 178 (2008) 258–268, http://dx.doi.org/10.1016/j.jpowsour.2007.12.011.

[10] J.T. Gostick, M.A. Ioannidis, M.W. Fowler, M.D. Pritzker, Pore network modeling of fibrous gas diffusion layers for polymer electrolyte membrane fuel cells, J. Power Sources 173 (2007) 277–290, http://dx.doi.org/10.1016/j.jpowsour.2007.04.059.

[11] J. Hinebaugh, Z. Fishman, A. Bazylak, Unstructured pore network modeling with heterogeneous PEMFC GDL porosity distributions, J. Electrochem. Soc. 157 (2010) B1651, http://dx.doi.org/10.1149/1.3486095.

[12] B. Markicevic, A. Bazylak, N. Djilali, Determination of transport parameters for multiphase flow in porous gas diffusion electrodes using a capillary network model, J. Power Sources 171 (2007) 706–717, http://dx.doi.org/10.1016/j.jpowsour.2007.06.053.

[13] G. Luo, Y. Ji, C.-Y. Wang, P.K. Sinha, Modeling liquid water transport in gas diffusion layers by topologically equivalent pore network, Electrochim. Acta 55 (2010) 5332–5341, http://dx.doi.org/10.1016/j.electacta.2010.04.078.

[14] M. Rebai, M. Prat, Scale effect and two-phase flow in a thin hydrophobic porous layer. Application to water transport in gas diffusion layers of proton exchange membrane fuel cells, J. Power Sources 192 (2009) 534–543, http://dx.doi.org/10.1016/j.jpowsour.2009.02.090.

[15] S.P. Kuttanikkad, M. Prat, J. Pauchet, Pore-network simulations of two-phase flow in a thin porous layer of mixed wettability: application to water transport in gas diffusion layers of proton exchange membrane fuel cells, J. Power Sources 196 (2011) 1145–1155, http://dx.doi.org/10.1016/j.jpowsour.2010.09.029.

[16] R. Wu, Q. Liao, X. Zhu, H. Wang, Impacts of the mixed wettability on liquid water and reactant gas transport through the gas diffusion layer of proton exchange membrane fuel cells, Int. J. Heat. Mass Transf. 55 (2012) 2581–2589, http://dx.doi.org/10.1016/j.ijheatmasstransfer.2012.01.002.

[17] P.K. Sinha, C.-Y. Wang, Liquid water transport in a mixed-wet gas diffusion layer of a polymer electrolyte fuel cell, Chem. Eng. Sci. 63 (2008) 1081–1091, http://dx.doi.org/10.1016/j.ces.2007.11.007.

[18] K.J. Lee, J.H. Kang, J.H. Nam, Liquid water distribution in hydrophobic gas-diffusion layers with interconnect rib geometry: an invasion-percolation pore network analysis, Int. J. Hydrogen Energy 39 (2014) 6646–6656, http://dx.doi.org/10.1016/j.ijhydene.2014.01.206.

[19] K.J. Lee, J.H. Nam, C.J. Kim, Steady saturation distribution in hydrophobic gas-diffusion layers of polymer electrolyte membrane fuel cells: a pore-network study, J. Power Sources 195 (2010) 130–141, http://dx.doi.org/10.1016/j.jpowsour.2009.06.076.

[20] K.-J. Lee, J.H. Nam, C.-J. Kim, Pore-network analysis of two-phase water transport in gas diffusion layers of polymer electrolyte membrane fuel cells, Electrochim. Acta 54 (2009) 1166–1176, http://dx.doi.org/10.1016/j.electacta.2008.08.068.

[21] P.K. Sinha, C.-Y. Wang, Pore-network modeling of liquid water transport in gas diffusion layer of a polymer electrolyte fuel cell, Electrochim. Acta 52 (2007) 7936–7945, http://dx.doi.org/10.1016/j.electacta.2007.06.061.

[22] E.F. Médici, J.S. Allen, Evaporation, two phase flow, and thermal transport in porous media with application to low-temperature fuel cells, Int. J. Heat. Mass Transf. 65 (2013) 779–788, http://dx.doi.org/10.1016/j.ijheatmasstransfer.2013.06.035.

[23] P.A. García-Salaberri, G. Hwang, M. Vera, A.Z. Weber, J.T. Gostick, Effective diffusivity in partially-saturated carbon-fiber gas diffusion layers: effect of through-plane saturation distribution, Int. J. Heat. Mass Transf. 86 (2015) 319–333, http://dx.doi.org/10.1016/j.ijheatmasstransfer.2015.02.073.

[24] I.V. Zenyuk, D.Y. Parkinson, G. Hwang, A.Z. Weber, Electrochemistry Communications Probing water distribution in compressed fuel-cell gas-diffusion layers using X-ray computed tomography, Electrochem. Commun. 53 (2015) 24–28.

[25] H. Dong, M.J. Blunt, Pore-network extraction from micro-computerized-tomography images, Phys. Rev. E - Stat. Nonlinear, Soft Matter Phys. 80 (2009) 1–11, http://dx.doi.org/10.1103/PhysRevE.80.036307.

[26] A. Rabbani, S. Jamshidi, S. Salehi, An automated simple algorithm for realistic pore network extraction from micro-tomography images, J. Pet. Sci. Eng. 123 (2014) 164–171, http://dx.doi.org/10.1016/j.petrol.2014.08.020.

[27] D. Wildenschild, A.P. Sheppard, X-ray imaging and analysis techniques for quantifying pore-scale structure and processes in subsurface porous medium systems, Adv. Water Resour. 51 (2013) 217–246, http://dx.doi.org/10.1016/j.advwatres.2012.07.018.

[28] A.P. Sheppard, R.M. Sok, H. Averdunk, Improved pore network extraction methods, in: Int. Symp. Soc. Core Anal., 2005, pp. 1–11 doi:SCA2005-20.

[29] U. Homberg, D. Baum, S. Prohaska, U. Kalbe, K.J. Witt, Automatic extraction and analysis of realistic pore structures from µ CT data for pore space characterization of graded soil, in: Int. Conf. Scour Erosi, Paris, 2012, pp. 345–352.

[30] J.Y. Arns, A.P. Sheppard, C.H. Arns, M.A. Knackstedt, A. Yelkhovsky, W.V. Pinczewski, Pore-level validation of representative pore networks obtained from micro-ct images, in: Proc. Int. Symp. Soc. Core Anal., 2007, pp. 1–12.

[31] P. Bhattad, C.S. Willson, K.E. Thompson, Effect of network structure on characterization and flow modeling using x-ray micro-tomography images of granular and fibrous porous media, Transp. Porous Media 90 (2011) 363–391, http://dx.doi.org/10.1007/s11242-011-9789-7.

[32] N.A. Idowu, C. Nardi, H. Long, T. Varslot, P.E. Øren, Effects of segmentation and skeletonisation algorithms on pore networks and predicted multiphase transport properties on reservoir rock samples, in: SPE Reserv. Characterisation Simul. Conf. Exhib., vol. 17, 2013, pp. 1–13.

[33] H. Dong, S. Fjeldstad, S. Roth, S. Bakke, P. Øren, Pore network modelling on carbonate: a comparative study of different micro-CT network extraction methods, in: Proc. Int. Symp. Soc. Core Anal., 2008, pp. 2008–2031.

[34] J. Roerdink, A. Meijster, The watershed transform: definitions, algorithms and parallelization strategies, Fundam. Inf. 41 (2000) 187–228, http://dx.doi.org/10.3233/FI-2000-411207.

[35] F. Meyer, The Watershed Concept and its Use in Segmentation: a Brief History, 2012. http://arxiv.org/abs/1202.0216.

[36] K.E. Thompson, C.S. Willson, W. Zhang, Quantitative computer reconstruction of particulate materials from microtomography images, Powder Technol. 163 (2006) 169–182, http://dx.doi.org/10.1016/j.powtec.2005.12.016.

[37] R.A. Ketcham, Computational methods for quantitative analysis of three-dimensional features in geological specimens, Geosphere 1 (2005) 32–41, http://dx.doi.org/10.1130/GES00001.1.

[38] I.-M. Sintorn, S. Svensson, M. Axelsson, Segmentation of individual pores in 3D paper images, Nord. Pulp Pap. Res. J. 20 (2005) 316–319.

[39] R.C. Atwood, J.R. Jones, P.D. Lee, L.L. Hench, Analysis of pore interconnectivity in bioactive glass foams using X-ray microtomography, Scr. Mater 51 (2004) 1029–1033, http://dx.doi.org/10.1016/j.scriptamat.2004.08.014.

[40] A. Amankwah, C. Aldrich, Rock image segmentation using watershed with shape markers, in: 2010 IEEE 39th Appl. Imag. Pattern Recognit. Work, IEEE, 2010, pp. 1–7, http://dx.doi.org/10.1109/AIPR.2010.5759719.

[41] K. Thompson, C. Willson, C. White, S. Nyman, J. Bhattacharya, A. Reed, Application of a new grain-based reconstruction algorithm to microtomography images for quantitative characterization and flow modeling, SPE J. 13 (2008) 164–176, http://dx.doi.org/10.2118/95887-PA.

[42] A.P. Sheppard, R.M. Sok, H. Averdunk, V.B. Robins, A. Ghous, Analysis of rock microstructure using high- resolution x-ray tomography, in: Proc. Int. Symp. Soc. Core Anal., 2006, pp. 1–12.

[43] Bazylak, Liquid water visualization in PEM fuel cells: a review, Int. J. Hydrogen Energy 34 (2009) 3845–3857, http://dx.doi.org/10.1016/j.ijhydene.2009.02.084.

[44] R. Flückiger, F. Marone, M. Stampanoni, A. Wokaun, F.N. Büchi, Investigation of liquid water in gas diffusion layers of polymer electrolyte fuel cells using X-ray tomographic microscopy, Electrochim. Acta 56 (2011) 2254–2262, http://dx.doi.org/10.1016/j.electacta.2010.12.016.

[45] J. Gostick, H. Gunterman, B. Kienitz, Tomographic imaging of water injection and withdrawal in PEMFC gas diffusion layers, ECS Trans. 33 (2010) 1407–1412, http://dx.doi.org/10.1149/1.3484632.

[46] H. Markötter, I. Manke, P. Krüger, T. Arlt, J. Haussmann, M. Klages, et al., Investigation of 3D water transport paths in gas diffusion layers by combined in-situ synchrotron X-ray radiography and tomography, Electrochem. Commun. 13 (2011) 1001–1004, http://dx.doi.org/10.1016/j.elecom.2011.06.023.

[47] T. Rosen, J. Eller, J. Kang, N.I. Prasianakis, J. Mantzaras, F.N. Buchi, Saturation dependent effective transport properties of PEFC gas diffusion layers, J. Electrochem. Soc. 159 (2012) F536–F544, http://dx.doi.org/10.1149/2.005209jes.

[48] I. Mayrhuber, F. Marone, M. Stampanoni, T.J. Schmidt, F.N. Buechi, Fast x-ray tomographic microscopy: investigating mechanisms of performance drop during freeze starts of polymer electrolyte fuel cells, ChemElectroChem. 2 (10) (2015) 1551–1559, http://dx.doi.org/10.1002/celc.201500132.

[49] A. Lamibrac, J. Roth, M. Toulec, F. Marone, M. Stampanoni, F. Buechi, Characterization of liquid water saturation in gas diffusion layers by x-ray tomographic microscopy, J. Electrochem. Soc. 163 (2016) F202–F209.

[50] J. Becker, R. Flückiger, M. Reum, F.N. Büchi, F. Marone, M. Stampanoni, Determination of material properties of gas diffusion layers: experiments and simulations using phase contrast tomographic microscopy, J. Electrochem. Soc. 156 (2009) B1175, http://dx.doi.org/10.1149/1.3176876.

[51] J. Pauchet, M. Prat, P. Schott, S.P. Kuttanikkad, Performance loss of proton exchange membrane fuel cell due to hydrophobicity loss in gas diffusion

layer: analysis by multiscale approach combining pore network and performance modelling, Int. J. Hydrogen Energy 37 (2012) 1628–1641, http://dx.doi.org/10.1016/j.ijhydene.2011.09.127.
[52] C.A. Schneider, W.S. Rasband, K. Eliceiri, NIH Image to ImageJ: 25 years of image analysis, Nat. Methods 9 (2012) 671–675.
[53] B.C. Lowekamp, D.T. Chen, L. Ibáñez, D. Blezek, The design of SimpleITK, Front. Neuroinform. 7 (2013) 45, http://dx.doi.org/10.3389/fninf.2013.00045.
[54] R. Beare, R. Beare, G. Lehmann, G. Lehmann, The watershed transform in ITK - discussion and new developments, Insight J. (2006) 1–24. http://hdl.handle.net/1926/202.
[55] L. Vincent, Morphological grayscale reconstruction in image analysis: applications and efficient algorithms, IEEE Trans. Image Process 2 (1993) 633–635, http://dx.doi.org/10.1109/83.217222.
[56] P.A. García-Salaberri, J.T. Gostick, G. Hwang, A.Z. Weber, M. Vera, Effective diffusivity in partially-saturated carbon-fiber gas diffusion layers: effect of local saturation and application to macroscopic continuum models, J. Power Sources 296 (2015) 440–453, http://dx.doi.org/10.1016/j.jpowsour.2015.07.034.
[57] B. Münch, L. Holzer, Contradicting geometrical concepts in pore size analysis attained with electron microscopy and mercury intrusion, J. Am. Ceram. Soc. 91 (2008) 1551–2916.
[58] W.B. Lindquist, The geometry of primary drainage, J. Colloid Interface Sci. 296 (2006) 655–668, http://dx.doi.org/10.1016/j.jcis.2005.09.041.
[59] P.-E. Oren, S. Bakke, O.J. Arntzen, Extending predictive capabilities to network models, SPE J. 3 (1998) 324–336, http://dx.doi.org/10.2118/52052-PA.

5.2 Capillary pressure curve simulations

We have shown in section 5.1 that simulations by pore networks extracted from images and full morphology simulations give very close results for liquid water injection experiments. Moreover, they succeed in predicting the distribution of water in a GDL that was imaged by X-ray tomography. In this section, additional simulations are carried out on other GDL images, to experimentally validate the capillary pressure curve simulations.

The images used in this section are the images of a compressed GDL SGL 24BA used in the previous section, as well as images of a compressed GDL Toray TGP-H-060. The images of TGP-H-060 were produced by the Paul Scherrer Institute according to a procedure identical to that which enabled the images of 24BA to be obtained. Figure 5.1 illustrates a full morphology simulation on a sub-sample of GDL 24BA.

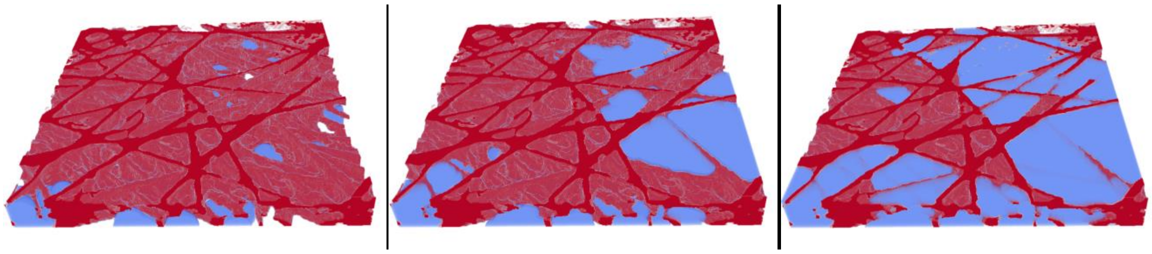

Figure 5.1 Full morphology simulation on a sub-sample of the 24BA image at different pressure levels (increasing pressure from left to right). The water is blue, the GDL is red. We see that the saturation of water increases when the pressure increases.

The capillary pressure curves give the capillary pressure P_c as a function of the saturation s of the medium. These curves make it possible to characterize the capillary properties of a porous material. These curves are central in the classical theory of two-phase flows in porous media. Indeed, generalized Darcy models rely on capillary pressure curves to model two-phase transports, as mentioned in section 2.2.3.1.

The capillary pressure curve can be measured by an ex-situ water injection experiment. The capillary pressure curve can also be simulated. Figure 5.2 shows a comparison of full morphology and experimental simulations for the capillary pressure curves of two types of GDL. The experimental measurement of the capillary pressure curves can be carried out using several experimental setups, as indicated in section 2.2.1.2. In the present case, liquid water is injected into the GDL. The ex-situ water injection experiment was carried out for the Impala project by the Paul Scherrer Institute. The description of the experimental setup is provided in [Lamibrac2016]. In the absence of precise measurement of the internal contact angle of these materials, the contact angles have been adjusted. The simulations are made with the contact angles $\theta = 115°$ for the 24BA and $\theta = 110°$ for the TGP-H-060. With these parameters, we find that the simulations are very close to the experimental curves for the rightmost branch of the capillary pressure curves. This branch corresponds to the injection of water into the GDL. This confirms that full morphology simulations based on tomographic GDL images are able to reliably predict water distributions in GDL during water injection experiments. The other branch of the capillary pressure curves corresponds to the extraction of water from the GDL. Different physical phenomena occur during extraction of water from the GDL, which we do not model during this thesis.

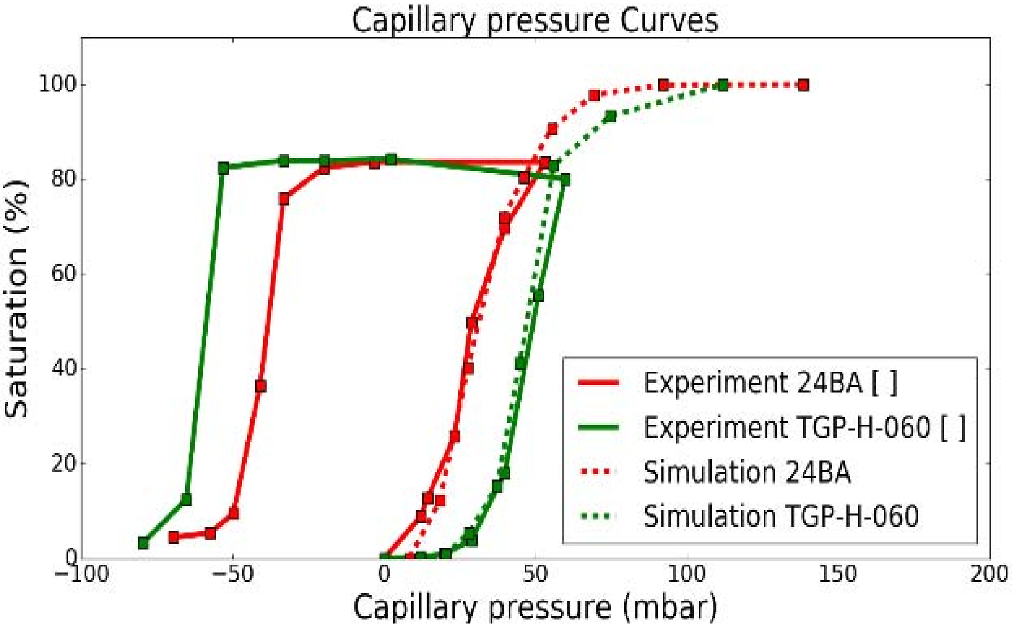

Figure 5.2 Comparison between experiment and full morphology simulation for capillary pressure curves. Two types of GDL are studied: GDL Toray TGP-H-060 (in green) and GDL SGL 24BA (in red). Figure created by author from data in [Lamibrac2016].

The GDL microstructure varies spatially. We therefore expect the capillary pressure curve to depend on the GDL sample on which the simulation is performed. We performed simulations on several subsamples of 24BA to study the spatial variability. We see in Figure 5.3 a) that there is some variability from one sub-sample to another (sub-sample size: 1.1mm * 1.1mm * 120µm). Figure 5.3 b) shows that the curve Pc (S) is not quite the same if we inject water from one side or the other. This effect is stronger if the sample is small.

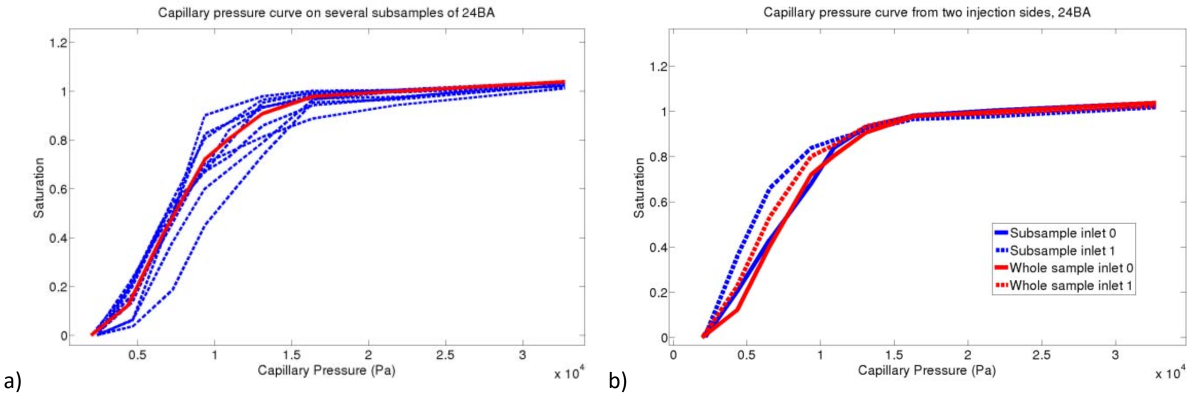

Figure 5.3 A) Variability of capillary pressure curves on sub-samples of GDL 24BA. In red, simulation on the complete sample. In blue, simulations on sub-samples. B) Simulations of capillary pressure curves, injecting water into the 24BA by a face or the opposite face. In red, capillary pressure curves for the complete sample. In blue, curves obtained on a sub-sample.

The question of spatial variability is dealt with theoretically in appendix 9.2. We propose here a similar analysis. Let us suppose that water transfers through the lateral faces of sub-samples can be neglected. This hypothesis is valid for samples large enough. Then the saturation on the complete sample is the arithmetic mean of the sub-sample saturations. We can visually verify this conclusion in Figure 5.3 a) by comparing the saturation on the complete sample and the saturations of the subsamples. The variability of an arithmetic mean of random variables is quantifiable on the basis of probability theory results.

To calibrate two-phase homogenized models of the generalized Darcy type, it is necessary to know the capillary pressure curve of the porous material. In the absence of data, the following analytical formula, called the Leverett-Udel correlation [Leverett1941] is often used:

$$P_c(s) = \sqrt{\frac{\varepsilon}{K}}\gamma\cos(\theta)\,J(s)$$

Équation 5.1

Where γ is the surface tension of the water, θ is the contact angle of the water on the solid material, ε is the porosity, K is the permeability, and $J(s)$ is some function of the saturation. To calibrate $J(s)$, the Leverett-Udel function [Udell1985] is often used:

$$J(s) = 1.417(1-s) - 2.120(1-s)^2 + 1.262(1-s)^3$$

Équation 5.2

Initially, this relationship was established empirically for capillary pressures curves of sand beds [Leverett1941]. Because of the lack of sufficient data on the permeability of the two GDLs studied in this chapter, we parameterize the Leverett curve without involving porosity and permeability. For this we define a characteristic pore radius R_{eff} and we set

$$P_c(s) = \frac{2\gamma\cos(\theta)}{R_{eff}}\frac{J(s)}{J(0.5)}$$

Équation 5.3

The shape of the curve is not modified, since only the constant before the function $J(s)$ is modified. The correspondence between these parameters and the parameters of the Leverett-Udel correlation is $R_{eff} = \frac{2}{J(0.5)}\sqrt{K/\varepsilon}$. Note that the parameters of the Leverett curve had to be adjusted in the absence of sufficient data on the permeability of the materials. Indeed, the GDLs considered are compressed. The compression changes both the permeability of the samples and their porosity. The porosity to be considered is also uncertain, as the total porosity of the GDL decomposes into macropores and micropores of the binder. These two types of pores do not have the same effect on the permeability and the capillary pressure.

Figure 5.4 shows a comparison between Leverett-Udel correlation and full morphology simulation for the capillary pressure curves of the two GDLs. The parameters used are as follows: $R_{eff} = 1.8\ \mu\mathrm{m}$ for GDL 24BA and $R_{eff} = 1.0\ \mu\mathrm{m}$ for GDL TGP-H-060. These values are lower than the average pore sizes of these two materials, as discussed in section 1.1.3. Note that the pore size distribution is calculated from the capillary pressure curve during a mercury injection porosimetry. The relationship between the two curves can be found in [Lenormand2003].

We see in Figure 5.4 that the shape of the Leverett curves imperfectly reflects the shape of the capillary pressure curve of the two GDLs. More generally, the validity of the Leverett-Udel correlation for GDL has been studied in several articles [Si2015] [Gostick 2006] [Liu 2015] [Schulz 2007]. Most conclude that the Leverett-Udel curve is poorly adapted to GDL. Indeed, GDL are complex materials whose microstructures are differents from that of the granular porous media on which the Leverett-Udel correlation has been established. Other correlations are more appropriate, such as van Genuchten or Brooks-Corey correlations [Si2015].

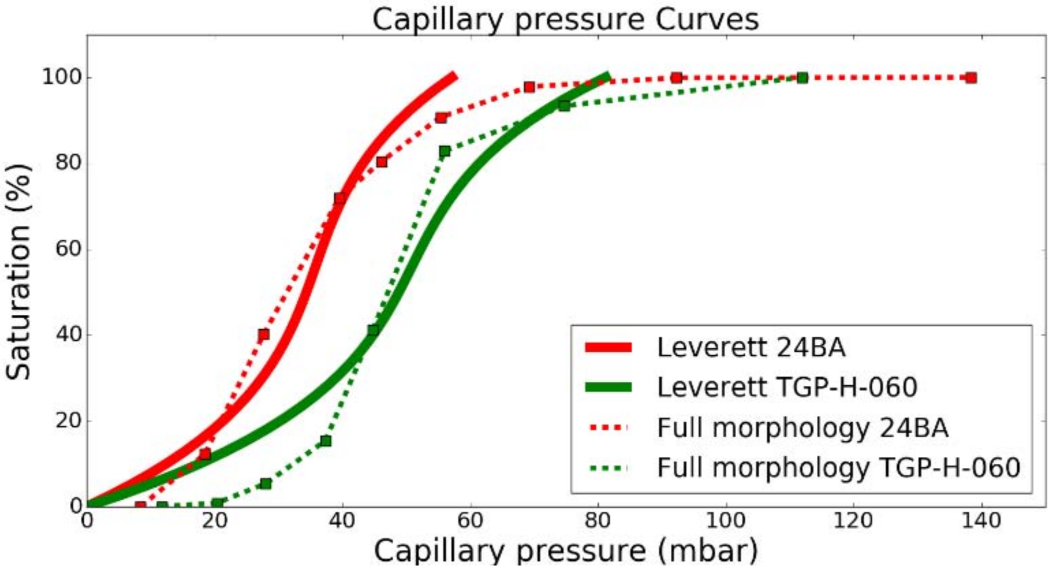

Figure 5.4 Comparison between the Leverett model and full morphology simulations for the capillary pressure curve.

5.3 Conclusion

This chapter is devoted to the modeling of liquid water injection experiments in GDLs of PEM fuel cells. We developed simulations based on tomographic images capable of effectively simulating water flows dominated by capillary forces. Two types of models have been developed, pores networks and full morphology.

These models were validated experimentally, using tomographic images of the distribution of water in the GDL during an ex-situ water injection experiment. We have validated that these simulations can reliably compute the capillary pressure curves of several types of GDL from images of their microstructure obtained by X-ray tomography. The pore network and full morphology models were compared between each other and give very close results. Thus, these simulation tools make it possible to characterize some two-phase transport in a GDL from their tomographic image. This information helps us to better understand the materials and are important elements for their improvement.

The full morphology model is easier to use than the pore network model because it works directly on the microstructure without any network extraction parameters. The full morphology model is perfectly suited for simulating capillary pressure curves. However, simulations on pore networks are more flexible than full morphology simulations with regard to boundary conditions for liquid water. In addition, the pore network tools developed here make it possible to model two-phase phenomena coupled with diffusive transports. It is used to model the actual operation of a fuel cell in Chapter 6. The pore network models are therefore preferable to the full morphology model when the physical phenomena to be modeled are more complex.

5.4 Bibliography

- [Gostick 2006] Capillary pressure and hydrophilic porosity in gas diffusion layers for polymer electrolyte fuel cells, Jeffrey T. Gostick, Michael W. Fowlera, Marios A. Ioannidisa, Mark D. Pritzkera, Y.M. Volfkovichb, A. Sakarsb, Journal of Power Sources, Volume 156, Issue 2, 1 June 2006, Pages 375–387

- [Lamibrac2016] A. Lamibrac, J. Roth, M. Toulec, F. Marone, M. Stampanoni, F. Buechi, Characterization of Liquid Water Saturation in Gas Diffusion Layers by X-Ray Tomographic Microscopy, J. Electrochem. Soc. 163 (2016) F202–F209.

- [Lenormand2003] INTERPRETATION OF MERCURY INJECTION CURVES TO DERIVE PORE SIZE DISTRIBUTION, R. Lenormand, international Symposium of the Society of Core Analysts, 2003

- [Leverett1941] MC Leverett, Capillary behavior in porous solids. American Institute of Mining and Metallurgical Engineers - Petroleum Development and Technology, 142 (152-168) 1941.

- [Liu 2015] Liquid water transport characteristics of porous diffusion media in polymer electrolyte membrane fuel cells: A review, Xunliang Liu, Fangyuan Peng, Guofeng Lou, Zhi Wen, Journal of Power Sources 299 (2015)

- [Schulz 2007] Modeling of Two-Phase Behavior in the Gas Diffusion Medium of PEFCs via Full Morphology Approach Volker Paul Schulz, Jürgen Becker, Andreas Wiegmann, Partha P. Mukherjee, and Chao-Yang Wang, Journal of The Electrochemical Society, 154 4 B419-B426 2007

- [Si2015] Chao Si, Xiao-Dong Wang, Wei-Mon Yan, and Tian-Hu Wang, *Review Article: A Comprehensive Review on Measurement and Correlation Development of Capillary Pressure for Two-Phase Modeling of Proton Exchange Membrane Fuel Cells,* Hindawi Publishing Corporation Journal of Chemistry Volume 2015, Article ID 876821, 17 pages

- [Udell1985] KS. Udell, Heat transfer in porous media considering phase change and capillarity - The heat pipe effect. International Journal of Heat and Mass Transfer, 28 (485-495) 1985.

Chapter 6 Water condensation in a GDL

The physical phenomenon studied in this chapter is a transport by diffusion through the GDL of water vapor produced in the cathodic catalytic layer, with condensation of part of the water vapor in a cold region of the GDL [Nam2003]. Since heat is produced in the catalytic layer, the catalytic layer is generally warmer than the GDL. The contact area between the rib of the bipolar plate and the GDL is generally the coldest place in the GDL because the bipolar plate is cooled by the cooling system of the fuel cell. This region is therefore favorable to the condensation of water vapor. The condensation of water in the GDL under the rib of the bipolar plate was confirmed by X-ray tomography images [Straubhaar2015]. The vapor may also condense pointwise where the surface energy is favorable to phase change, for example in hydrophilic areas, or in places where liquid water is already present [Ceballos2011]. It results from the condensation that pores are invaded by liquid water, which reduces the transfer of reactive gases to the cathodic catalytic layer.

This phenomenon of water vapor diffusion and condensation in GDL therefore involves diffusive transports in GDL (gas diffusion, heat conduction) and capillary forces at the level of the condensed water droplets. The simulation of this phenomenon implies to simulate diffusive transports and two-phase phenomena in a coupled way. We have shown in Chapter 5 that pore networks are well adapted to model capillary forces in the GDL. We have shown in Chapter 3 that pore networks extracted from images can simulate very fast diffusive transport. So, we use pore networks to simulate water condensation in GDL

The outline of this chapter is as follows. The first section presents the methodology used. The method of simulation of the water condensation in the GDL by pore network is presented, then the method of construction of the pore networds by Voronoi mesh is presented. The second section presents condensation simulations in Voronoi pore networks representing GDL. A section of perspectives and a conclusion complete this chapter.

6.1 Methodology

6.1.1 Network pore model of condensation in a GDL

The algorithm used to simulate water condensation in GDL was originally developed in [Straubhaar2015] for simulations on regular pore networks. We implement this algorithm into a pore network code capable of processing non-regular networks. Note that the algorithm is the same in both cases, but needed to be reimplemented in the non-regular pore network code.

6.1.1.1 Algorithm for condensation of water coupled with mass and heat diffusive transports

We present here the algorithm presented in [Straubhaar2015] and used in this thesis, to simulate the condensation of water in a GDL of PEM fuel cells in operation. This algorithm describes the evolution of the condensed liquid water distribution as a function of the capillary forces and the couplings between phase change, water vapor diffusion and heat transport.

Condensation occurs in two stages. The first stage of the condensation is a nucleation stage. The partial vapor pressure field is calculated from the vapor concentration field, obtained by simulating the diffusion of water vapor in the pore network. The partial vapor pressure field is compared to the equilibrium vapor pressure field, calculated by simulating the diffusion of heat in the pore network. Pores in which the partial vapor pressure is higher than the equilibrium vapor pressure, i.e. whose relative humidity is greater than 1, are considered as potential nucleation points. They are filled with water per an iterative procedure which consists in filling with water the pore with the highest relative humidity, then recalculating the concentration field of the water vapor, considering that on the links of the pore filled with water, the presence of a gas liquid interface requires that the partial vapor pressure be equal to the equilibrium vapor pressure, and so on until no more pores are present where relative humidity is greater than 1. This nucleation stage corresponds to steps 1 to 4 of the algorithm described below.

The second stage is a growth of the clusters of liquid water due to the condensation of water vapor. The rate of phase change is controlled by the flux of diffusion of the water vapor coming from the catalytic layer. The capillary forces control the direction of growth of the clusters of liquid water: the clusters grow in the direction of the link where the capillary pressure is lowest. Two clusters of liquid water coalesce when they are in contact, thereby equalizing the capillary pressures in the two clusters and pooling the flows of water vapor received by the two clusters. This stage of growth of the liquid water clusters corresponds to steps 5 to 9 of the algorithm described below.

The algorithm used is the following [Straubhaar2015] :

1. Identify different water clusters. If two pores completely filled with water are adjacent, they belong to the same cluster of water.
2. Calculate the water vapor volume fraction field x_v resulting from the vapor diffusion. The boundary conditions for calculating the diffusion of vapor are as follows. In each bond at the interface between an invaded pore and a pore not invaded by the liquid water, the local saturation pressure is imposed. In these links, $x_v = p_{vs}/P_{ref}$, where p_{vs} depends on the local temperature. The boundary conditions at the boundaries of the computational domain are imposed by the conditions of use of the fuel cell. They are described below.
3. If in some pores the partial vapor pressure calculated in step 2 is greater than the nucleation threshold, defined as the product of the equilibrium vapor pressure by a constant supersaturation factor, then identify the pore with the highest relative humidity, fill it with water, and impose $x_v = p_{vs}/P_{ref}$ in its links in contact with gaseous pores.
4. Repeat steps 2 and 3 until no more gaseous pores have a relative humidity greater than the supersaturation factor.
5. Calculate the molar condensation flow F_k at the boundary of each liquid cluster k.
6. For each cluster, determine the link at the boundary of the cluster with the lowest capillary pressure.

7. For each cluster, calculate the time t_k required to completely invade the pore adjacent to the link found in step 6: $t_k = c_l V_{ad,k}/F_k$, where $V_{ad,k}$ is the volume that remains to invade in the pore, and c_l is the molar concentration of liquid water.
8. Calculate the time step $dt = min(t_k)$.
9. Completely invade the pore adjacent to the link found in step 6 and update the volume of liquid in the pores invaded by the other clusters during dt.
10. Repeat steps 5-9 until a stationary solution is reached, ie the total phase change rate is zero, or until F_k becomes negative at the boundary of one of the clusters.

The supersaturation factor mentioned in step 3 is used to limit the number of pores invaded during nucleation. This factor was introduced originally in [Straubhaar2015] to compare simulations of condensation on regular networks to experimental results. We do not know at this stage whether this factor is relevant for morphological networks, which are supposed to better consider geometries and diffusive transports in GDL. Depending on the case, we take its value equal to 1, which amounts to not considering supersaturation, or 1.1, which amounts to limiting a little the nucleation. We no longer mention this factor afterwards, and assume that it was taken equal to 1 in the simulations.

6.1.1.2 Vapor pressure at the liquid-gas interface

We assume that, at the liquid-gas interfaces, the partial pressure of water vapor P_v is equal to the equilibrium vapor pressure P_{vs}:

$$P_v = P_{vs}$$

Équation 6.1

The saturating vapor pressure P_{vs} is modeled by the Antoine equation:

$$P_{vs}(T) = P_{ref} \times 10^{A - \frac{B}{T+C+273}}$$

Équation 6.2

where T is the temperature in °C, $P_{ref} = 101325\ Pa$, $\mathrm{A} = 5.40221$, $\mathrm{B} = 183.675$, $\mathrm{C} = -31.737$.

As mentioned above, we assume that, at the liquid-gas interfaces, $P_v = P_{sat}$. This equality is very often used when phase changes are modeled. It is justified by the fact that if the partial pressure of water vapor were not equal to the equilibrium vapor pressure, the resulting rate of change of phase would be greater by several orders of magnitude than the flow of water coming in by diffusion. Indeed, a model of evaporative flux at the liquid vapor interface such as the Herz-Knudsen-Schrage equation (also called Kucherov-Rikenglaz equation) [Ajaev2012], based on the kinetic theory of gases, shows that when $P_v \neq P_{sat}$, the phase change rate is proportional to the difference between P_v and P_{vs} :

$$J_{vapeur \rightarrow liquide} = (P_v - P_{vs}) \frac{2\hat{\sigma}}{2 - \hat{\sigma}} \sqrt{\frac{M}{2\pi RT}}$$

Équation 6.3

where $J_{vapeur \rightarrow liquide}$ is the evaporation flux at the liquid vapor interface and $\hat{\sigma}$ is an adimensioned parameter called the accommodation coefficient. This parameter is related to the details of the interaction of the gas with the liquid interface in the Knudsen layer. It is often unknown.

In practice, this rate of phase change is very high if there is a difference between vapor pressure and saturated vapor pressure. Indeed:

$$\sqrt{\frac{M}{2\pi RT}} \approx \sqrt{\frac{1.8 * 10^{-2} kg.mol^{-1}}{2 * 3.14 * 8.314 J.mol^{-1}.K^{-1} * 310K}} \approx 1.1 * 10^{-3} kg.s^{-1}.Pa^{-1}$$

Équation 6.4

In case of a deviation of a few Pa between P_v and P_{sat}, the rate of phase change would be very high in comparison with the rate of water production by the cell. The return to equilibrium $P_v = P_{vs}$ would be done very quickly. Therefore, we assume that at the interface of liquid water clusters, $P_v = P_{vs}$.

Thus, the rate of phase change is not controlled by the kinetics of the gas molecules at the liquid-gas interface. This is why, in our model of condensation, the diffusion of water vapor limits the rate of phase change.

6.1.1.3 Diffusion of water vapor

At the interface between the GDL and the catalytic layer, boundary conditions representing the production of water in the catalytic layer are imposed. A first option is to impose a surfacic flux of water vapor Q:

$$Q = \beta_{diffusion} \frac{i}{2F}$$

Équation 6.5

Where i is the current produced per unit area, F is the Faraday constant and $\beta_{diffusion}$ is an adimensioned factor modeling the proportion of produced water which is evacuated on the cathode side. 1-$\beta_{diffusion}$ then represents the proportion of produced water which passes through the membrane and is evacuated on the anode side. We take $\beta_{diffusion} = 0.8$. The total vapor flux is distributed over the different inlet links as a function of their surface area. A second option is to impose a relative humidity value at the interface between the GDL and the catalytic layer. This amounts to imposing Dirichlet boundary conditions on the concentration of water rather than imposing a flux of water vapor. In this case, a fixed concentration gradient between the catalytic layer and the channel induces the diffusion of water. The concentration profiles in the thickness of the GDL are then linear in the absence of water. On the other hand, these conditions may be less representative of the actual operating conditions of the battery.

At the channel, a concentration of water vapor is imposed, corresponding to the relative humidity in the channel. At the level of the liquid-gas interfaces, we impose $P_v = P_{vs}$. On the other boundaries of the domain, we impose zero flux conditions. Figure 6.1 illustrates the boundary conditions used for simulations of water vapor diffusion in GDL.

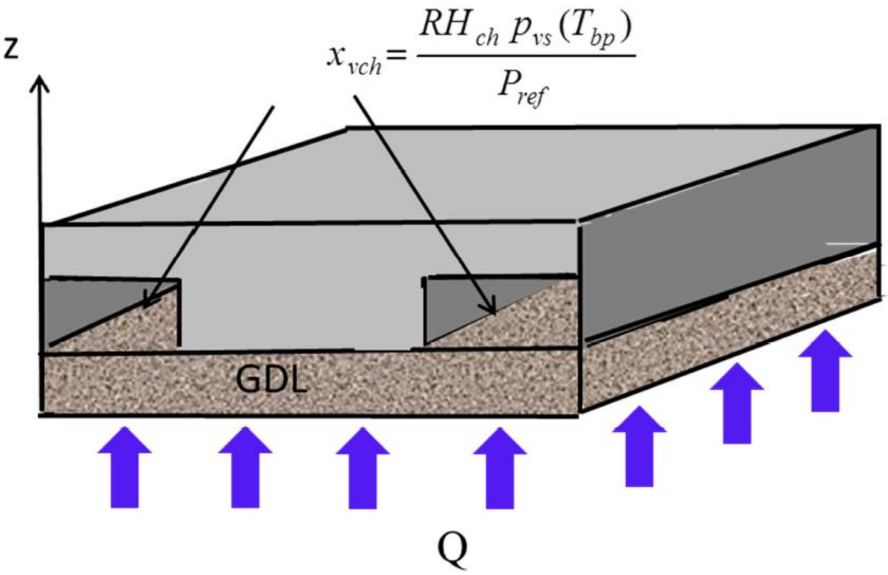

Figure 6.1 Boundary conditions for the transport of water vapor by diffusion. Figure extracted from [Straubhaar2015].

The diffusion conductances of the pore network are calculated by a method like the method explained in Chapter 3. It should be recalled that this method consists in approximating the geometry of the pores and the links of the network by simplified shapes on which analytic formulas give the conductances. This method captures some geometric effects, but progress is required to make these calculations more accurate. Another approach consists in calibrating the conductances with a free parameter, so that the effective diffusivity of the pore network is equal to the effective diffusivity of an experimentally measured GDL. This approach can make it possible to better evaluate the water vapor fluxes in the direction of the thickness of the GDL, which have a significant effect on the condensation of the water. However, since the GDL is anisotropic, it is possible that a single calibration parameter is not sufficient to calibrate the different components of the effective diffusivity tensor.

6.1.1.4 Heat transfer

At the interface between the GDL and the catalytic layer, boundary conditions modeling the heat production in the catalytic layer are imposed. A first option is to impose a surfacic flux of heat coming from the cathodic catalytic layer:

$$\Phi = \left(\frac{\Delta H^{vap}}{2F} - U\right) i$$

Équation 6.6

where Φ is the flux of heat produced by the chemical reaction per unit surface, ΔH^{vap} is the enthalpy of the chemical reaction of water production from dihydrogen, U is the cell voltage, I is the surface produced by the cell per unit surface, F is the constant of Faraday [Thomas2013].

$$\beta_{thermic}\Phi = -\lambda_{eff}^{\perp}\frac{\partial T}{\partial z}$$

Équation 6.7

Where $\lambda_{eff}^{\perp}$ is the effective thermal conductivity of the GDL in the through-plane direction, T is the temperature, z is the position in the through-plane direction of the GDL, $\beta_{thermic}$ is an adimensioned factor representing the heat fraction which is evacuated on the cathode side. $1 - \beta_{thermic}$ is the fraction of the heat that passes through the membrane and is evacuated on the anode side. We take $\beta_{thermic} = 0.5$. The total heat flux is distributed over the different inlet links as a function of their surface area. A second option is to impose a temperature value at the interface between the GDL and the catalytic layer. This amounts to imposing Dirichlet boundary conditions on temperature rather than imposing a heat flux. In this case, a fixed temperature gradient between MPL and channel controls the heat transport. The temperature profiles in the thickness of the GDL are then linear. On the other hand, these conditions may be less representative of the actual operating conditions of the fuel cell.

At the contact between the GDL and the rib of the bipolar plate, a temperature value is imposed. On the other boundaries of the domain, we impose zero heat flux conditions. Note that we imposed a zero flux at the channel for the simulations presented in section 6.2. It would be more realistic to impose a temperature value at the channel. Figure 6.2 illustrates the boundary conditions used for heat transport simulations in GDL.

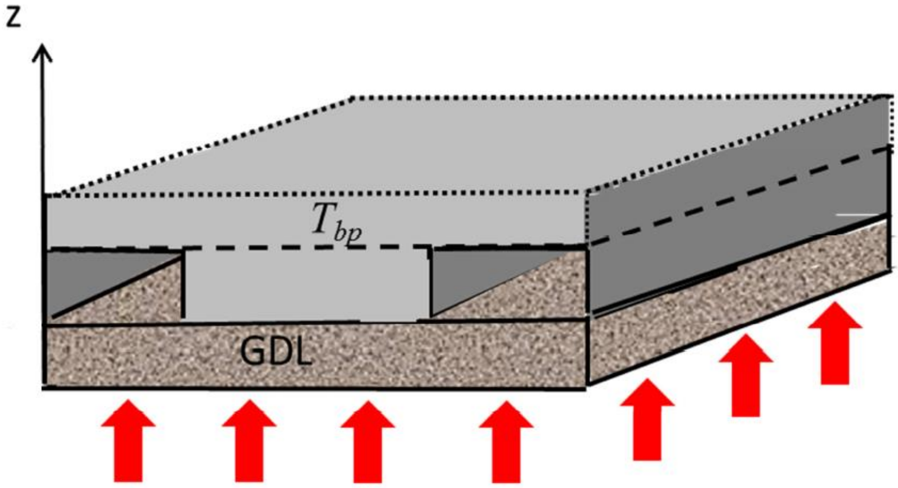

Figure 6.2 Boundary conditions for the transport of heat. Figure extracted from [Straubhaar2015].

We do not consider the heat sources due to the release of the latent heat of evaporation of the water during the phase change. We assume that this heat is immediately evacuated to the bipolar plate. The thermal conductances of the pore network are calculated by a method like the method explained in Chapter 3.

6.1.2 Construction of pore networks from Voronoi diagrams

The pore networks used in this chapter are constructed using a method based on the Voronoi diagrams, presented in [Gostick2013].

We generate a mesh of Voronoi from points randomly distributed in space. The Voronoi mesh can be generated with the Matlab function *voronoi*. Figure 6.3 shows a Voronoi mesh generated from random points. Once the mesh is constructed, the pores are defined as the cells volumes. There is therefore one pore per cell. Each cell of the Voronoi mesh is a polyhedron. A bond connects two pores if the cells of these pores have a common face. Thus, a pore has a random number of links, depending on the number of neighboring cells, which is linked to the local configuration of the Voronoi mesh. To introduce a solid phase in the Voronoi mesh, the mesh edges are considered as cylinders whose radius is calibrated to obtain the desired porosity. The conductances used in the diffusive transport simulations and the critical capillary pressures used in the two-phase transport simulations are calibrated using a geometric analysis of the pores and links constructed from the meshes. Pore network simulations can be carried out on the pore networks thus constructed.

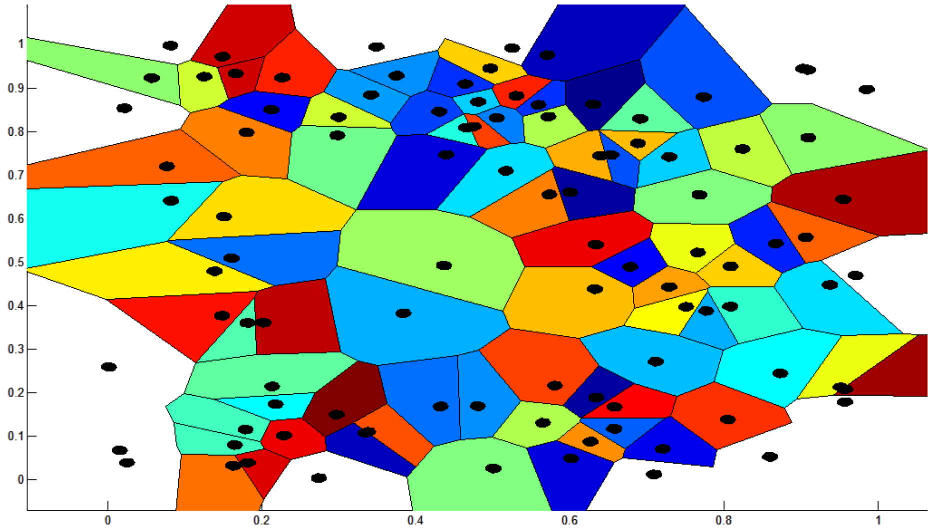

Figure 6.3 Voronoi mesh generated from a set of random points. The cells of the mesh are represented in color, the points from which the mesh is generated are represented in black.

The generation of non-regular pore networks from Voronoi meshes has a number of advantages. Voronoi meshes can be generated in the plane or in space, which makes it possible to construct two or three dimensional pore networks. It is possible to play on the size of the pores by generating meshes of Voronoi having more or less cells. We used the following formula to adapt the cell density n_{pore} of the Voronoi mesh to the experimental pore sizes distribution:

$$n_{pore} = \frac{\varepsilon}{V_{pore}}$$

Équation 6.8

Where n_{pore} is the number of cells per unit volume, ε is the porosity and $\overline{V_{pore}}$ is the mean volume of a pore, obtained for example from the experimental pore size distribution. With this method, we calibrate only the average pore size of the Voronoi pore network on the experimental pore size distribution. The shape of the pore size distribution of the Voronoi pore network results from the statistical properties of the Voronoi meshes.

It is possible to create two neighboring zones having different pore sizes by distributing a more dense random distribution of points in one zone than in the other and then generating the associated Voronoi mesh. The assembly of a GDL and a MPL is an example of a porous medium composed of two layers having different pore sizes. Figure 6.4 shows an example of a two-layer porous structure, generated from a Voronoi mesh. Finally, it is possible to create an anisotropic pores network by deforming the mesh in one direction by contracting or expanding the lengths in this direction. GDL are an example of anisotropic porous material.

We perform the simulations of this chapter on non-regular pore networks constructed from Voronoi meshes.

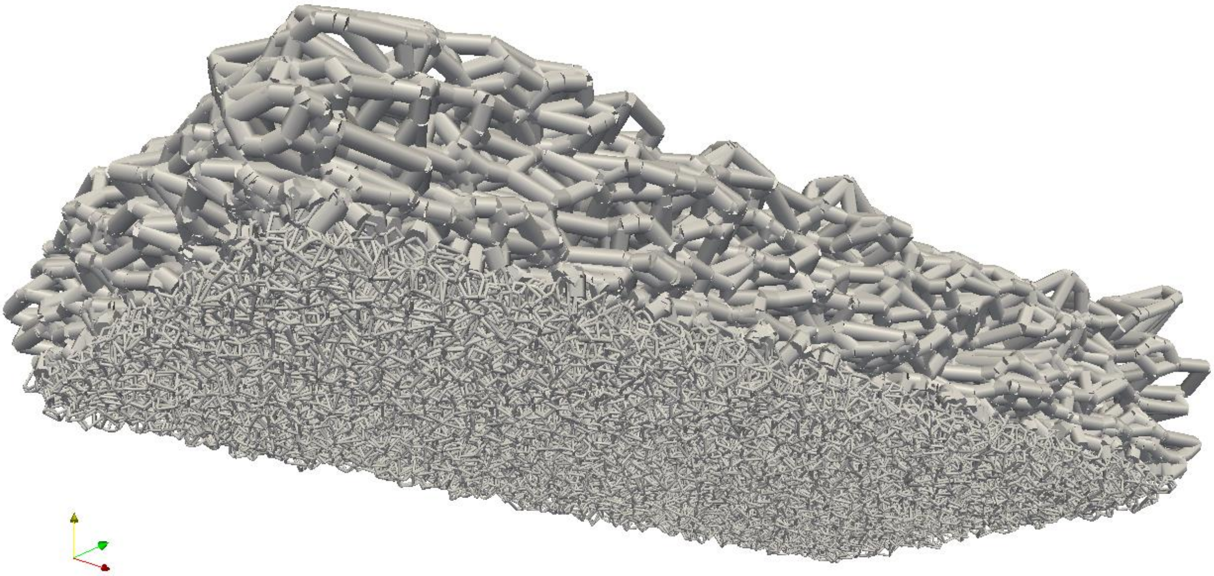

Figure 6.4 A porous microstructure generated from a Voronoi mesh. This microstructure is composed of two regions having different pore sizes. The pores are the polyhedral meshes of the Voronoi mesh. The edges of the meshes, thickened, constitute the solid. Figure created by author and also used in [Prat2015].

6.2 Results

6.2.1 Condensation simulations on Voronoi pore networks

We present in this section simulations of condensation in pore networks constructed from Voronoi meshes. These networks represent a GDL in a working fuel cell. The boundary conditions applied to these networks mimic, on one side, a catalytic layer and, on the other side, a rib-channel pattern of a bipolar plate, constituted by two half-channels located on either side of a rib. We first present a simulation of condensation on a 3D pore network. We discuss the results of this simulation. We then present simulations of condensation on two 2D pore networks. The only difference between the two 2D pore networks is the anisotropy of the microstructure. These simulations give a first example of the possibility of studying the effect of the anisotropy of the microstructure on the condensation of water.

6.2.1.1 Condensation simulations on a 3D Voronoi pore network

We present in this section a simulation carried out on a pore network generated from a mesh of Voronoi in 3D. The dimensions of this network are determined per the actual dimensions of a GDL and of a rib-channel pattern of bipolar plate: the thickness of the network is 300 µm, its width is 2 mm (for two half-channels of 0.5 mm and a 1mm rib), its depth is 1mm. The number of cells of the Voronoi mesh is adjusted so that the average diameter of a cell is 30 µm, which corresponds to the mean pore size of the GDLs (30 to 50 µm in diameter on average). The network is constructed with some anisotropy, contracting the lengths by a factor of 2 in the thickness during the generation of the Voronoi mesh. We did not put a MPL under this GDL network, that is, we simulate the condensation in a GDL in direct contact with a catalytic layer. Figure 6.5 shows the results of the condensation simulation on this network. The network configuration is visible on the 3-D visualizations shown in Figure 6.5. On the upper face of the pore network, the central zone is in contact with the rib, while the lateral zones are located under the channels. The lower face of the pore network is in contact with the catalytic layer.

Tableau 6-1 lists the boundary conditions and parameters used for this simulation of condensation. No-flux boundary conditions were imposed in the channels for heat transport.

Parameter	Value used
Relative humidity at the GDL-MPL interface	0.95
Relative humidity at the GDL-channels interface	0.60
Air pressure	1.5 bar
Temperature at the GDL-MPL interface	90 °C
Temperature at the GDL-rib interface	50 °C
Contact angle	110°, uniform
Binary diffusion coefficient of water vapor in air	$2.10^{-5}\ m^2.s^{-1}$

Tableau 6-1 Parameters used in the simulations of water condensation in the 3D Voronoi pore network.

Temperature

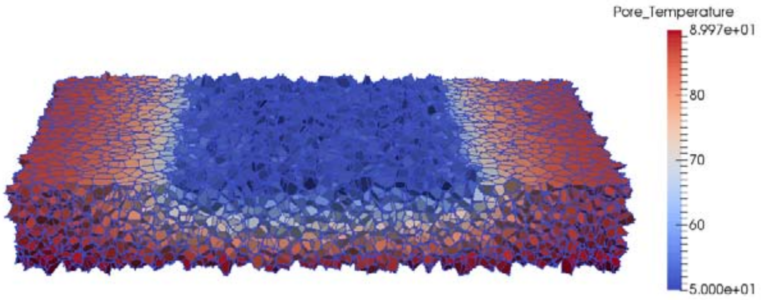

Temperature profiles

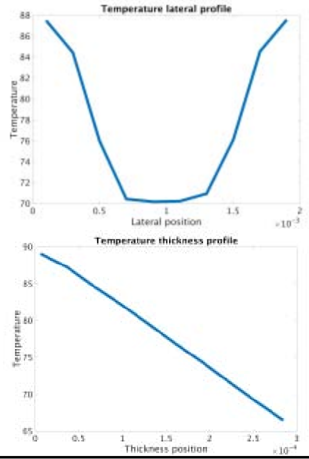

Equilibrium vapor pressure

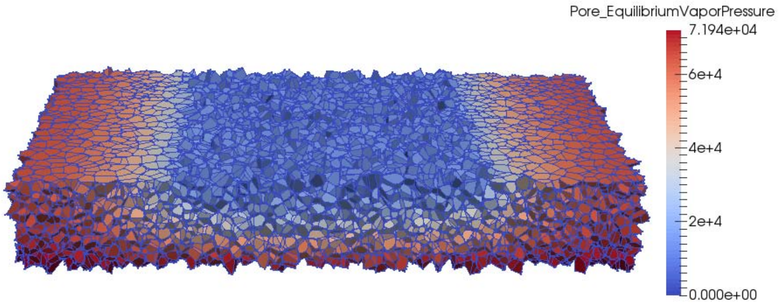

Equilibrium vapor pressure profiles

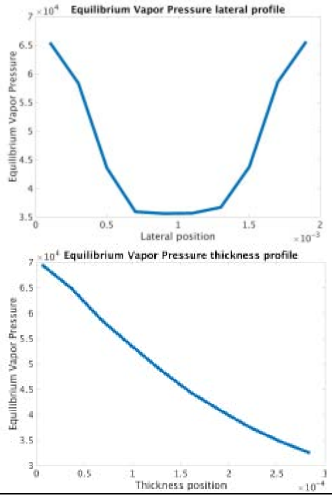

Relative humidity - begining

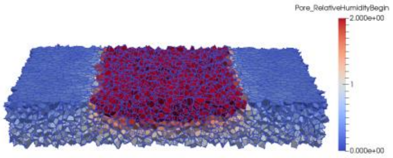

Relative humidity – nucleation end

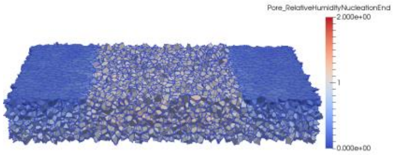

Relative humidity – growth end

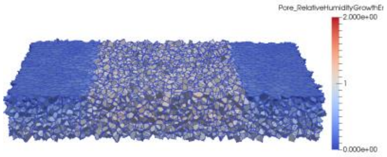

Relative humidity profile – in-plane

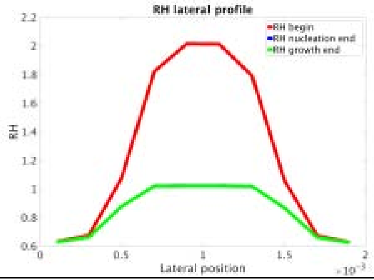

Relative humidity profile - through-plane

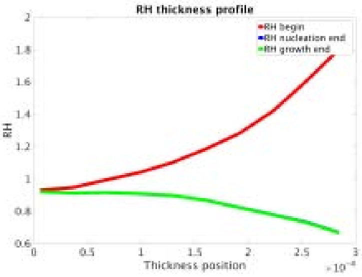

Max RH evolution during nucleation iterations

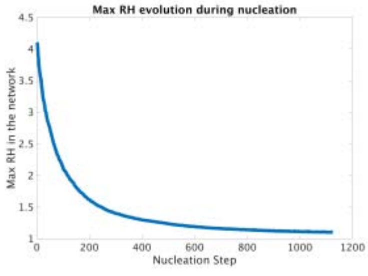

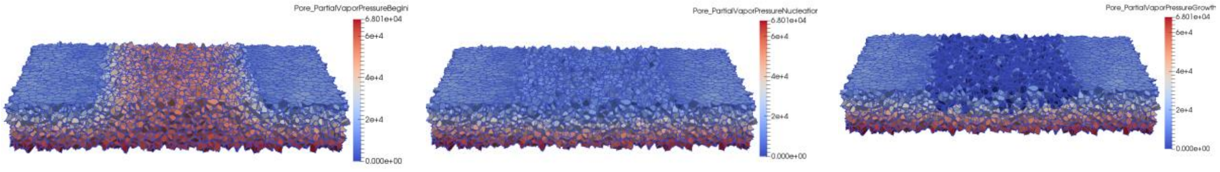
Partial vapor pressure - begining

Partial vapor pressure – nucleation end

Partial vapor pressure – growth end

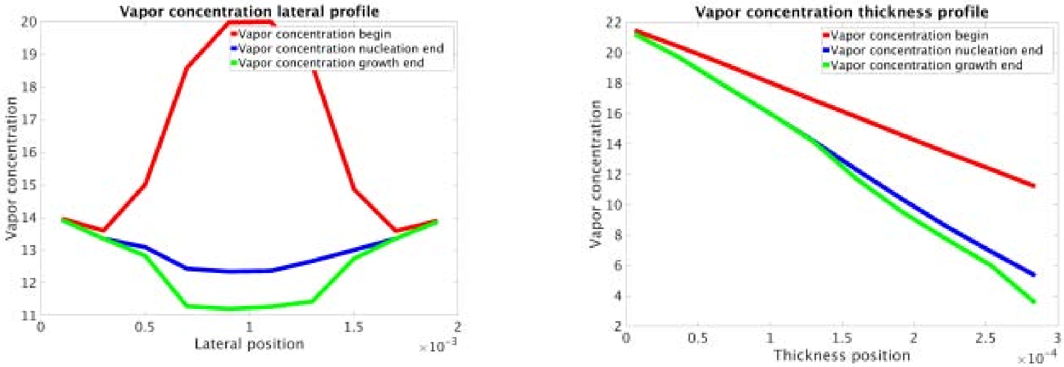
Concentration profile – in-plane

Concentration profile- through-plane

Water distribution at the end of condensation

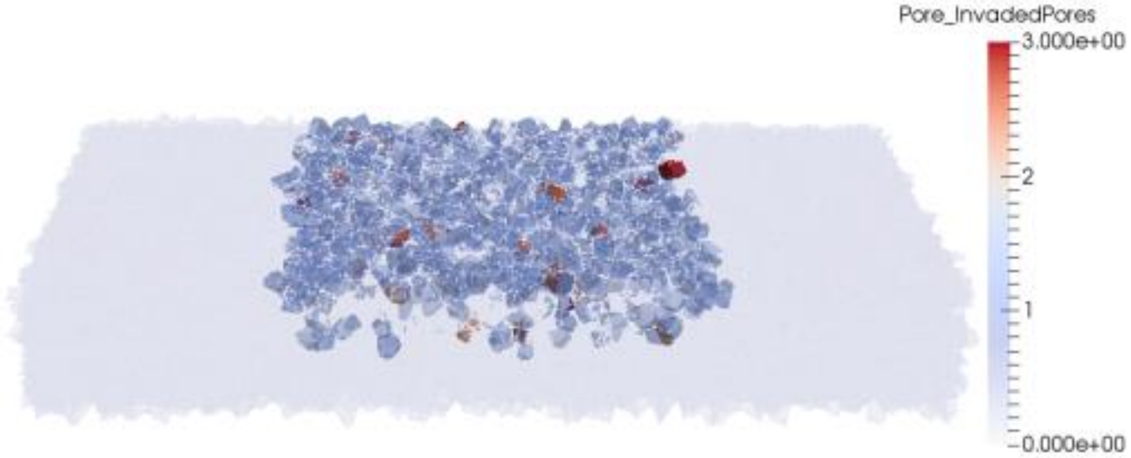

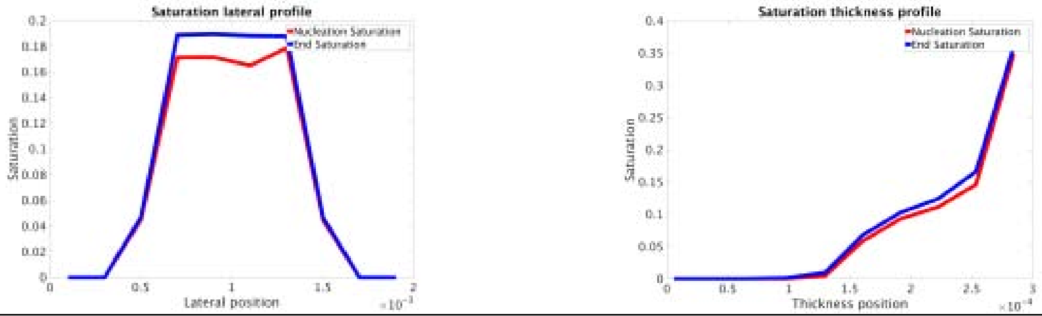
Saturation profile – in-plane

Saturation profile – through-plane

Figure 6.5 Condensation results on an isotropic Voronoi 3D network. Thickness of the GDL: 300µm. Width: 2mm, including 1mm under the rib, thickness: 1mm. Average diameter of a pore: 30µm. The in-plane profiles are profiles along the channel-rib-channel direction.

We see in Figure 6.5 that the temperature is lower under the rib than everywhere else in the GDL. Indeed, a higher temperature is imposed at the catalytic layer, and a zero heat flux is imposed on the channels and the lateral boundaries. The temperature is calculated at the beginning of the simulation. We assume that the temperature does not vary during the condensation. It results from the temperature field that the equilibrium vapor pressure is lower under the rib than elsewhere in the GDL. This makes the region under the rib a preferential region for condensation.

The relative humidity field varies greatly during the nucleation stage. The relative humidity field is initially much greater than 1 under the rib. The nucleation stage consists in iteratively invading the pore with the highest relative humidity, at the boundary of which the relative humidity is set at 1. This iterative procedure reduces the average value of the relative humidity field. At the end of the nucleation, all the pores have a relative humidity of less than or equal to 1. The vapor pressure field is deduced from the relative humidity and the equilibrium vapor pressure, so we do not comment on it.

The through-plane profile of the water vapor concentration shows that the water vapor concentration at the catalytic layer does not vary during the condensation. Indeed, we used Dirichlet boundary conditions for the concentration at the catalytic layer in this simulation. The concentration of water vapor at the interface between the GDL and the bipolar plate decreases during nucleation. The concentration profile in the plane shows that this is due to the decrease in relative humidity under the rib during nucleation. This is due to the increasing number of liquid-gas interfaces under the rib. The concentration of water vapor is imposed in the channels, thus it does not vary. The through-plane profiles of water vapor concentration remain linear, because the water saturation remains low in the GDL, so the pores are not blocked. Note that at the end of the nucleation stage the concentration of water vapor under the rib is less than the concentration of water vapor under the channel. This can result in a flux of water vapor from the canal to the GDL. Nevertheless, this flux appears to be low compared to the vapor flux coming from the catalytic layer, per the concentration profiles.

The saturation profiles at the end of the nucleation stage and at the end of the cluster growth stage indicate that the nucleation stage is responsible for most of the condensation in this simulation, while the cluster growth stage is very short. The 3D representation of the water distribution at the end of the condensation indicates that the water condensed directly under the rib, which is typical of the nucleation stage. The pores shown in dark blue are the pores filled with water as a result of nucleation. Pores whose colors vary from dark blue to red are pores filled with water during the stage of cluster growth. For this stage of cluster growth, the color of the pores is a function of the order in which the pores have been invaded over time. The capillary digitations, characteristic of the cluster growth step, are not visible, indicating that the stage of cluster growth was short. We can not say that it is realistic that the stage of cluster growth is so short, for the operating conditions simulated here. A more thorough calibration of the parameters would be required. It should be verified that the water vapor fluxes have realistic values, even if it is necessary to calibrate the diffusion conductances of the network using experimental characterizations of effective diffusivity. The anisotropy of the effective diffusivity is also an essential parameter for these simulations, which should be calibrated properly.

Thus, we have shown that the condensation simulations in a 3D Voronoi pore network give coherent temperature and concentration fields. Additional numerical checks would be necessary to be able to draw lessons on condensation in GDL from these simulations.

6.2.1.2 Condensation simulations on 2D Voronoi pore networks

We present in this section simulations carried out on two Voronoi pore networks in 2D. The dimensions of these networks are fixed according to the actual dimensions of a GDL and a rib-channel pattern of bipolar plate: the thickness of a network is 300 µm, its width is 2 mm (for two half-channels of 0.5mm and a 1mm rib). The number of cells in the Voronoi mesh is adjusted so that the mean diameter of a pore is 30 µm. The first network is isotropic. The second network is made strongly anisotropic, by contracting the lengths by a factor of 5 in the thickness during the generation of the Voronoi mesh. We have not put MPL under these GDL networks, that is, we simulate condensation in two GDLs in direct contact with catalytic layers. Figure 6.6 shows the results of the condensation simulation on the isotropic pore network, Figure 6.7 shows the results of the condensation simulation on the anisotropic pore network. The configuration of the networks is visible on the visualizations of the networks on Figure 6.6 and Figure 6.7. Note that the networks appear distorted on Figure 6.6 and Figure 6.7. The actual width of the networks is about 7 times larger than their thickness. On these visualizations, the upper faces of the pore networks are in contact with a bipolar plate consisting of two half-channels on either side of a central rib. The lower faces of the pore arrays are in contact with the catalytic layer. Tableau 6-2 lists the boundary conditions and parameters used for these simulations. No-flux heat boundary conditions were imposed in the channels. Tableau 6-2 lists the boundary conditions and parameters used for condensation simulations on Voronoi 2D pore networks.

Parameter	Value used
Relative humidity at the GDL-MPL interface	0.95
Relative humidity at the GDL-channels interface	0.80
Air pressure	1.5 bar
Temperature at the GDL-MPL interface	90 °C
Temperature at the GDL-rib interface	60 °C
Contact angle	110°, uniform
Binary diffusion coefficient of water vapor in air	$2.10^{-5}\ m^2.s^{-1}$

Tableau 6-2 Parameters used in simulations of water condensation in pore networks constructed from a 2D Voronoi mesh.

The interpretation of Figure 6.6 and Figure 6.7 is the same as for the 3D Voronoi network. We therefore only discuss the differences between the simulations, related to the effect of the anisotropy of the network.

The nucleation stage is more important in the isotropic network. This is because the area where the relative humidity is greater than 1 is greater in the isotropic network than in the anisotropic network. This relative humidity field difference is caused by a very different temperature field in both cases. The regions under the rib and under the channels have a very high temperature difference in the case of an isotropic lattice, whereas this difference is smaller in the case of an anisotropic lattice.

The concentration and temperature gradients in the plane are stronger in the isotropic case than in the anisotropic case. This is due to a lower effective diffusiviy in the plane and a lower effective thermal conductivity in the plane in the isotropic network than in the anisotropic network.

The distributions of liquid water are similar in both cases, except for the presence of an additional capillary digitation in the isotropic case. There is more liquid water under the rib than under the canals. The saturation of liquid water decreases in thickness as the distance from the rib increases. To obtain reliable results on the water distributions at the end of condensation, a verification of the criterion for stopping condensation simulations may be necessary. Additional simulations are required to better establish the effect of anisotropy on the condensation of water in GDL.

Temperature

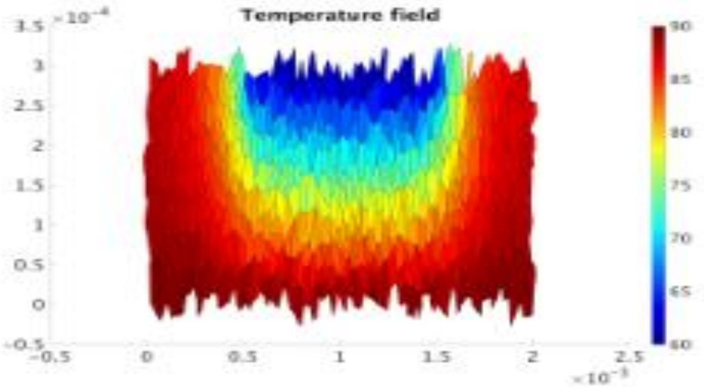

Temperature profiles

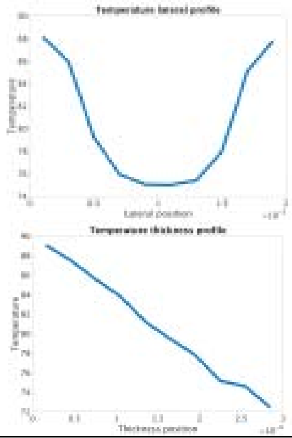

Equilibrium vapor pressure

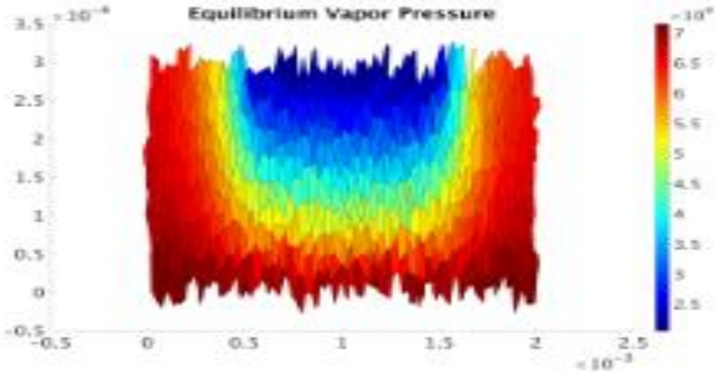

Equilibrium vapor pressure profiles

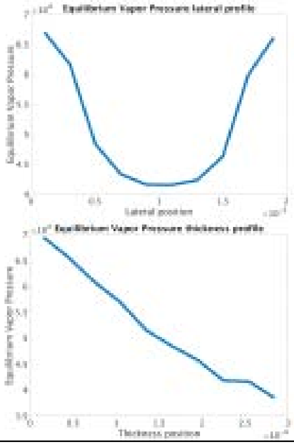

Relative humidity - begining

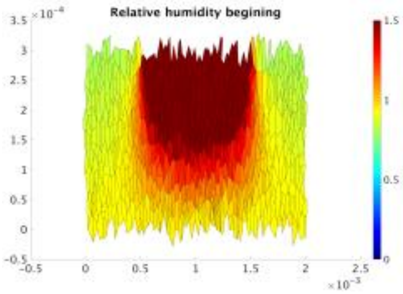

Relative humidity – nucleation end

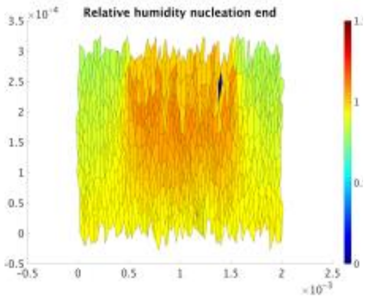

Relative humidity – growth end

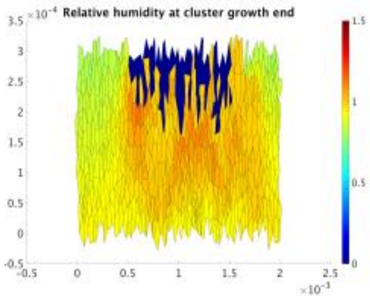

Relative humidity profile – in-plane

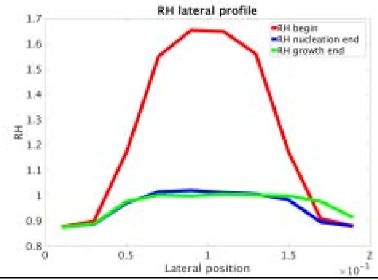

Relative humidity profile - through-plane

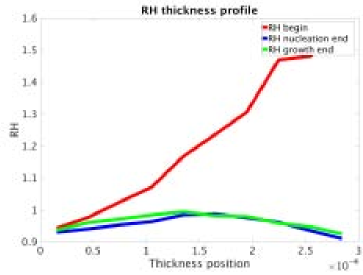

Max RH evolution during nucleation iterations

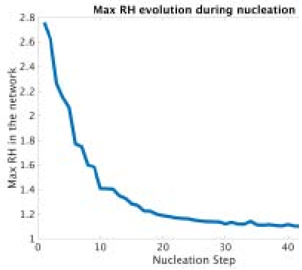

Partial vapor pressure - begining

Partial vapor pressure – nucleation end

Partial vapor pressure – growth end

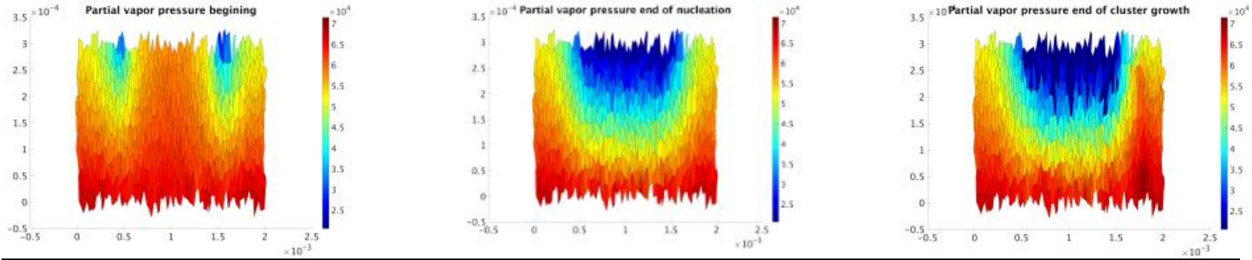

Concentration profile – in-plane

Concentration profile- through-plane

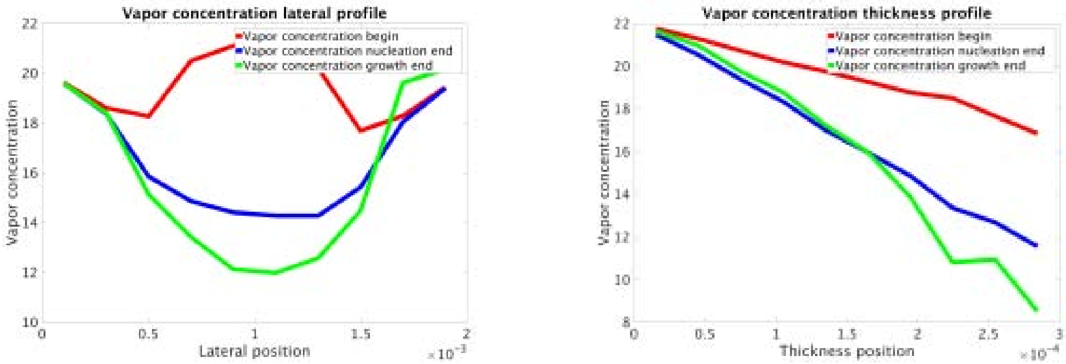

Water distribution at the end of condensation

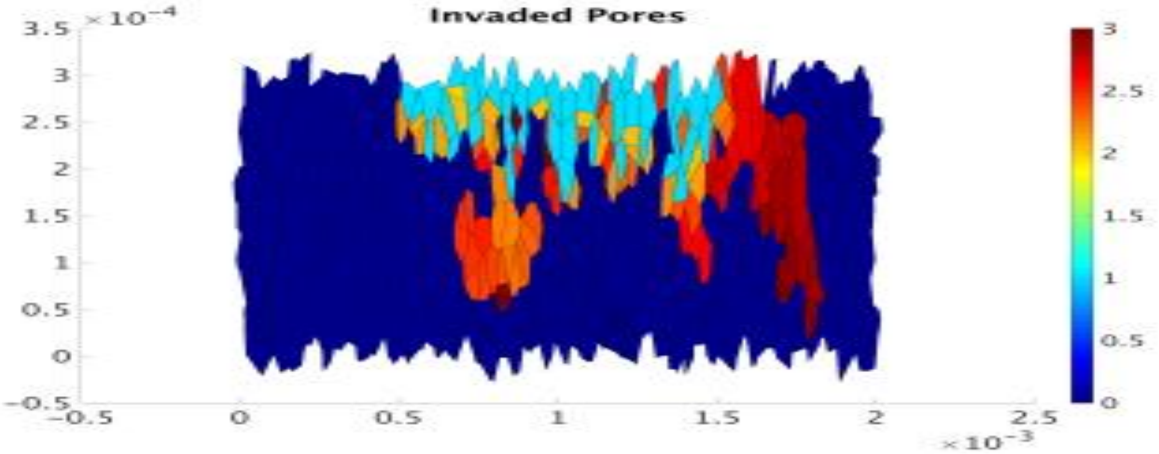

Saturation profile – in-plane

Saturation profile – through-plane

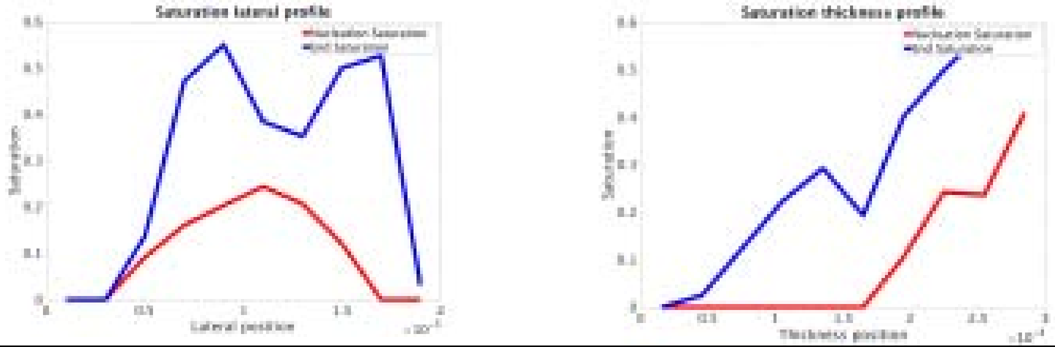

Figure 6.6 Condensation results on an isotropic 2D Voronoi pore network representing a GDL without a MPL.

Temperature

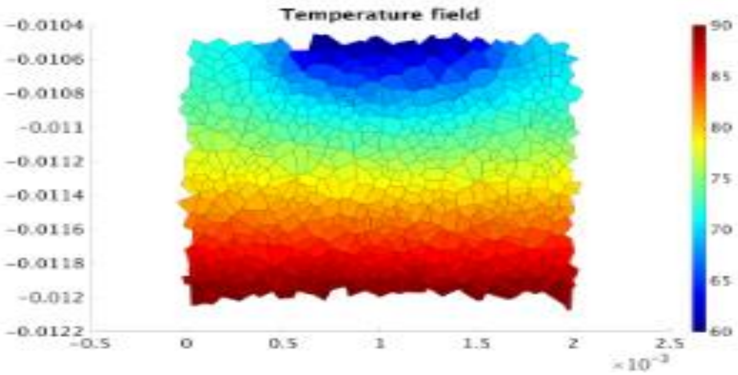

Temperature profiles

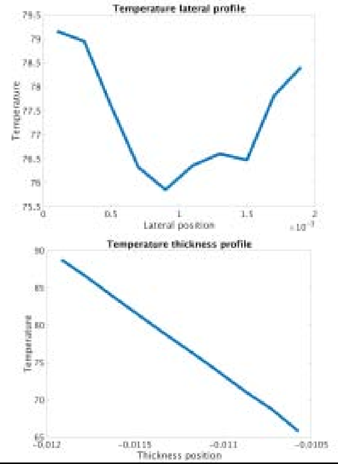

Equilibrium vapor pressure

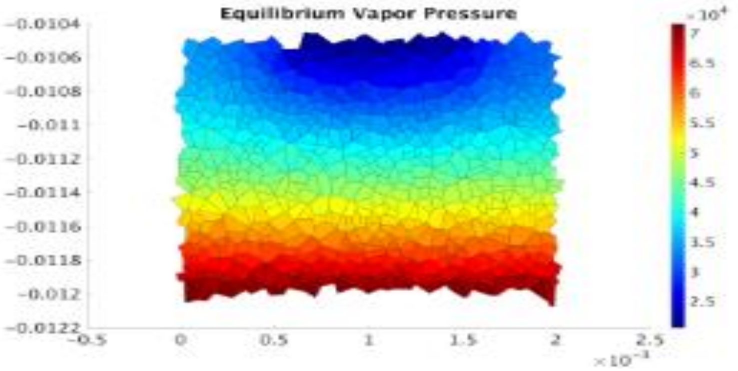

Equilibrium vapor pressure profiles

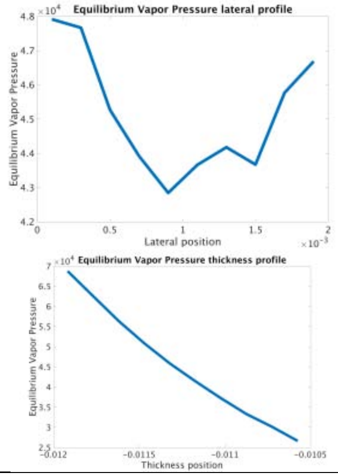

Relative humidity - begining

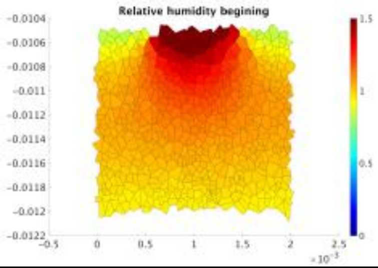

Relative humidity – nucleation end

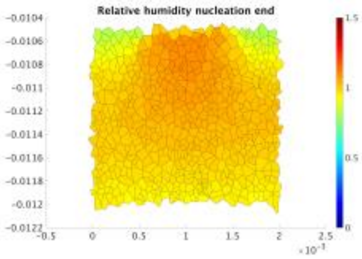

Relative humidity – growth end

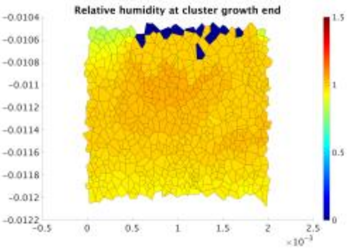

Relative humidity profile – in-plane

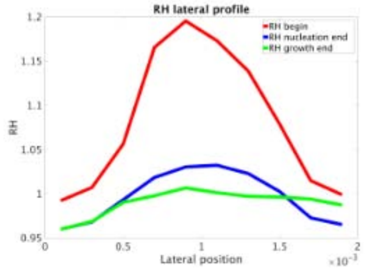

Relative humidity profile - through-plane

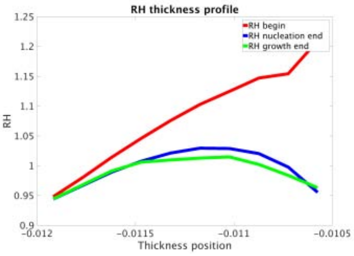

Max RH evolution during nucleation iterations

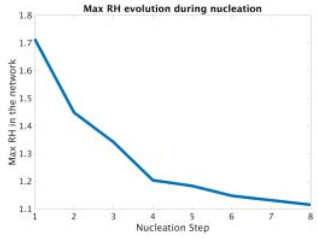

Partial vapor pressure - begining

Partial vapor pressure – nucleation end

Partial vapor pressure – growth end

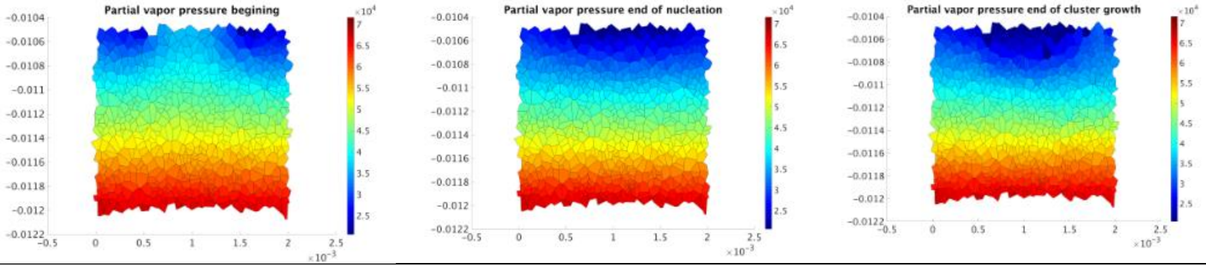

Concentration profile – in-plane

Concentration profile- through-plane

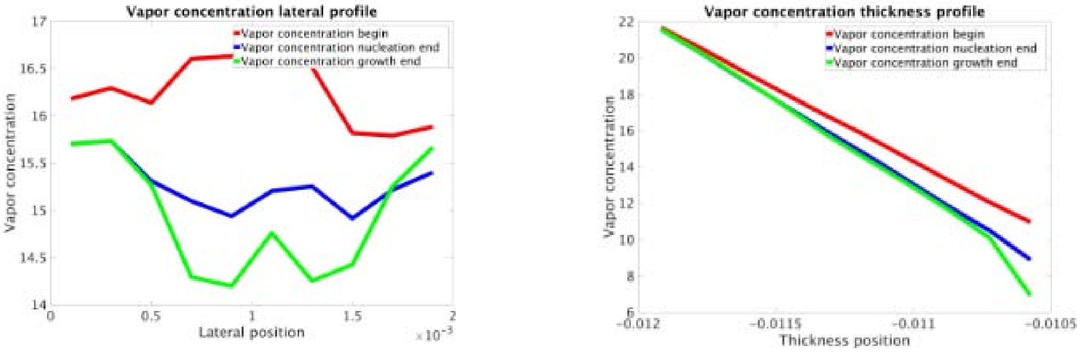

Water distribution at the end of condensation

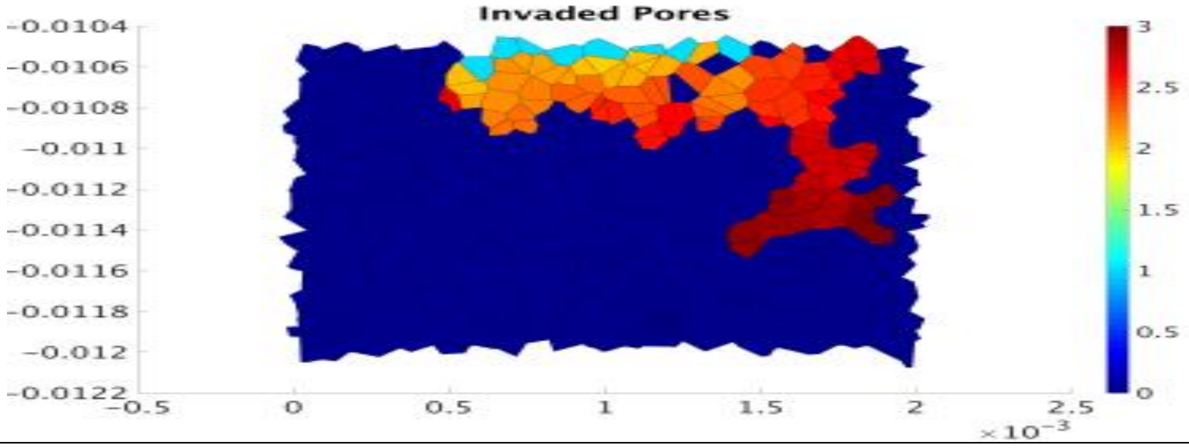

Saturation profile – in-plane

Saturation profile – through-plane

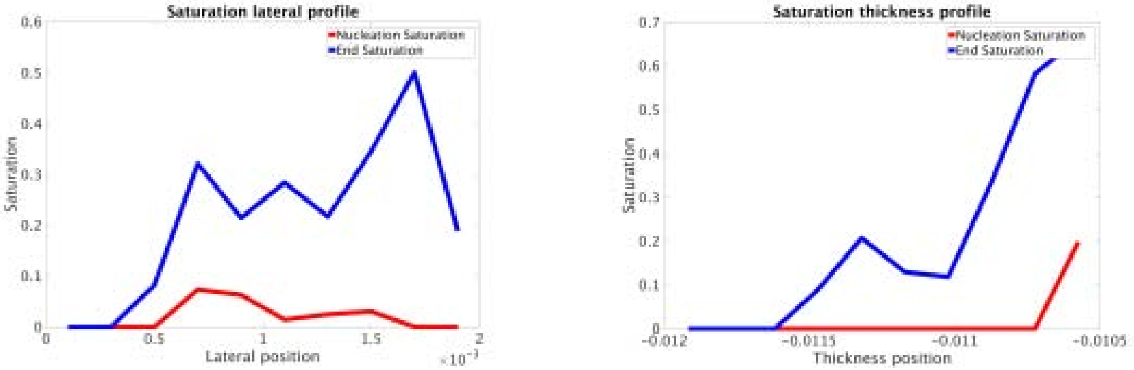

Figure 6.7 Condensation results on an anisotropic 2D Voronoi pore network representing a GDL without a MPL.

6.3 Perspectives

To better validate the physical assumptions made for these simulations, a rigorous comparison to experimental data is desirable. Tomographic images showing condensation in the GDL [Straubhaar2015] were carried out by the Paul Scherrer Institute as part of the European project Impala. A detailed comparison of the water distributions obtained by simulation and the water distributions visualized experimentally would be an important step towards this goal. Recall that similar work has been carried out in section 5.1.

A parametric study of this model should make it possible to better understand how the water condensation in the GDL depends on the operating conditions of the cell. The effect of the microstructure of the GDL on the condensation can be studied using the pore network models developed in this thesis. Suggestions for changes in materials to improve the performance of PEM fuel cells may result from these simulations.

Finally, it would be desirable to have a homogenized model of condensation, using partial differential equations. The homogenized models currently available do not model capillary forces and nucleation in the same way as the pore network model. This pore network model of condensation can be used as a reference for designing a condensation model at a homogenized scale.

6.4 Conclusion

The diffusion of water vapor through the GDL and the condensation of water in the GDL is a well-established phenomenon in PEM fuel cells in operation. In this chapter, we used a pore network condensation model originally developed in [Straubhaar2015] for regular pore networks. We used it on non-regular pore networks whose microstructures are closer to the real GDL microstructures.

We presented condensation simulations on pore networks constructed from 2D and 3D Voronoi meshes. We compared simulations carried out on two 2D pore networks whose microstructures differ only by the anisotropy. This allowed us to simulate the effect of the anisotropy on the temperature field and the water vapor concentration field in the GDL, as well as on the spatial distribution of the liquid water resulting from condensation. This paves the way to a study of the effect of GDL microstructure on water condensation.

Additional simulations and numerical verifications are required to study the effect of different parameters in these condensation simulations. A rigorous comparison with experimental data is desirable to validate the physical assumptions made in this condensation model.

6.5 Bibliography

- [Ajaev2012] Vladimir S. Ajaev, Interfacial Fluid Mechanics: A Mathematical Modeling Approach, Springer-Verlag, 2012

- [Gostick2013] J. T. Gostick. Random Pore Network Modeling of Fibrous PEMFC Gas Diffusion Media Using Voronoi and Delaunay Tessellations. Journal of The Electrochemical Society, 160 (8), F731– F743, 2013

- [Prat2015] M. Prat, T. Agaësse, Thin Porous Media, Chapter in book: Handbook of Porous Media, Edition: Third Edition, Chapter: 4, Publisher: CRC Press, Editors: Kambiz Vafai, pp.89-112, 2015

- [Straubhaar2015] Benjamin Straubhaar, Pore network modelling of condensation in Gas Diffusion Layers of Proton Exchange Membrane Fuel Cells, PhD thesis, INP Toulouse, 2015

- [Thomas2013] A. Thomas, G. Maranzana, S. Didierjean, J. Dillet, and O. Lottin, Measurements of Electrode Temperatures, Heat and Water Fluxes in PEMFCs: Conclusions about Transfer Mechanisms, Journal of The Electrochemical Society, 160 (2) F191-F204 (2013) F191

Chapter 7 Study of virtual microstructures

This chapter is devoted to the virtual design of new materials [Persson2013]. The materials are traditionally designed per a process based, for a large part, on experimentation and trial and error. This approach is slow compared to the pace of progress in the IT sector. In addition, climate change makes the development of new materials for energy urgent. Our goal here is to provide computer tools to help design porous fuel cell materials [Fell2010].

Virtually designing materials requires, first, to have a computerized representation of the materials, that is to say to define a relevant data structure and algorithmic operations on these data. The second step is to virtualize the design processes: design of new materials, performance testing of materials, possibly manufacturing processes. We discuss these topics in the following paragraphs.

We choose to represent virtually a porous material by its microstructure and the bulk transport properties of its constituents. Indeed, the effective diffusive transport properties of a material depend on the bulk transport properties of its constituents and its microstructure, as explained in section 2.1.1.2. Tuning the microstructure is a way to optimize the properties of materials [Antonietti2004]. Moreover, knowing the microstructure has become easier thanks to advances in tomography. We therefore focus on the microstructure.

We have chosen to represent the microstructures by 3D images. Recall that a 3D image is a discretization of a volume by a cartesian grid of voxels. Other geometric representations of solids are also used in computer-aided design (CAD), for example meshes or parametric surfaces [Shapiro2001]. Depending on the data structure chosen, this or that type of operation on the data will not have the same algorithmic complexity. The relative advantages and disadvantages of images and other representations of solids lead us to make conversions between representations if necessary. For example, we can mesh an image, or voxelize a mesh.

3D images can be created virtually, without computing tomography. Virtual microstructures make it possible to design, test and optimize materials that do not yet exist. Virtual images have been used to model the porous materials of fuel cells: the GDL [Thiedmann2012] [Thiedmann2009] [Froning2014] [Becker2011] [Daino2012] [Gaiselmann2012] [El-Hannach2014] [Tayarani-Yoosefabadi2016], the MPL [Becker2011] [Zamel2012] [El-Hannach2015], the catalytic layers [Mukherjee2006] [Kim2009] [Siddique2010] [Malek2011] [Lange2012] [Baker2012].

Let us note that the term "optimization of materials" [Torquato2005] designates two different activities in the literature. The first activity consists in calibrating the parameters of a model on experimental data available on a material. The second activity is to look for microstructures which maximize the desirable properties of a material to improve the performance of this material. The confusion arises from the fact that the two activities [Prill2015] use the same mathematical optimization tools. We are interested here in the second activity, sometimes also referred to by the term "microstructure sensitive design" [Adams2013].

Testing the effect of a material on the fuel cell performances can also be virtualized. The approach adopted in this thesis is to calculate the effective diffusion properties of the GDL, so that they can then be used in PDE based performance models at the MEA scale. This chain of computation makes it possible to go up from a virtual material to its effect on the performance of the cell, i.e. the polarization curve. Such a method could guide the development of new materials. However, the two-phase properties of the GDL should be better modeled in homogeneized performance models, for example by upscaling the condensation model of Chapter 6.

Finally, it is conceivable to physically model the manufacturing processes of materials. This could be particularly ambitious. We present an example of this approach for virtual generation of a GDL with a MPL coating.

This chapter is composed of three studies illustrating the possibilities of virtual microstructures.

The first study concerns the optimization of GDL microstructures for through-plane diffusive transports. We look for microstructures having both high solid phase effective conductivity and high gas phase effective diffusivity, these two objectives being a priori contradictory. We seek the optimum in the form of a regular pore network, whose elementary cell is parameterized geometrically by a small number of parameters. We introduce this problem of multi-objective and parametric optimization of the geometry and introduce some tools to analyze it.

The second study is devoted to the MPL-GDL assembly. We virtually generate images of a microstructure made using a coating process. The challenge is to show that it is possible to model manufacturing processes using virtual microstructures.

The third study is devoted to the modeling of electrical contact resistances between GDL fibers. The challenge is to represent the effect of a material invisible on the image, PTFE. We use simulations on virtual 3D images. We introduce an image analysis algorithm to identify the contacts between fibers.

The outline of this chapter is as follows. A first section presents the methodologies of each study. A second section presents the results of each study. Finally, a perspectives section and a conclusion section complete this chapter.

7.1 Methodology

7.1.1 Optimal porous microstructures for the through-plane diffusive transport of gases and electrons

The GDL have a porous structure for the gases to diffuse through the pores and the electrons to diffuse through the solid phase. These transports in the solid and gas phases both have an important effect on the performance of fuel cells. The diffusion of gases limits the maximum current that the fuel cell can provide. Electrical conduction in GDL induces ohmic losses, although the electrical resistance of the GDL is small in comparison with the ohmic resistance of the membrane and the electrical contact resistance between GDL and bipolar plate. The diffusion of heat, not taken into account here, has a decisive effect on the condensation and evaporation of the water in the cell.

In this chapter, we seek to optimize the microstructure of a GDL, with the aim of optimizing diffusive transport to increase the efficiency and electrical power of fuel cells. Increasing both the effective conductivity and the effective diffusivity of the GDL seems contradictory. Indeed, if we reason in terms of volume fractions of solid and gas phases, increasing the porosity increases the effective diffusivity but reduces the effective electrical conductivity. A more elaborate parametrization the microstructure is therefore required.

In this chapter, we look for optimal structures for the following optimization problem:

$$\begin{cases} \max\limits_{\mathrm{X}\in\Omega} D_{eff:gaz}(X) \\ \max\limits_{\mathrm{X}\in\Omega} C_{eff:solide}(X) \end{cases}$$

Équation 7.1

Where $C_{eff:solide}(X)$ and $D_{eff:gaz}(X)$ are respectively the relative through-plane electrical conductivity and the relative through-plane gas diffusivity of the microstructure X, and Ω denotes the set of microstructures studied. Relative here means divided by the bulk transport property of the phase in which the transport occurs. The optimization problems are generally defined with constraints on the space of solutions Ω. The only constraint that we set here, is that the microstructures in Ω have only two distinct phases, solid and gas.

Note that this is a simplified GDL optimization problem. To optimize GDL more realistically, the coupling with the other layers - MPL, catalytic layer and bipolar plate - should be taken into account. The bipolar plate and the GDL exchange gases through the channels, electrons through the rib, heat through the channels and rib. Gas and electrons must bypass the rib and channels respectively. Transport should therefore be considered both in the through-plane and the in-plane directions. However, we will show that this simplified problem makes it possible to highlight interesting facts that are also valid for more elaborate optimization problems.

This is a multi-objective optimization problem. We use the notion of Pareto optimum to define which microstructures are optimal. Let us recall the definition of a Pareto optimum for a n-objective minimization problem. Let $z^j, j = 1, \dots, n$ be the functions we seek to minimize. Let X and Y be two microstructures in Ω. We say that X dominates Y in the Pareto sense if for any objective j we have $z^j(X) \leq z^j(Y)$ with at least one strict inequality. X is said to be optimal in the Pareto sense if there is no other microstructures Y that dominates it in the Pareto sense.

One way to generate microstructures is to use virtual 3D images. Here we proceed differently. The microstructures that we study are shown in Figure 7.1. These are the elementary cells of the regular cubic pore networks used in Chapter 3. The advantage of these structures is that their transport properties can be analytically calculated. The relative effective diffusivity of the gas phase of a cell, $D_{eff:gaz}$, is given by the Équation 3.13. The relative effective conductivity of the solid phase of a cell, $C_{eff:solide}$, is given by the Équation 3.14.

To find optimal microstructures, we generate many microstructures by varying the geometric parameters of these structures. For each structure, we calculate the diffusivity and the effective conductivity. Then we analyze the results to detect the optimal Pareto structures.

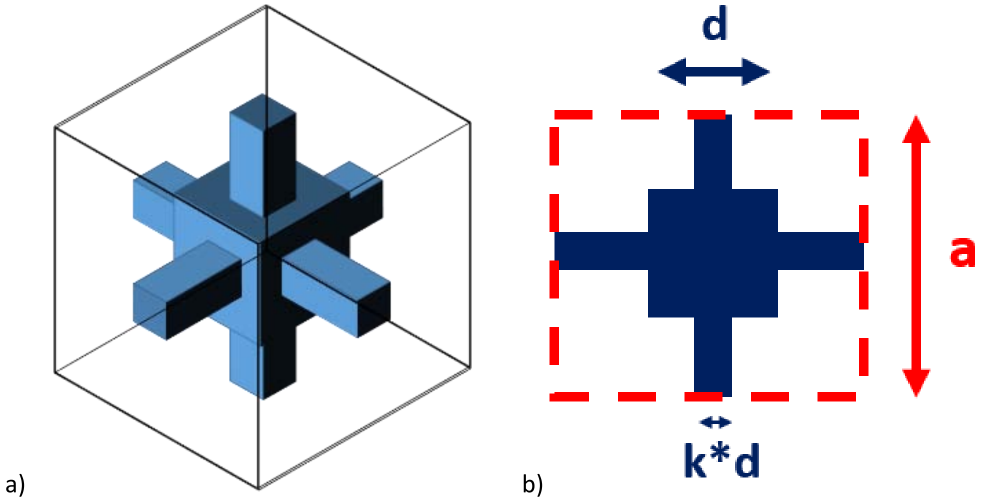

Figure 7.1 Diagrams of cubic porous structures used for microstructure optimization. A) 3D representation. B) 2D slice.

7.1.2 MPL-GDL assemblies

The gas diffusion layer is usually composed of two layers. The first is a fibrous porous material, referred to as GDL in this thesis. The second is a porous material made of carbon black powder mixed with a hydrophobic treatment, often PTFE [Park2012]. This layer is referred to as micro-porous layer (MPL). The MPL serves to reduce the contact resistance between the GDL and the catalytic layer, forming a continuous layer which serves as an interface between the GDL fibers and the grains of the catalytic layer. It also has a beneficial effect on water management [Park2012].

The MPL is manufactured by coating on one side of the GDL an ink containing the MPL in a soluble state [Park2012]. The MPL-GDL assembly is then heated to evaporate the solvents and melt the PTFE. During the coating, the MPL penetrates into the pores of the GDL. The penetration characteristics depend on the pore size of the GDL [Park2016]. Figure 7.2 is a sectional SEM image of a commercial MPL-GDL assembly, SGL 24BC. We can see that the MPL penetrates the GDL and that there are cracks in the MPL. We do not consider cracks in this study.

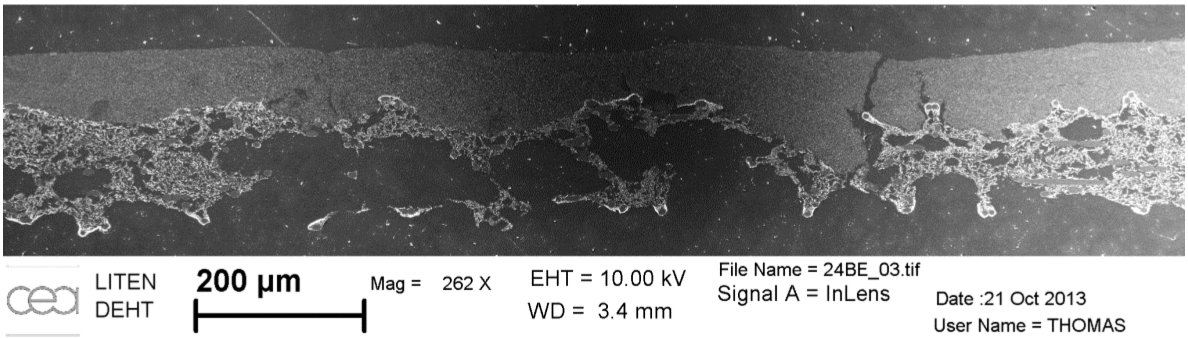

Figure 7.2 SEM image of a MPL-GDL assembly, SGL 24BC. The lighting is not uniform, which explains why the center of the image is darker than the sides.

We are interested in the microstructure and the effective diffusive transport properties of the MPL-GDL assembly [Wargo2012] [Burheim2015]. We virtually generate MPL-GDL assemblies. Then we simulate their effective diffusive transport properties by direct simulation on the microstructures. Finally, we analyze the effect of the penetration of MPL on the apparent transport properties of GDL.

7.1.2.1 Generating virtual MPL-GDL assemblies

We describe here the algorithm used to generate the MPL-GDL virtual microstructures.

We first generate a virtual GDL fibrous substrate. The algorithm used is very similar to that used in several articles [Schladitz2006] [Becker2011]. The fibers of the GDL are generated first. They are represented by cylinders. To generate cylinder images, we generate a cylinder mesh using the VTK python library and then convert it into an image using a python voxelization algorithm inspired by [Aitkenhead2010]. Another option for generating cylinders would be to use the Bresenham segment tracing algorithm [Bresenham1965] followed by morphological dilation. The dimensions of the cylinders used here are 9 voxels in diameter, because we have fixed the voxel size at 1 µm, and 500 voxels in length. The size of the image is 500 voxels in the X direction, 500 voxels in the Y direction and 200 voxels in the Z direction. We randomly distribute the cylinders in space, randomly drawing their center and direction according to uniform random variables. To obtain a preferential orientation of the fibers in the plane, which is more representative of the real GDLs, we modify the direction of the axis of the cylinders after it has been drawn randomly, dividing its component perpendicular to the plane by an anisotropy factor equal to 5. Figure 7.3 a) shows virtual GDL obtained with random realizations of the fiber distribution.

Once the fibers are generated, we add binder in the image. The binder is generated by a morphological closure algorithm applied to the fibers. The morphological closure consists in consecutively applying a morphological dilatation and an erosion of length L. The morphological dilation makes the solid phase thicken by a thickness of L voxels. The morphological erosion eliminates the voxels of the dilated solid phase which are located at less than L voxels of the fluid phase. The closure has the effect of filling the spaces between the fibers. The regions thus newly filled are assigned to the binder. The morphological closure distance, L, is increased until the desired volume fraction of binder is obtained. Figure 7.3 b) shows the distribution of binder obtained by varying L. We work in this study with a single GDL structure with 23% fibers and 7% binder, in volume fractions.

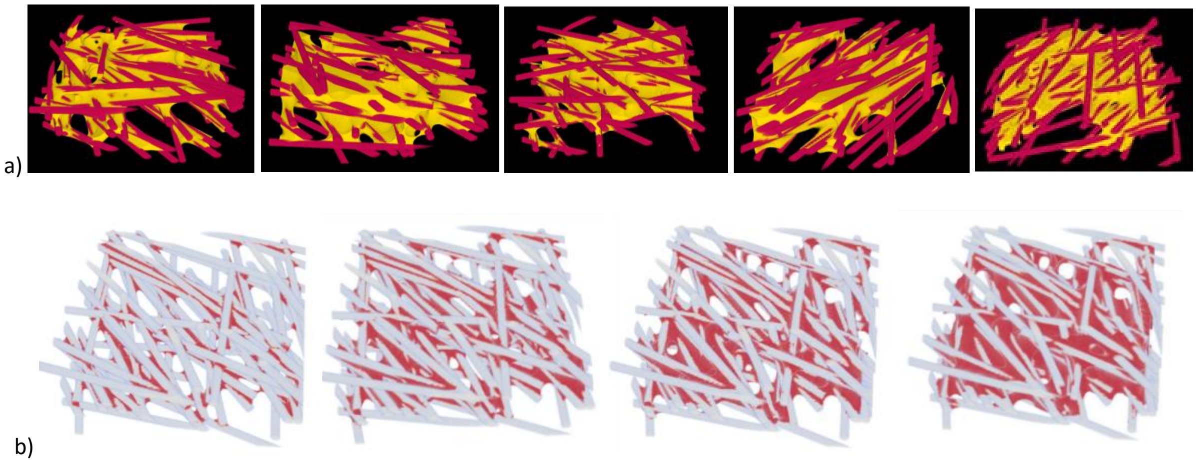

Figure 7.3 Virtual GDL. A) several random realizations of the fibers, with constant volume fraction of binder and volume fraction of fibers. B) variable volume fraction of binder obtained by varying the morphological closure distance.

Note that more sophisticated algorithms can be envisaged to virtually generate virtual microstructures. For example, we could generate curved fibers rather than straight fibers [Gaiselmann2013].

The second step is to generate a virtual MPL under the GDL. To mimic the MPL coating process, we model the penetration of MPL into the pores of the GDL. We use the full morphology algorithm to describe the penetration of MPL in GDL. That is, we put in the GDL balls of MPL, all the same radius, as if we simulated an injection of liquid water into the GDL. We have described the full morphology algorithm in section 5.1. Figure 7.4 shows the virtual structures obtained.

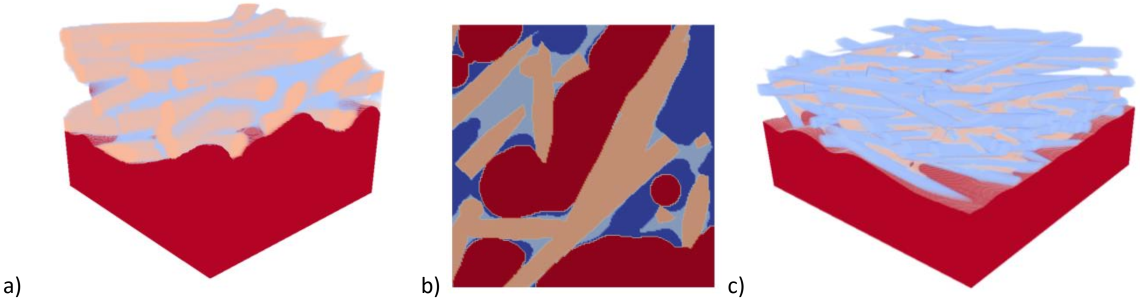

Figure 7.4 Virtual MPL-GDL assembly a) 3D rendering b) sectional view of the interpenetration zone c) 3D rendering of a larger virtual MPL-GDL assembly, not studied here.

Several virtual structures are generated with the same GDL support, but a variable MPL penetration. Figure 7.5 shows sectional views of these structures that show how MPL penetrates the GDL.

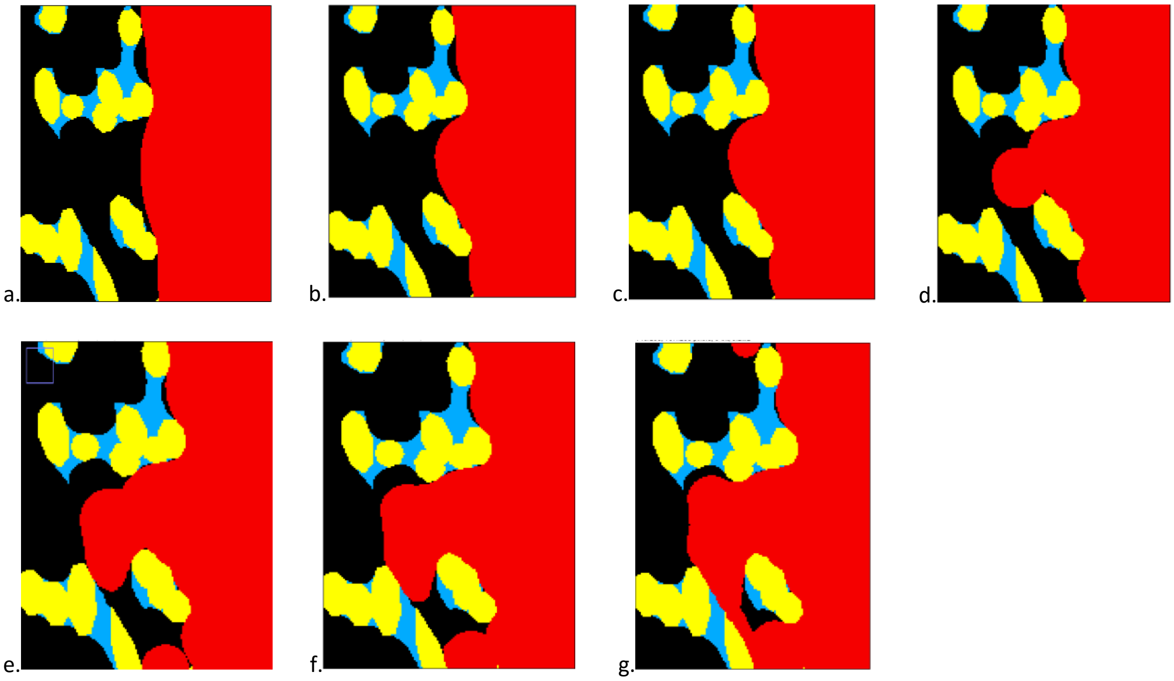

Figure 7.5 Section views of virtual MPL-GDL assemblies. Radius of the balls used to simulate MPL penetration, from a to g: 14, 16, 18, 20, 25, 30, 70 (in voxels). The thickness of MPL is varied to maintain a volume fraction of MPL of 50% in the image regardless of the level of penetration.

The algorithm we used to generate the GDL is like an algorithm already published. Our originality, compared to other articles [Zamel2012], is in the addition of the MPL by a physical algorithm. We used the Full Morphology algorithm, that we used in Chapter 5 to simulate the injection of water into a GDL. We assumed here that the capillary forces are dominant for the intrusion of the MPL ink into the GDL. But the viscous forces actually have a decisive influence on the penetration of the MPL. It would be possible to coonsider the effect of viscous forces by simulating a flow in the presence of viscous forces and capillary forces. An interesting perspective for this purpose is to modify the Full Morphology algorithm, by making the diameters of the balls dependent on the distance to the injection face. This type of approach is used in pore networks to model viscous flows or flows in the presence of gravity. Another perspective is to model the cracks that are often present in the MPL [Hizir2010].

These virtual microstructures allow us to study the effect of the penetration of MPL in the GDL on the effective diffusive transport properties of the assembly. We simulate the effective transport properties of the MPL-GDL assembly using the Ej-Heat method. This method is described in Chapter 3. The calculated effective properties are effective diffusivity and effective electrical and thermal conductivities. The parameters used for bulk conductivities and bulk diffusivities are listed in Tableau 7-1. Note that the properties of virtual GDL alone have been studied in several articles [Froning2014] [El-Hannach2014].

Bulk properties	Electric simulation	Thermic simulation	Diffusion simulation
Fibers	1	1	0
Binder	0.01	0.01	0.01
Gaz	0	0.001	1
MPL	0.01	0.01	0.01

Tableau 7-1 Bulk properties used for EJ-Heat simulations on virtual MPL-GDL assemblies.

7.1.2.2 Apparent properties of GDL: analytical model on a simplified geometry

We compare the diffusive transport properties of virtual microstructures with a simplified geometry of MPL - GDL assembly, shown in Figure 7.6. This simplified geometry is composed of two layers, MPL and GDL. The GDL is composed of gas, fiber and MPL.

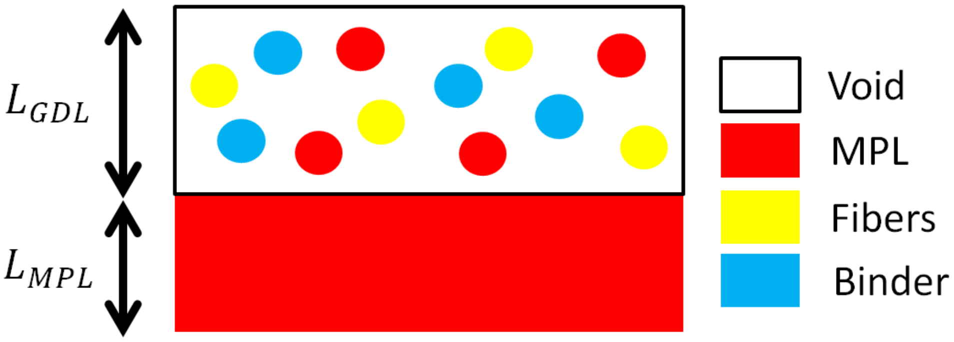

Figure 7.6 Schematic of the simplified MPL-GDL assembly microstructure used for analytical calculations.

Let x_{gas}, x_{fiber}, x_{binder}, x_{MPL} be the volume fractions in the GDL of gas, fibers, binder and MPL respectively. Let γ denote the volume fraction of MPL in the complete sample. Let L_{GDL} and L_{MPL} be the thicknesses of GDL and MPL respectively. Let C_{gas}, C_{fiber}, C_{binder}, C_{MPL} be the bulk transport properties of gas, fibers, binder and MPL respectively.

We vary the volume fraction of MPL in the GDL while keeping the volume fraction γ of MPL fixed in the total assembly.

$$\frac{x_{MPL}L_{GDL}+L_{MPL}}{L_{GDL}+L_{MPL}}=\gamma$$

Équation 7.2

The in-plane effective conductance of the assembly can be estimated by the arithmetic mean of the MPL and GDL conductances because these layers are parallel in this direction.

$$C_{eff}^{GDL+MPL,IP}=\frac{1}{L_{GDL}+L_{MPL}}\left[L_{MPL}C_{MPL}+L_{GDL}C_{eff}^{GDL}\right]$$

Équation 7.3

The effective through-plane conductance of the assembly can be estimated by the harmonic mean of the conductances of the MPL and the GDL, since these layers are in series in this direction.

$$C_{eff}^{GDL+MPL,TP}=(L_{GDL}+L_{MPL})\left[\frac{L_{MPL}}{C_{MPL}}+\frac{L_{GDL}}{C_{eff}^{GDL}}\right]^{-1}$$

Équation 7.4

We define the "apparent" effective property of the GDL, C_{app}^{GDL}, as the effect of the GDL on the property of the MPL-GDL assembly in the simplified geometry above. More precisely, in the in-plane direction, per Équation 7.3, we define the in-plane apparent effective property of the GDL $C_{app}^{GDL,IP}$ by the formula:

$$C_{app}^{GDL,IP} = \frac{1}{L_{GDL}}\left[(L_{GDL} + L_{MPL})C_{eff}^{GDL+MPL,IP} - L_{MPL}C_{MPL}\right]$$

Équation 7.5

In the direction through-plane, per Équation 7.4, we define the apparent effective property of the GDL, $C_{app}^{GDL,TP}$, by the formula:

$$C_{app}^{GDL,TP} = L_{GDL}\left[\frac{L_{GDL} + L_{MPL}}{C_{eff}^{GDL+MPL,TP}} - \frac{L_{MPL}}{C_{MPL}}\right]^{-1}$$

Équation 7.6

In these equations, we take $L_{GDL} = 100\ voxels$, which corresponds to the maximum thickness of the virtual GDL. This parameter sets the limit between MPL and GDL. This choice is partly arbitrary, because the thickness of the GDL is not necessarily uniform and moreover the limit is not well defined since there is interpenetration.

7.1.3 Model of electrical contact resistances between GDL fibers

We are interested in modeling the electrical behavior of GDLs. The electrical conduction in GDL is complex since it takes place through several phases: carbon fibers, PTFE and the binder, consisting of a mixture of phenolic resin and PTFE. Knowing the geometry of the different phases is essential to explain the anisotropy, to describe the interface between the GDL and the bipolar plate and more generally to describe the conduction of the current between the phases.

We are particularly interested in the anisotropy of effective electrical conductivity and the effect of PTFE. The effective electrical conductivity of the GDL is highly anisotropic: the conductivity in the plane is at least 10 times higher than the conductivity in the thickness, as explained in Chapter 4. The hypothesis studied here to explain this phenomenon is as follows. The current conduction in the plane is mainly in the highly conducting fibers of the GDL. On the other hand, the conduction of the current in the thickness is made by materials that are not conductive (PTFE or binder) that are located between the fibers. The effect of PTFE on the thermal conductivity of GDL Sigracet has been studied experimentally and modeled in [Sadeghifar2014]. PTFE is found on the surface of carbon fibers and between fibers for fibers close to the surface. Since PTFE is a weakly conductive material, the effect of PTFE is modeled in [Sadeghifar2014] by an additional electrical resistance. Although the PTFE layers are very thin, this resistance is not negligible.

To test this hypothesis, we introduce electrical contact resistances between the fibers and between the fibers and the binder, on 3D images of GDL. We then perform electrical transport simulations on the images to calculate the effect of contact resistances on the electrical properties. The models based on 3D images make it possible to considering the precise geometry of the phases, for example the distribution of the binder relative to the fibers.

However, the resolution of the image may be insufficient to see the PTFE. This is problematic for electrical simulation because the resistances are given by the voxel bulk conductivities: if there is no PTFE voxel, it seems that we can not model resistance due to PTFE.

We describe in this section the methodology we have developed to circumvent the lack of resolution for PTFE in tomographic images. We first use an algorithm to detect fibers individually in the 3D image. Then the interfaces between fibers are detected by image analysis. Finally, the conductivity of the voxels located in the interfaces between fibers is modified to take into account the contact resistance caused by the PTFE. Note that this approach is similar to that developed in [Roussel2015].

7.1.3.1 Generation of virtual GDL whose fibers are distinguished individually

To find the contacts between the fibers, we need to know the position of each fiber individually. On an X-ray tomographic image, all the fibers have the same gray level, so we do not distinguish the fibers individually. So we do not know where the interface between two fibers is. To overcome this difficulty, we could try to distinguish the fibers with a geometric criterion. This amounts to developing a fiber segmentation algorithm. Some segmentation algorithms are discussed in this document but left for future work. When we generate a virtual GDL the situation is simpler: we know the fibers individually when we generate them. We will therefore work in this section on virtual GDLs.

Virtual GDLs are generated as described in section 7.1.2.1. We insert cylinders in the image at random positions and orientations, representing straight carbon fibers. We give a different label to each fiber to be able to differentiate them individually. Once the desired fiber volume is reached, we proceed to the binder addition, using a morphological closure. Figure 7.7 shows the structures obtained.

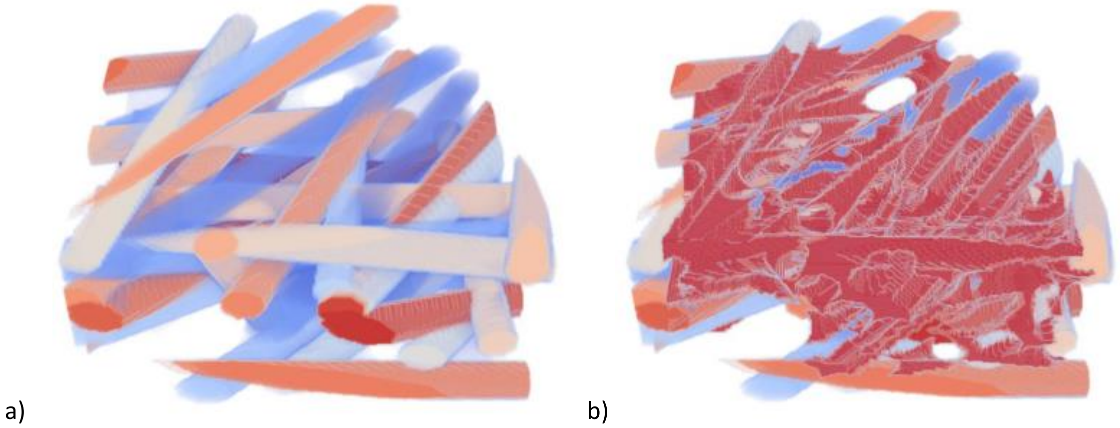

Figure 7.7 a) GDL with the fibers identified separately. B) Same GDL after adding the binder (in red).

The parameters used are as follows. The virtual GDL images have the sizes 500 * 500 * 200 voxels, the size of a voxel is 1 µm, the fiber diameter is 9 voxels, the fiber length is 500 voxels, the volume fraction of fibers is 30%, the binder volume fraction is 10%. The anisotropy is varied by changing the orientation of the cylinders.

7.1.3.2 Algorithm to identify boundaries between distinct phases

We describe in this section the algorithm used to locate the contacts between fibers and between fibers and binder.

In a first step, the regions situated between two different phases are identified by an edge detection algorithm called Sobel Edge Detector. This algorithm analyzes the values of the voxels around each voxel to assign a zero value to a voxel if all its neighbors belong to the same phase (voxels internal to a phase), but a non-zero value if the voxel has a neighbor belonging to another phase (voxels located at the boundary of a phase). We use the SobelEdgeDetection function of the SimpleITK python library.

In a second step, the voxels located in the edges are labelled as contact between two fibers or contact between fiber and binder. Concretely, we list the phases located in the neighborhood of each voxel. The neighborhood is defined so that each voxel has 6 neighbors, i.e. the diagonal voxels are not considered as neighbors. The voxels which have exactly two distinct neighboring phases A and B are attributed to the contact between A and B. The voxels which have one or more than two neighboring phases are not considered. The other types of contacts are not considered, for example between a fiber and air.

Figure 7.8 c) shows the result. In this image, the phases (fibers, binder, air) have distinct color codes and the contacts also have a distinct color code.

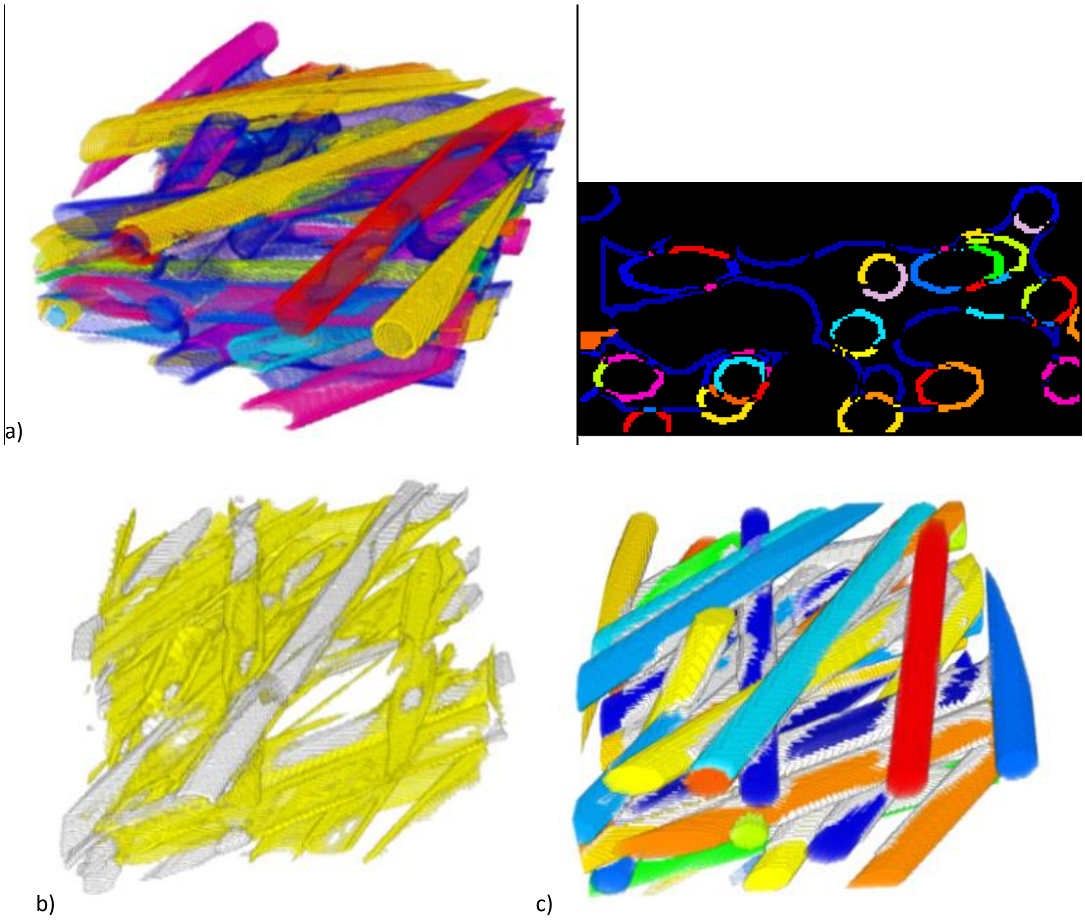

Figure 7.8 a) Contacts between the different elements of the image (3D view and section view). B) Contacts divided into 2 categories: yellow for contacts between fibers and binder, white for contacts between fibers. The contacts between the fibers are often cylindrical. It is an artifact related to the process of building virtual GDL, which inserts a new fiber by replacing the voxels already occupied. C) Final image where the locations of the different fibers, the binder and the contacts are known. The contacts between fibers and between binder and fibers are shown in white on this image. The colors correspond to the fibers and the binder.

7.1.3.3 Model of electrical contact resistances on 3D images

We perform direct electrical simulations on the GDL microstructures using the EJ-Heat method. We model the contact resistances between fibers by reducing the conductivity of the voxels in the contact zones. Indeed, these voxels contain PTFE in their volume, inserted between fibers or binder. We assign to these voxels an effective conductivity considering the presence of PTFE. Since we do not know the conductivity values at this stage, we do a sensitivity study on the conductivities. Three conductivity values are compared. Their values are listed in Tableau 7-2.

Test case name / Bulk conductivities	Initial GDL image, without contact identification	Contact resistance: same resistance as in fibers	Infinite contact resistance
void	0	0	0
binder	0.01	0.01	0.01
fibers	1	1	1
Contact binder/fiber	-	1	0
Contact fiber/fiber	-	1	0

Tableau 7-2 List of studied cases and their parameters, for electrical contact resistance simulations.

We have thus introduced a multi-scale method on 3D images, modifying the conductivities of the voxels to consider a phenomenon that is invisible on the image. This method allows to extend the applicability of simulations on 3D images beyond the constraint of resolution.

7.2 Results

7.2.1 Optimal cubic porous microstructures for through-plane diffusive transports of gases and electrons

Figure 7.9 a) presents a mapping of the effective conductivities and diffusivities of the cubic porous cells. The Pareto front of the optimization problem is shown in red in this figure. It corresponds to the upper right boundary of the accessible (diffusivity, conductivity) pairs.

Let d be the diameter of the pore, a be the step of the network, $\mathbf{u}=\boldsymbol{d}/\boldsymbol{a}$ be the pore size normalized by the network step, k be the constritivity such that k*d is the diameter of the links. Figure 7.9 b) shows the parameters u and k of the cubic cells located on the Pareto front. We find that all cells with k close to 0.6 are optimal, regardless of u. A certain dispersion around 0.6 is even possible. This suggests that the fine tuning of microstructure constrictivity is an interesting path for optimization. It should be noted that the volume fractions of solid and gas essentially depend on the pore size u. The constrictivity parameter k represents an additional degree of freedom which it is worth exploring. When u is very small or very large, there is less constraint on k to be optimal. This is understandable because in this case, k has little impact on the effective properties.

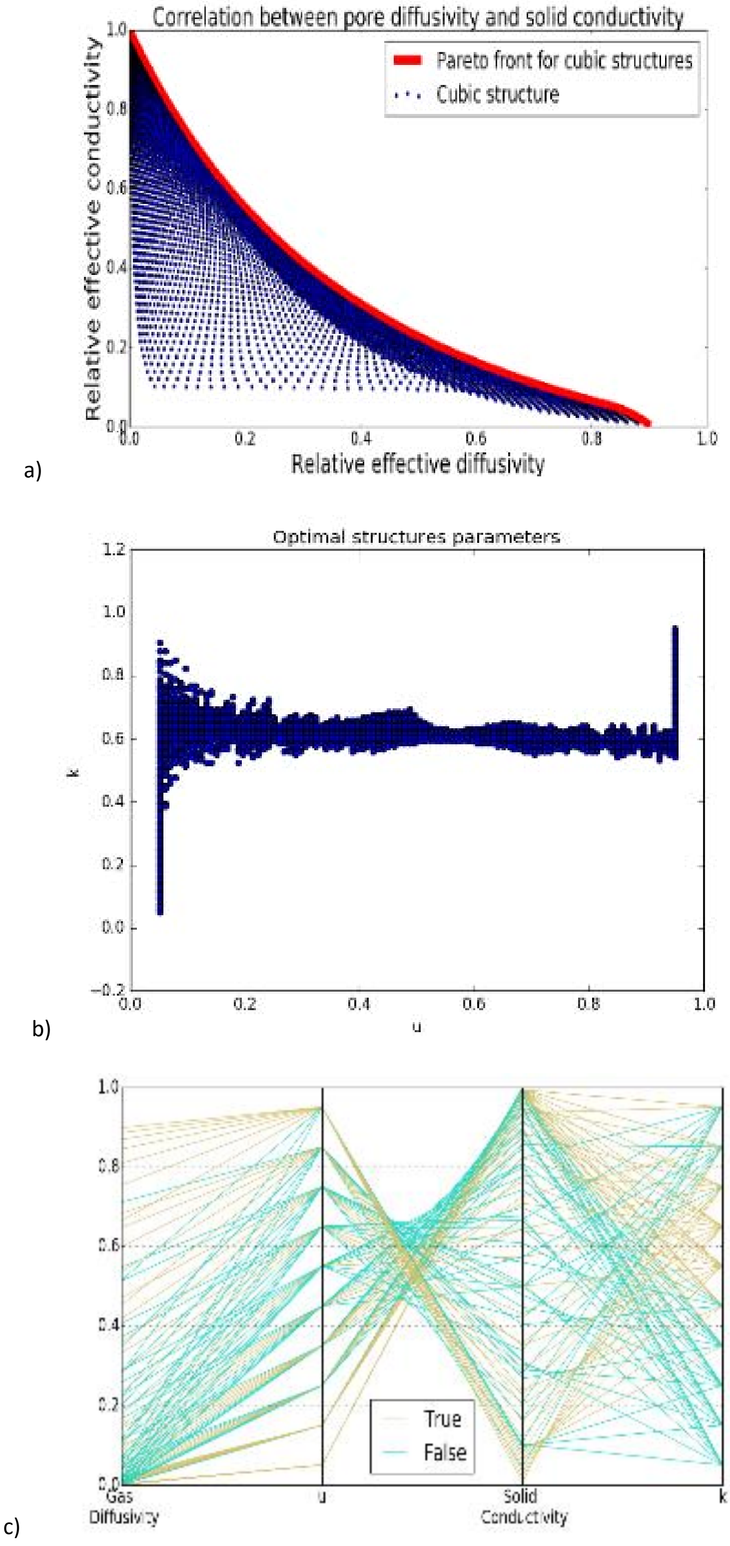

Figure 7.9 Properties of porous cubic cells for the optimization problem. A) Correlation between electrical conductivity and diffusivity. The optimal Pareto structures are in red. B) Geometric parameters of Pareto optimal cells. C) parallel coordinates graph of geometric parameters and effective properties. The yellow lines correspond to the optimal microstructures in the Pareto sense, the blue lines to non-optimal structures.

Figure 7.9 c) is a parallel coordinates graph of the geometric parameters and effective properties of the cells. This type of graph allows to represent spaces with multiple degrees of freedom. Each continuous line corresponds to a microstructure. Each column represents a property of the microstructures. We can access all the properties of a microstructure by following the continuous line from one column to another. The yellow lines correspond to the optimal microstructures in the Pareto sense, the blue lines correspond to the non optimal structures. We find that most optimal microstructures have constrictivity values around 0.6. Let us note that in order to increase the legibility of this graph, the sampling of u and k has been less detailed than for the figures a and b, which explains why we have relatively more optimal structures.

Figure 7.10 shows a comparison between the relative effective transport properties of the cubic cells and those of several GDLs. We find that the GDLs studied here are well below the Pareto front of the optimal structures. Cubic structures are more optimized than GDLs for through-plane transports. Thus, there is a considerable margin of progression of the real GDLs for this problem of optimization of the through-plane diffusive transport properties.

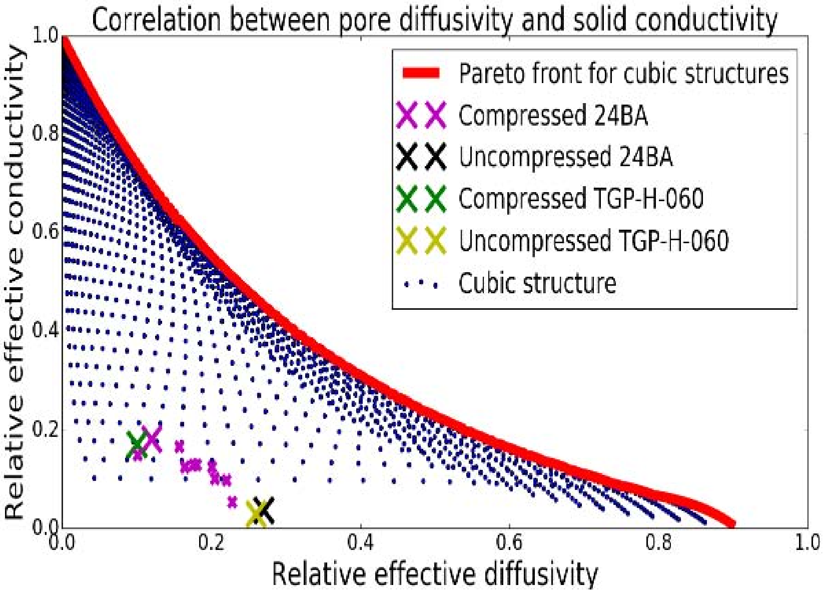

Figure 7.10 Comparison between the effective diffusive transport properties of the cubic cells and several commercial GDLs.

Cubic structures are probably close to being optimal for transport through-plane, in the sense that their tortuosity is equal to 1, all the pores being aligned. The real GDLs on the other hand are tortuous, which reduces their effective diffusivity and their effective conductivity in through-plane. However, tortuosity may have a beneficial effect for channel-rib configurations, that mix in-plane and through-plane transports. A more realistic optimization problem should consider both in-plane and through-plane transport.

We find that the compression has a double contradictory effect on the properties of GDL. Increasing the compression reduces the effective diffusivity [Rashapov2016], but increases the electrical contact with the bipolar plate. A virtual compression model [Gaiselmann2014] would allow to study this point.

In conclusion, we analyzed the diffusive transport properties of GDL and some virtual structures in terms of microstructure optimization. This analysis allowed us to compare the transport properties of several types of GDL, to problematize the effect of tortuosity and compression, and to identify the potential for optimizing the constrictivity of microstructures. Note that the notion of Pareto front allowed us to deal with a multi-objective optimization problem without needing to determine a weighting of the different objectives.

7.2.2 Properties of virtual MPL - GDL assemblies

We present here data on the virtual MPL - GDL assemblies. We first analyze the geometry of the virtual microstructures. Then we present the effective transport properties of the assembly, obtained by direct simulation on the microstructures. Finally, we analyze these effective transport properties using the notion of apparent effective property of the GDL.

7.2.2.1 Geometric analysis of the virtual microstructures

Figure 7.11 a) shows the volume fraction of MPL in GDL as a function of the penetration parameter. It is possible to obtain a variable amount of MPL in the GDL, depending on the penetration parameter chosen. Since we used a full morphology algorithm to model the penetration of MPL, the volume fraction of MPL in GDL - Figure 7.11 a) - is in fact related to the capillary pressure curve for water injection into GDL, as explained in section 5.2. This is the reason why we have taken as the abscissa of Figure 7.11, the inverse of the radius of the full morphology balls. This is like the parametrization of the Laplace capillary pressure curve, which is proportional to the inverse of the diameter of the meniscus.

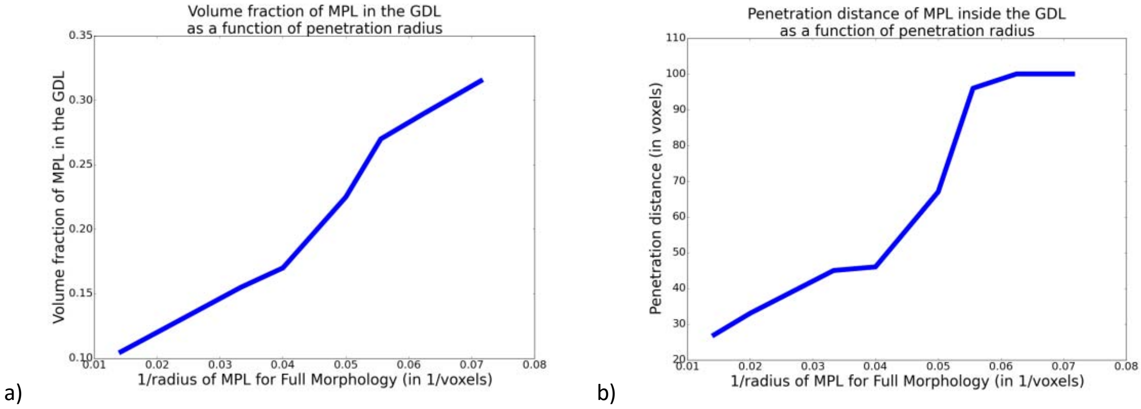

a) b)

Figure 7.11 a) Volume fraction of MPL in GDL, as a function of the inverse of the radius of the balls used to simulate MPL penetration. b) MPL penetration distance in GDL, as a function of the inverse of the radius of the balls.

Figure 7.11 b) shows the MPL penetration distance in GDL. This distance is calculated as the distance between the extreme point of the GDL (ie the lowest if the GDL is above the MPL), here corresponding to $L_{GDL} = 100\ voxels$, and the most advanced point of the MPL in the GDL. This penetration distance quantifies the thickness of the transition zone.

These data could be compared in the future to actual MPL-GDL assembly images to calibrate this model. Section views obtained by SEM could be used, as well as tomographic images. Due to the lack of contrast between MPL, fibers and binder with X-ray tomography, it would probably be easier to compare the geometries of the porous phases and to indirectly deduce the geometry of the MPL entering the GDL.

7.2.2.2 Simulation of the effective diffusive transport properties of the virtual microstructure

Figure 7.12 shows the effective diffusive transport properties of virtual MPL-GDL assemblies, obtained by direct Ej-Heat simulation on the virtual microstructures.

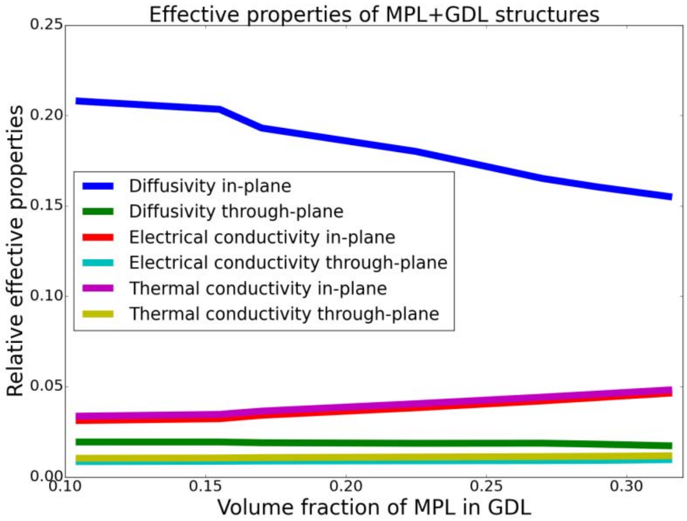

Figure 7.12 Effective diffusive transport properties of virtual MPL-GDL assemblies, obtained by direct Ej-Heat simulations.

Electrical and thermal transports have the same behavior, so in the following we will not comment the heat transport. Note that the only difference between the electrical and thermal simulations is that the gas phase of the GDL is very weakly conductive for heat but completely insulating for electricity. This results in a 10% difference between effective electrical and thermal conductivities.

The in-plane diffusivity increases by 30% when the penetration decreases. We propose the following explanation for this phenomenon. The in-plane diffusion occurs mostly in the pores of the GDL rather than the MPL, because the bulk diffusivity that we have taken for the MPL is 100 times less than the air bulk diffusivity. Penetration has a double contradictory effect in these simulations. On the one hand, some pores of the GDL become filled with solid when the MPL penetrates the GDL, which reduces the effective diffusivity. On the other hand, the thickness of the total sample changes as a function of the penetration, which changes the normalization thickness coefficient for the effective diffusivity. The total thickness increases from 137 voxels in case of strong penetration, to 179 voxels in case of low penetration. We quantify these two contradictory effects in the next section.

7.2.2.3 Apparent transport properties of the GDL

Figure 7.13 shows calculations of the apparent properties C_{app}^{GDL} of the GDL as a function of the volume fraction of MPL in the GDL, x_{MPL}. The variation of the electrical conductivity is very low, indicating that the electrical current is little modified by the penetration of the MPL. On the other hand, the effect is more pronounced for the apparent diffusivities, which decrease by about 40% when the volume fraction of MPL increases from 10% to 32%. The volume fraction of fibers being 23% and that of binder 7%, the porosity decreases from 60% to 38%, which corresponds to a porosity decrease of approximately 40%.

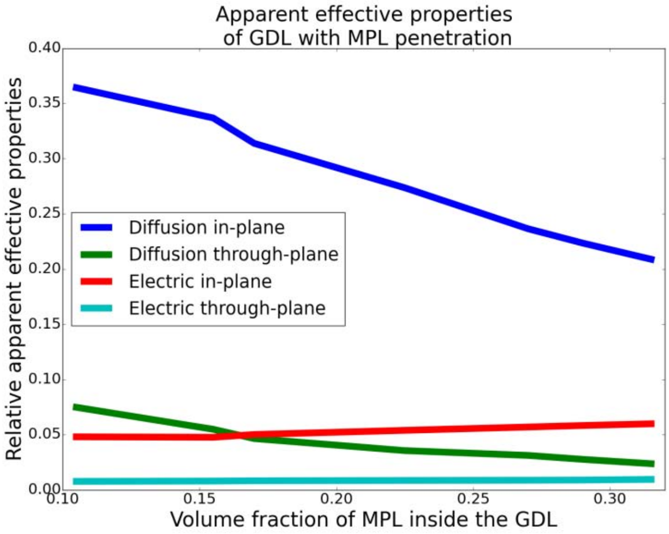

Figure 7.13 Effective apparent properties of the GDL, as a function of the volume fraction of MPL in GDL.

To explain these results, let us assume a linear dependence of the effective conductivities of the GDL with respect to the volume fractions of the phases in the GDL. The linear dependence of an effective property as a function of the volume fraction of the components is used in the estimates of effective properties by mixing laws. The bounds of Voigt and Reuss, presented in section 3.1.1.3.2, are also linear. Linearity can also result from the linearization of a non-linear function for a small variation of a parameter.

$$C_{eff}^{GDL} = x_{fibre}C_{fibre} + x_{binder}C_{binder} + x_{gas}C_{gas} + x_{MPL}C_{MPL}$$

Équation 7.7

Let us rewrite Équation 7.7 in the present case where the MPL replaces gas:

$$C_{eff}^{GDL} = x_{MPL}\left(C_{MPL} - C_{gas}\right) + x_{fibre}C_{fibre} + x_{binder}C_{binder} + C_{gas}\left(1 - x_{fibre} - x_{binder}\right)$$

Équation 7.8

In this simple model, the coefficient of linear variation is given by $C_{MPL} - C_{gas}$, because the change of effective property is related to the replacement of gas by MPL. This linear coefficient is higher for diffusivity than for electrical conductivity, because the contrast between the bulk properties of MPL and air is higher for diffusion than for electrical conduction. We find again with the simulations that this coefficient is negative. On the other hand, this simplistic and isotropic model is not sufficient to represent the difference of the in-plane and through-plane properties calculated by the simulations.

In summary, we have virtually generated MPL-GDL assemblies. We assumed that MPL penetrates GDL identically to water injected into GDL and subjected to capillary forces. We have characterized the geometry of the microstructure obtained, and explained the penetration volume as a function of the capillary pressure curve of the GDL. We have calculated the effective diffusive transport properties of the assembly and analyzed these properties by introducing the notion of apparent effective property of the GDL. This allowed us to explain the effect of penetration on the effective transport properties of the microstructure by the contrasts between the bulk transport properties of the phases. These results on the effective properties of the assembly should be confirmed by reproducing this study for other random realizations of the GDL. A parametric study on the anisotropy of GDL and the bulk properties of the constituents would be of interest to assist in the design of improved GDL-MPL assemblages.

7.2.3 Model of electrical contact resistances between GDL fibers

This section presents the results of the model of electrical contact resistances between fibers of a GDL. Six virtual GDLs were generated with different fiber anisotropies. The contacts between fibers were identified on the virtual images in order to model electrical contact resistances between fibers. The effective electrical conductivity tensor of each virtual GDL was calculated by direct simulation, Ej-Heat.

Figure 7.14 shows the comparisons between the effective electrical conductivities of the GDL in the case where the contacts between fibers are conductive and in the case where they are insulating. We find that the electrical anisotropy depends first on the geometric anisotropy of the microstructure. In any case, the electrical anisotropy increases if the contacts are insulating. This indicates that the contact resistances can have an effect although the contacts regions are very thin. In particular, we can obtain electrical anisotropies greater than 10 with contact resistances. These electrical anisotropy values are those measured experimentally on commercial GDLs, as discussed in section 4.2.1.2. The electrical properties of commercial GDL are therefore in the domain accessible by direct 3D simulation.

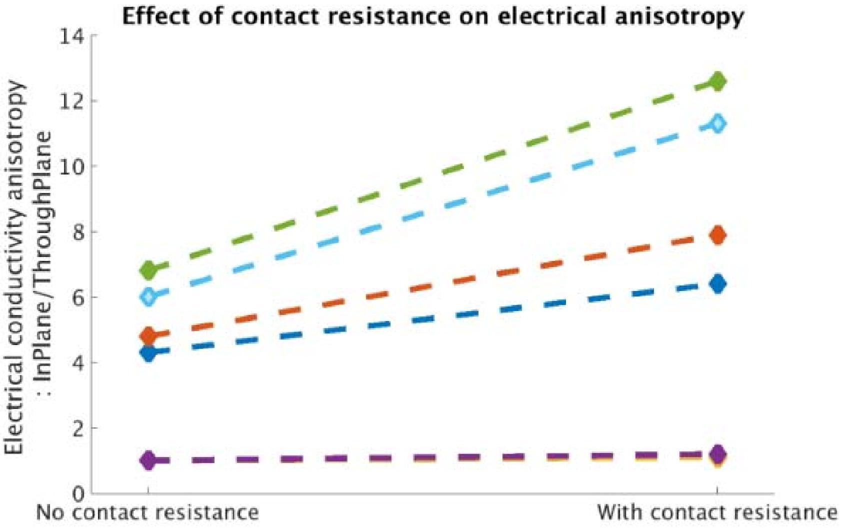

Figure 7.14 Effect of contact resistances between fibers on the anisotropy of electrical conductivities of virtual GDLs.

In summary, we have developed a methodology to add contact resistances between the different phases visible on a 3D image. With some parameters we find electrical anisotropies greater than 10, which is the case for commercial GDLs. It is thus possible to improve the electrical model of GDL by considering physical phenomena that occur at scales smaller than the resolution of the image. Note that virtual microstructures allow to precisely control the microstructure, which can help to better understand physical phenomena. Nevertheless, it is still not clear whether these experimental anisotropies are due to contact resistances between fibers or to contact resistances between the GDL and the bipolar plate. A comparison with experimental data on contact resistances in GDL would be necessary to conclude on the relevance of this model of resistances between fibers.

Beyond electrical conduction, this methodology of modifying the conductivities of voxels in certain voxels to model physical phenomena occurring within these voxels is a type of multi-scale method. It opens up possibilities for modeling physical phenomena occurring at scales smaller than the resolution of the image.

7.3 Perspectives

We present in this section some perspectives on the use of virtual microstructures to help design optimized porous materials.

7.3.1 Optimization of microstructures

The first step in implementing an optimization problem is to formulate relevant objectives. In the example given in this chapter we work only on through-plane diffusive transports. To make the optimization more representative of the actual design compromises of the GDLs, it would be interesting to consider in-plane transports as well, or even transports in the specific rib-channel configuration. Two-phase transport of liquid water and water condensation also plays an important role and should therefore be considered. It would be interesting also to prioritize the properties of the GDL, depending on their effect on the performance of the fuel cell. Performance models at the AME scale are the right tools to quantify the effect of a GDL transport property on performance. A simple way to prioritize objectives is to maximize a linear combination of objectives, with a weighting depending on the relative importance of each objective. It should be noted that the relative importance of the properties of GDL depends on the operating conditions, since the physical phenomena limiting the performances vary according to the operating conditions.

The second step in setting up an optimization problem is to formulate relevant constraints on the microstructures. These constraints may represent, for example, constraints in manufacturing the material or in assembling the material in the fuel cell. A first way of imposing constraints on the microstructure is to generate the microstructures by an algorithm that automatically respects these constraints. For example, the algorithm we use in this chapter to produce virtual GDLs respects the constraint that the material is made of straight fibers. A second way of imposing constraints would be to explore a subset of parameters of a microstructure generation algorithm, the subset of parameters that respect the constraints. This subset can be defined by the user if it has sufficient information. Or it can be preferentially explored by the optimization algorithm, using a method of penalty of constraints or a genetic algorithm for example.

We used in this chapter a parametric optimization of cubic porous cells, with microstructures parametrized by real numbers parameters. Cells geometry were also studied non-parametrically by topological optimization [Jung 2005], with interesting results concerning multifunctional materials in which the boundary between the phases is a minimal surface. Let us mention finally the existence of theoretical bounds on the crossed effective properties of composite materials [Torquato2004], which can be useful to evaluate the maximum progress that microstructures optimization can bring.

7.3.2 Generation of virtual microstructures

A crucial point for the optimization of microstructures is to explore sufficiently wide spaces of microstructures. We must therefore have powerful means to generate virtual microstructures. The microstructure spaces have very many degrees of freedom, but the effective properties of the materials are few, which makes some structures equivalent. The randomness in microstructures is an unavoidable element, which makes it necessary to consider different random realizations of the microstructures. Thus, an exhaustive exploration of microstructures is not a reasonable objective. Defining sub-sets and samplings of interesting microstructures is more interesting. In this perspective, the regular microstructures studied in section 7.2.1 are interesting because it is a set of quite diverse structures. They are useful, for example, in quantifying trade-offs between diffusive transport properties that may remain true for more realistic microstructures.

To understand the geometric features of microstructures, experimental tomographic images have a great role to play. Geometric algorithms used to generate virtual microstructures are often designed by understanding the geometric degrees of freedom of real structures. It is possible, for example, to image a series of materials obtained by varying a manufacturing parameter to understand the effect of this manufacturing parameter on the microstructure. Once the effect is understood qualitatively, it is possible to quantify it by image analysis.

Note that a simple way to model a manufacturing process virtually is to start from an experimental tomographic image and to introduce modifications in the image. For example, it is easy to introduce virtual holes by modifying a tomographic image of GDL with image editing software.

A more ambitious approach to generating microstructures is to model the physics of manufacturing processes. Nevertheless, some manufacturing processes represent real challenges for modeling, such as modeling the effect of chemical additives in inks on the microstructure of the MPL or catalytic layers.

Note that multi-objective optimization and the exploration of large quantities of degrees of freedom can be done with genetic algorithms. Finally, remember that the human brain is a good tool to solve design problems. A timely approach would be to appeal to the public to find optimized microstructures, along the lines of open outsourcing and participatory production.

7.4 Conclusion

This chapter is devoted to the use of virtual microstructures of fuel cells porous materials. This chapter presents proofs of concept and instructional illustrations to better understand the value of virtual microstructures in studying porous fuel cell materials and in helping to design optimized porous materials. We illustrate the potential of virtual microstructures with three studies.

The first study concerns the optimization of microstructures. We show that it is possible to study a multi-objective optimization problem of microstructure thanks to the notion of Pareto optimum. We find virtual structures more optimized than real GDL for through-plane diffusive transports. We introduce tools to represent microstructure spaces, that are spaces with many degrees of freedom: property mappings and parallel co-ordinate graphs.

The second study concerns MPL-GDL assemblies. We show that it is possible to represent realistic microstructures, based on an understanding of the geometric degrees of freedoms of real microstructures. We model a manufacturing process, the coating, in a simplified way, using the full morphology model. We study the effective transport properties of the assembly as a function of the penetration of the MPL in the GDL.

The third study concerns the electrical contacts resistances between GDL fibers. We introduce a contact resistance model on virtual GDLs and study it numerically. This study shows that physical phenomena occurring at scales smaller than the resolution of the image can be considered by a multi-scale modeling of voxel properties. Experimental data are required to conclude on the validity of the electrical contacts resistances model for GDL.

7.5 Bibliography

- [Adams2013] Brent L. Adams, Surya R. Kalidindi, David T. Fullwood, Microstructure-Sensitive Design for Performance Optimization, Butterworth-Heinemann, 2013

- [Aitkenhead2010] Adam H. Aitkenhead, Mesh voxelisation, Matlab File Exchange, The Christie NHS Foundation Trust, 2010

- [Antonietti2004] Markus Antonietti, Geoffrey A. Ozin, Promises and Problems of Mesoscale Materials Chemistry or Why Meso ?, Chem. Eur. J. 2004, 10, 28-41

- [Baker2012] Craig Baker, a microstructure model for a proton exchange membrane fuel cell catalyst layer, Master Thesis, Queen’s University, Kingston, Ontario, Canada, 2012

- [Becker2011] Jürgen Becker, Christian Wieser, Stephan Fell, Konrad Steiner, A multi-scale approach to material modeling of fuel cell diffusion media, International Journal of Heat and Mass Transfer, Volume 54, Issues 7–8, March 2011, Pages 1360–1368

- [Bresenham1965] J. E. Bresenham, « Algorithm for computer control of a digital plotter », IBM Systems Journal, vol. 4, no 1, 1er janvier 1965, p. 25–30

- [Burheim2015] Odne S. Burheim, Gregory A. Crymble, Robert Bock, Nabeel Hussain, Sivakumar Pasupathi, Anton du Plessis, Stephan le Roux, Frode Seland, Huaneng Su, Bruno G. Pollet, Thermal conductivity in the three layered regions of micro porous layer coated porous transport layers for the PEM fuel cell, international journal of hydrogen energy 40 (2015) 16775-16785

- [Daino2012] Michael M. Daino, Satish G. Kandlikar, 3D phase-differentiated GDL microstructure generation with binder and PTFE distributions, International journal of hydrogen energy 37 (2012) 5180-51 9
- [El-Hannach2014] Mohamed El-Hannach, Erik Kjeang, Stochastic Microstructural Modeling of PEFC Gas Diffusion Media, Journal of The Electrochemical Society, 161 (9) F951-F960 (2014)
- [El-Hannach2015] Mohamed El-Hannach, Randhir Singh, Ned Djilali, Erik Kjeang, Micro-porous layer stochastic reconstruction and transport parameter determination, Journal of Power Sources 282 (2015) 58e64
- [Fell2010] S. Fell, K. Steiner, A. Latz, J. Zausch, J. Becker, G. B. Less, J. H. Seo, S. Han, A. M. Sastry, Porous materials of electrochemical cells in the CAE design process, (2010), http://abcd.engin.umich.edu/wp-content/uploads/sites/215/2015/04/fell_porous_materials.pdf
- [Froning2014] Froning, D., Gaiselmann, G., Reimer, U. et al., Stochastic Aspects of Mass Transport in Gas Diffusion Layers, Transp Porous Med (2014) 103: 469. doi:10.1007/s11242-014-0312-9
- [Gaiselmann2012] Gerd Gaiselmann, Ralf Thiedmann, Ingo Manke, Werner Lehnert, Volker Schmidt, Stochastic 3D Modeling of Fiber Based Materials, Computational Materials Science, Volume 59, June 2012, Pages 75–86
- [Gaiselmann2013] Stochastic 3D modeling of non-woven materials with wet-proofing agent Gerd Gaiselmann, Dieter Froning, Christian Tötzke, Christian Quick, Ingo Manke, Werner Lehnert , Volker Schmidt , International Journal of Hydrogen Energy 38(20):8448-8460 · July 2013
- [Gaiselmann2014] Gerd Gaiselmann, Christian Tötzke, Ingo Manke, Werner Lehnert, Volker Schmidt, 3D microstructure modeling of compressed fiber-based materials, Journal of Power Sources 257 (2014) 52-64
- [Hizir2010] Fahri Erinc Hizir, Characterization and tailoring of the microporous layer - catalyst layer interfacial structure in polymer electrolyte membrane fuel cells, Master thesis, Pennsylvania State University, 2010
- [Jung2005] Y. Jung and S. Torquato, Fluid Permeabilities of Triply Periodic Minimal Surfaces, Physical Review E, 92, 255505 (2005).
- [Kim2009] Seung Hyun Kim, Heinz Pitsch, Reconstruction and Effective Transport Properties of the Catalyst Layer in PEM Fuel Cells, Journal of The Electrochemical Society, 156 (6) B673-B681 (2009)
- [Lange2012] Kyle J. Lange, Pang-Chieh Sui, Ned Djilali, Determination of effective transport properties in a PEMFC catalyst layer using different reconstruction algorithms, Journal of Power Sources 208 (2012) 354–365
- [Malek2011] Kourosh Malek, Tetsuya Mashio, Michael Eikerling Microstructure of Catalyst Layers in PEM Fuel Cells Redefined: A Computational Approach, Electrocatal (2011) 2:141–157
- [Mukherjee2006] Partha P. Mukherjee, Chao-Yang Wang, Stochastic Microstructure Reconstruction and Direct Numerical Simulation of the PEFC Catalyst Layer, Journal of The Electrochemical Society, 153 (5) A840-A849 (2006)

- [Park2012] Sehkyu Park, Jong-Won Lee, Branko N. Popov, A review of gas diffusion layer in PEM fuel cells: Materials and designs, International Journal of Hydrogen Energy, Volume 37, Issue 7, April 2012, Pages 5850–5865

- [Park2016] Jaeman Park, Hwanyeong Oh, Yoo Il Lee, Kyoungdoug Min, Eunsook Lee, Jy-Young Jyoung, Effect of the pore size variation in the substrate of the gas diffusion layer on water management and fuel cell performance, Applied Energy, Volume 171, 1 June 2016, Pages 200–212

- [Persson2013] Anubhav Jain, Shyue Ping Ong, Geoffroy Hautier, Wei Chen, William Davidson Richards, Stephen Dacek, Shreyas Cholia, Dan Gunter, David Skinner, Gerbrand Ceder, and Kristin A. Persson, Commentary: The Materials Project: A materials genome approach to accelerating materials innovation, APL Mater. 1, 011002 (2013)

- [Prill2015] T. Prill, S. Rief, and K. Steiner, Microstructure Modeling and Optimization of Transport Properties of Gas Diffusion Layers in PEM Fuel Cells, Combining Graph Based Approaches and Full Field Computations, ECS Conference on Electrochemical Energy Conversion & Storage with SOFC-XIV Abstract vol. MA2015-03 no. 3691, 2015

- [Roussel2015] Denis Roussel, Aaron Lichtner, David Jauffrès, Rajendra K. Bordia, Christophe L. Martin, Effective transport properties of 3D multi-component microstructures with interface resistance, Computational Materials Science, Volume 96, Part A, January 2015, Pages 277–283

- [Sadeghifar2014] Hamidreza Sadeghifar, Ned Djilali, Majid Bahrami, Effect of Polytetrafluoroethylene (PTFE) and micro porous layer (MPL) on thermal conductivity of fuel cell gas diffusion layers: Modeling and experiments, Journal of Power Sources, Volume 248, 15 February 2014, Pages 632-641

- [Schladitz2006] Katja Schladitz, Stefanie Peters, Doris Reinel-Bitzer, Andreas Wiegmann, Joachim Ohser, Design of acoustic trim based on geometric modeling and flow simulation for non-woven, Computational Materials Science, Volume 38, Issue 1, November 2006, Pages 56–66

- [Shapiro2001] Vadim Shapiro, Solid Modeling, in Handbook of Computer Aided Geometric Design, Editors: G. Farin, J. Hoschek, M.-S. Kim, Elsevier Science Publishers, 2001

- [Siddique2010] N.A. Siddique, Fuqiang Liu Process based reconstruction and simulation of a three-dimensional fuel cell catalyst layer, Electrochimica Acta 55 (2010) 5357–5366

- [Tayarani-Yoosefabadi2016] Z. Tayarani-Yoosefabadi, D. Harvey, J. Bellerive, E. Kjeang, Stochastic microstructural modeling of fuel cell gas diffusion layers and numerical determination of transport properties in different liquid water saturation levels, Journal of Power Sources 303 (2016) 208-221

- [Thiedmann2009] Ralf Thiedmann, Christoph Hartnig, Ingo Manke, Volker Schmidt, Werner Lehnert, Local Structural Characteristics of Pore Space in GDLs of PEM Fuel Cells Based on Geometric 3D Graphs, Journal of the Electrochemical Society 156, B1339 - B1347 (2009)

- [Thiedmann2012] Ralf Thiedmann, Gerd Gaiselmann, Werner Lehnert, Volker Schmidt, Stochastic Modeling of Fuel-Cell Components, in book Fuel Cell Science and Engineering: Materials, Processes, Systems and Technology, editors Detlef Stolte, Bernd Emonts, Wiley-VCH Verlag & Co. KGaA, 2012

- [Torquato2004] S. Torquato and A. Donev, Minimal Surfaces and Multifunctionality, Proceedings of the Royal Society of London A, 460, 1849 (2004).
- [Torquato2005]. Torquato, Microstructure Optimization, Chapter in Handbook of Materials Modeling, Editors: Sidney Yip, pp 2379-2396, 2005
- [Wargo2012] E.A. Wargo, V.P. Schulz, A. Cecen, S.R. Kalidindi, E.C. Kumbur, Resolving macro- and microporous layer interaction in polymer electrolyte fuel cells using focused ion beam and X-ray computed tomography, Electrochimica Acta 87 (2013) 201– 212
- [Zamel2012] Nada Zamel, Jürgen Becker, Andreas Wiegmann, Estimating the thermal conductivity and diffusion coefficient of the microporous layer of polymer electrolyte membrane fuel cells, Journal of Power Sources 207 (2012) 70– 80

Chapter 8 Conclusion

Transport in porous electrodes plays a crucial role in the operation of fuel cells. In this thesis, we concentrated on a porous material involved in fuel cell electrodes, the gas diffusion layers (GDL). The GDL are traversed by flows of gases, electrons, heat and water in vapor and liquid form. To enable these multiple transports, essentials to the operation of the fuel cell, the GDLs are composed of a fluid phase and a solid phase, itself composed of several materials. The objective of this thesis is to model the transport properties of GDL, to better understand them and to be able to optimize them. The microstructure of the GDL plays a crucial role on the compromises between the multiple functions of the GDL and the efficiency of transport in the electrodes. To better understand the microstructure of porous materials on transport, we took advantage of the advances in imaging techniques that allow us to know precisely the microstructure of porous electrode materials. We focused on the GDL because we had images of its microstructure, obtained by X-ray tomography.

We have set up tools to analyze tomographic images, and simulation tools working on 3D images. The first simulation tool we used is an open source tool for direct simulation of diffusive transport on microstructures. A second simulation tool that we used is a pore network simulation code that we have developed. We used pore networks to simulate diffusive transport phenomena such as gas diffusion, electrical conduction and thermal conduction, and to simulate two-phase phenomena such as the transport of liquid water in the capillary digitation regime and the condensation of water in the GDL. To use the pore networks on tomographic images, we have developed a procedure for extracting pores from 3D images of porous microstructures.

We validated quantitatively our models by comparison with experience. We have validated that the pores networks allow to simulate the transport of liquid water in the GDL in the presence of capillary forces. To perform this validation, we compared the water distributions simulated by pore networks with X-ray tomographic images showing the distribution of water in the GDL at micrometric scales. These images were realized during an ex-situ water injection experiment in a GDL, by the Paul Scherrer Institute, in the framework of the European project Impala. We also validated the full morphology simulation method for this water injection experiment. Moreover, we showed a second time the reliability of water injection simulations in GDL, showing that the simulations allow to predict the experimental capillary pressure curves of two types of GDL, from images of their microstructure. This is the first time that this demonstration is done with such precision for fibrous media such as GDL. These results make it possible to reinforce the numerous articles using pore networks to model the two-phase transports in the GDL. These results also show that two-phase transports in the fluid phase of porous media such as GDL can be computed reliably using simulations on images obtained by X-ray tomography.

We also compared the effective diffusive transport properties obtained by simulations with some experimentally measured effective transport properties of the GDLs. This allowed us to show that direct simulations of diffusion on tomographic images make it possible to reliably determine the effective diffusivities of the GDL. This confirms the relevance of X-ray tomography to imaging porous materials, as it allows to accurately determine the geometry of the fluid phase. On the other hand, we have shown the limits of X-ray images to determine the physical properties of the solid phase, such as the effective electrical conductivity. Indeed, the solid phase is composed of several materials with distinct electrical properties, which are not distinguishable by X-ray tomography. To circumvent this difficulty, we implemented an algorithm to artificially reconstruct the distribution of materials in the solid phase, and we introduced electrical contact resistances on the tomographic images. Nevertheless, new experimental data on the solid phase of the GDL must be gathered to parameterize and validate this electric model of the solid phase.

Finally, we illustrated the possibility of studying porous microstructures generated virtually on a computer. We have shown that it is possible to design virtually microstructures and to characterize them by simulation, with the aim of finding more efficient materials. This approach is likely to provide insight into the design of porous materials in the future, complementary to the experimental approach.

8.1 Main results

Here we list the main results obtained in each chapter of this manuscript.

8.1.1 Numerical verifications of diffusive transport simulations

We have implemented pore network and direct simulation tools to simulate diffusive transport properties of GDL using tomographic images.

We verified that the explicit jumps direct simulation method, EJ-Heat, gives very precise results on several vurtual microstructures. This reinforces the many articles using the explicit jumps direct simulation method for PEM fuel cell porous materials.

We tested the numerical accuracy of pore networks extracted from tomographic images for simulations of diffusive transports. We found that the simulation results depend on the formulas used to consider the geometry of the pores and the links in the diffusive transport conductances. We have proposed several formulas for conductances, using several shapes descriptors for pores and links. We have found that the effectiveness of a formula depends on the type of microstructure. We have not found a formula that works well for all microstructures. Nevertheless, we have identified a formula for conductances that produces better results than other formulas. We proposed as perspectives some more elaborate computation procedures for diffusive transport conductances, which take into account more precisely the geometry of the pores and constrictions.

We studied simulations of diffusive transports by regular pore networks. The pore size and constriction size distributions were extracted by geometric analysis of a GDL image obtained by X-ray tomography. These size distributions and some hypothesis on the geometry of the elementary pores were used to calibrate the regular pore network. We compared the diffusive transport properties of the regular pore network with direct simulations on a tomographic image of a GDL, which served as a reference value. We found that the regular pore networks that we studied overestimate the transport properties. We attributed this to the absence of tortuosity in the regular pore networks. This analysis highlights the need to introduce additional calibration parameters for regular pore networks, in addition to the pore size and link size distributions, which are not sufficient to consider geometric effects such as tortuosity. A general calibration methodology for regular pore networks remains to be determined. One perspective would be to use the effective transport properties measured experimentally to calibrate the conductances of the regular pore network.

8.1.2 Experimental validation of diffusive transport simulations

We have implemented tools to calculate the diffusive transport properties of GDL from X-ray tomographic images. These tools include filtering and segmentation tools for processing raw tomographic images, a code for direct simulations by the explicit jump method, a pore network extraction tool from an image of a porous microstructure, and a pore network simulation code.

We have shown that direct simulations on tomographic images of GDL allow to predict the effective diffusive transport properties of the fluid phase, such as the effective diffusivity. This is possible because the macropores are clearly visible by X-ray tomography, which leads to a good knowledge of the geometry of the fluid phase. It should be noted that the porosity of the GDLs that we studied is composed of macropores and micropores located in the binder. Micropores are not distinguishable by X-ray tomography due to limited resolution. The porosity of the segmented image was therefore equal to the porosity of the macropores, which is lower than the total porosity of the GDL measured experimentally. We have observed that in the case of the GDL studied, neglecting the microporosity of the binder induces only a small error on the effective diffusivity. We have concluded that the microporosity of the binder of these GDLs has a low effective diffusivity, which can be due to poorly connected micropores, very tortuous micropores or micropores having a high factor of constrictivity.

By comparing electrical conductivity simulations with experimental characterizations, we have identified gaps in the electrical model that we use to simulate the electrical conductivity of GDLs. The effect of PTFE and the effect of electrical contact resistances between fibers and between the GDL and the measuring electrodes is not well known. Note that X-ray tomography is less well suited for imaging the solid phase of GDL because the contrast between binder, carbon fibers and PTFE is too low to distinguish them from the tomographic image. Moreover, the resolution of the image is often too low to distinguish the geometrical contacts between the constituents of the GDL. We proposed algorithms to artificially reconstruct the geometry of the fibers and the binder in the solid phase, and to model the effect of electrical contact resistances between the fibers (the latter model is presented in section 7.1.3). More appropriate experimental data are required to parameterize and validate these models.

We compared simulations of effective diffusive transport properties based on tomographic images with experimental characterizations of these properties. Examination of the agreements and differences between the simulations and the experiments allowed us to better understand the effect of the bulk transport properties of the binder on the effective transport properties of the GDL. We have shown that direct simulations based on tomographic images make it possible to evaluate the effective diffusivities of the GDL easily with simulations. Simulations make it possible to calculate the anisotropies of effective diffusivity, which are difficult to measure experimentally.

8.1.3 Injection of liquid water into a GDL

This chapter is devoted to the modeling of an experiment of injection of liquid water in a GDL. We validated our modeling by comparing the simulated liquid water distributions with a tomographic image showing the experimental liquid water distribution of in GDL during the liquid water injection experiment.

We have advanced the state of the art on modeling the behavior of liquid water in GDL on several points. First, we have shown that the pore network simulations allow to predict with good precision the distribution of liquid water during an ex-situ experiment of injection of liquid water in the GDL. Second, we have developed a method for extracting a pore network from a tomographic image, based on the watershed segmentation algorithm. We have shown that this extraction method gives good results for fibrous media such as GDL. Third, we have implemented image processing tools to quantitatively compare 3D images of water distributions, either simulated by pore networks or obtained experimentally by X-ray tomography. Finally, we have shown that the pore networks simulations and full morphology simulations give close results, although their operating principles are different. This helped to consolidate the two simulation approaches. In addition, the comparison between water distributions simulated by these two methods on the same image provides a means of verifying the reliability of the procedure of pore network extraction from the image.

In addition, we computed capillary pressure curves for several GDLs, using full morphology simulations on X-ray tomographic images of a GDL. We compared these simulation results with experimentally obtained capillary pressure curves. The very good agreement of the simulated and experimental capillary pressure curves allowed us to validate once again the full morphology simulations for the water injection experiments in a GDL. We have also shown that the Leverett correlation, commonly used in PEM fuel cell models, incorrectly models the actual GDL capillary pressure curves.

8.1.4 Water condensation in a GDL

We have implemented a pore network simulation algorithm for the condensation of water in GDL. We have illustrated the capabilities of these simulations on several virtual pore networks with different microstructures. We compared the simulations on two pore networks representing two GDL with different anisotropies. We have found that the temperature and water vapor concentration fields are different for these two different microstructures. Thus, these simulations of water condensation in GDL, used with tools to generate pore networks with realistic microstructures, have the ambition to lead to a better understanding of the effect of the GDL microstructure on the water management in fuel cells.

Further simulations are required to study this model of water condensation in GDLs in greater detail. A rigorous comparison with experimental results is desirable to validate the physical assumptions of this model.

8.1.5 Study of virtual microstructures

We developed computer tools to generate virtual microstructures. We generated virtual microstructures by randomly distributing in space the constituents of materials, such as fibers. We used morphological operations, such as dilations and erosions, to mimic the effect of manufacturing processes such as the deposition of a layer by coating on a GDL, or the addition of a binder in a GDL.

We formulated a problem of optimization of GDL microstructure for the optimization of through-plane effective diffusivities and electrical conductivities. Transports in the plane of the GDL and the presence of liquid water were not considered to simplify the problem. We presented a methodology and data visualizations to address this problem. We have shown that the real GDL microstructures are not optimal for this problem. We have shown that the compression of the GDL must be considered for the optimization of the microstructures. We have shown that the geometric constrictivity parameter has a potential for optimization.

We generated virtual microstructures for the assembly of GDL and MPL layers. We studied the effective diffusive transport properties of these assemblies by simulation. We investigated how the penetration of the MPL into the GDL affects the effective transport properties of the MPL-GDL assembly.

We developed a model of electrical contact resistances between the GDL constituents, such as fibers. We implemented an algorithm to detect the contacts between the constituents in a tomographic image of a GDL. The contact resistances were modeled by decreasing the conductivities of the voxels located at the interfaces between the constituents. This methodology demonstrates the possibility of making multi-scale modeling using direct simulations on microstructure images.

8.2 Recommendations and perspectives

Here we present a list of general recommendations and perspectives. More specific perspectives can be found at the end of each chapter and article in this document.

The first recommendation we make is to take advantage of advances in imaging techniques and advances in algorithms for quantitative image analysis. Indeed, the quantitative use of images of materials is a field in full growth and rich of opportunities. Imaging techniques are making great strides. The algorithms and methodologies of quantitative image analysis also make rapid progress. Open source codes make these advances quickly available. We have shown in this thesis that image-based models provide added value for modeling physical phenomena and modeling the effect of the microstructure on these phenomena. Moreover, the know-how developed to acquire images of a material and analyze the collected data can often be transposed to other materials.

A first series of perspectives concerns the exploitation of the GDL models that we have developed. The relative thermal conductivities and gas diffusivities of GDLs in the presence of liquid water can be calculated by pore network simulations or direct simulations on images which show a liquid water distribution in a GDL. This is interesting because these relative transport properties are difficult to measure experimentally. The effect of compression on the transport properties of GDLs can be studied, based on tomographic images of compressed GDL or virtualy generated images of compressed GDL. Finally, the electrical model of GDL should be improved, modeling more precisely the contact between the GDL and the rib of the bipolar plate.

A second series of perspectives concerns the use of our methodology for other materials and other physical phenomena. Our models based on tomographic images can be used for other porous materials, such as other types of GDL, other porous fuel cell materials, or porous materials used in other devices such as electrolysers and batteries. Acquiring know-how on other imaging modalities would widen the range of accessible materials. Examples of other imaging modalities include X-ray tomography on a synchrotron, FIB-SEM tomography, SEM slice views. Finally, it is possible to add physical phenomena in the pore network models, for example phenomena occurring in catalytic layers such as the production of current and water [El-Hannach2011].

A third series of perspectives concerns the geometrical and statistical modeling of materials microstructures. A first problem is the search for geometric parameters capturing the effect of the microstructure on the effective transport properties. For diffusive transports, these parameters are, for example, the porosity, the tortuosity, the constrictivity and some parameters quantifying connectivity and dead-ends, such as accessible porosity. For two-phase phenomena, the pore size and constriction size distributions are good candidates, but the link between these parameters and the effective two-phase properties should be studied in more detail. A second problem is the design of optimized microstructures. Numerous optimization methodologies exist. We have seen that a parametric model of the unit cells of a periodic microstructure is a useful first step to quickly evaluate which parameters are influential. This approach could be used for the optimization of catalytic layer agglomerates. Finally, a third problem is the modeling of the effect of manufacturing processes on microstructures. Such models linking the microstructures to their manufacturing processes can be useful for better understanding and optimization of manufacturing processes. Making tomographic images of materials obtained by varying manufacturing parameters is probably a necessary step in collecting the data necessary for these models.

Chapter 9 Appendices

9.1 Simulations tools on tomographic images

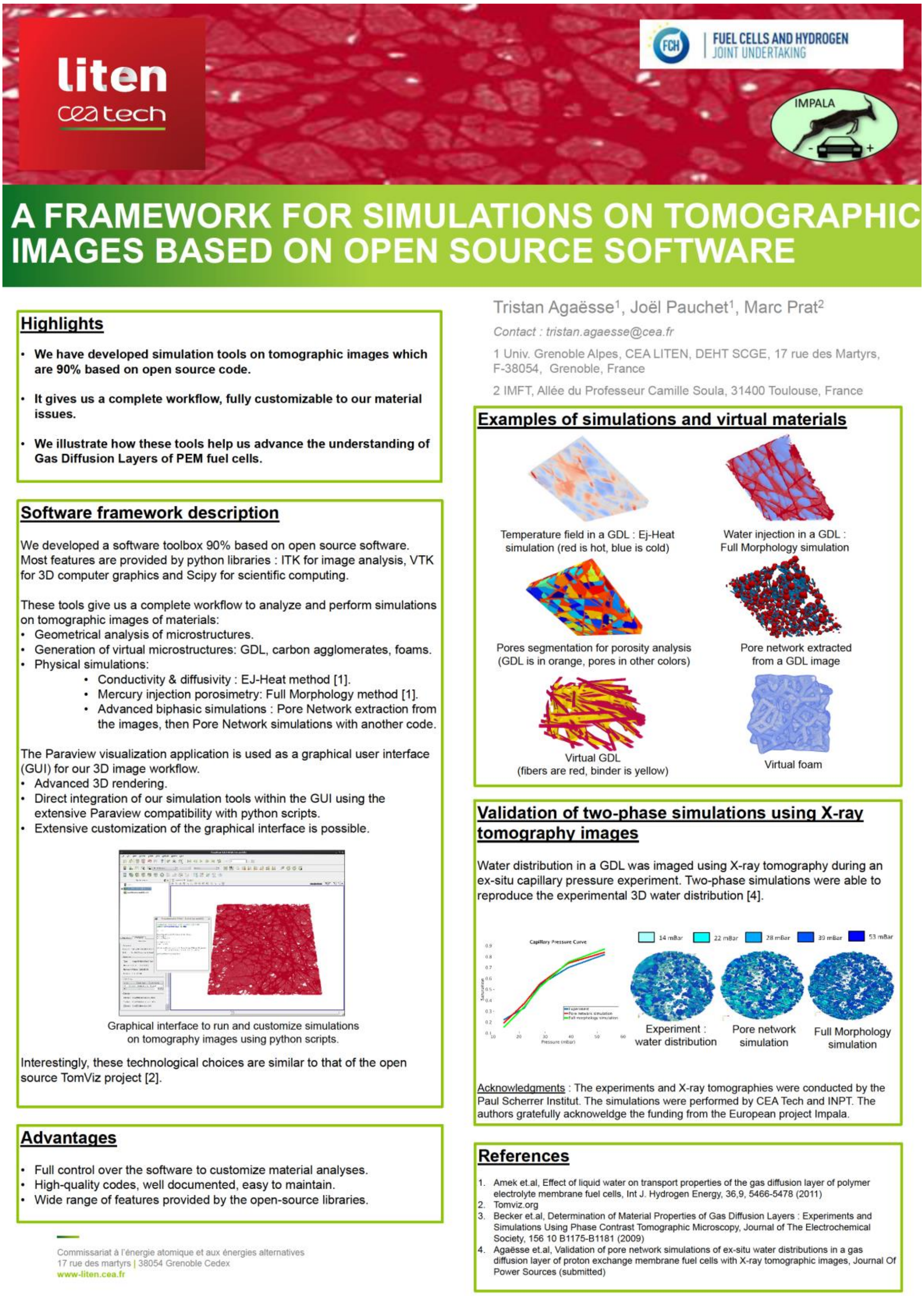

A FRAMEWORK FOR SIMULATIONS ON TOMOGRAPHIC IMAGES BASED ON OPEN SOURCE SOFTWARE

Tristan Agaësse[1], Joël Pauchet[1], Marc Prat[2]

Contact : tristan.agaesse@cea.fr

1 Univ. Grenoble Alpes, CEA LITEN, DEHT SCGE, 17 rue des Martyrs, F-38054, Grenoble, France

2 IMFT, Allée du Professeur Camille Soula, 31400 Toulouse, France

Highlights

- **We have developed simulation tools on tomographic images which are 90% based on open source code.**
- **It gives us a complete workflow, fully customizable to our material issues.**
- **We illustrate how these tools help us advance the understanding of Gas Diffusion Layers of PEM fuel cells.**

Software framework description

We developed a software toolbox 90% based on open source software. Most features are provided by python libraries : ITK for image analysis, VTK for 3D computer graphics and Scipy for scientific computing.

These tools give us a complete workflow to analyze and perform simulations on tomographic images of materials:
- Geometrical analysis of microstructures.
- Generation of virtual microstructures: GDL, carbon agglomerates, foams.
- Physical simulations:
  - Conductivity & diffusivity : EJ-Heat method [1].
  - Mercury injection porosimetry: Full Morphology method [1].
  - Advanced biphasic simulations : Pore Network extraction from the images, then Pore Network simulations with another code.

The Paraview visualization application is used as a graphical user interface (GUI) for our 3D image workflow.
- Advanced 3D rendering.
- Direct integration of our simulation tools within the GUI using the extensive Paraview compatibility with python scripts.
- Extensive customization of the graphical interface is possible.

Graphical interface to run and customize simulations on tomography images using python scripts.

Interestingly, these technological choices are similar to that of the open source TomViz project [2].

Advantages

- Full control over the software to customize material analyses.
- High-quality codes, well documented, easy to maintain.
- Wide range of features provided by the open-source libraries.

Commissariat à l'énergie atomique et aux énergies alternatives
17 rue des martyrs | 38054 Grenoble Cedex
www-liten.cea.fr

Examples of simulations and virtual materials

Temperature field in a GDL : Ej-Heat simulation (red is hot, blue is cold)

Water injection in a GDL : Full Morphology simulation

Pores segmentation for porosity analysis (GDL is in orange, pores in other colors)

Pore network extracted from a GDL image

Virtual GDL
(fibers are red, binder is yellow)

Virtual foam

Validation of two-phase simulations using X-ray tomography images

Water distribution in a GDL was imaged using X-ray tomography during an ex-situ capillary pressure experiment. Two-phase simulations were able to reproduce the experimental 3D water distribution [4].

Experiment : water distribution

Pore network simulation

Full Morphology simulation

Acknowledgments : The experiments and X-ray tomographies were conducted by the Paul Scherrer Institut. The simulations were performed by CEA Tech and INPT. The authors gratefully acknoweldge the funding from the European project Impala.

References

1. Amek et.al, Effect of liquid water on transport properties of the gas diffusion layer of polymer electrolyte membrane fuel cells, Int J. Hydrogen Energy, 36,9, 5466-5478 (2011)
2. Tomviz.org
3. Becker et.al, Determination of Material Properties of Gas Diffusion Layers : Experiments and Simulations Using Phase Contrast Tomographic Microscopy, Journal of The Electrochemical Society, 156 10 B1175-B1181 (2009)
4. Agaësse et.al, Validation of pore network simulations of ex-situ water distributions in a gas diffusion layer of proton exchange membrane fuel cells with X-ray tomographic images, Journal Of Power Sources (submitted)

9.2 Probabilistic model for the variability of materials

The properties of fuel cell materials, such as the effective diffusivity of gases through an MEA, present statistical variability at the rib-canal scale, ie typically on samples of 1 mm². Note that fuel cells are made of MEA sheets of several cm² to several m², whereas the typical thickness of an MEA is less than one millimeter. Because of this difference in size, the manufacturing constraints are such that it is difficult to control accurately the effective transport properties in the thickness of the MEA. For example, there may be defects in the assemblies between the layers of the MEA.

Therefore, the properties of MEA vary randomly spatially. In the theoretical framework of probabilities, the properties of materials are therefore random variables. However, transport properties are a deterministic parameter in the usual PEMFC models. Should we consider the fluctuations of the transport properties around the mean value in the performance models ? How can an effective deterministic property be obtained from a random property ?

We show that a probability theory framework is well suited to describe this problem. It includes a modeling of the randomness of the properties of the materials as well as Monte Carlo simulations to calculate their effect on the performances. We present a statistical averaging methodology. In a probabilistic framework, averaging involves weights as a function of the probability of occurrence of the different values. We are therefore led to quantify the statistical distribution of the properties of materials. This requires specific studies, such as sampling experimental measurements, or simulations on random models of microstructures.

9.2.1 Probabilistic model for MEA materials transport properties

The configuration we are studying is as follows. We decompose the MEA into elementary rib-channel patterns, as shown in Figure 9.1. We assume that there is no exchange in the plane of the MEA between the rib-channel patterns. We assume that the properties of the materials differ from one elementary pattern to another, to represent the inhomogeneities of the materials.

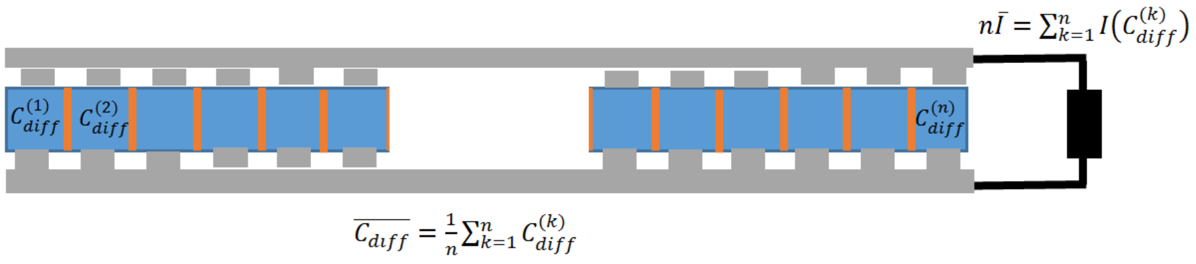

Figure 9.1 AME in blue, bipolar plates in gray. Slice view. We have decomposed the AME into elementary patterns (separations in red) for the purposes of modeling the spatial variability between patterns. $C_{diff}^{(k)}$ denotes the through-plane effective diffusivity. We assume that there are no exchanges through the orange separations. The elementary patterns are thus generators in parallel in the fuel cell electrical circuit (in black, an example of an electrical circuit with a resistance).

We model the through-plane effective diffusivity of the GDL of the pattern k by a random variable $C_{diff}^{(k)}$. The randomness on $C_{diff}^{(k)}$ depends on the size of the pattern. Let us recall why, by means of some notions of probability. Let us denote U_i the random variables representing the effective conductivities of elementary sub-samples. We assume that the U_i are statistically independent and follow the same probability law, for example a uniform distribution in the interval [0,1]. Let us denote $U^{(n)}$ the normalized through-plane effective transport property of a sample consisting of n elementary sub-samples. More precisely, we normalize $U^{(n)}$ by the size of the sample to compare it with U_i :

$$U^{(n)} = \frac{1}{n}\sum_{i=1}^{n} U_i$$

Équation 9.1

Here the parallel configuration studied allowed us to use a simple model: the effective property is the sum of the effective properties of the sub-samples. In a more general case, the Wiener bounds can provide an estimate of the effective properties of a material as a function of the properties of its subsamples. The average value of the through-plane effective transport property of the complete MEA, normalized by the surface area of the MEA, is equal to the average value of the conductivities of the elementary cells:

$$E\left(U^{(n)}\right) = E\left(\frac{1}{n}\sum_{i=1}^{n} U_i\right) = \frac{1}{n}\sum_{i=1}^{n} E(U_i) = E(U_1)$$

Équation 9.2

We find that the average value is the same for the complete AME as for the elementary cells.

The variance of the effective conductivity of the complete AME, normalized by the surface of the AME, is obtained from the variance of the conductivities of the elementary cells by a classical calculation:

$$Var\left(U^{(n)}\right) = Var\left(\frac{1}{n}\sum_{i=1}^{n} U_i\right) = \frac{1}{n^2}\sum_{i=1}^{n} Var(U_i) + terms\ with\ zero\ covariance\ = \frac{1}{n^2} nVar(U_1)$$
$$= \frac{1}{n} Var(U_1)$$

$$Var\left(U^{(n)}\right) = \frac{1}{n} Var(U_1)$$

Équation 9.3

Thus, the variance of the effective mean conductivity of the complete MEA decreases with the lateral size of the MEA sample. This is explained by the fact that the uncertainties of the sub-samples properties compensate.

For readers unfamiliar with the theory of probabilities, we recall here informally an essential result of probabilities, the central limit theorem. This theorem asserts in substance that the probability law of $\sqrt{n}U^{(n)}$ converges to a normal distribution $N\left(E(U_1), Var(U_1)\right)$, that is to say a normal distribution centered on $E(U_1)$ with a variance equal to $Var(U_1)$. And this, whatever the initial probability law U, if $Var(U_i) < +\infty$.

9.2.2 Effect on performances of the spatial variability of the materials transport properties

The polarization curve of the cell can be obtained from simulations on elementary patterns. Indeed, the elementary patterns of AME are arranged in parallel on the surface of the AME so the currents add up. Thus, at fixed voltage, the total current intensity is the arithmetic mean of the currents of the elementary patterns. We assume that the operating conditions (stoichiometry, pressure ...) are the same for each elementary unit of AME. We have assumed that there are no in-plane transfers between the elementary patterns. We can therefore study with a performance model at the rib-canal scale the effect of the variability of transport properties between patterns on the polarization curve of the whole cell.

In the case of nonlinearities of performances with respect to material transport properties, the spatial variability of materials will have a non-linear effect on performances. Let $C \to I(C)$ denote the function which associates the current produced by a pattern to the transport properties of this pattern, with fixed operating conditions. In the case where the function $C \to I(C)$ is not linear, $\langle I(C) \rangle \neq I(\langle C \rangle)$ where $\langle \cdot \rangle$ denotes the arithmetic mean. Let us take a concrete example: if the intensity is non-linear with respect to the GDL diffusivity, a weak GDL diffusivity in a pattern is not compensated by a strong GDL diffusivity in another pattern.

To decide whether to consider the randomness of a property in the models, we must study the sensitivity and the nonlinearity of the model with respect to this property, as well as the range of variability of this property. Indeed, we can consider linearizing the performance model around the mean value of the property of the material, which makes it possible to neglect the randomness of this property, because then $\langle I(C) \rangle = I(\langle C \rangle)$. The precision of this approximation depends on the sensitivity of the model with respect to this parameter, the level of non-linearity with respect to this parameter and the variation range of the parameter.

In case we can not linearize the model, a tool to evaluate the effect of the random variability of a parameter is the Monte Carlo simulation. This involves performing multiple simulations by randomly drawing the parameter value. To reduce computing time, it may be worthwhile to replace the complete performance model with a meta-model. A perspective would be to obtain such a meta-model using an experimental design, for example by the kriging method. Such methods allow to approximate the meta-model using a few simulation points to estimate the effect of several variables. A meta-model with quadratic terms would allow us to consider non-linearities.

9.2.3 Conclusion

The transport properties of fuel cell materials vary spatially. We present the basis of a theoretical probability framework for the modeling of PEMFCs. Materials are usually modeled using deterministic effective properties. In the case of nonlinearity of the performance with respect to the transport properties of materials, the variability of materials can have a non-trivial effect on performance. This has an implication concerning the experimental characterization of the materials: a measurement method taking account of this variability should be used. We propose a discussion on the possibility of linearizing the performance model with respect to the properties of a material. This allows discussing which parameters of an MEA model should be the subject of further statistical studies. We suggest to use microscopic models and imagery to quantify the statistical variability.

9.3 Analytical calculations of the properties of the cubic unit cells of regular pore networks

We present here the calculations giving the properties of the cubic regular pores networks studied in Chapter 3.

9.3.1 Description of the geometry studied

The geometry studied is the same as in Chapter 3. It is represented in Figure 9.2. Let d denote the diameter of the pores, a the setp of the network, k*d the diameter of the bonds. In this appendix, we work on a unit cell of the network.

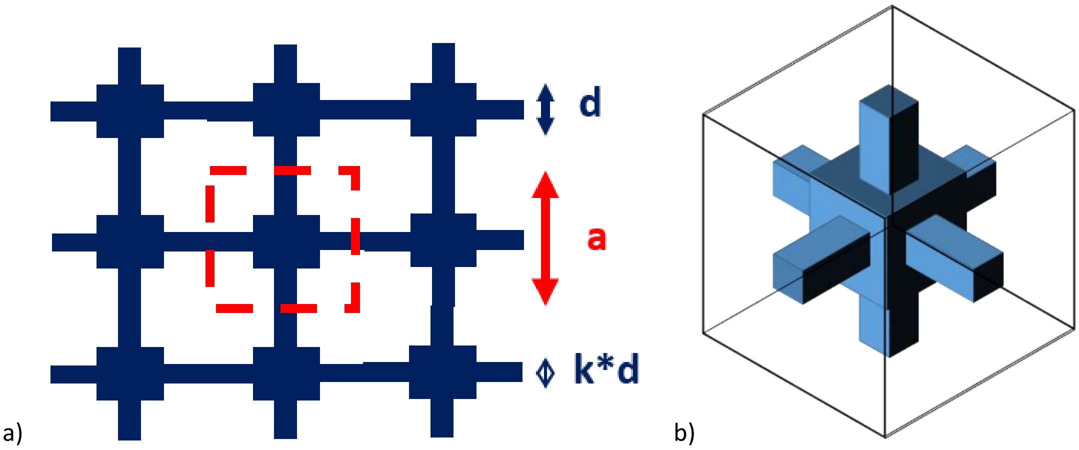

Figure 9.2 a) 2D section of the cubic lattice. B) 3D representation of a unit cell.

9.3.2 Transport properties of the gas phase

The relative effective diffusivity of a unit cell, $D_{eff:gas}$, is given by the following formula :

$$D_{eff:gas} = \frac{L}{S}\frac{D}{D_0} = u\left(1 - \frac{1}{k^2} + \frac{1}{k^2 u}\right)^{-1}$$

Équation 9.4

The volume fraction of gas is given by the following formula :

$$\varepsilon = (1 - 3k^2) + 3u^2k^2$$

Équation 9.5

Let us prove these formulas. The calculations are done by dividing the unit cell into 3 sections on which the geometry is invariant, as shown in Figure 9.3.

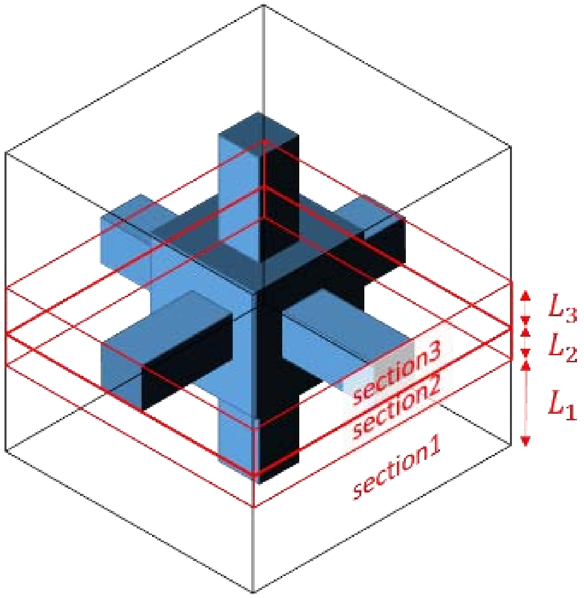

Figure 9.3 Diagram of the cubic unit cell. The three sections used to calculate the properties of this unit cell are shown. Sections 1 and 2 are shown once for simplicity, but they are in fact symmetrical with respect to Section 3.

Section 1

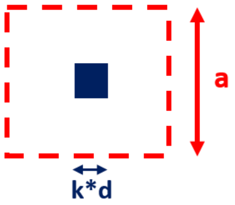

$$\mathcal{A}_1^{gas} = k^2 d^2$$

$$L_1 = \frac{a-d}{2}$$

Section 2

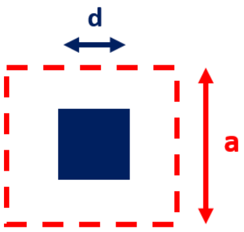

$$\mathcal{A}_2^{gas} = d^2$$

$$L_2 = \frac{d-kd}{2}$$

Section 3

We do not consider the lateral links (hatched in the figure below) for diffusivity because they do not contribute to in-plane diffusion. On the other hand, we consider for the porosity.

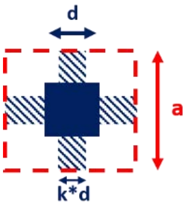

$$\mathcal{A}_3^{gas} = d^2$$

$$L_3 = \frac{kd}{2}$$

The conductance D of the unit cell is obtained by taking the harmonic sum of the conductances of the 3 sections. Indeed, the sections are in series for transport in this direction

$$\begin{aligned}\frac{D}{D_0} &= \left[\frac{2L_1}{\mathcal{A}_1^{solid}} + \frac{2L_2}{\mathcal{A}_2^{solid}} + \frac{2L_3}{\mathcal{A}_3^{solid}}\right]^{-1} \\ &= \left(\frac{d}{d^2} + \frac{a-d}{(kd)^2}\right)^{-1} \\ &= a\left(\frac{a}{d}\left(1 - \frac{1}{k^2}\right) + \frac{1}{k^2}\left(\frac{a}{d}\right)^2\right)^{-1}\end{aligned}$$

From this we deduce

$$D_{eff:gas} = \frac{L}{S}\frac{D}{D_0} = u\left(1 - \frac{1}{k^2} + \frac{1}{k^2 u}\right)^{-1}$$

The porosity is obtained from the volume of the three sections.

$$\begin{aligned}\varepsilon &= \frac{1}{a^3}\left(d^3 + 3(a-d)(kd)^2\right) \\ &= u^3(1 - 3k^2) + 3u^2k^2\end{aligned}$$

9.3.3 Transport properties of the solid phase

The relative effective electrical conductivity $C_{eff:solid}$ of a unit cell is given by the following formula:

$$C_{eff:solid} = \frac{L}{S}\frac{C}{C_0} = \left(\frac{1-u}{1-u^2k^2} + \frac{ku}{1-2ku+u^2(2k-1)} + \frac{(1-k)u}{1-u^2}\right)^{-1}$$

Équation 9.6

Let us prove this formula. The calculations are made by dividing the unit cell into 3 sections on which the geometry is invariant, as shown in Figure 9.3.

Section 1

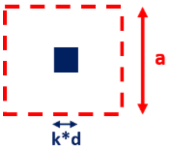

$$\mathcal{A}_1^{solid} = a^2 - k^2 d^2$$

$$L_1 = \frac{a-d}{2}$$

Section 2

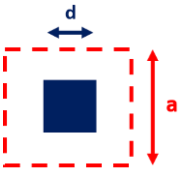

$$\mathcal{A}_2^{solid} = a^2 - d^2$$

$$L_2 = \frac{d-kd}{2}$$

Section 3

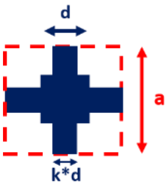

$$\mathcal{A}_3^{solid} = a^2 - d^2 - 4kd\left(\frac{a-d}{2}\right)$$

$$L_3 = \frac{kd}{2}$$

The conductivity C of the unit cell is obtained by taking the harmonic sum of the conductivities of the three sections. Indeed, the sections are in series for transport in this direction

$$\begin{aligned}\frac{C}{C_0} &= \left[\frac{2L_1}{\mathcal{A}_1^{solide}} + \frac{2L_2}{\mathcal{A}_2^{solide}} + \frac{2L_3}{\mathcal{A}_3^{solide}}\right]^{-1} \\ &= \left[\frac{a-d}{a^2-k^2d^2} + \frac{d-kd}{a^2-d^2} + \frac{kd}{a^2-d^2-2kd(a-d)}\right]^{-1}\end{aligned}$$

From this we deduce :

$$C_{eff:solid} = \frac{L}{S}\frac{C}{C_0} = \left[\frac{1-u}{1-k^2u^2} + \frac{(1-k)u}{1-u^2} + \frac{ku}{1-u^2-2ku(1-u)}\right]^{-1}$$

9.4 Constrictivity equation

This appendix deals with the equation of constrictivity. We first present this equation and then verify numerically its validity on simples microstructures.

9.4.1 Presentation of the constrictivity equation

We present in this section the constrictivity equation that was introduced in [Gaiselmann2014]. It is a correlation between the effective diffusivity of a porous material and a small number of geometric parameters of the microstructure. These geometrical parameters are defined rigorously and can be calculated on tomographic images. The constrictivity equation giving the effective diffusivity as a function of these geometric parameters is the following:

$$\frac{L}{S}\frac{D_{eff}}{D_0} = 2.03\frac{\varepsilon^{1.57}\beta^{0.72}}{\tau^2}$$

Équation 9.7

where ε is the volume fraction of the conductive phase, τ is the geometrical tortuosity, β is the constrictivity.

Geometric tortuosity is defined as the average length of the shortest path between the inlet and the outlet. It can be calculated directly on a 3D image of the material [Gaiselmann2014] [Cecen2012]. The constrictivity β is defined by the formula :

$$\beta = \left(\frac{r_{constriction}}{r_{pore}}\right)^2$$

Équation 9.8

where $r_{constriction}$ and r_{pore} are the mean constriction size and the mean pore size, respectively. The role of constrictivity in diffusive transports has also been studied in [Holzer2013].

This equation sheds new light on the geometric parameters that have an impact on diffusive transports in a porous material. Compared to the classical theory of effective diffusivity, where effective diffusivity is a function of porosity and of effective tortuosity rather than geometric tortuosity, this equation makes it possible to rigorously define the geometric tortuosity and calculate it on a tomographic image.

This equation has been established for solid oxide fuel cell electrodes and random graphs with a single connected component and without a dead end. It is valid only for diffusive transports through a phase whose properties are homogeneous.

The exponent 2 in the factor τ^2 of the equation of the constrictivity can be justified theoretically by considering that τ represents a change in the length scale intended to account for the difference in length of the microscopic paths and the macroscopic paths obtained by homogenization [Bazant2010].

9.4.2 Numerical verification of the constrictivity equation

We verify here the validity of the equation of the constrictivity on a simple microstructure. The microstructure used here is a regular cubic cell, presented in the previous section.

The porosity ε, tortuosity τ and constrictivity β of a cubit cell are given by the following formulas:

$$\varepsilon = u^3(1 - 3k^2) + 3u^2k^2$$

$$\tau = 1$$

$$\beta = k^2$$

The relative effective diffusivity of a cubit cell is given by the Équation 9.4.

Figure 9.4 shows the comparisons between this analytical formula and the approximation given by the constrictivity equation. Depending on the geometric parameters of the unit cell, the agreement between real diffusivity and the equation of the constrictivity good or not. The difference is less than 50% for the effective diffusivity of the unit cells of parameters u> 0.4 and k <0.8, which is considered a reasonable agreement. For the effective conductivity of the solid, the difference is less than 50% if the networks have a pore size u> k. Let us note that the analytical formula giving the constrictivity of the solid in these unit cells is an approximation, obtained by neglecting the effects of boundaries with the neighboring cells.

Another structure on which it would be possible to test the constrictivity effect is a link with a linearly decreasing profile, as used in section 3.1.1.1.3.2. The advantage of this structure is that the effective conductance and the equation of the constrictivity can be calculated analytically. These calculations confirm that the equation of the constrictivity is an approximation, more or less correct depending on the geometries.

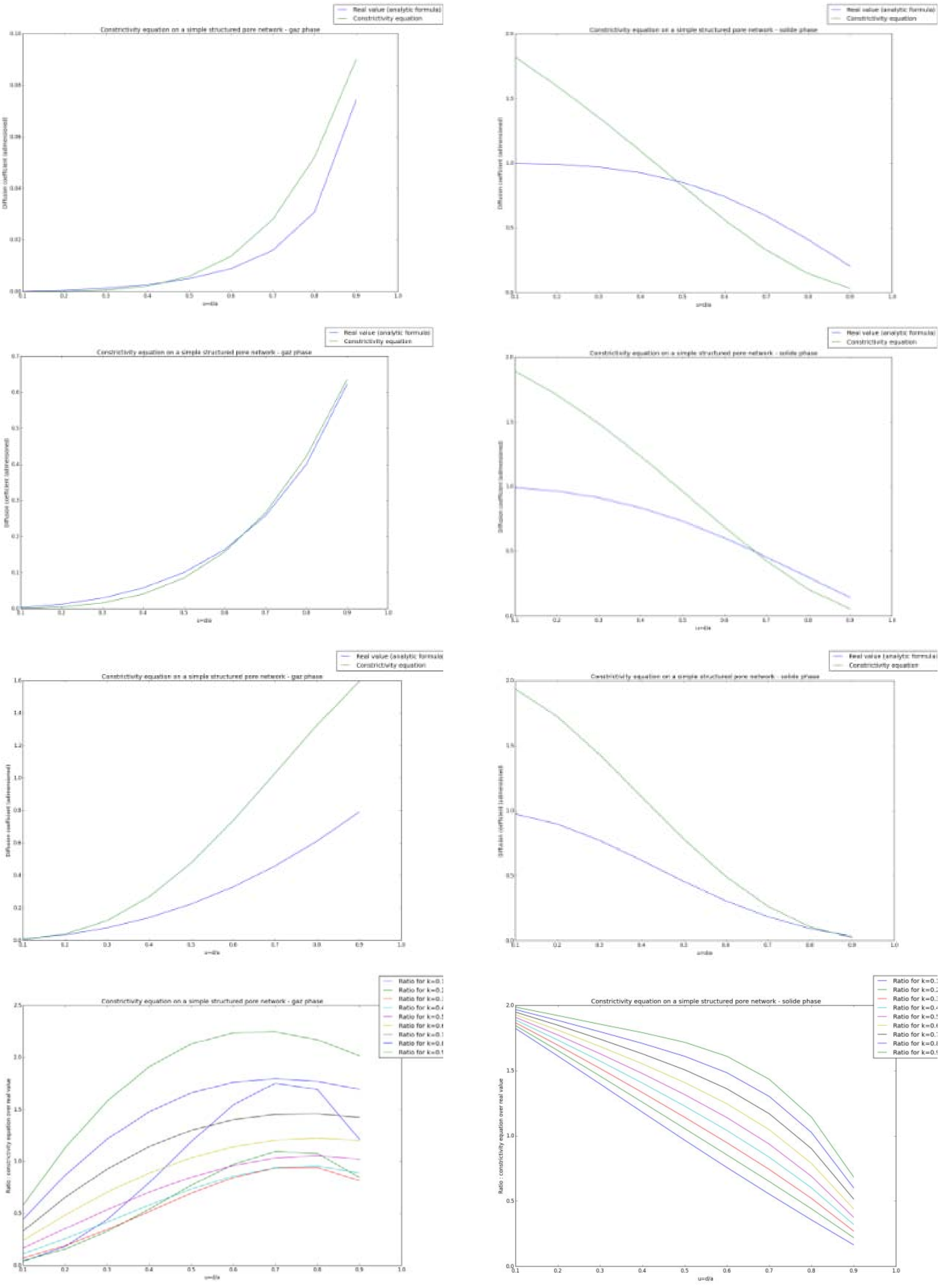

Figure 9.4 Comparison between constrictivity equation and analytical formulas for the effective properties of diffusive transport on a regular cubic lattice. Left: transport in the gas phase. Right: transport in the solid phase. From top to bottom: k = 0.1, k = 0.5, k = 0.9, ratio of constrictivity equation and analytical calculations.

9.4.3 Conclusion

The equation of constrictivity has the advantage of intuitively parameterizing the microstructures to estimate their effective diffusive transport properties. It constitutes an advance in comparison to the classical formula of effective diffusivity involving the effective tortuosity of the porous material, since it makes it possible to decompose this effective tortuosity into two rigorously defined and calculable effects, a geometric tortuosity effect and a constrictivity effect.

Nevertheless, the equation of constrictivity remains an approximation. It provides a good approximation of the effective transport properties of some microstructures, a less good approximation for other microstructures. However, we found that it gives deviations of less than 50% for most of the structures that we tested.

9.4.4 Bibliography

- [Bazant2010] Martin Bazant. 10.626 Electrochemical Energy Systems. Spring 2010. Massachusetts Institute of Technology: MIT OpenCourseWare, http://ocw.mit.edu. License: Creative Commons BY-NC-SA.

- [Cecen2012] A. Çeçen, E. A. Wargo, A. C. Hanna, D. M. Turner, S. R. Kalidindi and E. C Kumbur, 3-D Microstructure Analysis of Fuel Cell Materials: Spatial Distributions of Tortuosity, Void Size and Diffusivity, J. Electrochem. Soc. 2012, volume 159, issue 3, B299-B307

- [Gaiselmann2014] G. Gaiselmann, M. Neumann, V. Schmidt, O. Pecho, T. Hocker, L. Holzer, Quantitative relationships between microstructure and effective transport properties based on virtual materials testing, AIChE Journal, Volume 60, Issue 6, June 2014, pages 1983–1999

- [Holzer2013] L. Holzer, D. Wiedenmann, B. Münch, L. Keller, M. Prestat, Ph. Gasser, I. Robertson, B. Grobéty, The influence of constrictivity on the effective transport properties of porous layers in electrolysis and fuel cells, J Mater Sci (2013) 48:2934–2952